

EARTH OBSERVATIONS AND SOCIETAL IMPACTS

GUEST EDITORS: YUEI-AN LIOU, CHUNG-RU HO, YURIY KULESHOV, AND JEAN-PIERRE BARRIOT





Earth Observations and Societal Impacts

Advances in Meteorology

Earth Observations and Societal Impacts

Guest Editors: Yuei-An Liou, Chung-Ru Ho, Yuriy Kuleshov,
and Jean-Pierre Barriot



Copyright © 2014 Hindawi Publishing Corporation. All rights reserved.

This is a special issue published in "Advances in Meteorology." All articles are open access articles distributed under the Creative Commons Attribution License, which permits unrestricted use, distribution, and reproduction in any medium, provided the original work is properly cited.

Editorial Board

Paulo Artaxo, Brazil
Guy Brasseur, USA
Mladjen Ćurić, Serbia
Raymond Desjardins, Canada
Klaus Dethloff, Germany
Panuganti C. S. Devara, India
Julio Diaz, Spain
Shouting Gao, China
Luis Gimeno, Spain

Sven-Erik Gryning, Denmark
Ismail Gultepe, Canada
Hiroyuki Hashiguchi, Japan
Didier Hauglustaine, France
Ivar S. A. Isaksen, Norway
Yasunobu Iwasaka, Japan
Hann-Ming H. Juang, USA
George Kallos, Greece
Harry D. Kambezidis, Greece

Richard Leitch, Canada
Monique Leclerc, USA
Gwo-Fong Lin, Taiwan
Edward Llewellyn, Canada
Kyaw T. Paw, USA
Sara C. Pryor, USA
Eugene Rozanov, Switzerland
Zhihua Zhang, China

Contents

Earth Observations and Societal Impacts, Yuei-An Liou, Chung-Ru Ho, Yuriy Kuleshov, and Jean-Pierre Barriot
Volume 2014, Article ID 619203, 3 pages

Improving the Operational Methodology of Tropical Cyclone Seasonal Prediction in the Australian and the South Pacific Ocean Regions, J. S. Wijnands, K. Shelton, and Y. Kuleshov
Volume 2014, Article ID 838746, 8 pages

Comparison of the Synoptic Environments Conducive to Eastward versus Southeastward Transport of Asian Dust Events, Fujung Tsai and Wei-Nai Chen
Volume 2014, Article ID 467659, 13 pages

Unusual Warming in the Coastal Region of Northern South China Sea and Its Impact on the Sudden Intensification of Tropical Cyclone Tembin (2012), Zhe-Wen Zheng
Volume 2014, Article ID 250752, 7 pages

Double Compressions of Atmospheric Depth by Geopotential Tendency, Vorticity, and Atmospheric Boundary Layer Affected Abrupt High Particulate Matter Concentrations at a Coastal City for a Yellow Dust Period in October, Hyo Choi and Mi Sook Lee
Volume 2014, Article ID 756230, 13 pages

Changes in Glaciers and Glacial Lakes and the Identification of Dangerous Glacial Lakes in the Pumqu River Basin, Xizang (Tibet), Tao Che, Lin Xiao, and Yuei-An Liou
Volume 2014, Article ID 903709, 8 pages

Validation of ASTER Surface Temperature Data with *In Situ* Measurements to Evaluate Heat Islands in Complex Urban Areas, Bonggeun Song and Kyunghun Park
Volume 2014, Article ID 620410, 12 pages

Impacts of Two Types of El Niño and La Niña Events on Typhoon Activity, Po-Chun Hsu, Chung-Ru Ho, Shin-Jye Liang, and Nan-Jung Kuo
Volume 2013, Article ID 632470, 8 pages

A WebGIS-Based Information System for Monitoring and Warning of Geological Disasters for Lanzhou City, China, Fang Miao and Qi Yuan
Volume 2013, Article ID 769270, 9 pages

Impacts of Pond Change on the Regional Sustainability of Water Resources in Taoyuan, Taiwan, Yuei-An Liou, Tai-Sheng Wang, and Hai-Po Chan
Volume 2013, Article ID 243456, 6 pages

Spatial Downscaling of TRMM Precipitation Using Geostatistics and Fine Scale Environmental Variables, No-Wook Park
Volume 2013, Article ID 237126, 9 pages

Editorial

Earth Observations and Societal Impacts

Yuei-An Liou,^{1,2} Chung-Ru Ho,^{2,3} Yuriy Kuleshov,⁴ and Jean-Pierre Barriot⁵

¹ Center for Space and Remote Sensing Research (CSRSR), National Central University, Chungli 32001, Taiwan

² Taiwan Group on Earth Observations, Zhubei 30274, Taiwan

³ Department of Marine Environmental Informatics, National Taiwan Ocean University, Keelung 20224, Taiwan

⁴ Bureau of Meteorology, GPO Box 1289, Melbourne, VIC 3001, Australia

⁵ Geodesy Observatory of Tahiti, University of French Polynesia, BP 6570, 98702 Faaa-Tahiti, French Polynesia

Correspondence should be addressed to Yuei-An Liou; yueian@csrsr.ncu.edu.tw

Received 4 May 2014; Accepted 4 May 2014; Published 5 June 2014

Copyright © 2014 Yuei-An Liou et al. This is an open access article distributed under the Creative Commons Attribution License, which permits unrestricted use, distribution, and reproduction in any medium, provided the original work is properly cited.

“You cannot manage what you cannot measure.” It is an old adage that is still true today. Unless we observe and measure the Earth environment in a consistent manner, we cannot effectively manage it for improvement. “Earth Observation” thus plays an increasing important role in the sustainable development of the globe. It involves the very close investigation and measurement on the Earth and the derived results from the direct or indirect observations and measurements are the crucial information used to construct the supporting policies for the environments, postdisaster management, and so forth [1–6].

The 3rd International Conference on Earth Observations and Societal Impacts, ICEO&SI 2013 (<http://2013.iceo-si.org.tw/home>), followed the tradition set by the previous meetings (ICEO&SI 2011 and 2012) by focusing on observations of the Earth environment and their societal impacts. With the success of ICEO&SI 2013 jointly cohosted by Taiwan Group on Earth Observations (<http://tgeo.org.tw/>) and National Cheng Kung University, more than 250 academics, researchers, engineers, and students from 15 countries had wonderful stays in Tainan. All in all, 104 papers were presented in 12 sessions including 5 keynote speeches, 56 oral papers, and 43 posters, which turned into this special issue as one of the academic fruits. This special issue consists of 10 articles, which are ordered according to topic: weather/climate, disasters/energy, and water/agriculture. The main scientific findings are briefly introduced below.

Tropical cyclones (called typhoons in the Western Pacific) are the most severe weather phenomena, which

have significant impacts on the coastal communities when they approach the coast or make landfall. Preparedness to typhoons is one of the key factors to limit the impact of such devastating events. In this special issue, improving the operational methodology of tropical cyclone seasonal prediction in the Australian and the South Pacific ocean regions has been described. New approach (support vector regression methodology) for estimating tropical cyclone activity in the coming season to assist the Australian Bureau of Meteorology in preparing an operational outlook for the likelihood of an above median number of tropical cyclones seasonally for the Australian region (AR; 5°S to 40°S, 90°E to 160°E) and the South Pacific Ocean (SPO; 5°S to 40°S, 142.5°E to 120°W) has been investigated. New explanatory variables to improve the accuracy of seasonal tropical cyclone predictions have also been investigated. Correlation analysis and subsequent cross validation of the generated models show that the Dipole Mode Index (DMI), describing the intensity of the Indian Ocean Dipole, performs well as an explanatory variable for tropical cyclone prediction in both AR and SPO. Other variables, which yielded high correlation with the number of tropical cyclones, were Niño4 SST anomalies (for AR) and Niño1+2 SST anomalies (for SPO region). For both AR and SPO, the developed model which utilised the combination of explanatory variables Niño1+2 SST anomalies, Niño4 SST anomalies, and DMI had the best forecasting performance. The developed model is recommended for operational tropical cyclone seasonal forecasting in the AR and SPO regions.

Aerosols can be found over oceans, deserts, mountains, forests, ice sheets, and so on. They drift in the air from

the stratosphere to the surface and have major impacts on climate and health. Dust as a kind of aerosols can travel a long distance to affect different areas. The strength of low-level trough and surface anticyclonic system are important in determining the transport route of Asian dust event. With model simulations, it is found that the transportation of dusts from Gobi Desert toward Korea is the combination of dusts transported from the desert under westerly wind with particulate matters and gases from vehicles on the road of the city caused high aerosol concentrations near the ground surface maxima during the sunset time.

Through investigating a case study for a typhoon in Taiwan region, unusual warming in the coastal region of northern South China Sea and its impact on the sudden intensification of tropical cyclone Tembin (2012) are described in this issue. Tropical cyclone Tembin (2012) passed twice and made landfall over south tip of Taiwan in August 2012. During its passage, an unusual sea surface warming was observed around 22.5°N, 117°E in the coastal region of northern South China Sea. Subsequently, Tembin (2012) passed over this extreme warming region and its intensity was enhanced dramatically from Category 1 to Category 3 within less than 1-day time interval. This unusual warming seems to largely prompt the intensification of Tembin. The results indicate that a distinct positive short-wave radiation influx anomaly may dominate the generation of the unusual warming in the shore region during Tembin's passage. This result is validated by the distributions of free cloudy coverage shown in satellite infrared images.

Advanced Spaceborne Thermal Emission Reflection Radiometer (ASTER) surface temperature data were compared with *in situ* measurements to validate the use of ASTER data for studying urban heat islands at eight sites in Changwon, Korea, during the summer and fall of 2012. Comparisons showed that ASTER derived temperatures were generally 4.27°C lower than temperatures collected by *in situ* measurements during the daytime, except on cloudy days. However, ASTER temperatures were higher by 2.23–2.69°C on two dates during the nighttime. Temperature differences between a city park and a paved area were insignificant. Differences between ASTER derived temperatures and onsite measurements are caused by a variety of factors including the application of emissivity values, while the complex spatial characteristics of urban areas are not considered. Therefore, to improve the accuracy of surface temperatures extracted from infrared satellite imagery, a revised model is proposed whereby temperature data is obtained from ASTER and emissivity values for various land covers are extracted based on *in situ* measurements.

El Niño-Southern Oscillation is one of the most important climate drivers on the planet and its variability has significant impact on tropical cyclones. In this issue, impacts of two types of El Niño and La Niña events on typhoon activity were presented. The HadISST (Hadley Centre Sea Ice and Sea Surface Temperature) dataset is used to define the years of El Niño, El Niño Modoki, and LaNiña events, from 1950 to 2012, and to find out the impacts of these events on typhoon activity. The results show that the position and the intensity of typhoon are affected by different phases

on ENSO. The formation positions of typhoon are farther eastward moving in El Niño years than in La Niña years and much further eastward in El Niño Modoki years. The life time and the distance of movement are longer, and the intensity of typhoons is stronger in El Niño and in El Niño Modoki years than in La Niña years.

Monitoring and warning of geological disasters accurately and in a timely fashion would dramatically mitigate casualties and economic losses. A WebGIS-based information system was designed for monitoring and warning of geological disasters. This system provides scientific suggestions to commanders for quick response to the possibility of geological disaster.

Global change may refer to the changes of atmosphere, oceans, geology, topography, and ecology. It is one of the important issues to the human society. Satellite imagery as a tool is very helpful to detect the changes. Satellite images were used to investigate the evolutions of glaciers and glacial lakes in the Pumqu river basin. They found that the magnitudes of glacier retreat rate and glacial lake increase rate during the period of 2001–2013 are more significant than those for the period of the 1970s–2001. Changes occurred not only by nature, but also by anthropic activities. The impact of changes in farm ponds on the regional agricultural environment in Taoyuan, Taiwan, with multiyear SPOT satellite imagery was explored. Results show that farm ponds have decreased from 1993 to 2010 by human activities. They suggested that, for the sustainable agriculture, farm ponds shall be classified and cherished as a public asset for the future development.

Satellite imagery has been demonstrated usefully for global, regional, and local studies. However, some detailed studies cannot be made with coarse spatial resolution of passive microwave imagery. A geostatistical downscaling scheme was developed to generate fine scale precipitation information from Tropical Rainfall Measuring Mission (TRMM) data. The results of this scheme reflect detailed characteristics with better predictive performance.

This special issue aims to summarize the most recent developments and ideas in the field. It will serve as a valuable asset for the scientists and engineers working on the scientific and technological problems of Earth Observations and various environment issues. Our continuous efforts will illustrate the core mission by inspecting terrestrial environment information to offer solid solutions for the societal needs.

Acknowledgments

We are grateful to all the authors who contributed to this issue and to all the reviewers whose suggestions have helped improve the quality of the papers published in this issue.

Yuei-An Liou
Chung-Ru Ho
Yuriy Kuleshov
Jean-Pierre Barriot

References

- [1] S. K. Kar, Y. A. Liou, and K. J. Ha, "Aerosol effects on the enhancement of cloud-to-ground lightning over major urban areas of South Korea," *Atmospheric Research*, vol. 92, no. 1, pp. 80–87, 2009.
- [2] Y. A. Liou, S. K. Kar, and L. Y. Chang, "Use of high-resolution formosat-2 satellite images for post-earthquake disaster assessment: a study following the 12 may 2008 Wenchuan earthquake," *International Journal of Remote Sensing*, vol. 31, no. 13, pp. 3355–3368, 2010.
- [3] Y. A. Liou, H. C. Sha, T. M. Chen et al., "Assessment of disaster losses in rice field and yield after tsunami induced by the 2011 Great East Japan earthquake," *Journal of Marine Science and Technology*, vol. 20, no. 6, pp. 618–623, 2012.
- [4] F. C. Ming, C. Ibrahim, C. Barthe et al., "Observation and a numerical study of gravity waves during tropical cyclone Ivan (2008)," *Atmospheric Chemistry and Physics*, vol. 14, pp. 641–658, 2014.
- [5] C. H. Cheng, F. Nnadi, and Y. A. Liou, "Energy budget on various land use areas using reanalysis data in Florida," *Advances in Meteorology*, vol. 2014, Article ID 232457, 13 pages, 2014.
- [6] Y. A. Liou and S. K. Kar, "Evapotranspiration estimation through remote sensing and various surface energy balance algorithms—a review," *Energies*, vol. 7, no. 5, pp. 2821–2849, 2014.

Research Article

Improving the Operational Methodology of Tropical Cyclone Seasonal Prediction in the Australian and the South Pacific Ocean Regions

J. S. Wijnands,¹ K. Shelton,² and Y. Kuleshov^{1,2}

¹ The University of Melbourne, Parkville, VIC 3010, Australia

² Bureau of Meteorology, Docklands, VIC 3008, Australia

Correspondence should be addressed to Y. Kuleshov; y.kuleshov@bom.gov.au

Received 23 July 2013; Revised 20 December 2013; Accepted 6 January 2014; Published 17 March 2014

Academic Editor: Jean-Pierre Barriot

Copyright © 2014 J. S. Wijnands et al. This is an open access article distributed under the Creative Commons Attribution License, which permits unrestricted use, distribution, and reproduction in any medium, provided the original work is properly cited.

Tropical cyclones (TCs) can have a major impact on the coastal communities of Australia and Pacific Island countries. Preparedness is one of the key factors to limit TC impacts and the Australian Bureau of Meteorology issues an outlook of TC seasonal activity ahead of TC season for the Australian Region (AR; 5°S to 40°S, 90°E to 160°E) and the South Pacific Ocean (SPO; 5°S to 40°S, 142.5°E to 120°W). This paper investigates the use of support vector regression models and new explanatory variables to improve the accuracy of seasonal TC predictions. Correlation analysis and subsequent cross-validation of the generated models showed that the Dipole Mode Index (DMI) performs well as an explanatory variable for TC prediction in both AR and SPO, Niño4 SST anomalies—in AR and Niño1+2 SST anomalies—in SPO. For both AR and SPO, the developed model which utilised the combination of Niño1+2 SST anomalies, Niño4 SST anomalies, and DMI had the best forecasting performance. The support vector regression models outperform the current models based on linear discriminant analysis approach for both regions, improving the standard deviation of errors in cross-validation from 2.87 to 2.27 for AR and from 4.91 to 3.92 for SPO.

1. Introduction

Tropical cyclones (TCs) are extreme weather events that form each season over tropical oceans. In the Australian Region (AR; 5°S to 40°S, 90°E to 160°E) and the South Pacific Ocean (SPO; 5°S to 40°S, 142.5°E to 120°W) TCs mainly occur during the six months from November to April; however, TCs do occur outside the TC season. TCs can have a major impact on human life when they make land-fall. For example, in 1974 the Australian city of Darwin was devastated by TC Tracy, killing 71 people [1]. The main dangers of TCs are destructive winds, heavy rainfall, flooding, and storm surges. Besides the impact on human life, TCs can have a severe impact upon Pacific island countries and their economies. For example, the small island of Tikopia located in the SPO (12° 18' S 168° 50' E) was completely devastated in 2002 by TC Zoe [2].

Preparation for TCs is an important element to reduce the destructive impacts of TC land-falls. Therefore, the Bureau of

Meteorology aims to predict the likelihood of TC activity for several regions at the start of each TC season. Currently the operational statistical model of the Bureau of Meteorology consists of two linear discriminant analysis (LDA) models, one based on the Southern Oscillation Index (SOI) and one based on Niño3.4 Sea Surface Temperatures (SST) [3]. The results have been disseminated in a form of TC seasonal outlooks, to provide local communities and government authorities with early advice about expected TC activity. For public release, the models produce probabilities of above median tropical cyclone activity; however, they can also produce the most likely number of TCs in the upcoming season.

A different statistical model-based approach is to use machine learning algorithms. A recent pilot study by Richman and Leslie [4] indicates that support vector regression performs well for TC prediction. In this paper we investigate the use of machine learning algorithms for the Bureau of Meteorology TC forecasting regions.

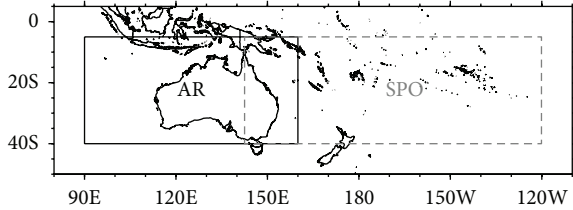


FIGURE 1: Map of two study areas: AR is defined as the area 90°E - 160°E and 5°S - 40°S and SPO is defined as the region 142.5°E - 120°W and 5°S - 40°S .

2. Data and Methodology

The Bureau of Meteorology's National Climate Centre (NCC) has developed a TC archive for the Southern Hemisphere, in close collaboration with international partners [5]. The number of TCs for each season can be obtained from the Southern Hemisphere TC archive via the Pacific Tropical Cyclone Data Portal of the Bureau of Meteorology (<http://www.bom.gov.au/cyclone/history/tracks/>). The Southern Hemisphere TC archive has been developed by consolidating best track data prepared by Regional Specialised Meteorological Centres (RSMCs) Nadi (Fiji) and Tropical Cyclone Warning Centres (TCWCs) Brisbane, Darwin and Perth (Australia) and Wellington (New Zealand). To estimate TC intensity, Dvorak methodology is used operationally by the RSMCs and TCWCs with the World Meteorological Organization's responsibilities for issuing TC warning and preparing best track data [6]. To keep consistency with previous studies, the genesis of a TC is defined when a cyclonic system first attains a central pressure equal to or less than 995 hPa [7–11]. AR is defined as the area 90°E - 160°E and 5°S - 40°S and SPO is defined as the region 142.5°E - 120°W and 5°S - 40°S (Figure 1). NCC of the Australian Bureau of Meteorology has operational responsibilities to issue TC seasonal outlooks for both the AR and the SPO region and to provide Australians and population of countries in the South Pacific Ocean with early warning advice about TC activity expected in the coming season. Consequently, there is an overlap between two areas under investigation. This overlap was taken in consideration in this study; if a TC was recorded in both AR and SPO region, we included it in our analysis for both areas.

Operational tropical cyclone seasonal prediction in AR started with pioneering work by Nicholls [12, 13] who developed statistical methodology for forecasting TC activity in the upcoming season based on state of the El Niño—Southern Oscillation (ENSO). ENSO is a large-scale climate phenomenon that occurs across the tropical Pacific Ocean and has two distinctly different phases: warm (El Niño) and cold (La Niña), with an intervening neutral phase. Relationships between ENSO and TC activity in the Western Pacific and its smaller subregions such as AR are well understood and described in the literature (e.g., [8, 14, 15]). These relationships allow forecasting TC seasonal activity in October for six months ahead using values of ENSO indices which describe the state of the atmosphere and ocean in

the central Pacific in the preceding months of July–August–September. Explanatory variables that have been investigated in this study include a number of ENSO indices such as Niño1+2, Niño3, Niño3.4 and Niño4 SST anomalies, 5VAR index, Multivariate ENSO Index (MEI), and El Niño Modoki Index. Detailed description of the ENSO indices used in this study can be found in Trenberth [16], Ashok et al. [17], Wolter and Timlin [18], and Kuleshov et al. [9]. Two other well-established indices which have been used as potential predictors of TC activity in AR and SPO are the Dipole Mode Index (DMI) and the Southern Oscillation Index (SOI).

Values for Niño1+2, Niño3, Niño3.4, and Niño4 SST anomalies have been obtained from the Climate Prediction Center (CPC) of the National Oceanic and Atmospheric Administration (NOAA) (<http://www.cpc.ncep.noaa.gov/data/indices/ersst3b.nino.mth.81-10.ascii>). 5VAR is an NCC-internal ENSO index, based on the first principal component of monthly Darwin mean sea level pressure (MSLP), Tahiti MSLP, and Niño3, Niño3.4, and Niño4 SST indices [9–11]. Data for MEI have been obtained from NOAA (<http://www.esrl.noaa.gov/psd/enso/mei/table.html>). The Japan Agency for Marine–Earth Science and Technology (JAMSTEC) provides data for the El Niño Modoki Index (<http://www.jamstec.go.jp/frsgc/research/d1/iod/DATA/emi.monthly.txt>) and the Dipole Mode Index (http://www.jamstec.go.jp/frsgc/research/d1/iod/DATA/dmi_HadISST-jan1958-dec2012.txt). Data for SOI have been obtained from the Bureau of Meteorology (<ftp://ftp.bom.gov.au/anon/home/ncc/www/sco/soi/soiplaintext.html>).

Since meteorological satellites came into operational use at the end of the 1960s, the reliability of TC data has improved significantly [19]. Earlier data are not considered sufficiently accurate for modelling purposes and therefore data prior to the 1969–70 season have not been included in our analysis. Kuleshov et al. [10, 11] have identified this point as an outlier in several models. The SPO best track database contains data up until the 2010–11 season, whereas AR contains best track information up to the 2011–12 season. Therefore, seasons from 1970–71 to 2010–11 data have been used for SPO, while 1970–71 to 2011–12 data have been used for AR.

Using Weka [20] the performance of several machine learning algorithms has been investigated. Weka (Waikato Environment for Knowledge Analysis) is a collection of machine learning algorithms for data mining tasks, developed by the University of Waikato in New Zealand. This open source software package includes algorithms such as decision trees, nearest neighbour classifiers, and regression models. We applied various machine learning algorithms to the TC data set, including isotonic regression, least median squared regression, linear regression, multilayer perceptron, pace regression, normalised Gaussian radial basis function network, support vector regression, K-nearest neighbours classifier, K^* instance-based classifier, locally weighted learning, additive regression, conjunctive rule, decision table majority classifier, M5 rules, M5P, decision stump, REP-Tree decision tree, bagging in combination with decision tree algorithms, and random subspace in combination with decision tree algorithms. To avoid artificial skill we did not use all training data to fit the models, but instead

performed a cross-validation analysis for each of the potential prediction models. Therefore, the model prediction for each TC season was an out of sample prediction. First, we utilised all explanatory variables for each algorithm to make an initial selection of algorithms with potential skill. This selection was made by ranking all models based on the root mean squared error (RMSE) statistic. Then, we focussed on improving the performance of promising algorithms for seasonal TC prediction by selecting different combinations of explanatory variables.

There was a large difference between all models, as some showed very little skill in the seasonal prediction of TCs. Most decision trees that we investigated did not perform very well, possibly due to the small number of years of data that is currently available. Overall, out of the algorithms that we investigated, the machine learning algorithm that performed best for the seasonal prediction of TCs was support vector regression. This algorithm exhibited the lowest RMSE in cross-validation and will be the focus of the remainder of this paper.

The support vector regression model is an extension to ε -support vector regression [21]. We assume we have a set of observations y_i and several explanatory variables $x_{1,i}$, $x_{2,i}$, $x_{3,i}$, ..., $x_{n,i}$ with i the number of observations and n the number of explanatory variables. In ε -support vector regression the goal is to find a function $f(\underline{x})$ that predicts the observations and has a maximum error smaller than or equal to ε , while being as flat as possible, meaning none of the coefficients is very large relative to the rest of the coefficients. For a linear function $f(\underline{x})$ this can be described by:

$$f(\underline{x}) = \langle \underline{w}, \underline{x} \rangle + b \text{ with } \underline{w}, \underline{x} \in R^n, b \in R \quad (1)$$

and n the number of explanatory variables.

In this equation \underline{x} is a vector with explanatory variables, \underline{w} is a vector containing coefficients, and b is the bias term. We search for optimal solution by changing coefficients vector \underline{w} . The notation $\langle \underline{w}, \underline{x} \rangle$ denotes the dot product between \underline{w} and \underline{x} . Flatness for $f(\underline{x})$ means searching for a set of small coefficients in vector \underline{w} . The idea behind this is to make the model less sensitive to errors in measurement or random shocks in explanatory variables, leading to better prediction performance.

To solve (1) the following is used:

$$\begin{aligned} &\text{Minimise } \frac{1}{2} \langle \underline{w}, \underline{w} \rangle \\ &\text{subject to } \begin{cases} y_i - \langle \underline{w}, \underline{x}_i \rangle - b \leq \varepsilon \\ \langle \underline{w}, \underline{x}_i \rangle + b - y_i \leq \varepsilon. \end{cases} \end{aligned} \quad (2)$$

The formulation described above can sometimes be infeasible, when no function exists where the maximum error is ε . To solve this problem the methodology is extended by adding slack variables ξ_i and ξ_i^* to the model. In case the absolute error for observation y_i , given by $|y_i - f(x_i)|$, is larger than ε , one of the slack variables ξ_i or ξ_i^* will be equal to the excess error and the other slack variable will be set to 0. Instead of minimising $(1/2)\langle \underline{w}, \underline{w} \rangle$, we minimise $(1/2)\langle \underline{w}, \underline{w} \rangle$ plus a penalty for errors exceeding the threshold ε .

TABLE 1: Correlation with number of TCs in AR.

Explanatory variable	Month with highest correlation	Correlation
Niño4 SST anomalies	September	-0.672
Dipole Mode Index	September	-0.615
Niño3.4 SST anomalies	Average Aug/Sep	-0.611
5VAR index	August	-0.597
El Niño Modoki Index	September	-0.590
SOI	August	0.583
Niño3 SST anomalies	September	-0.523
MEI	September	-0.520
Niño1 + 2 SST anomalies	September	-0.289

Consider

$$\begin{aligned} &\text{Minimise } \frac{1}{2} \langle \underline{w}, \underline{w} \rangle + C \sum_{i=1}^n (\xi_i + \xi_i^*) \\ &\text{subject to } \begin{cases} y_i - \langle \underline{w}, \underline{x}_i \rangle - b \leq \varepsilon + \xi_i \\ \langle \underline{w}, \underline{x}_i \rangle + b - y_i \leq \varepsilon + \xi_i^* \\ \xi_i, \xi_i^* \geq 0. \end{cases} \end{aligned} \quad (3)$$

The complexity factor $C > 0$ is used to mathematically enforce more importance on the flatness of $f(\underline{x})$ or the amount up to which deviations larger than ε are tolerated. Equation (3) shows the approach that is used for seasonal TC prediction. Further information on support vector regression is provided by Smola and Schölkopf [22].

3. Results

3.1. Selection of Explanatory Variables. To decide which explanatory variables to use, an initial correlation analysis has been performed. As seasonal prediction has to be performed in October before the TC season starts, only values for September or earlier months can be used for forecasting. The values for the preceding months July, August, and September were investigated and also the two and three month averages for August and September and July, August and September. Results for several potential explanatory variables in AR are shown in Table 1 ranked by absolute correlation. Table 2 presents the results of correlation analysis for SPO; however, explanatory variable are listed in the same order as in Table 1 rather than ranked by absolute correlation, to assist readers in comparing the results for both regions. The explanatory variables with a high absolute correlation would presumably work well when used in a model to predict TC activity. This analysis has been performed separately for AR and SPO region to select the most promising predictors for each region. As for AR the best track data were available until the 2011-12 season; correlations between number of TCs and the explanatory variables have been investigated over the 1970-71–2011-12 period. For SPO this period was 1970-71–2010-11.

This analysis assisted us in selecting the indices with high correlation with regional TC activity. High correlation with some indices could be easily traced to teleconnections with

TABLE 2: Correlation with number of TCs in SPO.

Explanatory variable	Month with highest correlation	Correlation
Niño4 SST anomalies	August	-0.157
Dipole Mode Index	August	-0.216
Niño3.4 SST anomalies	September	0.056
5VAR index	September	0.055
El Niño Modoki Index	Average Aug/Sep	-0.307
SOI	August	0.064
Niño3 SST anomalies	September	0.149
MEI	July	0.127
Niño1+2 SST anomalies	Average Jul/Aug/Sep	0.252

the environment favourable for TC genesis and development in the selected regions of the Southern Hemisphere [8]; for example, negative (positive) Niño4 SST anomalies in AR (SPO) could be explained through cooler (warmer) SST in the TC genesis region. On the other hand, for some indices it is not so straight forward, for example, negative (positive) Niño1+2 SST anomalies in AR (SPO) which we found in this study. In addition, we found that combination of explanatory variables gives better results than using only one variable (details are in following sections).

Concurrently, exploring variants of ENSO Modoki for the seasonal prediction of Coral Sea TC activity, Ramsay et al. [23] also found that predictive skill is maximised when indices capturing the relative changes to equatorial SSTs in the Pacific are included; hence, the use of Niño 4 and Niño1+2 together in their study too. While further detailed research is required to explain teleconnections which have some influence there, it is clear that the combination of Niño indices describes better the basinwide equatorial Pacific SST anomaly variations than any Niño index alone. However, correlation between the indices should be taken in consideration when combining them. For example, Niño4, Niño3, and Niño3.4 indices are strongly correlated (using the data from <http://www.cpc.ncep.noaa.gov/data/indices/ersst3b.nino.mth.81-10.ascii> one can find a correlation of 0.77 for September Niño4 with Niño3 (1970–2012) indicating that these indices indeed similarly explain SST variability in the central Pacific). On the other hand, correlation for Niño1+2 with Niño4 is only 0.59 which suggests that a combination of these two indices would add value to more comprehensive description of basinwide changes related to ENSO. Note the Niño1+2 and Niño4 indices have previously been combined into the Trans-Niño index (http://www.cgd.ucar.edu/cas/catalog/climind/TNI_N34/) so there is a history of using these together. However, to the best of our knowledge, there is no literature on relationship between Niño1+2 variability and Australian climate. The physical link between Niño1+2 and the variability of TCs in Australian and SPO regions will be a subject of our future research but is beyond the scope of the current study.

The aim of this analysis was to select the months with the highest correlation for all potential model variables. In the

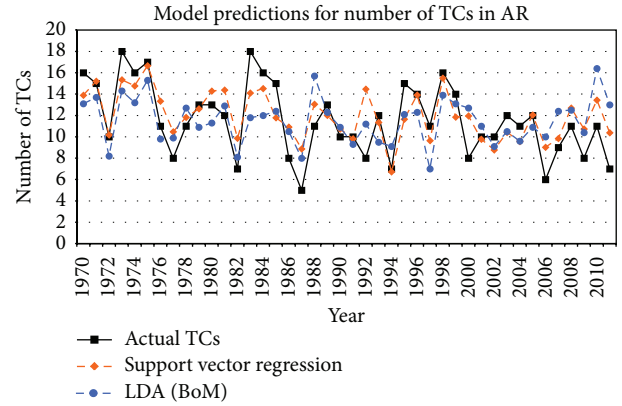


FIGURE 2: Leave-one-out cross-validation results AR.

TABLE 3: Goodness-of-fit statistics AR.

	Support vector regression	LDA (Bureau of Meteorology)
R^2	53.3%	27.4%
Adjusted R^2	49.6%	23.6%
St. dev. errors	2.266	2.874

remainder of this paper the months in Tables 1 and 2 will be used to model TC activity for AR and SPO, respectively.

3.2. Support Vector Regression Models. For both AR and SPO the combination of explanatory variables Niño1+2 SST anomalies, Niño4 SST anomalies, and DMI has the best forecasting performance. This was tested using leave-one-out cross-validation. Although the El Niño Modoki Index had the highest correlation with number of TCs in SPO, utilising this variable in the support vector regression resulted in worse forecasting performance than the model that was finally selected. As a result of the correlation analysis the values of the explanatory variables are taken from different months for AR and SPO. The support vector regression model for AR uses September values for all three explanatory variables, while for SPO the three-month average over July, August, and September is used for Niño1+2 SST anomalies and the August value for Niño4 SST anomalies and DMI. The explanatory variables have been normalised before support vector regression was applied.

Both AR and SPO support vector regression models used the polynomial kernel $K(\mathbf{x}, \mathbf{y}) = \langle \mathbf{x}, \mathbf{y} \rangle^p$. In support vector regression input variables are mapped into a feature space using this kernel function. The regression function then aims to separate data points using boundaries in this feature space. The polynomial kernel allows for linear separation (exponent $p = 1$) or nonlinear separation boundaries (exponent $p \geq 2$) [24]. For our data set we obtained the best results using linear separation ($p = 1$). The algorithm for support vector machines for regression used the adaption of the stopping criterion by Shevade et al. [25]. The complexity parameter C was optimised using cross-validation and is 1.1 for AR and 2.5 for SPO.

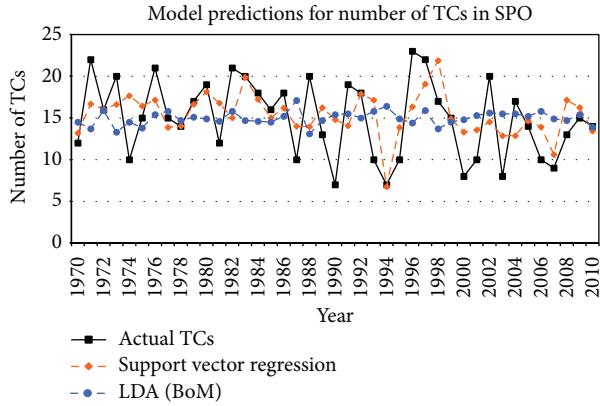


FIGURE 3: Leave-one-out cross-validation results SPO.

TABLE 4: Goodness-of-fit statistics SPO.

	Support vector regression	LDA (Bureau of Meteorology)
R^2	26.6%	-13.7%
Adjusted R^2	20.7%	-19.7%
St. dev. errors	3.925	4.910

3.3. *Cross Validation Results.* Figures 2 and 3 show the results of the leave-one-out cross-validation for AR and SPO, respectively. In other words, for every year, the target season is left out of the training period and all other seasons are used to create the model and then a forecast is made for the season left out.

Goodness-of-fit statistics are given in Tables 3 and 4. In these tables R^2 , which is the percentage of explained variance, is calculated as $R^2 = 1 - (SS_{res}/SS_{tot})$. In this formula $SS_{res} = \sum_{i=1}^n (y_i - f(x_i))^2$ is the sum of squares of the residuals, with y_i the actual number of TCs for year i , $f(x_i)$ the out of sample prediction for the number of TCs in year i , and $n = 42$ for AR and $n = 41$ for SPO. $SS_{tot} = \sum_{i=1}^n (y_i - \bar{y})^2$ is the total sum of squares, with \bar{y} the average actual number of TCs. A negative value of R^2 for SPO indicates that the variance of the errors is larger than the variance of the observations. Hence, it means that a model predicting the period average number of TCs, in this case 15, will yield a better prediction than the current LDA (Bureau of Meteorology) methodology. Adjusted R^2 is a measure that adjusts R^2 to account for the number of explanatory variables that are utilised. As R^2 increases when extra explanatory variables are added to a model, adjusted R^2 allows for a better comparison of models with a different number of explanatory variables. Adjusted $R^2 = 1 - (1 - R^2)((n - 1)/(n - p - 1))$ with $n = 42$ for AR, $n = 41$ for SPO, $p = 3$ the number of explanatory variables of the support vector regression model, and $p = 2$ for the LDA model.

First, it is clear that forecasting TC numbers for SPO is more difficult than for AR, as both models have significantly better performance for AR. The correlation analysis that was performed already showed this. Second, the graphs as well

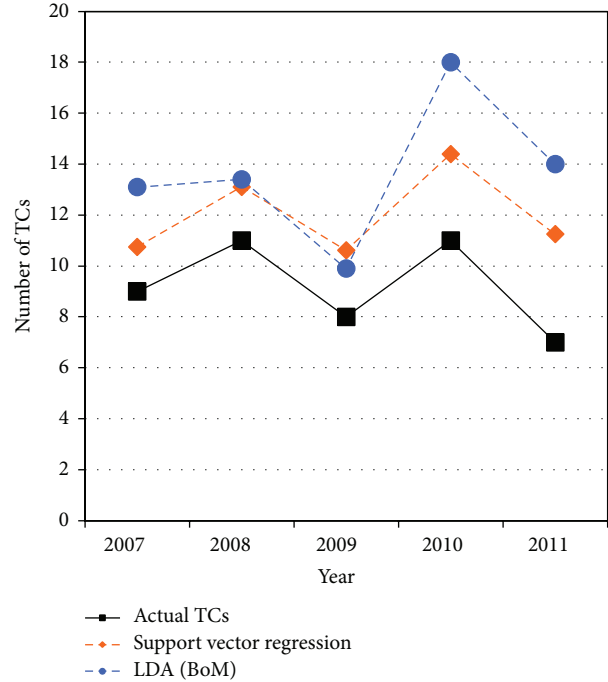


FIGURE 4: Independent forecasts for AR (2007–2011).

TABLE 5: MAE for independent forecasts (seasons from 2007-08).

Region	Support vector regression	LDA (Bureau of Meteorology)
AR	2.823	4.480
SPO	1.893	2.375

as the goodness-of-fit statistics show that the support vector regression models perform better in predicting TC numbers than the LDA method.

3.4. *Independent Forecasts 2007–2011.* With cross-validation the number of TCs for each fold is predicted using data from years that occur after the predicted year (except for the prediction for the final season), which is not possible in reality. To simulate the operational forecasting performance of the model, a forecast is made for the most recent seasons. Data from the 1970-71–2006-07 seasons are used to train the support vector regression and linear discriminant analysis models, in order to predict the number of TCs for the 2007-08–2011-12 seasons. For SPO the 2011-12 predictions were ignored as best track data were not yet available for this season. The results are shown in Figures 4 and 5. (In Figures 4 and 5, a TC season is indicated as a year when the season begins, e.g., for 2007-08 TC season which lasts from November 2007 to April 2008 inclusive; the season is indicated as 2007.)

This graph for AR shows that support vector regression is more consistent in forecasting TC activity than linear discriminant analysis, as it follows a similar pattern as the observed number of TCs. For SPO support vector regression also performs better than the LDA methodology, which

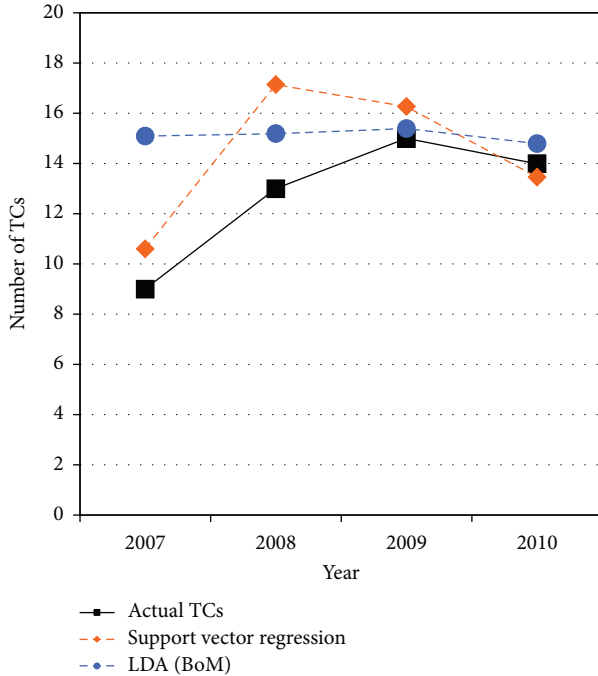


FIGURE 5: Independent forecasts for SPO (2007–2010).

TABLE 6: Standard deviation of errors for independent forecasts (seasons from 2007-08).

Region	Support vector regression	LDA (Bureau of Meteorology)
AR	1.011	2.441
SPO	1.930	2.600

predicts around 15 TCs for every year and fails to capture the interannual variability in TC activity. Support vector regression for SPO performs better, although the 2008-09 TC season prediction shows it is not a very consistent model. For both models the mean absolute error (MAE) of the model prediction versus actual TC number for AR and SPO is shown in Table 5 and the standard deviation of errors in Table 6. These tables show that the MAE for AR is larger, although the standard deviation of errors for AR is smaller than for SPO. It should be noted that the sample size for this analysis is small.

In order to quantify the impact of utilising different ensembles of seasons for model development, we calculated these statistics as well (Tables 7 and 8) utilising the predictions from the cross-validation analysis. Only the seasons from 2007-08 until 2011-12 for AR and 2007-08 until 2010-11 for SPO are included to calculate MAE and standard deviation of errors.

For SPO, the MAE and standard deviation of errors are similar in the hindcasts and forecasts for the seasons after 2007-08. However, for AR we observe that the errors in the forecast are larger than in the hindcast. This could indicate that errors increase for predictions further into the future. A larger sample would be required to test this.

TABLE 7: MAE in cross validated hindcasts (seasons from 2007-08).

Region	Support vector regression	LDA (Bureau of Meteorology)
AR	2.223	3.740
SPO	1.896	2.025

TABLE 8: Standard deviation of errors in cross validated hindcasts (seasons from 2007-08).

Region	Support vector regression	LDA (Bureau of Meteorology)
AR	0.979	1.923
SPO	1.942	2.724

4. Discussion

The aim of this study is to improve the accuracy of seasonal TC predictions, as the performance of the Bureau of Meteorology's LDA models has been less efficient in recent years [3]. The results show that a support vector regression approach can indeed improve upon the current methodology for both AR and SPO. This research is consistent with past studies where support vector regression was used. For example, Richman and Leslie [4] have investigated the application of machine learning algorithms for seasonal prediction of TCs, concluding that support vector regression leads to better results than linear regression models. Furthermore, their study identified the Quasi-biennial Oscillation (QBO) as an explanatory variable that boosts model performance. This variable is only recorded from 1979 onwards [26]. Therefore, less training data will be available for model development, as the 1970-71–1978-79 seasons cannot be used. Moreover, the physical reasons for improved model performance with QBO included as an additional variable are not clear. Analysing the influence of the QBO on TC activity, Camargo and Sobel [27] concluded that although there was a statistically significant relationship between the QBO and TCs in the Atlantic from the 1950s to the 1980s that relationship is no longer present in later years. As for other regions, only in AR is the relationship of TCs with the QBO significant for 1953–1982; however, similar to the case of the Atlantic, the significance disappears in 1983–2008. This change could possibly be attributed to changes in observational procedures [27]. Thus, inclusion of the QBO in the support vector regression model requires caution and needs further detailed investigation.

Different methods for variable selection can also be explored. The current correlation analysis ranks explanatory variables based on the correlation with observed TCs and selects the most promising month per predictor based on correlation. However, in the subsequent variable selection the variables with the highest correlation with observed TCs are sometimes not even selected in the final support vector regression model. In addition, for the region where the correlation of explanatory variables with the observed number of TCs was highest (AR), the final model utilises September values for all selected explanatory variables. For the region where the correlation was not that high (SPO),

the final model also uses values from earlier months. For example, in the support vector regression model for the SPO the three month average over July, August, and September is used for Niño1+2 SST anomalies and the August value for Niño4 SST anomalies and DMI. From a methodological perspective, it could be decided to use September values for all explanatory variables instead.

Our analysis gives some indications that errors could increase for predictions further into the future, although a larger sample size is required to obtain a conclusive answer. A prudent approach would be to update the model annually. In case annually updating the model is not possible, an approach researched by Nicholls [13] can be investigated. He suggests that predicting the change in TC numbers from last season to the upcoming season, rather than predicting the expected numbers directly from the explanatory variables, could reduce the confounding effect of possible secular changes in TC numbers, explanatory variables, or of relationships between them. A recent study by Dowdy and Kuleshov [28] confirms there has been a significant downward trend in the number of TCs in the AR over the 32-year period 1981-82 to 2011-12. Using the approach suggested by Nicholls [13] the forecasting errors for later years could possibly be reduced.

As the statistical models for AR give better results than for SPO, different explanatory variables for SPO could be explored in future research. Current explanatory variables used for SPO have a low correlation with observed TC activity. The consideration of new variables may increase model performance for SPO. An alternative approach to seasonal prediction of TCs is using coupled ocean-atmosphere dynamical climate model [10, 11, 29]. At the Australian Bureau of Meteorology, the Predictive Ocean Atmosphere Model for Australia (POAMA) is currently used operationally for preparing seasonal climate outlooks for AR. Superior skill of POAMA compared to statistic model for predicting seasonal rainfall in AR and SPO has been demonstrated [30]. A pilot study to explore POAMA-based methodology to predict TC seasonal activity in AR and SPO conducted under the Pacific Australia Climate Change Science and Adaptation Planning program (PACCSAP) demonstrated potential skill of the model to improve accuracy of TC forecasting comparing with current operational model [31]. These two avenues—improving statistical model-based methodology and developing new dynamical climate model-based methodology—will be further explored in our future research with the aim to improve skill of operational seasonal TC prediction in AR and SPO.

5. Summary

For AR a support vector regression model outperforms the current Bureau of Meteorology methodology based on linear discriminant analysis. In cross-validation results support vector regression reduces the standard deviation of the errors from 2.874 to 2.266. This methodology can be used to improve the accuracy of current TC predictions for AR. Similarly, the current linear discriminant analysis model has limited capability in accurately predicting SPO TC activity.

Although the developed support vector regression model for SPO gives a significant improvement in performance over the current linear discriminant analysis methodology, performance is still quite low and further research is necessary to improve the skill of seasonal TC predictions in SPO.

Conflict of Interests

The authors declare that there is no conflict of interests regarding the publication of this paper.

Acknowledgments

The Australian Agency for International Development (AusAID) and the Australian Government Department of Climate Change and Energy Efficiency (DCCEE) provided support for this research through the PACCSAP's project "Seasonal prediction of tropical cyclones." Dr. Andrew Watkins from the National Climate Centre, Australian Bureau of Meteorology provided useful comments on an earlier version of the paper.

References

- [1] J. Mottram, *Report on Cyclone Tracy*, prepared by J. Mottram, Australian Government Publishing Service, Canberra, Australia, 1977.
- [2] L. Anderson-Berry, C. Iroi, and A. Rangi, "The environmental and societal impacts of cyclone Zoe and the effectiveness of the tropical cyclone warning systems in Tikopia and Anuta," James Cook University Centre for Disaster Studies, 2003.
- [3] K. L. Shelton and Y. Kuleshov, "Evaluation of statistical predictions of seasonal tropical cyclone activity," *Journal of Climate*. In preparation.
- [4] M. B. Richman and L. M. Leslie, "Adaptive machine learning approaches to seasonal prediction of tropical cyclones," *Procedia Computer Science*, vol. 12, pp. 276–281, 2012.
- [5] Y. Kuleshov, R. Fawcett, L. Qi et al., "Trends in tropical cyclones in the South Indian Ocean and the South Pacific Ocean," *Journal of Geophysical Research D*, vol. 115, no. 1, Article ID D01101, 2010.
- [6] V. F. Dvorak, "Tropical cyclone intensity analysis using satellite data," NOAA Tech. Report NESDIS 11, 1984.
- [7] N. Nicholls, L. Landsea, and J. Gill, "Recent trends in Australian region tropical cyclone activity," *Meteorology and Atmospheric Physics*, vol. 65, no. 3-4, pp. 197–205, 1998.
- [8] Y. Kuleshov, F. C. Ming, L. Qi, I. Chouaibou, C. Hoareau, and F. Roux, "Tropical cyclone genesis in the Southern Hemisphere and its relationship with the ENSO," *Annales Geophysicae*, vol. 27, no. 6, pp. 2523–2538, 2009.
- [9] Y. Kuleshov, L. Qi, R. Fawcett, and D. Jones, "Improving preparedness to natural hazards: tropical cyclone prediction for the Southern Hemisphere," in *Advances in Geosciences*, J. Gan, Ed., vol. 12 of *Ocean Science*, pp. 127–143, World Scientific Publishing, Singapore, 2009.
- [10] Y. Kuleshov, Y. Wang, J. Apajee, R. Fawcett, and D. Jones, "Prospects for improving the operational seasonal prediction of tropical cyclone activity in the southern hemisphere," *Atmospheric and Climate Sciences*, vol. 2, no. 3, pp. 298–306, 2012.
- [11] Y. Kuleshov, C. Spillman, Y. Wang et al., "Seasonal prediction of climate extremes for the Pacific: tropical cyclones and extreme

- ocean temperatures,” *Journal of Marine Science and Technology*, vol. 20, no. 6, pp. 675–683, 2012.
- [12] N. Nicholls, “A possible method for predicting seasonal tropical cyclone activity in the Australian region,” *Monthly Weather Review*, vol. 107, no. 9, pp. 1221–1224, 1979.
- [13] N. Nicholls, “Recent performance of a method for forecasting Australian seasonal tropical cyclone activity,” *Australian Meteorological Magazine*, vol. 40, no. 2, pp. 105–110, 1992.
- [14] J. C. L. Chan, “Tropical cyclone activity over the western North Pacific associated with El Niño and La Niña events,” *Journal of Climate*, vol. 13, no. 16, pp. 2960–2972, 2000.
- [15] Y. Kuleshov, L. Qi, R. Fawcett, and D. Jones, “On tropical cyclone activity in the Southern Hemisphere: trends and the ENSO connection,” *Geophysical Research Letters*, vol. 35, no. 14, Article ID L14S08, 2008.
- [16] K. E. Trenberth, “The definition of el Niño,” *Bulletin of the American Meteorological Society*, vol. 78, no. 12, pp. 2771–2777, 1997.
- [17] K. Ashok, S. K. Behera, S. A. Rao, H. Weng, and T. Yamagata, “El Niño Modoki and its possible teleconnection,” *Journal of Geophysical Research C*, vol. 112, no. 11, 2007.
- [18] K. Wolter and M. S. Timlin, “El Niño/Southern Oscillation behaviour since 1871 as diagnosed in an extended multivariate ENSO index (MEI.ext),” *International Journal of Climatology*, vol. 31, no. 7, pp. 1074–1087, 2011.
- [19] G. J. Holland, “On the quality of the Australian tropical cyclone data base,” *Australian Meteorological Magazine*, vol. 29, pp. 169–181, 1981.
- [20] M. Hall, E. Frank, G. Holmes, B. Pfahringer, P. Reutemann, and I. H. Witten, “The WEKA data mining software: an update,” *ACM SIGKDD Explorations Newsletter*, vol. 11, pp. 10–18, 2009.
- [21] V. Vapnik, *The Nature of Statistical Learning Theory*, Springer, 2000.
- [22] A. J. Smola and B. Schölkopf, “A tutorial on support vector regression,” *Statistics and Computing*, vol. 14, no. 3, pp. 199–222, 2004.
- [23] H. Ramsay, M. Richman, and L. Leslie, “Exploring variants of ENSO Modoki for the seasonal prediction of Coral Sea tropical cyclone activity,” Submitted to *Journal of Climate*.
- [24] A. Ben-Hur, C. S. Ong, S. Sonnenburg, B. Schölkopf, and G. Rätsch, “Support vector machines and kernels for computational biology,” *PLOS Computational Biology*, vol. 4, no. 10, Article ID e1000173, 2008.
- [25] S. K. Shevade, S. S. Keerthi, C. Bhattacharyya, and K. R. K. Murthy, “Improvements to the SMO algorithm for SVM regression,” *IEEE Transactions on Neural Networks*, vol. 11, no. 5, pp. 1188–1193, 2000.
- [26] Climate Prediction Center—Noaa, “30 mb zonal wind index—CDAS,” 2013, <ftp://ftp.cpc.ncep.noaa.gov/wd52dg/data/indices/qbo.u30.index>.
- [27] S. J. Camargo and A. H. Sobel, “Revisiting the influence of the quasi-biennial oscillation on tropical cyclone activity,” *Journal of Climate*, vol. 23, no. 21, pp. 5810–5825, 2010.
- [28] A. J. Dowdy and Y. Kuleshov, “An analysis of tropical cyclone occurrence in the Southern Hemisphere derived from a new satellite-era dataset,” *International Journal of Remote Sensing*, vol. 23, no. 10, pp. 7382–7397, 2012.
- [29] A. Charles, Y. Kuleshov, and D. Jones, “Managing climate risk with seasonal forecasts,” in *Book Management—Current Issues and Challenges*, chapter 23, pp. 557–584, InTech, 2012.
- [30] A. Cottrill, H. Hendon, E. -P. Lim et al., “Seasonal forecasting in the Pacific using the coupled model POAMA-2,” *Weather and Forecasting*, vol. 28, pp. 668–680, 2013.
- [31] K. Shelton, A. Charles, H. Hendon, and Y. Kuleshov, “Dynamical seasonal tropical cyclone prediction for the Australian and South Pacific Regions,” *Journal of Climate*. In preparation.

Research Article

Comparison of the Synoptic Environments Conducive to Eastward versus Southeastward Transport of Asian Dust Events

Fujung Tsai¹ and Wei-Nai Chen²

¹ Department of Marine Environmental Informatics, National Taiwan Ocean University, Keelung 202, Taiwan

² Research Center for Environmental Changes, Academia Sinica, Taipei 115, Taiwan

Correspondence should be addressed to Fujung Tsai; fujung@mail.ntou.edu.tw

Received 26 October 2013; Accepted 24 November 2013; Published 4 February 2014

Academic Editor: Chung-Ru Ho

Copyright © 2014 F. Tsai and W.-N. Chen. This is an open access article distributed under the Creative Commons Attribution License, which permits unrestricted use, distribution, and reproduction in any medium, provided the original work is properly cited.

Asian dust events that travel eastward and southeastward in the lower troposphere affect different areas near the coastal East Asia. To understand the synoptic differences between the two types of dust events, four dust events from 2006 to 2009 are selected for each type and the synoptic environment is compared. Surface measurements, trajectory analyses, and a regional dust model are also applied to further analyze each type. Results show that the strength of the low-level trough and the surface anticyclonic system are important in determining the transport route of dust event. A deep 700–850 hPa trough extending far south beyond 30°N associated with an intense surface anticyclone with maximum pressure greater than 1020 hPa over coastal East Asia favors southeastward movement of dust event. The prevailing northwesterlies or northerlies behind the deep trough and ahead of the intense surface anticyclone promote the southeastward movement of dust event. Since intense surface anticyclones often associated with strong dust events, severe dust activities tend to move southeastward. In contrast, a shallow trough accompanied by a weak surface high locating north of 30°N over the coastal East Asia favors an eastward transport route.

1. Introduction

Asian dust is mainly generated from China during spring-time, when cyclonic activity and the induced strong surface wind favor the generation of dust from the dry surface. The generated dust particles can be transported downwind over long distances [1, 2]. The transport pathways for dust include eastward routes to Korea, Japan, and the North Pacific, as well as southeastward routes to Southeast China, Taiwan, Hong Kong, and even the South China Sea [3]. According to previous studies, the annual emissions of Asian dust can be as large as 460 Tg to 800 Tg [4, 5], and half of the dust parcels experience long-range transport [4]. Thus, it can be expected that these long-range transport events can significantly affect the downwind areas.

Previous studies show that both eastward and southeastward transport increase aerosol concentration over the coastal areas of East and Southeast China [6–9]. During eastward transport, major dust events normally occur once

or twice annually in Korea, with aerosol concentrations increasing up to $1105 \mu\text{g m}^{-3}$ [7]. In spring 2001, the maximum aerosol concentration of approximately $200 \mu\text{g m}^{-3}$ to $450 \mu\text{g m}^{-3}$ was observed over the coast of Japan and Korea [10, 11]. On the other hand, during southeastward transport, concentrations of particulate matter less than $10 \mu\text{m}$ in diameter (PM_{10}) can be enhanced over 400, 600, and $1000 \mu\text{g m}^{-3}$ in cities over or near Southeast China, such as Hong Kong, Xiamen, and Taiwan, respectively [12–14]. Southeastward dust events are occasionally observed reaching far south beyond 20°N into the South China Sea [13, 15, 16], and the depositions were observed to enhance phytoplankton growth [17, 18].

The synoptic characteristics of the eastward dust event have been explored in previous studies [2, 19, 20]. Through aircraft measurement, Dickerson et al. [20] found that the eastward propagation of cyclones and associated fronts provide the mechanism for the lifting and long-range transport

of dust, whereas behind the surface cold front, the dust parcel was lifted from the surface to approximately 4000 m because of the strong surface wind associated with anticyclone. Liu et al. [19] simulated an Asian dust event in 2001 and found that mechanical and convective turbulence mixed the dust particles from the surface, and the upward motion ahead of the cyclones is responsible for transporting dust to high altitudes and into the westerlies, making it available for long-range transport.

Unlike eastward transport, the synoptic environment for the southeastward transport is distinctive. Liu et al. [9] found that the major southeastward dust events from 2002 to 2006 were transported behind the lower tropospheric trough in the descending areas and descend with height to the southeastern coast of China. Yu et al. [21] also found that the southeastward transport of Asian dust is often associated with a surface anticyclone breaking away from the Siberian-Mongolian High at the high latitudes. When the surface anticyclone moves southeastward, dust can be carried to the subtropics. In these previous studies, although the synoptic environment favoring the eastward and southeastward movement of dust events is discussed, the difference between lower level transport of the two types is unclear. It is still unknown why some dust events moving near the surface layer are allowed to be transported far southeastward into the South China Sea, whereas others are transported shallower and eastward and mainly affect the East Asian midlatitudes. Tsai et al. [22] classified the transport route of dust parcel into three types, including upper-level, lower-level, and descending types. In the lower-level type, dust parcel is transported behind a lower-level trough near the surface layer where the associated surface high is intense. However, the synoptic differences between the low-level dust events that result in eastward and southeastward transport routes remain undiscussed.

To clarify this problem, this study compares the synoptic environment between the major eastward and southeastward dust events from 2006 to 2009 and investigates their differences. Four dust events that reached coastal East Asia during these years are selected for each type, and their synoptic conditions in the lower troposphere and surface level are compared. In addition, a southeastward and an eastward dust event that occurred sequentially in 2006 are selected as cases for analysis. In Section 3, the synoptic characteristics of the two types of dust event are presented and compared. In Section 4, one of each type is selected for case study and the trajectory simulation, synoptic analyses, and 3D regional dust simulations are used to investigate the synoptic environment favoring the two types of dust transport. The synoptic differences between the southeastward and eastward transport of dust events in the lower troposphere are summarized and concluded in Section 5.

2. Data and Model

2.1. Particulate Matter. The PM_{10} concentrations are obtained from the Wanli (121.7°E, 25.2°N) and Hengchun (121.8°E, 21.9°N) stations in Taiwan (Figure 1). The two stations are the Taiwan Environmental Protection

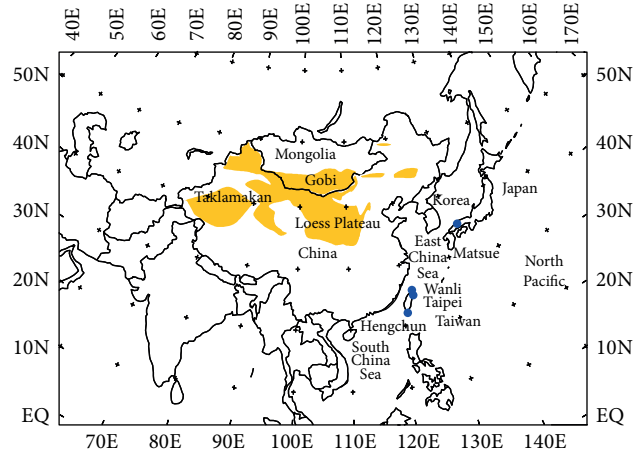


FIGURE 1: TAQM model domain and dust observation sites (blue dot) at Wanli, Taipei, and Hengchun in Taiwan and Matsue in Japan. Deserts over China are indicated by shaded areas.

Administration (EPA) stations in the northern and southern tips of Taiwan, respectively. They are commonly used to represent the background aerosol concentrations due to their locations right next to the ocean.

2.2. Lidar. The lidar measurements are obtained from Taipei (121.53°E, 25.01°N), Taiwan, and Matsue (133.01°E, 35.48°N), Japan (Figure 1). The Taipei lidar system is installed in the Taipei Aerosol and Radiation Observatory at the National Taiwan University, about 20 km from the EPA Wanli station. The system measures the vertical distribution of aerosol backscattering (532 nm and 355 nm), extinction, and depolarization (at 532 nm) by detecting the Rayleigh/Mie backscattering of atmospheric molecules and aerosol particles. At Matsue (Shimane Prefectural Institute of Public Health and Environmental Science), both aerosol backscattering (532 nm and 1064 nm) and depolarization (at 532 nm) are measured with a laser power of 20 mJ for both wavelengths, with a repetition rate of 10 Hz and telescope diameter of 20 cm. More details on the lidar characteristics can be found in the studies by Chen et al. [23] and Shimizu et al. [24].

The lidar depolarization ratio used to identify dust particles is defined as the ratio of the returned light in perpendicular polarization to the parallel polarizations. Owing to the irregular shape of the dust particles, the intensity of the return lights between perpendicular and parallel polarization (depolarization ratio) is different for dust particles when compared with anthropogenic aerosol. A depolarization ratio greater than 0.06 is suggested for distinguishing dust particles from other type aerosol particles [25].

2.3. Meteorological Data. The National Centers for Environmental Prediction (NCEP)—National Center for Atmospheric Research (NCAR) Reanalysis [26]—is used to analyze the synoptic conditions during the dust event. The global reanalysis data have a spatial resolution of $2.5^\circ \times 2.5^\circ$ and a temporal resolution of 6 h, including geopotential height, air

TABLE 1: The date of selected eastward and southeastward dust events in Taiwan and Japan respectively, their peak hour at Wanli, Taiwan, and Matsue, Japan, obtained from surface or lidar measurements, their maximum PM₁₀ concentration at northern (Wanli) and southern tip (Hengchun) of Taiwan, and number of Japanese stations that observed the dust events.

Type of dust event	Observed date	Peak hour at Taiwan or Japan (UTC)	N. Taiwan maximum ($\mu\text{g m}^{-3}$)	S. Taiwan maximum ($\mu\text{g m}^{-3}$)	Number of Japanese stations with dust observation
Southeastward	2006/3/19-20	3/19 08:00	268	136	10
	2006/3/28-30	3/28 13:00	124	156	14
	2007/1/28-29	1/28 14:00	234	160	0
	2009/4/25-26	4/25 06:00	1000	378	9
Eastward	2006/3/23-24	3/23 02:00	81	68	20
	2006/4/24-25	4/24 00:00	155	46	40
	2007/5/26-27	5/26 07:00	61	32	46
	2009/3/17-19	3/17 00:00	80	34	41

temperature, vertical velocity (ω), 3D wind field, and sea-level pressure.

2.4. Model Descriptions. The dust module in the Taiwan Air Quality Model (TAQM-Dust) is added to simulate regional dust distributions over East Asia [11, 22]. The original TAQM is a 3D regional model used to simulate the distribution of trace gases and particles [27]. The TAQM-Dust model domain covers East Asia from approximately 10°N to 60°N and 60°E to 140°E (Figure 1), with a horizontal resolution of 81 km. Vertically, the model is divided into 15 sigma levels, with vertical resolution ranging from roughly 40 m near the surface to 1 km to 2 km near the tropopause of 100 hPa. During dust seasons, dust particles can have a residence time of more than a week in the model domain. Thus, a 10-day simulation of the model is performed ahead of the selected episode, and the subsequent simulation is used for analyses.

For the calculation of dust transport, meteorological data used as an input to the dust model are obtained from NCAR/Penn State Mesoscale Meteorological Model (MM5) [28–30] simulations. Initial and boundary conditions for MM5 are obtained from the European Center for Medium-Range Weather Forecast (ECMWF) Tropical Ocean and Global Atmosphere advanced analysis.

A dust module, including emission, transport, and depositions of dust, has been incorporated into TAQM. The dust emission module was developed based on Wang et al. [31]. In the emission module, the dust particles are divided into 12 size bins ranging from 0.13 μm to 20.13 μm . Dust transport is computed using the Bott [32] scheme, which minimizes the problem of numerical diffusion. Dust removal by wet and dry deposition, including gravitational settling of dust particle above the surface layer, is included in the dry deposition processes.

3. Synoptic Characteristic of the Two Types

To compare the synoptic difference between the eastward and southeastward dust event, eight major dust events of the two types from 2006 to 2009 are selected and the lower

tropospheric and surface maps of the events are compared. Table 1 lists the eight dust events. Among these events, four southeastward events reached southern Taiwan, with maximum PM₁₀ concentrations of more than 130 $\mu\text{g m}^{-3}$, greater than that of any other event. The first (19-20 March 2006) and the fourth (25-26 April 2009) dust events are the two severe dust events during the recent decades. On the other hand, four eastward events are selected because a maximum number of surface stations (around 40 stations) in Japan observed the dust events (http://www.data.kishou.go.jp/obs-env/kosahp/kosa_data_index.html), except for the first dust event on March 2006. The first eastward event was observed by 20 surface stations, slightly less than other selected eastward events. It is selected because it occurs immediately after the first southeastward dust event on 19-20 March 2006. Thus the two continuous dust events are used as cases for comparison.

Figure 2 shows the synoptic map of the southeastward and eastward dust events at 700 hPa, an altitude where low-level dust events are usually located [9, 25]. When the associated cyclone and the trough of the dust event move over the east coast of Asia, the southward extension of the trough of the southeastward dust events reaches far south beyond 30°N and often approaches Taiwan. As a result of the deep trough, the 3060 gpm isopleths over the coastline are located south of 30°N. By contrast, the southward extension of the trough of eastward event only approached south of Japan, reaching close to 30°N. The 3060 gpm isopleths of the eastward events mostly locate north of 30°N over the coastline, except for the first eastward event (Figure 2(e)). The deep and shallow trough promotes southeastward and eastward transport of dust events out of the coastal East Asia, respectively.

Figure 3 shows the surface map for the two types of dust events. The surface anticyclonic circulation of the southeastward dust event covers a wide area of the eastern coast of China, with a maximum pressure often greater than 1020 hPa. Compared with the southeastward event, the synoptic pattern for the eastward event is distinctive. The associated cyclonic circulation is strong over Mongolia and northern China, whereas the anticyclonic circulation is often weak, covering only a small area of the eastern coast, with a maximum

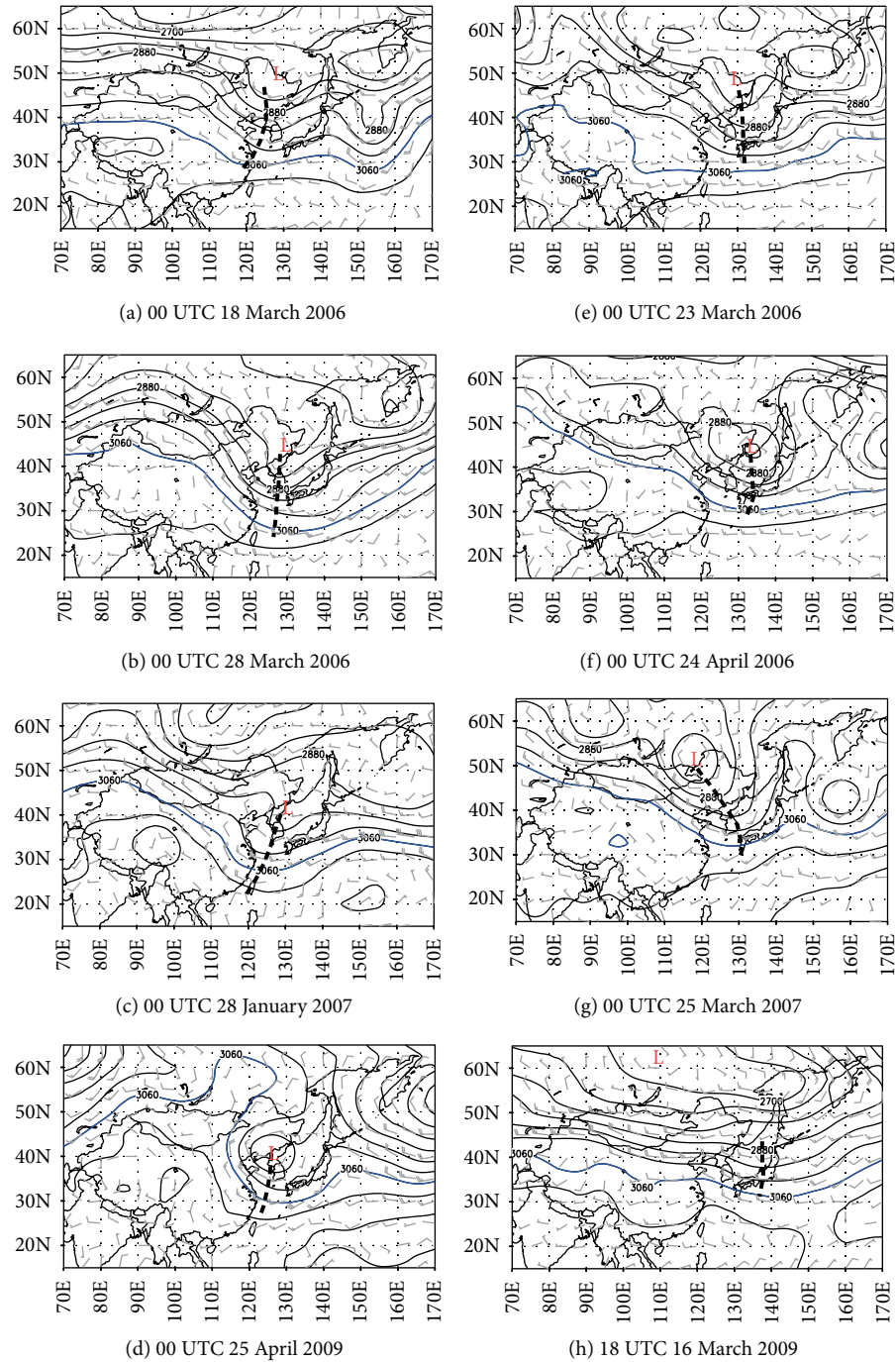


FIGURE 2: 700 hPa synoptic maps for the (a)–(d) southeastward and (e)–(h) eastward dust events. The full barb and half barb represent 10 and 5 m s^{-1} , respectively. Geopotential heights (gpm, solid lines) are analyzed at 60 gpm intervals.

pressure of less than 1020 hPa. The strong cyclonic and weak anticyclonic circulation is favorable for zonally transport of dust events.

Previous study also indicates that the surface condition of cyclonic and anticyclonic systems over the source areas is important in determining the strength or transport pathway of dust activity [26, 33]. When the surface anticyclone is greater than 1040 hPa during dust generation, dust event is often transported in the lower troposphere because of the

strong descending motion of the anticyclonic circulation [26]. In addition, if surface pattern exhibits a low-high dipole orienting in northeast-southwest direction over the source areas, the dust activity is more active [33]. In this study, the surface synoptic map of the southeastward dust events is mostly dominated by the intense high-pressure system and similar low-high dipole. Two of the selected southeastward events are also the severest dust events in recent years. Thus, an intense surface high accompanied with active dust activity

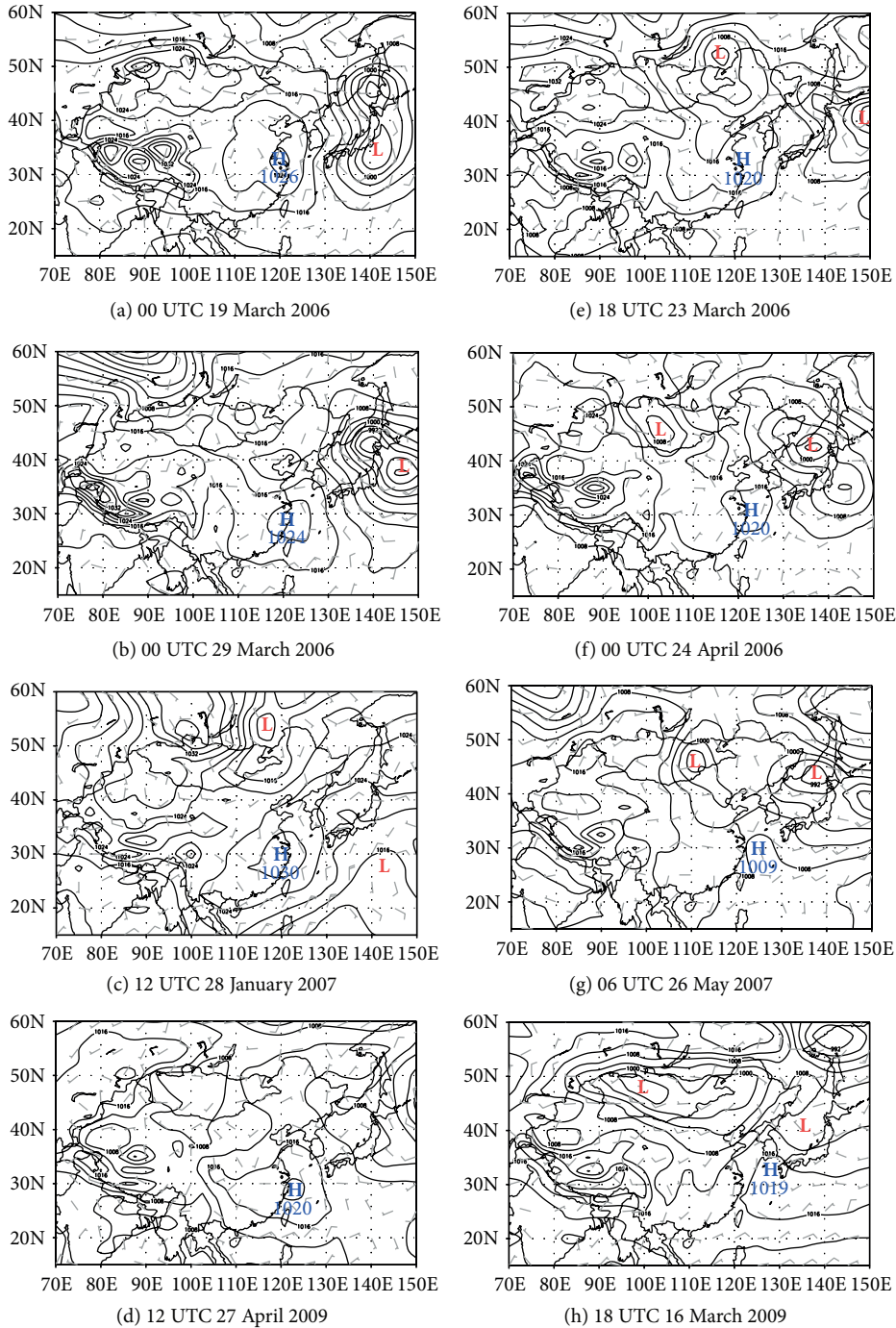


FIGURE 3: Surface weather maps for the (a)–(d) southeastward and (e)–(h) eastward dust events. The full barb and half barb represent 10 and 5 m s^{-1} , respectively. Sea-level pressure is analyzed at 4 hPa intervals.

generated by the strong surface winds potentially favors southeastward transport route.

4. Case Study

4.1. First Events of the Two Types. To illustrate further the difference in the synoptic environment between the two types of dust events, the first event of each type is selected for case study. The selected southeastward dust event occurred on

16–20 March 2006, with observed PM_{10} concentration reaching more than $268 \mu\text{g m}^{-3}$ in the northern tip of Taiwan (Table 1) and approaching $400 \mu\text{g m}^{-3}$ over Taipei city. Following this event, the eastward dust event was observed on 22–24 March over Japan by 20 surface stations.

Figure 4 shows the vertical profile of the total depolarization ratios of lidar measured at Taipei, Taiwan, and Matsue, Japan, and compares with model results. For the southeastward-moving dust event, the dust clouds are observed

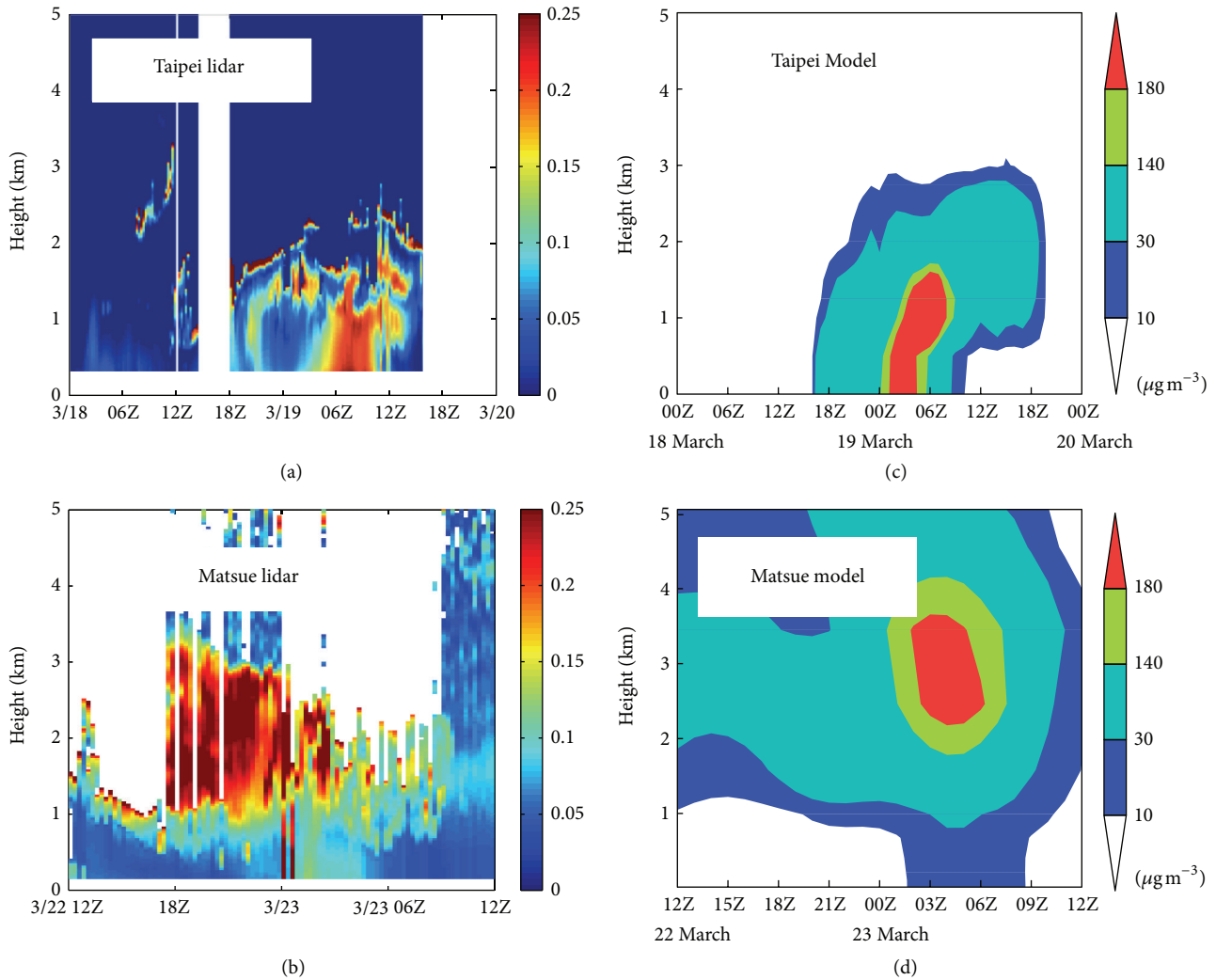


FIGURE 4: Vertical distributions of dust observed by lidar total depolarization ratio (>0.06 indicates dust) for the (a) southeastward event at Taipei, Taiwan, on 18–20 March and (b) eastward event at Matsue, Japan, on 22–23 March and compared with model simulation at (c) and (d), respectively.

at Taipei on 19 March, with dust concentrations remaining mostly below 1.5 km (Figure 4(a)). For the eastward dust event, lidar results show that the dust events peak from 1 km to 3 km on late 22 March to early 23 March and descend to the surface layer on early 23 March at Matsue (Figure 4(b)).

For model verification, Figure 4 also shows the model simulation of dust profiles at the same time and locations of the two dust events in comparison with the lidar observations. At both stations, the simulated peak concentrations mostly concur with the lidar measurements. However, small discrepancies are also found. For example, the simulated peak concentration in Taipei occurs at 0300 UTC on 19 March, which is 4 h earlier than observation (Figure 4(c)). In Matsue, the model results may underpredict the dust concentration on late 22 March and predict the maximum concentration from around 2.5 km to 4 km, instead of 1 km to 3 km on early 23 March (Figure 4(d)). The discrepancy has resulted from meteorological simulations, which produce

slightly faster southeastward transport and higher eastward transport during dust events compared with actual situation.

Figure 5 shows the backward trajectories of the two events obtained from the National Oceanic and Atmospheric Administration (NOAA) Hybrid Single Particle Lagrangian Integrated Trajectory (HYSPLIT) website (<http://www.ready.noaa.gov/>) [34]. The two trajectories originated from Taipei (0800 UTC 19 March) and Matsue (0200 UTC 23 March) at the hour of maximum concentrations. The initial heights of the trajectory for Taipei (200, 500, and 800 m) and Matsue (1700, 2000, and 2300 m) are every 300 m within altitudes where high dust concentrations are observed by lidar. Backward trajectories were performed for four days. Result shows that the southeastward dust event passes through deserts of China on 16–17 March 2006 and moves southeastward toward Taiwan during downwind transport. Following this event, the eastward event passes through the

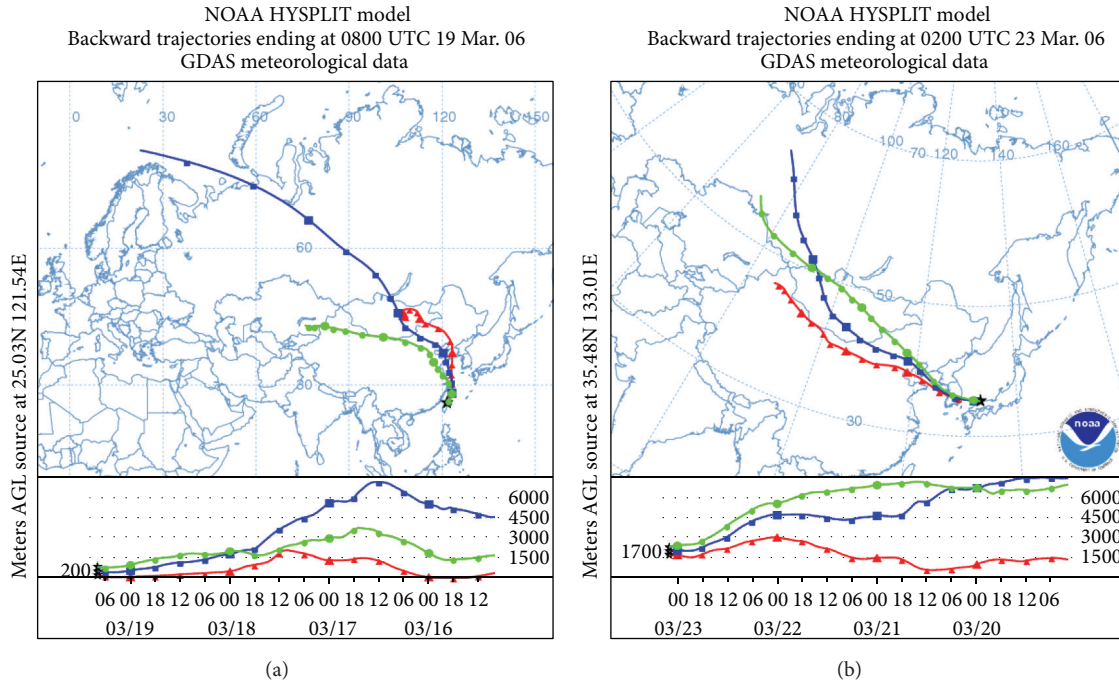


FIGURE 5: NOAA HYSPLIT backward trajectories of (a) southeastward and (b) eastward dust events and their vertical profiles initiated from Taipei, Taiwan, and Matsue, Japan, respectively. Initial heights are 200, 500, and 800 m for the southeastward event and 1700, 2000, and 2300 m for the eastward event. Trajectories are marked every 6 hours.

deserts in Mongolia and northern China on 20-21 March but moves eastward downwind to Japan.

Figure 6 analyzes the atmospheric circulation at 500, 700, and 850 hPa, following the downwind transport of the southeastward dust event. The lowest-level trajectories predicted by the HYSPLIT trajectory model in Figure 5 are added in Figure 6, so the movement of the dust parcels toward the downwind areas can be better identified. Figure 6 shows that the southeastward dust event is initiated at around 16 March, when simulated dust cloud is concentrated over northern and western China in the lower troposphere (Figure 6(c)). After initiation of the dust event, some dust particles are mixed upward from the ground and travel in the free troposphere. At this time, a 500 hPa trough moves across the western border of Mongolia and China on 16 March (Figure 6(a)), and a short wave 700 hPa trough (heavy dash line) is located in southern Mongolia (Figure 6(b)). Behind the trough, the northwesterly winds associated with cold advection prevail, leading to the development of the trough.

Figure 6 also shows that the traced dust parcel (square with x) is located among the dust clouds generated ahead of the trough (heavy dash line) and is uplifted to 700 hPa due to ascending motion (heavy solid line). Note that the dust parcel identified by the backward trajectory is located at 770 hPa, which is close to 700 hPa. Likewise, the synoptic maps for the closest pressure level of the dust parcel are analyzed in this study.

On 18 March, as the intensified trough moves away from the eastern coast of China, the 500 hPa trough lags the trough

in the lower troposphere and the resulting strong cold advection behind the trough favors the intensification of the trough (Figures 6(e) and 6(f)), resulting in the deepening and intensification of the trough. The 700 hPa to 850 hPa trough extends from northeastern China at around 50°N southward beyond 30°N because of the deepening of the trough. Thus, the prevailing wind becomes approximately northerly behind the 850 hPa trough (Figure 6(f)). Following the strong prevailing northerlies, substantial dust clouds follow the traced dust parcels, turning from mainly eastward to almost southward toward the low latitudes of Southeast China. Along the southward transport, the traced dust parcels also descend rapidly from around 700 hPa to 850 hPa because of the sinking motion of the northerlies behind the deep trough. Figure 6(f) and other similar figures in Figures 6 to 7 also show that the traced dust parcels are located right over the simulated dust clouds when traveling downwind. The result indicates the consistency between the trajectory and the regional model simulation.

On 19 March, the traced dust parcels move almost southward toward northern Taiwan (Figure 6(i)). At this time, the northerly or northwesterly winds remain strong over northern Taiwan. Thus, the low-level dust clouds keep moving southward, passing Taiwan toward the South China Sea in the next two days.

Following the passage of the southeastward dust event, the eastward transport dust event occurs two days later in northern China. The dust event is initiated at 0600 UTC on

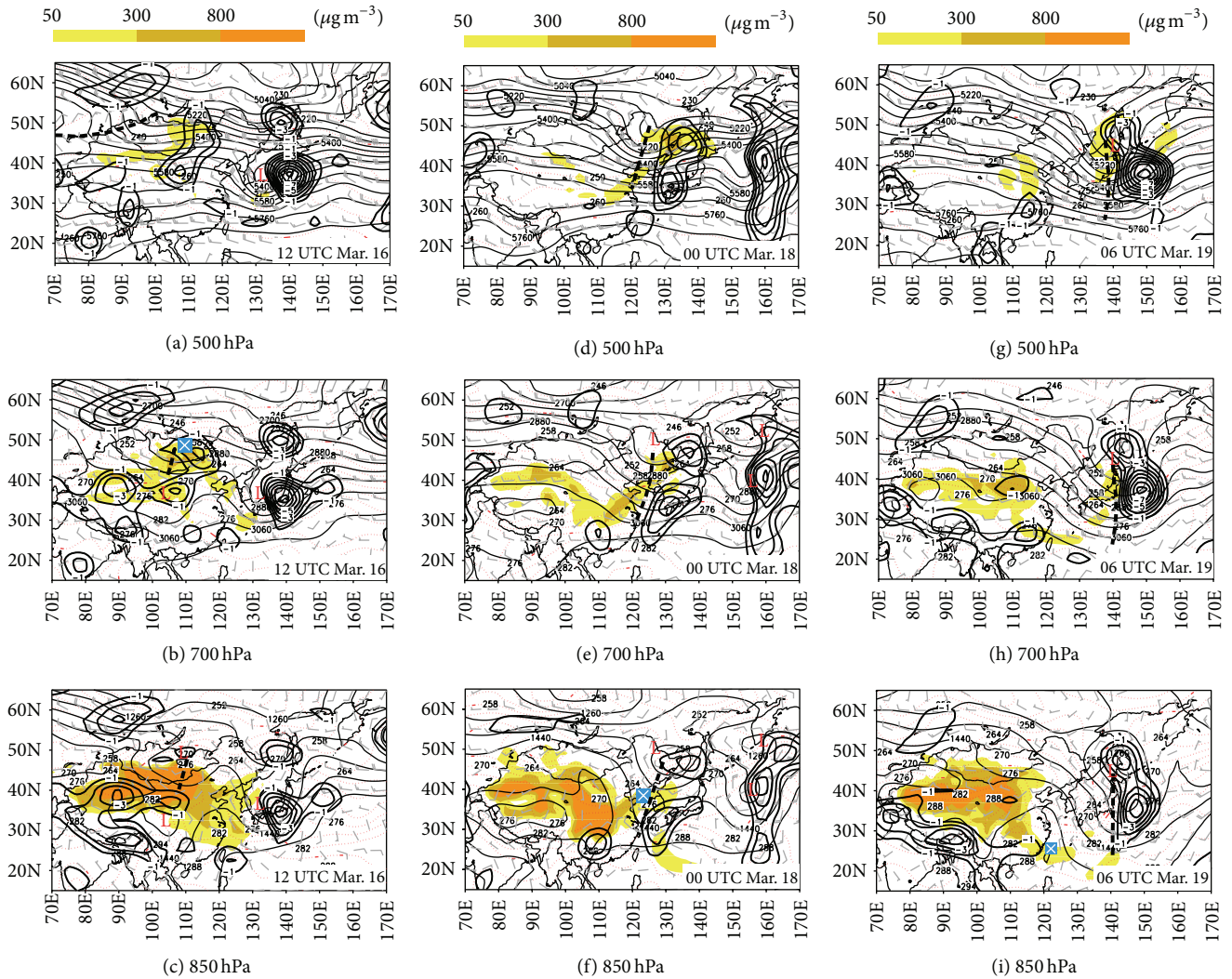


FIGURE 6: Synoptic maps for southeastward event at 500 hPa, 700 hPa, and 850 hPa of (a)–(c) 1200 UTC on 16 March, (d)–(f) 0000 UTC on 18 March, and (g)–(i) 0600 UTC on 19 March, respectively. The full and half bars represent 10 and 5 m s^{-1} , respectively. Geopotential heights (solid lines) are analyzed at 60 gpm intervals. Temperatures (dot line) are analyzed at 5°C intervals at 500 hPa and 3°C intervals at others. Upward motion (heavy solid lines) is analyzed at 10 Pa s^{-1} intervals. Dust parcels identified by trajectory model (square with x), upper-level troughs (heavy dash line), and simulated dust concentrations (shaded) are plotted.

21 March when a 500 hPa shortwave trough moves over Mongolia (Figure 7(a)). At 700 hPa, the northwesterlies behind the trough prevail, and the cold advection supports the development of the trough (Figure 7(b)). Near the southern end of the 700 hPa trough, the traced dust parcel in the lowest level of Figure 5(b) is generated among the dust clouds due to strong surface winds during dust generation. After mixing and rising upward to 700 hPa, the traced dust parcel continues to move slightly upward in response to weak ascending motion (heavy solid lines) near the cyclone center. It then ascends for about half a day before descending behind the trough in the next day (also see Figure 5(b)).

About one day later, the associated trough has moved toward the eastern coast of China (Figures 7(d)–7(f)). The cold advection is strong behind the trough in the lower troposphere (Figures 7(e) and 7(f)), leading to further trough

development. The trough extends southward in the midlatitudes to about 35°N (Figures 7(d)–7(f)). The traced dust parcel, located behind the trough where northwesterlies prevail, travels mainly eastward and slightly southward, remaining at around 40°N (Figure 7(e)). At the same time, some dust clouds at the higher altitudes (500 hPa to 700 hPa) travel eastward ahead of the trough in ascending areas. Similar to many high-level transport events, these ascending dust clouds travel eastward under the prevailing westerlies and affect the areas further downwind.

On 23 March, when the trough nearly moves from the eastern coast of China, the trough slightly deepens and extends southeastward to Japan and the western North Pacific, reaching about 30°N (Figures 7(g)–7(i)). At this time, northwesterlies prevail behind the trough. Following the prevailing wind, the dust clouds together with the traced dust parcel

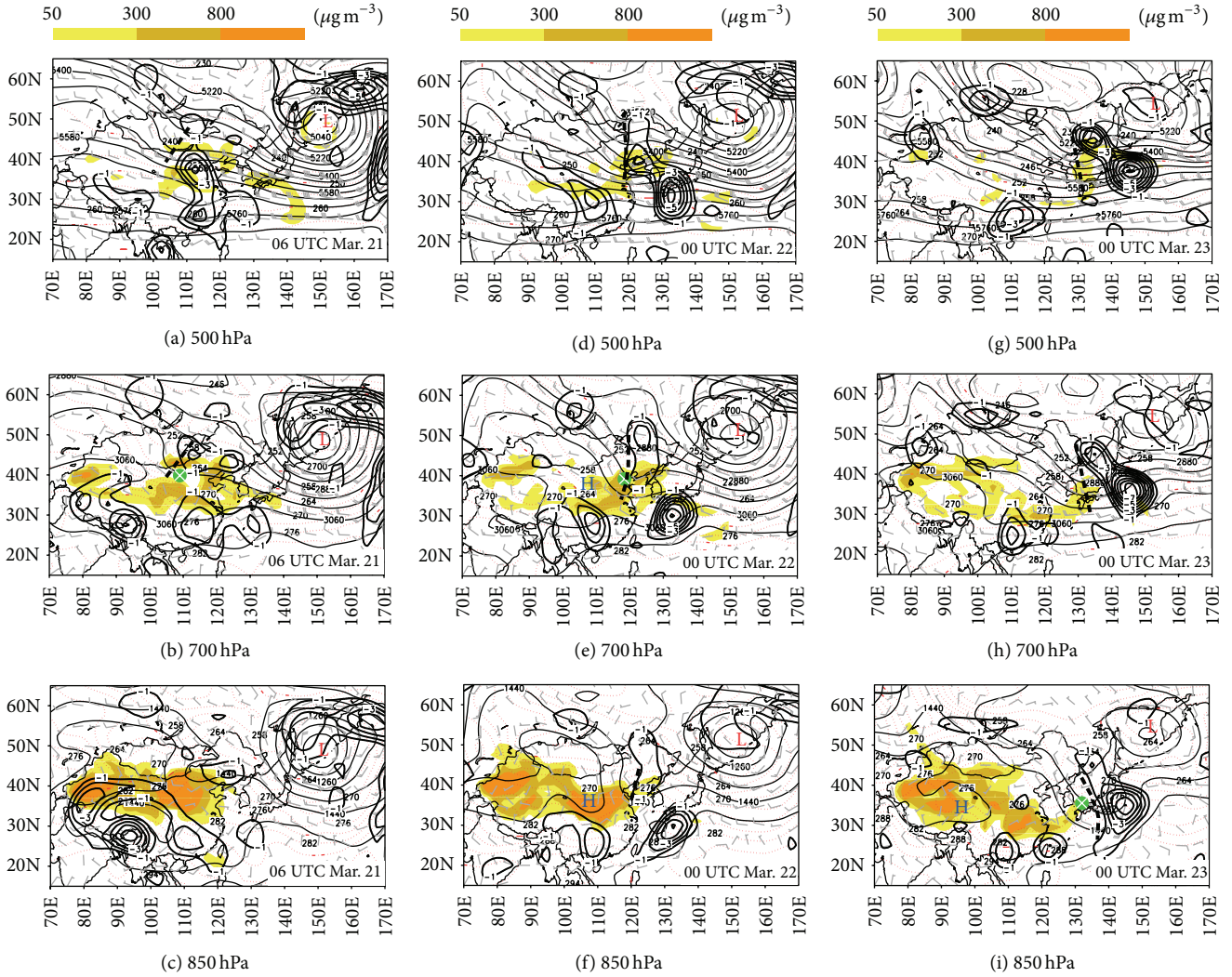


FIGURE 7: As in Figure 6, but for eastward dust event at 500, 700, and 850 hPa of (a)–(c) 0600 UTC on 21 March, (d)–(f) 0000 UTC on 22 March, and (g)–(i) of 0000 UTC on 23 March, respectively.

move slightly southeastward downwind toward Japan, in which the traced dust parcel also sinks to 850 hPa due to the descending motion behind the trough.

After leaving the continent, both the southeastward and eastward transport events pass through Taiwan and Japan and dissipate over the marginal sea of the western North Pacific Ocean. Figure 8 shows the model results of the dust events at this stage. During the southeastward movement, the surface cold front passes over Taiwan on 19 March (Figure 8(a)). Behind the cold front, the surface anticyclone has moved from Mongolia to Shanghai city (about 121°E, 31°N) at the same time. The anticyclonic circulation covers most of the eastern coast, reaching as far as southern Taiwan (23°N). Owing to the circulation to the east of the surface high, the prevailing winds are almost northerlies in the lower troposphere offshore of China. The dust clouds, with concentrations up to 300 $\mu\text{g m}^{-3}$ at the southern rim of the surface high, follow the prevailing northerlies and move southward along the Asian continent. Due to the rapid movement of the

surface anticyclone and strong surface winds (up to 15 m s^{-1}), the dust clouds quickly move past northern Taiwan toward the South China Sea (Figure 8(b)).

On 21 March, as the surface anticyclone (about 138°E, 26°N) moves offshore to the North Pacific, the wind speeds to the southwest of the anticyclone decrease to approximately 5 m s^{-1} , resulting in a deceleration in dust transport over the area (Figure 8(b)). At the same time, the prevailing easterlies to the south of the surface high-pressure system circulate the dust clouds back toward the eastern coast of the continent (Figure 8(b)). After the passage of the surface anticyclone on 21 March, the dust clouds remain around southern Taiwan and the northern South China Sea, with concentrations up to 140 $\mu\text{g m}^{-3}$ reaching as far south as 20°N.

For the eastward dust event, the dust clouds move off the eastern coast behind the associated surface front on 23 March (Figure 8(c)), with concentrations up to 300 $\mu\text{g m}^{-3}$ extending from southern Japan to northern Taiwan. At this time, the weak surface anticyclone remains over eastern China

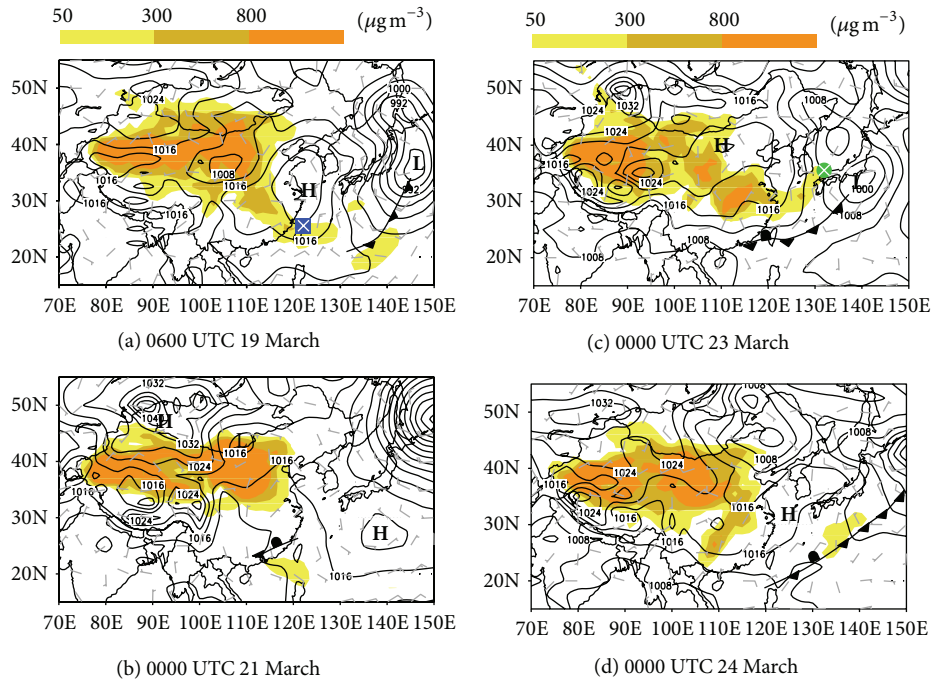


FIGURE 8: Surface maps and simulated dust distributions for the southeastward event at (a) 0600 UTC on 19 March and (b) 0000 UTC on 21 March and eastward event at (c) 0000 UTC on 23 March and (d) 0000 UTC on 24 March. Sea-level pressure is analyzed at 4 hPa interval. The full and half barbs represent 10 and 5 m s⁻¹, respectively. The traced dust parcels predicted by the trajectory model are marked (circle or square with x).

(around 40°N), far behind the offshore dust clouds, whereas the leading front becomes almost stationary over central Taiwan. Under the slower system, the dust clouds persist over the midlatitudes behind the front. As a result, high dust concentrations are distributed over Southeast China and the East China Sea instead of moving southeastward. One day later (Figure 8(d)), when the surface anticyclone moves southeastward over Shanghai city, some dust clouds with concentration up to 200 $\mu\text{g m}^{-3}$ already move eastward to the south of Japan away from the anticyclonic circulation, while other dust clouds behind the anticyclone remain over Southeast China. At the same time, the surface wind over the dust clouds decreases to less than 5 m s⁻¹. Under the weak anticyclonic circulation and the slow system, the dust residual slowly dissipates over the nearby areas in the midlatitudes.

4.2. Other Events of the Two Types. Similar to the first events of the two types, the synoptic map and the trajectories for the rest of the dust events are analyzed. The trajectories started from Wanli, the northern tip of Taiwan, for the southeastward event and Matsue, Japan, for the eastward events, with altitudes originating from 200 m, 500 m, and 800 m, similar to the first dust events. The maximum observed dust concentration or lidar measurement from the two stations (Table 1) is traced forward or backward until the locations of the traced dust parcel relative to the lower tropospheric and surface maps that discussed in Figures 2 and 3 are found, except 850 hPa instead of 700 hPa in Figure 2 is used as the low tropospheric map. Dust parcel originating from 800 m is

plotted at 850 hPa because this is the closest level of the dust parcel, while dust parcel originating from 200 m is plotted on the surface map.

Figure 9 shows the traced dust parcel relative to the 850 hPa and surface synoptic map over the coastal East Asia for the southeastward and eastward dust events. At 850 hPa, although the traced dust parcels of the two events are all located behind the trough, the traced dust parcel of the southeastward event reaches far south behind the deep trough while the traced dust parcel of the eastward event remains in the midlatitudes. At surface, the results show that the dust parcels of the southeastward events all locate south of the strong surface anticyclone near Southeast China while the parcels of the eastward events all remain between the surface cyclone and anticyclone over Japan, a result consistent with the study of the first event of the two types.

5. Conclusions

This study contrasts two types of Asian dust events during 2006–2009 to understand the synoptic environment that favors a substantial southeastward and eastward transport of Asian dust off the coastal East Asia. The synoptic maps, lidar observations, and a dust model simulation are applied for the analyses. The results show that the synoptic environments in the lower troposphere and surface levels are important factors resulting in difference between southeastward and eastward transports of the dust event and are summarized as follows.

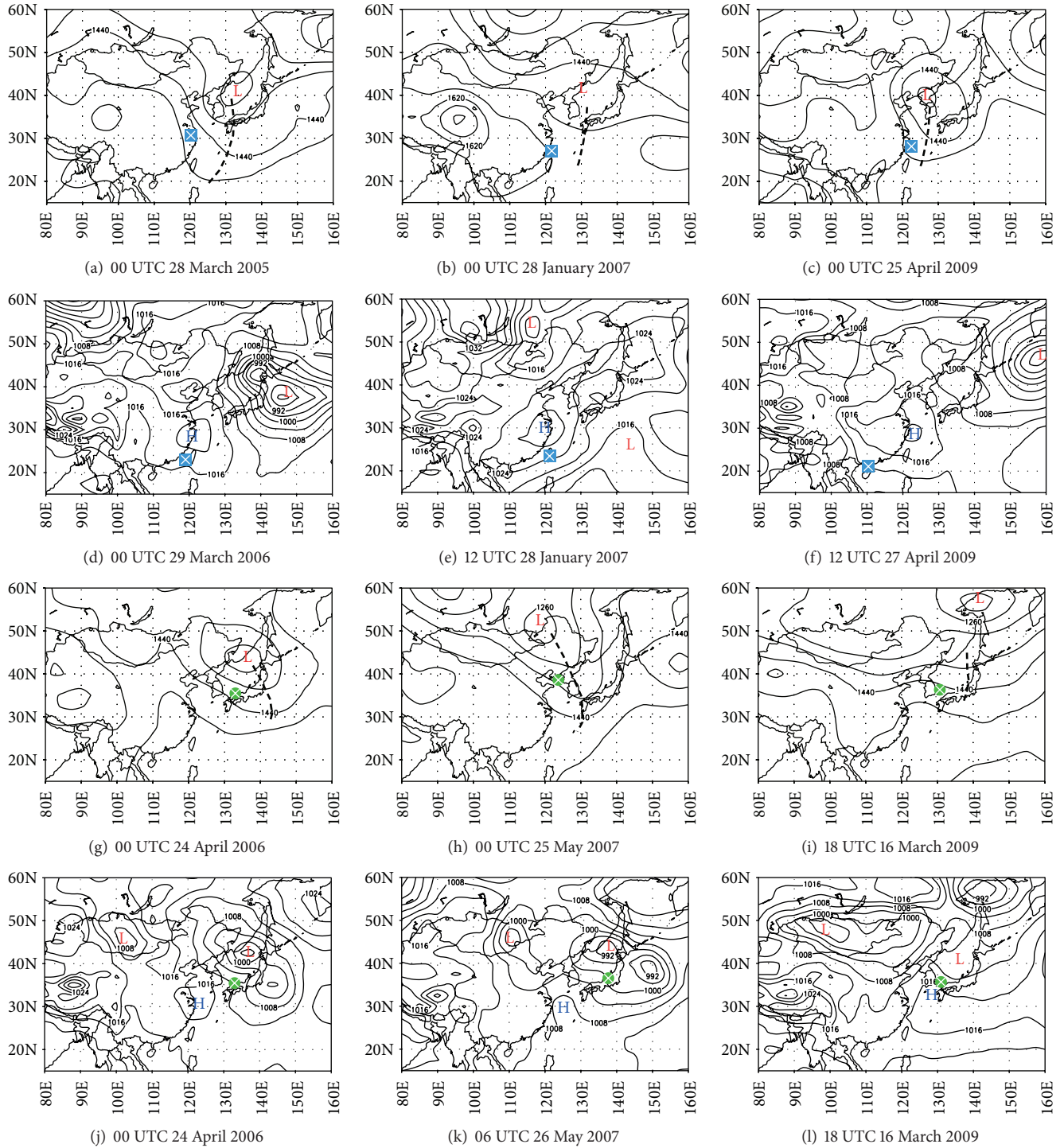


FIGURE 9: Location of dust parcel relative to 850 hPa and surface synoptic maps over coastal East Asia for other southeastward [(a)–(c) and (d)–(f)] and eastward [(g)–(i) and (j)–(l), respectively] dust events, except the two first events in Figures 6–8.

Figure 10 shows that during the dust transport in the free troposphere, the extent of the trough is different between eastward and southeastward transport. The trough associated with the southeastward transport event deepens and extends far southward beyond 30°N when moving over the eastern coast (Figure 10(a)). The prevailing northwesterlies to

northerlies behind this trough carry the dust parcel almost directly southward to the low latitudes, resulting in deep southeastward transport. The rapid descent in the southeastward transport than in the eastward transport can also be attributed to the dust transport behind a deep trough where descending motion is stronger than in a shallow trough.

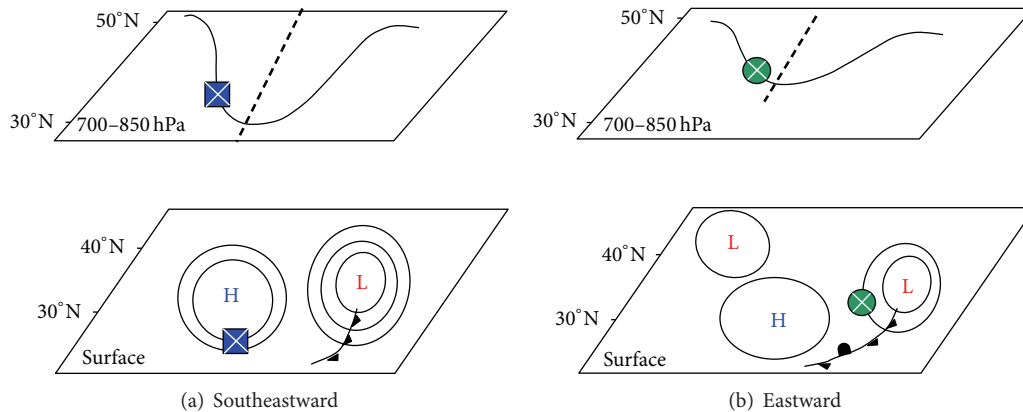


FIGURE 10: Schematic diagram showing the locations of the traced dust parcels (circle or square with x) relative to synoptic maps in the lower troposphere and at surface for (a) southeastward- and (b) eastward-moving events. Lower-level trough (heavy dash line) and surface front (solid line with triangle) are plotted. High- (H) and low- (L) pressure systems are marked.

Similar phenomena are not seen in the eastward transport dust event because the trough is shallower and remains north of 30°N when moving over the eastern coast (Figure 10(b)). Dust clouds follow the westerlies to northwesterlies behind the shallower trough moving mainly eastward rather than southward.

Furthermore, when both dust events move off the coast to downwind areas, they also descend behind the associated surface front locating around the southern or eastern rim of the anticyclone. The associated anticyclonic circulations of the southeastward dust events are strong and cover a wide area of East and Southeast China, with a maximum pressure of more than 1020 hPa reaching south beyond 30°N. The surface anticyclone in the southeastward event moves southeastward immediately behind the dust parcel. Thus, under the rapid movement of the system and the strong northerlies to the east of the surface anticyclone, the southeastward transport dust event continues to move southward following the circulation. Since intense surface anticyclones often associated with strong surface winds and severe dust events, southeastward dust events often related to strong dust events.

For the eastward event, the anticyclonic circulation is weak, with maximum pressure less than 1020 hPa locating north of 30°N when moving over the eastern coast. The weak and slow movement of the anticyclone and the leading frontal system in the eastward transport event result in the persistence of the anticyclonic circulation, and thus the dust clouds over the midlatitudes.

The arrival of eastward dust events can affect the air quality over the coastal East Asia, while southeastward dust transport over the subtropical areas can have significant impacts not only on the air quality of the areas but also on the marine biogeochemistry by providing crustal nutrients to these nutrient-limited areas [12–14, 17, 18].

Conflict of Interests

The authors declare that there is no conflict of interests regarding the publication of this article.

Acknowledgments

The authors gratefully acknowledge National Oceanic and Atmospheric Administration (NOAA) Air Resources Laboratory (ARL) for providing the HYSPLIT model (<http://www.arl.noaa.gov/ready.html>) for use in this paper. The authors would also like to thank Dr. Nobuo Sugimoto of the National Institute for Environmental Studies in Japan for providing the Matsue lidar data on the lidar network (<http://www-lidar.nies.go.jp/>) for use in the paper. The authors also appreciate the Japanese Meteorological Agency for providing the information of dust event (http://www.data.kishou.go.jp/obs-env/kosahp/kosa_table_2006.html). The authors also thank two reviewers' suggestions. This study was supported by NSC 102-2611-M-0190-017-.

References

- [1] M. Uematsu, R. A. Duce, J. M. Prospero, L. Chen, J. T. Merrill, and R. L. McDonald, "Transport of mineral aerosol from Asia over the North Pacific ocean," *Journal of Geophysical Research*, vol. 88, no. 9, pp. 5342–5352, 1983.
- [2] I. G. McKendry, J. P. Hacker, R. Stull, S. Sakiyama, D. Mignacca, and K. Reid, "Long-range transport of Asian dust to the Lower Fraser Valley, British Columbia, Canada," *Journal of Geophysical Research D*, vol. 106, no. 16, pp. 18361–18370, 2001.
- [3] J. Sun, M. Zhang, and T. Liu, "Spatial and temporal characteristics of dust storms in China and its surrounding regions, 1960–1999: relations to source area and climate," *Journal of Geophysical Research D*, vol. 106, no. 10, pp. 10325–10333, 2001.
- [4] X. Y. Zhang, R. Arimoto, and Z. S. An, "Dust emission from Chinese desert sources linked to variations in atmospheric circulation," *Journal of Geophysical Research D*, vol. 102, no. 23, pp. 28041–28047, 1997.
- [5] B. Laurent, B. Marticorena, G. Bergametti, and F. Mei, "Modeling mineral dust emissions from Chinese and Mongolian deserts," *Global and Planetary Change*, vol. 52, no. 1–4, pp. 121–141, 2006.
- [6] Y. Iwasaka, H. Minoura, and K. Nagaya, "The transport and spacial scale of Asian dust-storm clouds: a case study of the

- dust-storm event of April 1979 (China, Japan Islands),” *Tellus B*, vol. 35, no. 3, pp. 189–196, 1983.
- [7] Y. S. Chung, “On the observations of yellow sand (dust storms) in Korea,” *Atmospheric Environment A*, vol. 26, no. 15, pp. 2743–2749, 1992.
- [8] Y. Chun, K. O. Boo, J. Kim, S. U. Park, and M. Lee, “Synopsis, transport, and physical characteristics of Asian dust in Korea,” *Journal of Geophysical Research D*, vol. 106, no. 16, pp. 18461–18469, 2001.
- [9] T. H. Liu, F. Tsai, S. C. Hsu et al., “Southeastward transport of Asian dust: source, transport and its contributions to Taiwan,” *Atmospheric Environment*, vol. 43, no. 2, pp. 458–467, 2009.
- [10] I. Mori, M. Nishikawa, T. Tanimura, and H. Quan, “Change in size distribution and chemical composition of kosa (Asian dust) aerosol during long-range transport,” *Atmospheric Environment*, vol. 37, no. 30, pp. 4253–4263, 2003.
- [11] F. Tsai, T. H. Liu, S. C. Liu, T. Y. Chen, T. L. Anderson, and S. J. Masonis, “Model simulation and analysis of coarse and fine particle distributions during ACE-Asia,” *Journal of Geophysical Research*, vol. 109, no. 19, 2004.
- [12] J. Li, Z. Han, and R. Zhang, “Model study of atmospheric particulates during dust storm period in March 2010 over East Asia,” *Atmospheric Environment*, vol. 45, no. 24, pp. 3954–3964, 2011.
- [13] S. H. Wang, S. C. Tsay, N. H. Lin et al., “First detailed observations of long-range transported dust over the northern South China Sea,” *Atmospheric Environment*, vol. 45, no. 27, pp. 4804–4808, 2011.
- [14] C. M. Liu, C. Y. Young, and Y. C. Lee, “Influence of Asian dust storms on air quality in Taiwan,” *Science of the Total Environment*, vol. 368, no. 2–3, pp. 884–897, 2006.
- [15] I. I. Lin, J. P. Chen, G. T. F. Wong, C. W. Huang, and C. C. Lien, “Aerosol input to the South China Sea: results from the MODerate resolution imaging spectro-radiometer, the quick scatterometer, and the measurements of pollution in the troposphere sensor,” *Deep-Sea Research Part II*, vol. 54, no. 14–15, pp. 1589–1601, 2007.
- [16] J. Zhao, F. Zhang, Y. Xu et al., “Chemical characteristics of particulate matter during a heavy dust episode in a coastal city, Xiamen, 2010,” *Aerosol and Air Quality Research*, vol. 11, no. 3, pp. 300–309, 2011.
- [17] S. H. Wang, N. C. Hsu, S. C. Tsay et al., “Can Asian dust trigger phytoplankton blooms in the oligotrophic northern South China Sea?” *Geophysical Research Letters*, vol. 39, no. 5, Article ID L05811, 2012.
- [18] F. Tsai, Y. S. Fang, and S. J. Huang, “Case study of Asian dust event on March 19–25, 2010 and its impact on the marginal sea of China,” *Journal of Marine Science and Technology*, vol. 21, no. 3, pp. 353–360, 2013.
- [19] M. Liu, D. L. Westphal, S. Wang et al., “A high-resolution numerical study of the Asian dust storms of April 2001,” *Journal of Geophysical Research D*, vol. 108, no. 23, pp. 1–21, 2003.
- [20] R. R. Dickerson, C. Li, Z. Li et al., “Aircraft observations of dust and pollutants over northeast China: insight into the meteorological mechanisms of transport,” *Journal of Geophysical Research D*, vol. 112, no. 24, Article ID D24S90, 2007.
- [21] J. Y. Yu, Y. M. Cuo, and J. Y. Tu, “On the space-time characteristics of East Asian dust storm,” *Environmental Protection*, vol. 25, no. 2, pp. 178–198, 2002 (Chinese).
- [22] F. Tsai, G. T. J. Chen, T. H. Liu, W. D. Lin, and J. Y. Tu, “Characterizing the transport pathways of Asian dust,” *Journal of Geophysical Research*, vol. 113, no. 17, 2008.
- [23] W. N. Chen, S. Y. Chang, C. C. K. Chou, Y. W. Chen, and J. P. Chen, “Study of relationship between water-soluble Ca^{2+} and lidar depolarization ratio for spring aerosol in the boundary layer,” *Atmospheric Environment*, vol. 41, no. 7, pp. 1440–1455, 2007.
- [24] A. Shimizu, N. Sugimoto, I. Matsui et al., “Continuous observations of Asian dust and other aerosols by polarization lidars in China and Japan during ACE-Asia,” *Journal of Geophysical Research D*, vol. 109, no. 19, Article ID D19S17, 2004.
- [25] D. Liu, Z. Wang, Z. Liu, D. Winker, and C. Trepte, “A height resolved global view of dust aerosols from the first year CALIPSO lidar measurements,” *Journal of Geophysical Research D*, vol. 113, no. 16, Article ID D16214, 2008.
- [26] E. Kalnay, M. Kanamitsu, R. Kistler et al., “The NCEP/NCAR 40-year reanalysis project,” *Bulletin of the American Meteorological Society*, vol. 77, no. 3, pp. 437–471, 1996.
- [27] F. T. Jeng, J. S. Chang, K. H. Chang, H. Huang, and T. Liu, *Taiwan Air Quality Model User Manual*, Graduate Institute of Environmental Engineering, National Taiwan University, Taipei, Taiwan, 2000 (Chinese).
- [28] R. A. Anthes and T. T. Warner, “Development of hydrodynamic models suitable for air pollution and other mesometeorological studies,” *Monthly Weather Review*, vol. 106, pp. 1045–1078, 1978.
- [29] J. Dudhia, “A nonhydrostatic version of the Penn State-NCAR mesoscale model: validation tests and simulation of an Atlantic cyclone and cold front,” *Monthly Weather Review*, vol. 121, no. 5, pp. 1493–1513, 1993.
- [30] G. A. Grell, J. Dudhia, and D. R. Stauffer, “A description of the fifth generation Penn State/MCAR mesoscale model (MM5),” Technical Note NCAR/TN-398+STR, National Center for Atmospheric Research, Boulder, Colo, USA, 1994.
- [31] Z. Wang, H. Ueda, and M. Huang, “A deflation module for use in modeling long-range transport of yellow sand over East Asia,” *Journal of Geophysical Research D*, vol. 105, no. 22, pp. 26947–26959, 2000.
- [32] A. Bott, “A positive definite advection scheme obtained by nonlinear renormalization of the advective fluxes,” *Monthly Weather Review*, vol. 117, no. 5, pp. 1006–1015, 1989.
- [33] J. Y. Yu, Y. W. Wang, and C. W. Chang, “Asian dust storm activity and its association with atmospheric circulation from 1995 to 2006,” *Terrestrial, Atmospheric and Oceanic Sciences*, vol. 21, no. 2, pp. 375–391, 2010.
- [34] R. R. Draxler and G. D. Hess, “Description of the HYSPLIT-4 modeling system,” NOAA Technical Memorandum ARL-224, Environmental Research Laboratory (ERL), 1997.

Research Article

Unusual Warming in the Coastal Region of Northern South China Sea and Its Impact on the Sudden Intensification of Tropical Cyclone Tembin (2012)

Zhe-Wen Zheng

Institute of Marine Environmental Science and Technology and Department of Earth Science, National Taiwan Normal University, Taipei 11677, Taiwan

Correspondence should be addressed to Zhe-Wen Zheng; zwz@ntnu.edu.tw

Received 27 October 2013; Accepted 28 November 2013; Published 29 January 2014

Academic Editor: Yuriy Kuleshov

Copyright © 2014 Zhe-Wen Zheng. This is an open access article distributed under the Creative Commons Attribution License, which permits unrestricted use, distribution, and reproduction in any medium, provided the original work is properly cited.

Tropical cyclone Tembin (2012) passed twice and made landfall over south tip of Taiwan in August 2012. During its passage, an unusual sea surface warming was generated at 22.5°N, 117°E in the coastal region of northern South China Sea. Subsequently, Tembin passed over this extreme warming region and its intensity was enhanced drastically and suddenly from Category 1 to Category 3 within less than 1-day time interval. This unusual warming seems to largely prompt the intensification of Tembin. Next, the relationship between this extreme warming and rapid intensification of Tembin is identified by atmospheric model Weather Research and Forecast (WRF) with updated time-varying lower boundary condition. In addition, given the tight relationship between generation of unusual warming in the shore region and following possible TC intensification, a series of numerical experiments based on oceanic model Regional Oceanic Modeling System (ROMS) were designed and executed to resolve the possible generated mechanism of the extreme warming. The results indicate that a distinct positive short-wave radiation influx anomaly may dominate the generation of the unusual warming in the shore region during Tembin's passage. This result is validated by the distributions of free cloudy coverage shown in satellite infrared images.

1. Introduction

The phenomena of sea surface temperature (SST) cooling in response to a tropical cyclone (TC) passage have been investigated comprehensively in numerous studies (e.g., [1–5]). TC's passage has been shown to markedly lower the sea surface temperature (SST) under certain circumstances [1–4, 6, 7]. Furthermore, because evaporation and conduction are directly dependent upon the air-sea temperature difference, SST drops would directly determine the energy fed into the storm from the ocean [8] and thus their impact on TC intensity evolutions [9–11].

However, on the contrary, the generation of an unusual sea surface warming during a TC passage does not attract too much investigative attention [12], because they are much rare relatively to the generation of a cooling case. Its impact on the TC intensity changes is not even clear sufficiently yet. Given the same concept but in a different way, that

warming may cause TC intensification through feeding more energy from ocean to TC through air-sea exchange. Moreover, extreme warming which occurred near the coastal region is extraordinary important, because it may cause TC rapid intensification just prior to making landfall in heavily populated coastal region. In other words, the generation of that warming near the coastal region may directly link to the possible increase of threats of TC on those people and economic activity surrounding the coastal region.

Tembin (2012) lingered over northern South China Sea (NSCS) from 24 August to 27 August and passed through an extreme warming patch at 22.5°N, 117°E on 25 August. After encountering the distinct warming patch generated along northeastern SCS, intensity of Tembin is enhanced drastically and suddenly from category 1 to category 3 within less than 1-day time interval. Air-sea interaction which occurred during the passage of Tembin provides us with a unique opportunity to clarify the relationship between that coastal

warming and the consequential possible intensification of TCs. One of the main goals of this work is to identify the causation between warming occurring in the coastal region and following TC intensification from a more convinced, dynamic based tool/perspective. On the other hand, we further hope to clarify the possible mechanism(s) causing the generation of warming within the coastal region that eventually may trigger a TC rapid intensification just prior to its landfall and thus may increase the threats to those economical activities and people living near the coastal low-lying region [13].

2. Data and Methods

In this work, the cyclonic track and intensity data are obtained from the Unisys weather (<http://weather.unisys.com/hurricane/>). Microwave SST products retrieved from Tropical Rainfall Measuring Mission (TRMM) Microwave Imager (TMI) are used to characterize the evolution of unusual warming in the shore region generated during Tembin's passage [2]. In Section 3, numerical experiments using atmospheric model Weather Research and Forecast (WRF) are conducted to evaluate the impact of SST warming occurring in the coastal region on the TC intensity changes of Tembin. Initial and boundary conditions for WRF were produced from Global Forecast System (GFS) FNL global analysis field with a $1^\circ \times 1^\circ$ spatial resolution in a 6-hour temporal interval. Meanwhile, a series of numerical experiments based on oceanic numerical model Regional Ocean Modeling System (ROMS) were conducted in Section 4 to help the understanding of the generation of extreme warming in the coastal region of northern SCS (NSCS) during Tembin's passage. Initial and boundary condition for ROMS were derived from HYCOM/NCODA system outputs [14]. Heat and momentum fluxes in ROMS were calculated from atmospheric parameters obtained from GFS (available at <http://nomads.ncdc.noaa.gov/>) with a bulk formula during the model run. More details about the configuration of ROMS model are given by Zheng et al. [15].

3. Warming versus TC Rapidly Intensification

3.1. Observations. Figure 1(a) shows the SST collected on 25 August. One can see that there is one distinct warming occurring in the coastal region along the NSCS continental shelf at around 22.5°N , 117.5°E , though the SST is not very uniform in this region because of the passage of previous TC Kai-Tak (12–17 August). Relative to cooling also caused by Tembin's passage, the extreme warming generated at the coastal region along NSCS is more distinct and unique. Figures 1(b)–1(f) show the corresponding SST evolution during Tembin's passage and demonstrate the generation and evolution of the unusual warming in the coastal region. From Figure 1, one can see that the warming patch grows up from August 22 to August 25 and starts to decay on August 26. Finally, it disappears while the cooling in response to Tembin passage took place.

In addition to the generation of unusual warming in the coastal region along the continental shelf of NSCS, more interesting is the relationship between the warming and consequential TC intensity changes. Figure 2 shows the TC intensity change of Tembin before and after encountering the warming patch located at the coastal region. From Figure 2, it is evident that from 12:00 UTC 25 August to 6:00 UTC 26 August, after Tembin encountering the distinct warming patch occurring along the NSCS continental shelf, the strength of Tembin rapidly intensified from Category 1 to Category 3 within 18-hour temporal interval. Next, after passing the Dongsha atoll, the strength of Tembin weakened steadily until it leaves the study area. This result suggests a crucial scenario that the extreme coastal warming may serve as a booster for increasing the intensity of a TC in a very short time period. It is worth claiming that this possible intensification of TC intensity may directly increase the threats to those people living in the coastal low-lying region, because this unusual warming occurs in the coastal region just prior to the landfall of a given TC.

3.2. Simulations. Here, the tight relationship between surface warming and following possible TC rapid intensification shown in previous section by observations is further validated. In this section, WRF is applied to elucidate the effect of different SST on TC intensity changes. For comparison, two numerical experiments based on WRF were designed and executed. In both experiments, all parameters configurations were set by default values as provided by WRF community. To reveal the effect resulting from lower boundary condition to TC intensity changes, the configurations of update_SST were turned on in both WRF experiments. This setting would allow the influence of lower boundary condition (sea surface warming) entering the atmospheric fields and thus influencing the TC intensity changes. The only different condition between both experiments is the configuration of different SST as time-independent lower boundary condition.

In both experiments, the lower boundary conditions were all provided by Microwave SST retrieved from TMI. In warming run (EXP warming), the warming patch is enclosed by a 1 degree by 2 degree rectangle box centered at the original warming patch with SST of 30.5°C . In contrast run (EXP nonwarming), the box area of warming SST is replaced by 28.5°C . This configuration is designed to make sure that the passage of Tembin would pass adequately through the warming and the nonwarming area for evaluating the difference from different lower boundary on TC intensity changes.

Figure 3 shows the simulated intensities evolution of Tembin retrieved from experiments EXP warming and EXP nonwarming. However, it is noted that because of the presence of a nearby strong TC Bolaven (Category 4, 20–28 August), it is very difficult to simulate the moving track of Tembin properly without nudging. The timing of Tembin passing over the warming patch is slightly different from the real situation (as shown by best-track data). Nevertheless, relative to the nonwarming scenario, with the influence of warming from lower boundary condition, the intensity

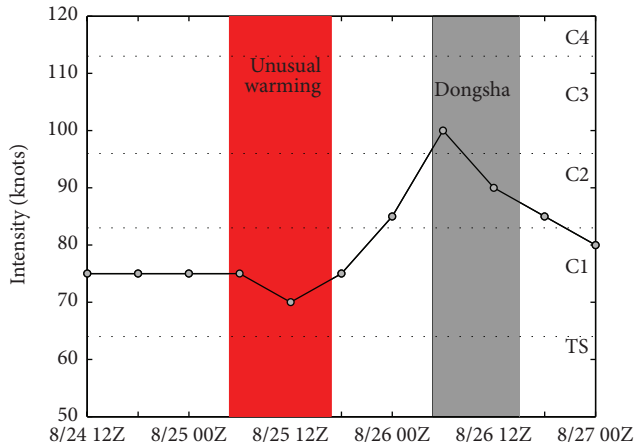


FIGURE 2: Correspondent time series of TC intensity change during Tembin's rapid intensification and following TC intensity weakening.

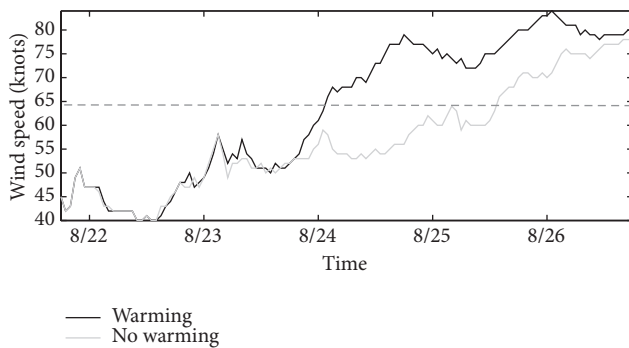


FIGURE 3: WRF simulated intensities of Tembin during the passage of warming (nonwarming) patch. Gray dashed line denotes the intensity of Category 1 in Saffir-Simpson hurricane wind scale.

changes of Tembin are well documented to show a distinct rapid intensification once it passed over the box region with different SST (warming) setting. The result derived from WRF numerical experiments identifies the causal relationship between coastal warming and consequence of TC rapid intensification. After identifying the tight relationship between them, the next key issue is to know what kinds of mechanism would cause an extreme warming in the coastal region. Given the tight relationship between warming and following possible TC rapid intensification, to get further understanding about the generation of warming in the coastal region would be very helpful for improving the TC intensity prediction in particular near the coastal region just prior to TC's landfall.

4. What Causes the Warming in the Coastal Region of NSCS?

Because the dynamic relationship and interactions among related variables (e.g., wind, current, topography, and air-sea flux exchange) would be very hard to infer from the

observations data alone, to obtain a comprehensive understanding about the generation of the extreme warming in the coastal region of NSCS, a series of numerical experiments dealing with the influence from wind, currents, and influx from atmosphere based on ROMS were designed and conducted here. First, in EXPstd, all contributions from both ocean and atmosphere were turned on to attempt to reproduce the results as well as those shown by satellite observations. Figures 4(a)–4(d) show the simulated SSTs during the intensification of Tembin in EXPstd. One can see that the warming in the shore region along NSCS coast is reproduced reasonably well in EXPstd. The coastal warming disappears until the strong surface cooling response occurs after the passage of Tembin. Next, to distinguish the main contributions (key mechanism) resulting in the coastal warming, two more contrast experiments (EXP1 and EXP2) were further executed.

In EXP1, all configurations were set as EXPstd except the air-sea flux exchange which was zeroed out. In EXP2, influences of TC wind forcing were removed by masking out high wind with wind speed more than 18 m s^{-1} from the wind field to evaluate the role of wind forcing play in this case, but all other contributions were kept as EXPstd. The threshold of 18 m s^{-1} is decided referring to the analysis of accumulated cyclone energy for a tropical cyclone [16]. Comparing the results derived from EXP1 and EXPstd (seeing Figure 4), one can see that, without the input of sea surface heat flux (SHF), there is no longer distinct warming patch generated at the coastal region along NSCS continental shelf, though other forcings are the same as those used in standard experiment (EXPstd). This implies that the input of SHF plays a key role in the generation of this unusual warming.

Comparing results of EXP2 with those results of EXPstd, it can be seen that, without TC wind forcing (no TC wind driven currents), the warming is still revealed at similar position prior to TC passage, though cooling caused by Tembin largely decreases. This implies that the influences of removing TC wind forcing reflect mainly on the relaxation period after the passage of TC. This result dismisses the scenario of current convergence causing downwelling in the coastal region, thus prompting the coastal warming, as noted in previous studies [12, 17, 18]. In other words, there must be other mechanisms dominating the warming occurring during Tembin passage in addition to the inference proposed by Tsai et al. [12]. Nevertheless, at the same time, the key issue of "how does the warming generate?" has been narrowed to SHF exchange occurring through the air-sea interface only. In this case, wind driven current convergence plays a somewhat surprising minor role in contributing to the generation of warming. This underplay is attributed to the block of high mountain topography in the central part of Taiwan.

In ROMS, total SHF was estimated by incoming short wave radiation, outgoing long wave radiation, sensible heat flux, and latent heat flux. Here, by comparing the contributions of each heat flux terms to the total SHF in our model scheme for EXPstd, it is found that the warming patch generated in front of Tembin's passage is mainly contributed by an unusual increase of positive short wave radiation

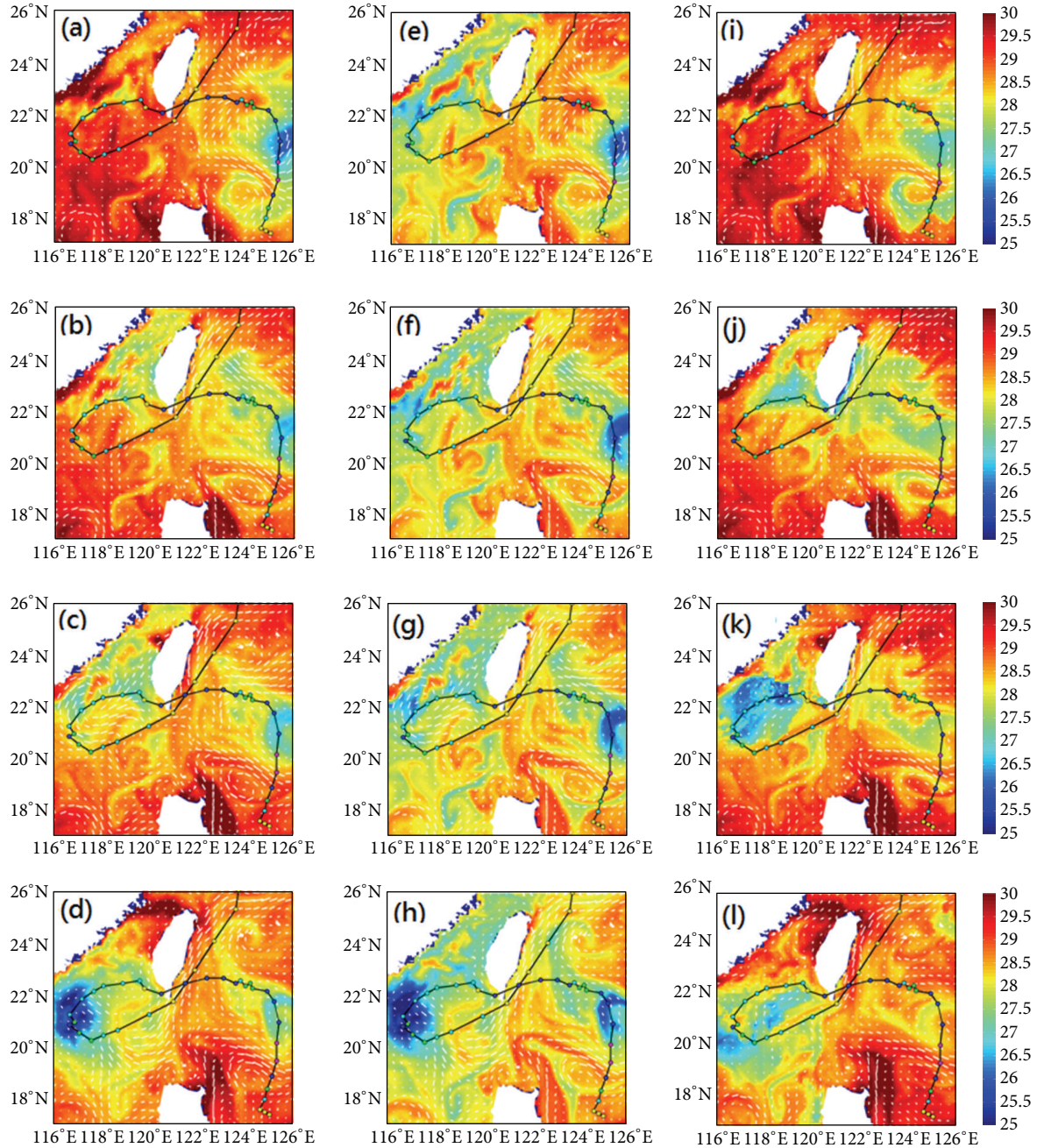


FIGURE 4: (a)–(d) ROMS simulated SST (unit: degree C) during the intensification of Tembin (23 August, 25 August, 26 August, and 28 August) in EXPstd. (e)–(h) Same as (a)–(d) but for EXP1. (i)–(l) Same as (a)–(d) but for EXP2.

anomaly which occurred on 21–22 August, two days. The impact of this short wave radiation anomaly can be seen clearly in ROMS simulated SSTs, especially on 21 August (figures not shown). Subsequently, we need to figure out the source of where this positive short wave radiation anomaly comes to answer the question of “how does the warming during Tembin’s passage generate?”

Previous studies pointed out that the incoming solar (shortwave) radiation is primarily determined by latitude, season, time of day, and cloudiness [19, 20]. During Tembin’s

passage, the previous three factors can be taken as constant, and thus there is only one factor remaining to influence the shortwave radiation influx during Tembin’s passage. Thus, we examine the evolution of cloud system prior to Tembin’s passage from 21 August to 24 August. Figure 5 shows the cloud coverage from 21 August to 24 August. On 21 August, one can see the existence of a heavy cloud system over MainLand China (extending from Indochina peninsula to northeast corner of China) and another cloud system gathered by TC Tembin from a “channel-like” cloudless belt

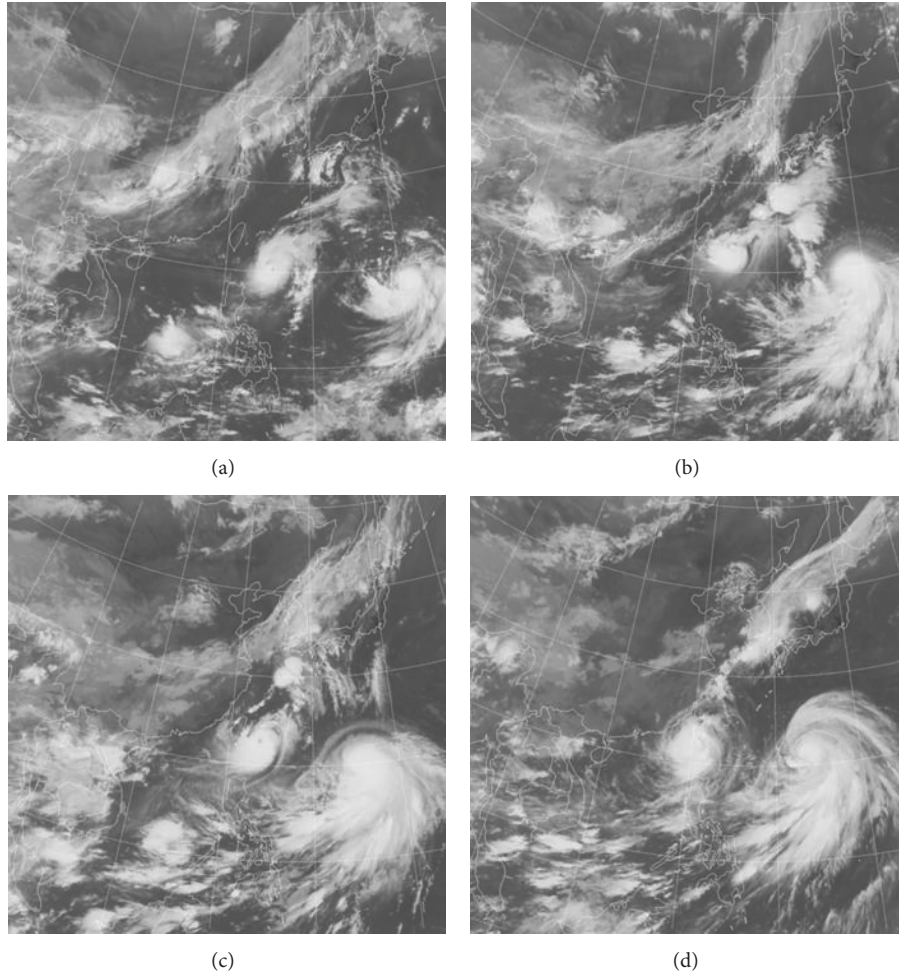


FIGURE 5: IR1_LCC images at (a) UTC 8 : 32 on 21 August, (b) UTC 8 : 32 on 22 August, (c) UTC 8 : 32 on 23 August, and (d) UTC 8 : 32 on 24 August, derived from CWB of Taiwan.

over Taiwan and Taiwan strait (TS) (seeing the channel in Figure 5(a)). On 22 August, with the approach (westward) of Tembin toward Taiwan, the cloudless belt is squeezed and getting thinner. Nevertheless, there is still a cloudless channel located over the TS and the west-half of Taiwan. Subsequently, due to the steady approach of Tembin, as a result, on 23 August, the original channel is occupied by the cloud system accompanied with Tembin's passage; meanwhile, both TS and Taiwan are covered by left part of the cloud system gathered by Tembin. On 24 August, the thick cloud system gathered by Tembin covers most parts of Taiwan and TS.

As mentioned above, in our case, incoming short wave radiation is mainly a function of cloud coverage only. Intuitively, the evolution of cloud coverage within the study area can be used to reflect the variations of amount of incoming shortwave radiation. Therefore, the results obtained from cloud coverage shown by satellite IR images in this section show somewhat surprising consistent with the inference we concluded from oceanic numerical experiments that the generation of warming in the coastal region along NSCS

during Tembin's passage mainly resulted from a strong positive shortwave radiation influx anomaly.

5. Conclusions

In 2012, passage of Tembin over an unusual warming occurring at the coastal region along NSCS suggests a crucial scenario that a distinct warming occurring in the coastal region may booster a rapid intensification of TC intensity just prior to its landfall. This process is extraordinarily important because the generation of that warming may cause sudden intensification of TC just prior to making landfall and thus increase the threats on those people and economic activity surrounding the low-lying coastal region over the world.

In this work, we first present a rather convincing evidence based on WRF to identify the relationship between unusual sea surface warming occurring in the coastal region and consequently rapid intensification of TC intensity based on the case of Tembin (2012). The results show that the presence of unusual warming in the shore region plays a key role

in the following rapid intensification of Tembin. Given the tight relationship between surface warming in the coastal region and consequently possible TC intensification, it is believed that the more we understand about the generation of that coastal warming, the better we can do about the TC intensity forecast especially for those sudden intensification events taking place just prior to their landfall. Next, a series of oceanic numerical experiments based on ROMS were executed to resolve the generated mechanism of those unusual warming occurring in the coastal region.

According to analyses on a series of sensitive experiments and estimation of heat budget balance in our model scheme, the generated mechanism of the extreme warming during Tembin's passage is shown to be highly associated with a distinct positive shortwave radiation influx anomaly. Accordingly, this finding is verified by the evolution of cloudless area during Tembin's passage shown by satellite IR images. This is a new and interesting process that has not been investigated adequately. Further investigations were needed to provide a more comprehensive understanding about the details of this process.

This work combines evidences and tools from ocean and atmosphere fields simultaneously, not only for identifying the tight relationship between the unusual warming in the coastal region and consequently possible TC intensification but also for shedding a new light on the process of generation of unusual warming in the coastal region. Given the possible increase of threats due to the sudden intensification of TC close to the coastal region, it is especially worth highlighting the necessity of monitoring the variations of incoming shortwave radiation nearby the coastal region in front of a TC passage through satellite IR images.

Conflict of Interests

The author declares that there is no conflict of interests regarding the publication of this paper.

Acknowledgments

This work was supported by the National Science Council of Taiwan through Grants NSC 101-2611-M-003-001 and NSC 100-2119-M-003-006. Microwave TMI SST data were provided by REMSS. Boundary conditions for ROMS derived from HYCOM/NCODA system were provided by HYCOM Consortium through <http://hycom.org/>. Composite infrared images were provided by Typhoon DataBase of Central Weather Bureau, Taiwan.

References

- [1] J. F. Price, "Upper ocean response to a hurricane," *Journal of Physical Oceanography*, vol. 11, no. 2, pp. 153–175, 1981.
- [2] F. J. Wentz, C. Gentemann, D. Smith, and D. Chelton, "Satellite measurements of sea surface temperature through clouds," *Science*, vol. 288, no. 5467, pp. 847–850, 2000.
- [3] I. Lin, W. T. Liu, C.-C. Wu et al., "New evidence for enhanced ocean primary production triggered by tropical cyclone," *Geophysical Research Letters*, vol. 30, no. 13, pp. 51–1, 2003.
- [4] N. D. Walker, R. R. Leben, and S. Balasubramanian, "Hurricane-forced upwelling and chlorophyll a enhancement within cold-core cyclones in the Gulf of Mexico," *Geophysical Research Letters*, vol. 32, no. 18, Article ID L18610, pp. 1–5, 2005.
- [5] F. M. Monaldo, T. D. Sikora, S. M. Babin, and R. E. Sterner, "Satellite imagery of sea surface temperature cooling in the wake of Hurricane Edouard (1996)," *Monthly Weather Review*, vol. 125, no. 10, pp. 2716–2721, 1997.
- [6] Z.-W. Zheng, C.-R. Ho, and N.-J. Kuo, "Importance of pre-existing oceanic conditions to upper ocean response induced by Super Typhoon Hai-Tang," *Geophysical Research Letters*, vol. 35, no. 20, Article ID L20603, 2008.
- [7] Z.-W. Zheng, C.-R. Ho, Q. Zheng, N.-J. Kuo, and Y.-T. Lo, "Satellite observation and model simulation of upper ocean biophysical response to Super Typhoon Nakri," *Continental Shelf Research*, vol. 30, no. 13, pp. 1450–1457, 2010.
- [8] D. F. Leipper and D. Volgenau, "Hurricane heat potential of the Gulf of Mexico," *Journal of Physical Oceanography*, vol. 2, pp. 218–224, 1972.
- [9] S. W. Chang and R. A. Anthes, "The mutual response of the tropical cyclone and the ocean," *Journal of Physical Oceanography*, vol. 9, no. 1, pp. 128–135, 1979.
- [10] P. G. Black and G. J. Holland, "The boundary layer of tropical Cyclone Kerry (1979)," *Monthly Weather Review*, vol. 123, pp. 2007–2028, 1995.
- [11] L. R. Schade and K. A. Emanuel, "The ocean's effect on the intensity of tropical cyclones: results from a simple coupled atmosphere-ocean model," *Journal of the Atmospheric Sciences*, vol. 56, no. 4, pp. 642–651, 1999.
- [12] Y. L. Tsai, C. S. Chern, and J. Wang, "Numerical study of typhoon-induced ocean thermal content variations on the northern shelf of the South China Sea," *Continental Shelf Research*, vol. 42, pp. 64–77, 2012.
- [13] I.-I. Lin, C.-H. Chen, I.-F. Pun, W. T. Liu, and C.-C. Wu, "Warm ocean anomaly, air sea fluxes, and the rapid intensification of tropical cyclone Nargis (2008)," *Geophysical Research Letters*, vol. 36, no. 3, Article ID L03817, 2009.
- [14] J. A. Cummings, "Operational multivariate ocean data assimilation," *Quarterly Journal of the Royal Meteorological Society*, vol. 131, no. 613, pp. 3583–3604, 2006.
- [15] Z.-W. Zheng, C.-R. Ho, Q. Zheng, Y.-T. Lo, N.-J. Kuo, and G. Gopalakrishnan, "Effects of preexisting cyclonic eddies on upper ocean responses to Category 5 typhoons in the western North Pacific," *Journal of Geophysical Research C*, vol. 115, no. 9, Article ID C09013, 2010.
- [16] S. J. Camargo and A. H. Sobel, "Western North Pacific tropical cyclone intensity and ENSO," *Journal of Climate*, vol. 18, no. 15, pp. 2996–3006, 2005.
- [17] Y. Tsai, C.-S. Chern, and J. Wang, "Typhoon induced upper ocean cooling off northeastern Taiwan," *Geophysical Research Letters*, vol. 35, no. 14, Article ID L14605, 2008.
- [18] D. A. Mitchell, W. J. Teague, E. Jarosz, and D. W. Wang, "Observed currents over the outer continental shelf during Hurricane Ivan," *Geophysical Research Letters*, vol. 32, no. 11, pp. 1–4, 2005.
- [19] J. A. Knauth, *Introduction to Physical Oceanography*, Prentice-Hall, Englewood Cliffs, NJ, USA, 1978.
- [20] R. H. Stewart, *Introduction to Physical Oceanography*, Orange Grove Books, 2009.

Research Article

Double Compressions of Atmospheric Depth by Geopotential Tendency, Vorticity, and Atmospheric Boundary Layer Affected Abrupt High Particulate Matter Concentrations at a Coastal City for a Yellow Dust Period in October

Hyo Choi¹ and Mi Sook Lee²

¹ Department of Atmospheric and Environmental Sciences, Gangneung-Wonju National University, Gangneung 210-702, Republic of Korea

² Research Institute of East Sea Life Sciences, Gangneung-Wonju National University, Gangneung 210-702, Republic of Korea

Correspondence should be addressed to Hyo Choi; du8392@hanmail.net

Received 2 October 2013; Accepted 17 November 2013; Published 23 January 2014

Academic Editor: Chung-Ru Ho

Copyright © 2014 H. Choi and M. S. Lee. This is an open access article distributed under the Creative Commons Attribution License, which permits unrestricted use, distribution, and reproduction in any medium, provided the original work is properly cited.

Using GRIMM-aerosol sampler, NOAA-HYSPLIT model, and 3D-WRF-3.3 model, the transportation of dusts from Gobi Desert toward Gangneung city, Korea was investigated from 09:00 LST October 27 to 04:00 LST October 28, 2003. Maximum PM₁₀ (PM_{2.5}, PM₁) concentration was detected with 3.8 (3.4, 14.1) times higher magnitude than one in non-Yellow Dust period. The combination of dusts transported from the desert under westerly wind with particulate matters and gases from vehicles on the road of the city caused high PM concentrations near the ground surface at 09:00 LST and their maxima at 17:00 LST near sunset with further pollutants from heating boilers in the resident area. Positive geopotential tendency at the 500 hPa level of the city ($\partial\Phi/\partial t$; m day^{-1}) corresponding to negative vorticity of $-4 \times 10^{-5} \text{ sec}^{-1}$ ($-2.5 \times 10^{-5} \text{ sec}^{-1}$) at 0900 LST (21:00 LST; at night) was $+83 \text{ m day}^{-1}$ ($+30 \text{ m day}^{-1}$) and it caused atmospheric depth between 500 hPa level and the ground surface to be vertically expanded. However, its net reduction to -53 m/12 hrs until 21:00 LST indicated synoptic-scale atmospheric layer to be vertical shrunken, resulting in the increase of PM concentrations at 17:00 LST. Simultaneously, much shallower microscale stable nocturnal surface inversion layer (NSIL) than daytime thermal internal boundary layer induced particulate matters to be merged inside the NSIL, resulting in maximum PM concentrations at 17:00 LST.

1. Introduction

In dry spring, air quality in the Korean eastern coastal region was greatly affected by huge amounts of dusts transported from the elevated ground of 1500 m above sea level of Taklamakan, Gobi, and Ordos Deserts and Loess plateau in Nei-Mongo in the northern China. In recent years, Yellow Dust Storm with various names of Yellow Sand Storm, Asian Dust Storm, and KOSA has been detected in even autumn and winter, showing a relatively lower concentration of particulate matters than one in spring [1–6]. The most concentrated region of Yellow Dust Storm has been known as northwest China, which included five provinces of Xinjiang, Inner-Mongolia (Nei-Mongo), Ningxi, Shanxi, and Gansu [7].

Zhang and Zhong [8] and Choi and Zhang [9] indicated that the regions of dust storm occurring more than 30 days per year coincide with those regions with both relative humidity of air less than 40% as the representation of the surface water content of the soil layer and surface wind speed greater than 10 m s^{-1} . Tegen and Fung [10] explained that, among the total quantity of dust particulates generated from the deserts, its 30% is deposited near the source area and the 20% is redistributed on a local scale and the other half of them are expected to be subject to their long-range transports. The estimation of dust loading controlled by wind velocity has mainly been used, considering size distribution of soil particles and surface roughness in terms of friction velocity. Thus, the dust generated in Gobi Desert and Nei-Mongo in

the northern China is to serve as one of the major particulate matter sources all across the Asia and Pacific and it makes a great contribution to low visibility and air quality in spring in northern Asian countries and even USA [11–15].

Kim et al. [16] showed that, during a Yellow Dust period in China, dusts generated from Gobi Desert were transported toward Seoul in the central region of Korea. Lee and Chung [17] also explained that a great amount of dusts from Gobi Desert were transported toward the Korean eastern mountainous coast, and the transported dusts from the desert usually included great amounts of particulate matters of not only coarse PM mode, but also fine one with various gases. Then, the transported dusts were combined with particulate matter and gases emitted from the downwind Korean cities, resulting in very high PM and gases concentrations with apparent temporal variations.

In the Yellow Dust researches, meteorological approach was usually focused on the beginning stage of the generation of dust storm and weather conditions for the formation of the dust storm, considering synoptic weather situation [18]. When most of modelers perform the transport model, they have usually treated atmospheric boundary layer to be constant, even actually not constant, assuming 1.5 km or 2 km height above the ground surface. However, Choi and Zhang [9] insisted that the transportation of dusts from Gobi Desert toward the far downwind area like Korean peninsula is initially greatly affected by synoptic- and mesoscale wind fields. Choi and Speer [19], Choi and Choi [20], and Choi et al. [21, 22] further insisted the effects of variability of atmospheric boundary layer depth during the day and night on high concentrations of locally emitted particulate matters combined with dusts from the north China. Owing to no much considering those subjects in the transport model of dusts, the occurrence of abrupt high concentrations of dust particles in the downwind local area have been still obscured so far.

In recent, Choi [23] showed the trapping effect of a calm zone by lee side-internal gravity waves and cyclonic winds on sudden high concentrations of particulate matters combined with the Yellow Dusts from Gobi Desert in the Korean eastern coast. Differently, Uzan and Alpert [24] explained that the highest air pollution events such as SO_2 and NO_x concentrations (not particulate matter) from Israel's largest coal-fired power plant occurred during summer at 12:00~15:00 h through the average coincident drop of the boundary layer height down to 450 m above the ground. Even though they did not consider the transportation of gases from other city into the research area, the research result indicated that pollutant concentration should be directly affected by the depth of atmospheric boundary layer.

Precisely understanding the evolution of atmospheric boundary layer is also one of the most important aspects for the horizontal transportation of the dust and its sudden high concentration in the far downwind area like Korea, considering synoptic and mesoscale motions of atmosphere. Choi and Lee [25] made primary research on abrupt high PM concentration during the dust period in October, 2003, considering shrunken atmospheric boundary layer, but they

did not explain dynamically any relation of synoptic-scale atmospheric shrunken process with diurnal variations of atmospheric boundary layer. The purpose of this study is to explain the effects of double compression of not only synoptic-scale atmospheric layer varied by geopotential tendency and vorticity at 500 hPa level, but also microscale atmospheric boundary layer on the occurrence of abrupt high particulate matter concentration in the mountainous coastal region of Korea, during a Fall Yellow Dust period.

2. Study Area

Figure 1 indicates Northeastern Asia including the study area near Gangneung city ($37^{\circ}45'N$, $128^{\circ}54'E$; 20 m height above Mean Sea Level) in the Korean eastern coastal region. Gangneung city consists of high mountains in the west of the city, coastal basin in its center, and sea in its east and its population is about 230,000 with no special industries.

The city has the characteristics of continental and marine climates due to its location between mountains and sea. Particularly, fall season is short, and weather in winter is mild due to the passage of the East Korea Warm Current (EKWC; branch currents of Kuroshio Warm Current) bounding for north along the eastern coast of Korean peninsula. As it is a clean coastal city without special industries, air pollution sources are mainly vehicles of about 50,000 on the road, flying dusts from the road, and heating boilers in the resident area and the city has typical urban characteristics. In Spring, air quality is greatly affected by the dust particles transported from the northern China, especially Gobi Desert and Neimongo (Inner Mongolia) such as arid area in China and Mongolia.

3. Aerosol Measurement and Numerical Model

3.1. Measurement of Aerosol. GRIMM-1107 aerosol sampler was equipped at Gangwon Regional Meteorological Administration (20 m height above Mean Sea Level) in the downtown of Gangneung city adjacent to the East Sea of Korea on October 26~29, 2003, under air quality at Gangneung city to be greatly affected by dusts transported from Gobi Desert. GRIMM-1107 aerosol sampler is characterized as a portable particle analyzer measuring particulates of $0.3\sim 20\ \mu\text{m}$ by way of laser-light scattering, with a monitor on particulate matter concentrations (PM_{10} , $\text{PM}_{2.5}$, and PM_1) to offer dual technology consisting of both optical and gravimetric analysis.

After air of various particle sizes passes through a flat laser beam produced by a precisely focused laser and several collimator lenses, the scattered light is detected by a 15-channel, pulse-height analyzer for size classification at every 5 seconds and then the counts from each size classification are directly converted to mass by an established equation to be specifically designed for PM_{10} , $\text{PM}_{2.5}$, and PM_1 ambient air analysis [22]. PM_{10} , $\text{PM}_{2.5}$, and PM_1 are presented on the monitor and stored in a data log with every 10-minute averaged PM concentrations and total counts of different sizes.

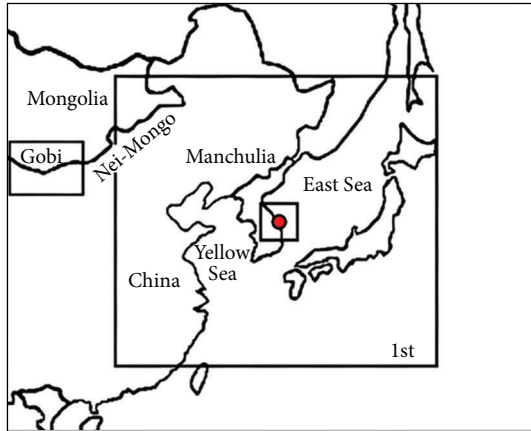


FIGURE 1: Topography of the northeastern Asia including Gangneung city ($37^{\circ}45'N$, $128^{\circ}54'E$) with the establishment of a GRIMM aerosol sampler. Large and small squares in the center indicate the first domain with a 27 km grid interval on 91×91 horizontal grids and the third domain with a 3 km by three-nesting techniques in the WRF model simulation. A square in the left and a circle in the center denote Gobi Desert and Gangneung city equipped with an aerosol sampler, respectively.

3.2. Numerical Model and Input Data. For the numerical simulation of the generation of meteorological phenomena, Weather Research & Forecasting Model (WRF) version 3.3—a three-dimensional, nonhydrostatic grid point model with a terrain following coordinate system—was adopted on the route of dust transportation from China to Gangneung city in the eastern coast of Korea from 00:00 UTC (Local Standard Time (LST) = 9 h + UTC (Coordinated Universal Time); 09:00 LST in Korea), October 27 through 00:00 UTC, October 29, 2003. In the numerical simulation, one way-triple nesting process from a coarse-mesh domain to a fine-mesh domain was performed using a horizontal grid spacing of 27 km covering a 91×91 grid square in the largest domain. The second and third domains also consist of the same grid square of 91×91 with 9 km and 3 km horizontal grid intervals, respectively [20].

National Centers for Environmental Prediction/National Center for Atmospheric Research (NCEP/NCAR) reanalysis-Final Analyses (FNL) $1.0^{\circ} \times 1.0^{\circ}$ resolution data were used as meteorological input data of WRF model and the data were vertically interpolated onto 36 levels with sequentially larger intervals increasing with height from the surface to the upper boundary level of 100 hPa [20]. Among various parameterization schemes of WRF model, WSM 6 scheme was used for microphysical processes for the heat and moist budgets in the atmospheric boundary layer, and the YSU PBL scheme for the planetary boundary layer. Furthermore, the Kain-Fritsch (new Eta) for cumulus parameterization, the five thermal diffusion model for land surface, and the RRTM long wave radiation scheme and Dudhia short wave radiation schemes were also used. Input terrain data with a horizontal resolution of 1° (about 110 km) were used for the first-largest domain, and 1 km horizontal resolution data were for the second and third domains [23].

Horizontal wind, air temperature, and 500 hPa height change for 24 hours (i.e., geopotential tendency ($\partial\Phi/\partial t$); m/day), relative vorticity ($\times 10^{-1} \text{ sec}^{-1}$) were evaluated in northeastern Asia and further both horizontal and vertical profiles of wind, air temperature, potential temperature, and potential vorticity for investigating the development of atmospheric boundary layer near Gangneung city of the Korea, sequentially in the three-mesh domains in the WRF model. For the verification of numerical results of the meteorological elements, wind, air temperature, and relative humidity by Gangwon Regional Meteorological Administration were used.

4. Result and Discussion

4.1. Aerosol Concentration during a Non-Yellow Sand Period.

Figure 2 indicates hourly distribution of PM_{10} , $PM_{2.5}$, and PM_{10} concentrations at Gangneung city with no special industry in the eastern mountainous coast of Korea from 00:00 LST (09:00 LST), October 26 to 18:00 LST, October 29, 2003. Its main air pollution sources to affect local PM concentrations are vehicles on the road and heating boilers in the resident area. As air temperature of Gangneung city is in the range of $10\sim 15^{\circ}C$ for daytime hours in the late October and is lower than about $10^{\circ}C$ at night, heating boilers in the resident area are put into operation for a few hours around sunset and sunrise. This operation can partially affect the increase of particulate matter and gases such as CO and NO_x concentrations.

A low pressure system of 999 hPa was located in the northern border of Mongolia and a high pressure system of 1021 hPa in the East Sea of Korea on weather map supplied by Korea Meteorological Administration (KMA) at 09:00 LST, October 26 (Figure 3(a)). The pressure patterns produced northwesterly wind near Gobi Desert and the wind could blow dusts generated by Gobi Desert toward Manchuria in the north-eastern China. Under this situation, the dusts could not be transported toward Gangneung city in the eastern coast of the Korean peninsula (triangle).

As weather map or wind fields generated by a meteorological numerical model just show flow patterns of air particles at a certain height and at a given time of a special day. Thus, if we want to know the flow patterns of air particles continuously at different heights, we use many numbers of weather maps or simulated wind fields by a model at every 3 or 6 hours intervals for several days. On the other hand, particle trajectory using NOAA-HYSPIT model, which consists of meteorological model for wind field and Lagrangian random walk model on particle diffusion and dispersion, can supply the moving paths of air particles and their positions with different flowing heights at every 6 hours for several days, continuously. Thus, the position of air particle at a certain time on the moving trajectory of air for several days should be exactly the same as flow pattern of air at a given time weather map of a special day or wind field by a numerical model at a certain height. However, it is very difficult to chase the track of air particle on the weather map. Thus, we commonly use backward trajectory of air

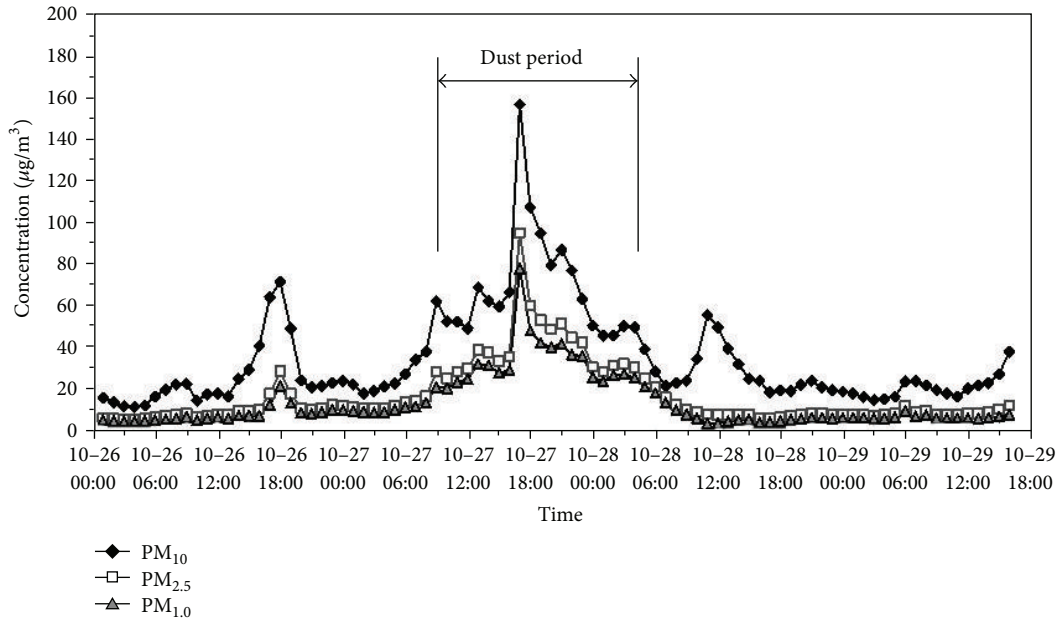


FIGURE 2: Hourly distributions of PM_{10} , $\text{PM}_{2.5}$, and PM_1 concentrations at Gangwon Meteorological Administration in the downtown of Gangneung city, Korea from October 26~29, 2003.

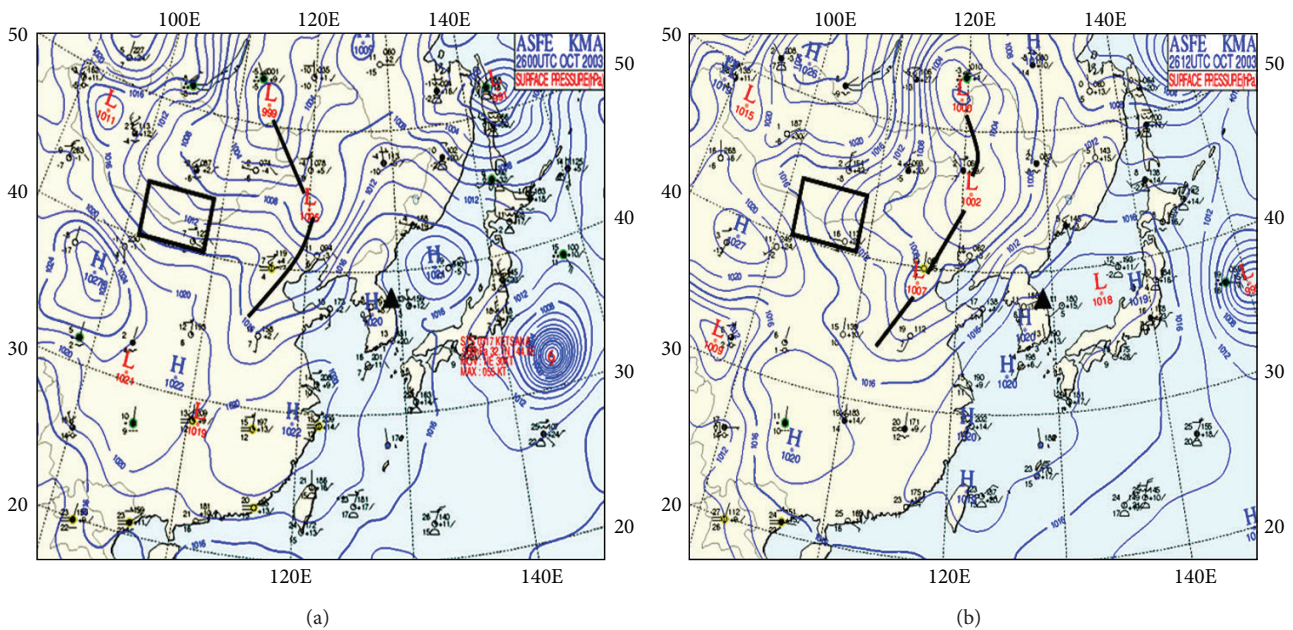


FIGURE 3: Surface weather maps at (a) 09:00 LST (00:00 UTC), October 26, 2003, and (b) 21:00 LST (12:00 UTC), supplied by KMA [26]. Square and thick line in (a) and (b) indicate Gobi Desert extending from the southern Mongolia to the northern China and cold front. Northwesterly wind in the left of cold front and southwesterly wind in the right of the front produced a main stream of dust particles originated from Gobi Desert toward Liaoning province in the northeastern China, which is far away from Gangneung city.

particle by NOAA-HYSPLIT model, which focuses only main stream of the majority of particles, not showing diffusion and dispersion of whole particles. Choi and Speer [19] described that the trajectories of whole particles in the wide area of different height such as in Seoul city and Korean eastern coast could be shown using Lagrangian Random Walk Model combined with meteorological model, but if we want to know

the main stream of particles, not considering whole particles, HYSPLIT model is strongly recommended. In general, to investigate flow pattern of air in the wide area, it is necessary to review weather maps and horizontal wind fields generated by a meteorological numerical model.

For depicting backward trajectories of dust particles with time, NOAA HYSPLIT model (hybrid single particle

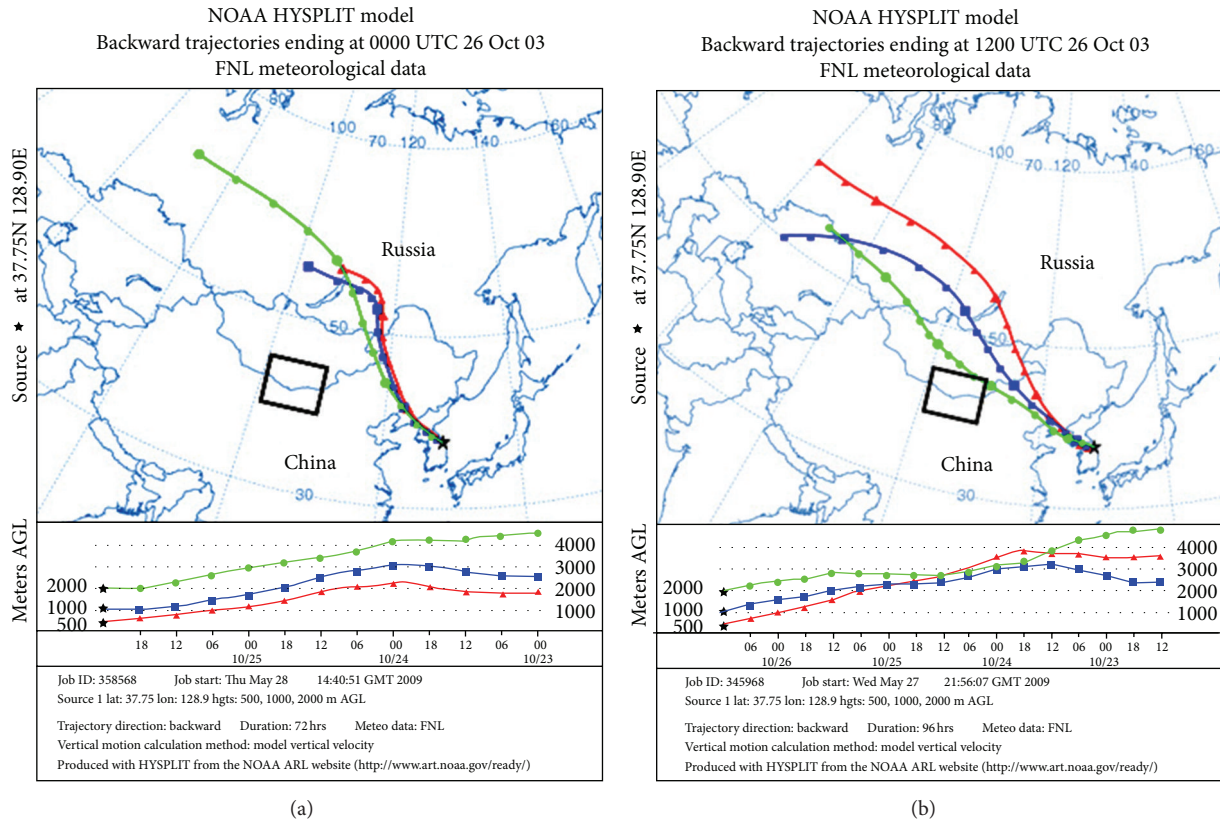


FIGURE 4: Backward trajectories of air masses at 2000 m, 1000 m, and 500 m heights by NOAA HYSPLIT model ending at (a) 09:00 LST (00:00 UTC), October 26, 2003 and (b) 21:00 LST (12:00 UTC). Clean air masses from above 2 km height of the north-eastern Mongolia flew toward Gangneung city at each level in (a) and ones from above 3 km height outside Gobi Desert (Nei-Mongo in the northeastern China) reached 1000 m and 2000 m heights of the city, without dust transportation to the city in (b). As weather map or wind fields generated by a meteorological numerical model just show flow patterns of air at a certain height and at a given time of a special day, but particle trajectory using NOAA-HYSPLIT model supplies the moving path (main stream) of majority of air particle and its position at every 6 hours for several days, continuously.

Lagrangian integrated trajectory) from the Air Resources Laboratory (ARL) using FNL meteorological data was adopted and the heights of dust particle trajectories were set up at 2000 m, 1000 m, and 500 m, respectively (Figure 4). This model showed very detailed information on temporal transportation routes of dust particles for several days and their flowing height and spreading area. Weather map or wind fields generated by a meteorological model just show flow patterns of air at a given time, but particle trajectory using NOAA HYSPLIT model supplies the moving path of particle and its position at every 6 hours for several days, continuously. Thus, this moving trajectory for several days is different from a given time weather map or wind field given by a numerical model. Unfortunately some environmental scientists misunderstand their differences. Thus, back trajectories with a time step of 6 hours over a period of 72 or 96 hours using the HYSPLIT model were depicted at 500 m, 1000 m, and 2000 m above ground level in order to detect possible links between diurnal variation of PM concentrations and pathway of dust particles transported from Gobi Desert and Nei-Mongo (Inner Mongo) in the northern China toward a Korean eastern coastal city.

At 09:00 LST (00:00 UTC), October 26, clean air masses originated from over 2 km height in the north-eastern Mongolia far away from Gobi Desert reached Gangneung city at 500 m, 1000 m, and 2000 m heights and the city was under no influence of dusts in Gobi Desert (Figure 4(a)). At 21:00 LST, the previous low pressure system moved toward the east and stretched toward the south-eastern China with pressure centers of 1000 hPa, 1002 hPa, and 1007 hPa, respectively (Figure 3(b)). A high pressure system of 1026 hPa was located in the northern Mongolia, but Gobi Desert was still under the influence of the low pressure system.

The pressure patterns over Mongolia, China, and Korea caused northwesterly wind near Gobi Desert in the left of cold front and southwesterly in the right. Dusts driven by those winds should pass by Manchuria of the north-eastern China in the north of the Korean peninsula, resulting in no influence of dust transportation from China to Gangneung city of Korea (triangle). Figure 4(b) showed that, on backward trajectory, relatively clean air particles from above 3 km height of Gobi Desert reached 1000 m and 200 m heights of the Korean city at 21:00 LST, October 26, but it was very difficult to expect dust transportation from Gobi Desert to

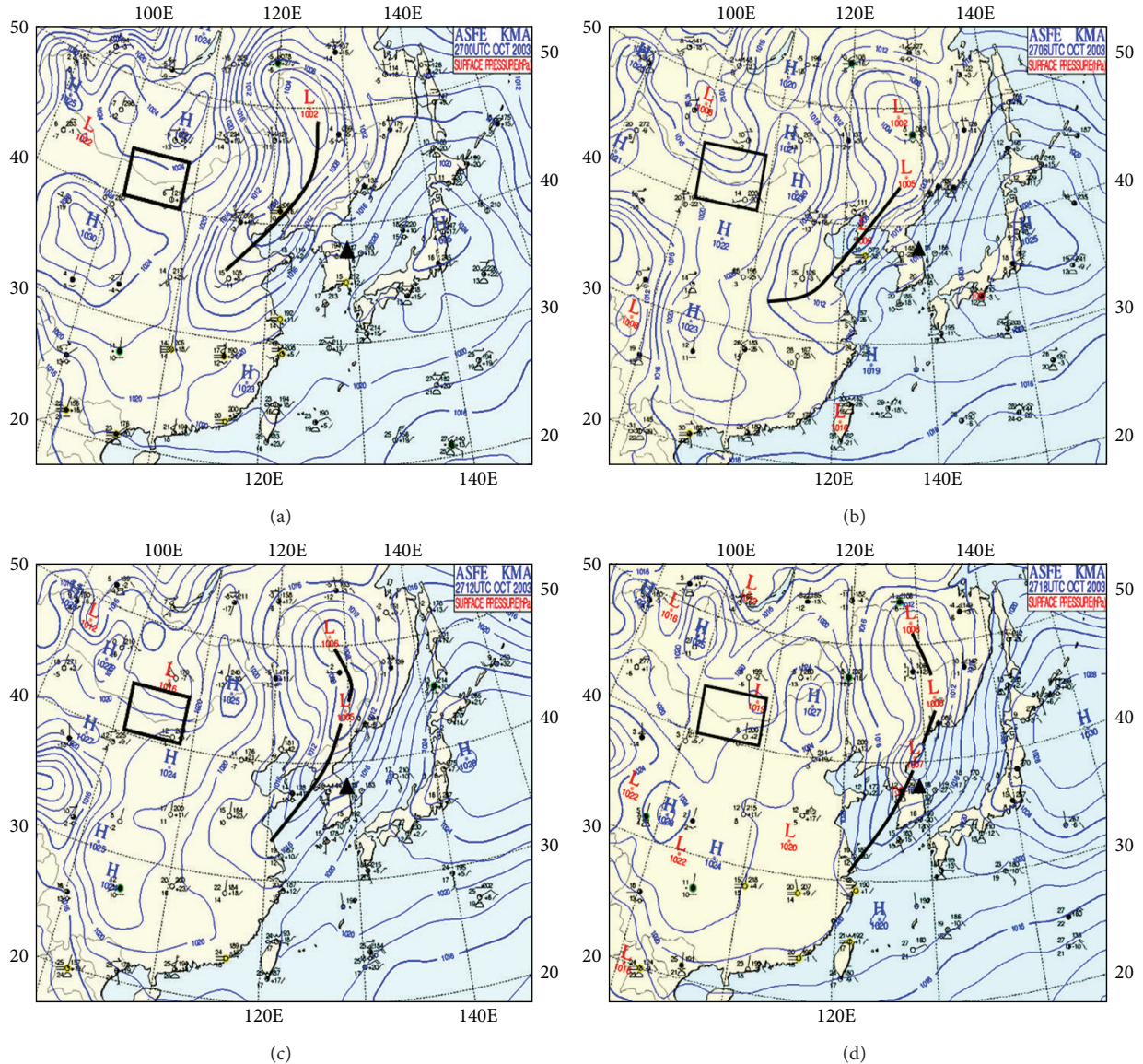


FIGURE 5: As shown in Figure 3, except for (a) 09:00 LST (00:00 UTC), (b) 15:00 LST (06:00 UTC), (c) 21:00 LST (12:00 UTC), October 27, 2003, and (d) 03:00 LST (18:00 UTC), October 28. Dust particles originated from Gobi Desert move toward eastern Nei-Mongol, Manchuria, and northern Korea with their flowing southwestward in the left of cold front and northeastward in the right of the front, as the front moves toward the Korean peninsula, sequentially with time.

the city. Nontransportation of dust from Gobi Desert and the northern China toward the city continued to be until 08:00 LST, October 27 in Figure 2.

In Figure 2, on October 26, especially before 09:00 LST October 27, under no intrusion of dust from Gobi Desert or Nei-Mongol (Inner Mongolia) in the northern China toward the city (non-Yellow Dust period), PM_1 , $PM_{2.5}$, and PM_{10} concentrations near the ground surface of Gangneung city were generally very low, more or less than $20 \mu g m^{-3}$, $10 \mu g m^{-3}$, and $5 \mu g m^{-3}$, except for PM_{10} of $69.87 \mu g m^{-3}$ at 18:00 LST, October 26, respectively. High PM_{10} , $PM_{2.5}$, and PM_1 concentrations were detected at 09:00 LST at the beginning time of office and 18:00 LST at the ending time

of office hour, due to high density of traffic vehicles on the road at both times. Particularly maximum PM concentrations at 18:00 LST rather than 09:00 LST were shown due to additionally nighttime more operating of heating boilers in the resident area of the city, shortly after sunset. This hourly PM concentration showed a typical urban type-high PM concentrations around 09:00 LST in the morning and 18:00 LST near the sunset.

4.2. Aerosol Concentration during a Yellow Sand Event Period. During the intrusion of dust transported from Gobi Desert of the northern China toward the city from 09:00 LST October 27~04:00 LST, October 28 (Yellow Dust period),

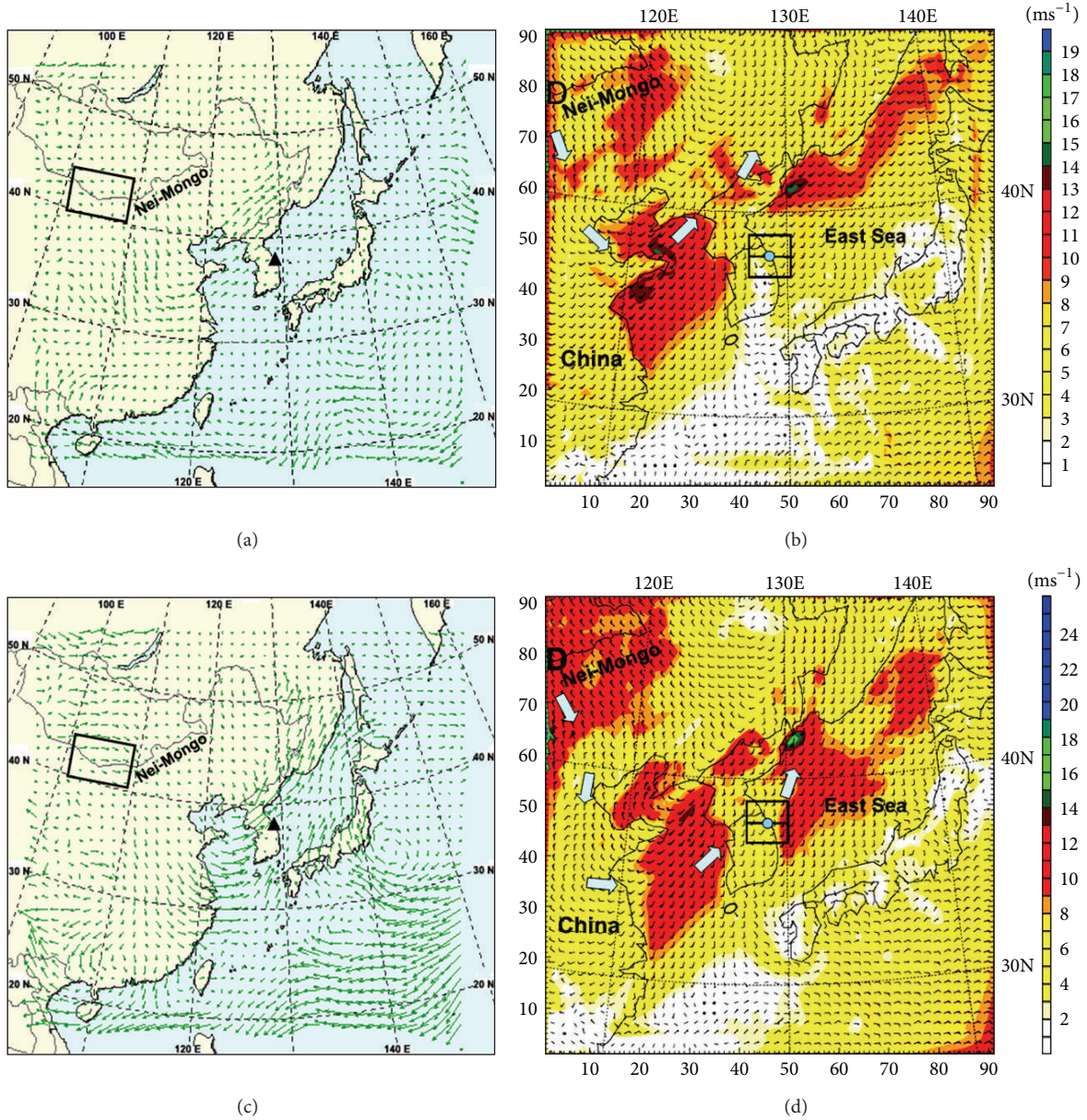


FIGURE 6: (a) Moisture flux (m/s) at 850 hPa level (about 1.5 km height) supplied by KMA [26] and (b) surface wind (m/s) simulated by WRF model at 09:00 LST, October 27, 2003, and (c) and (d) are at 17:00LST (a maximum PM concentration), respectively. Small square and triangle in (a) and (c) denote Gobi Desert and Gangneung city (Korea). Small square in (b) and (d) denotes the vicinity of Gangneung (the 3rd domain of WRF model) at 09:00 LST, October 27, 2003 and 17:00 LST (occurrence time of maximum PM concentration). D and big arrow denote the eastern part of Gobi Desert in the northwest of Nei-Mongo and a dust transportation route. In (a), (b), (c), and (d), dust particles originated from Gobi Desert moved toward Nei-Mongo under westerly wind at both the surface and 1.5 km height and then, followed northerly and northwesterly toward the Chinese eastern coast and the Yellow Sea, further moving toward the northern Korea and Gangneung city.

PM₁₀ concentration was in the range of 48.20~154.57 $\mu\text{g m}^{-3}$ and its maximum concentration was 3.8 times higher than the maximum concentration of nondust period.

Similarly, PM_{2.5} (PM₁) concentration was in the range of 26.92~93.19 $\mu\text{g m}^{-3}$ (19.63~76.05 $\mu\text{g m}^{-3}$) with a maximum concentration of 3.4 (14.1) times higher than one of nondust period and their hourly variations of PM concentrations were similar each other (Figure 2). High PM₁₀ (PM_{2.5} and PM₁) concentration was detected with 60.59 $\mu\text{g m}^{-3}$ (26.92 $\mu\text{g m}^{-3}$,

19.63 $\mu\text{g m}^{-3}$) at 09:00 LST, October 27 (the beginning time of office hour), when a high traffic density on the road took place. PM concentration after 09:00 LST had a rapid increasing trend until 17:00 LST.

As shown in surface weather maps of Figure 5(a), one can expect that dusts generated in Gobi Desert in the northern China could be transported following isobaric lines of a high pressure, showing arrow movement of air masses in the figure. As shown in surface winds simulated by WRF-3.3

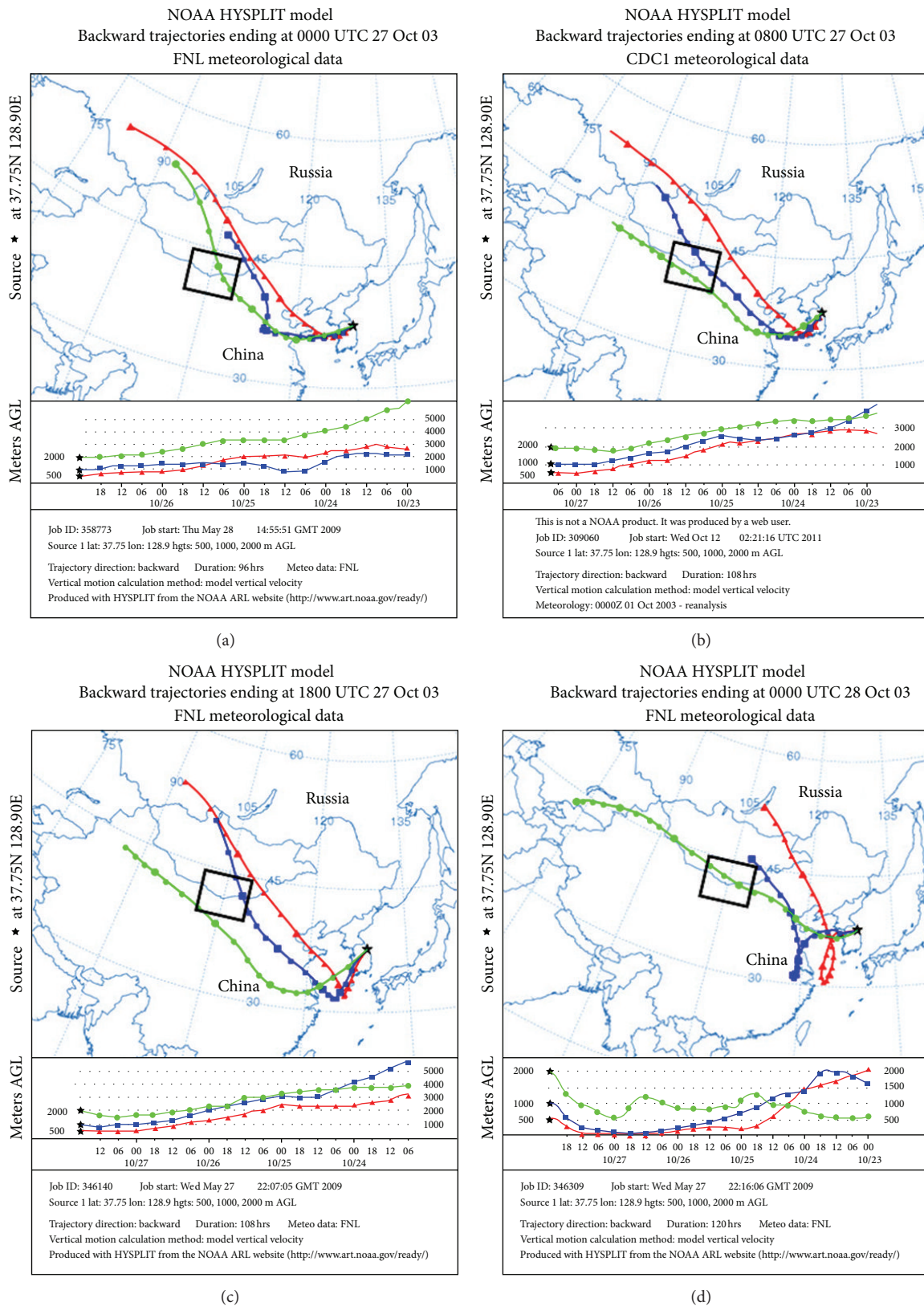


FIGURE 7: Backward trajectories of air masses by NOAA HYSPLIT model ending at (a) 09:00 LST (00:00 UTC), October 27, 2003, (b) 17:00 LST (08:00 UTC; a maximum PM concentration), (c) 03:00 LST (18:00 UTC), October 28, and (d) 09:00 LST (00:00 UTC), respectively.

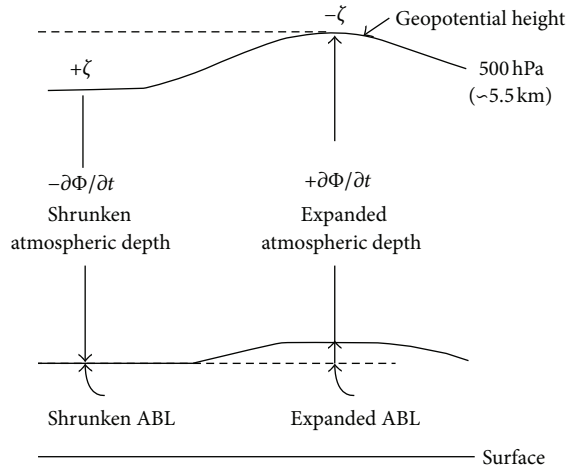


FIGURE 8: Schematic profile of geopotential height change with time (geopotential tendency ($\partial\Phi/\partial t$); m day^{-1}) at 500 hPa level (approximately 5.5 km height) and atmospheric boundary layer (ABL), modified from Choi et al. [28]. Negative geopotential tendency ($\partial\Phi/\partial t$) means the decrease of geopotential height for 24 hours (i.e., shrunken atmospheric layer) and vice versa. Positive vorticity ($+\zeta = \partial v/\partial x - \partial u/\partial y$) at the 500 hPa level, which implies the downward motion of air toward the ground corresponds to negative geopotential tendency area and vice versa.

model, strong northerly surface wind in the north of China and southwesterly in the south prevailed (Figures 6(a) and 6(c)). In general, dusts generated from dried soil of the desert ground could be uplift to about 3 km height over the ground surface due to strong surface wind and daytime thermal convection [7], and then they moved eastward below the lower level than 3 km height.

Figure 6(a) at 09:00 LST, October 27, and Figure 6(c) at 17:00 LST of the occurrence time of a maximum PM concentration indicate transportation routes of moisture fluxes at about 1.5 km height (850 hPa level) in Mongolia, China, Korea, and Japan, which well show the movement of air parcel with water vapor. From these figures, it is very easy to find the transportation route of dust particles combining with air, water vapor, and dust. In Figures 6(a), 6(b), 6(c), and 6(d), dust particles originated from Gobi Desert moved toward Nei-Mongo under westerly wind at both the surface and 1.5 km height and then followed northerly and northwesterly toward the Chinese eastern coast and the Yellow Sea, further moving toward the northern Korea and Gangeung city.

In Figure 7(a), backward trajectories of dust particles generated in Gobi Desert at 09:00 LST (00:00 UTC) on October 25 flew from about 3 km height of the desert toward Gangeung city in the Korean east coast and reached 1000 m and 2000 m levels of the city at 09:00 LST (00:00 UTC), October 27 after three days. The dusts passed by about 2~3 km heights of Nei-Mongo in the northern China could reach the city at 1000 m and 500 m heights. Thus, dusts transported from Nei-Mongo could directly make a contribution to the increase of PM concentrations in the city as shown in Figure 2. At 21:00 LST (4 hours after the occurrence of maximum PM concentration), a high pressure system of

1025 hPa was located in the eastern Mongolia and a low pressure system of 1006 hPa was in the northeastern China (Figure 5(b)).

As the previous high and low pressure systems moved toward the east, cold front passed by the northern part of Korean peninsula and stretched toward Manchuria in the north-eastern China. This kind of pressure pattern over Mongolia, China, and Korea caused northerly wind near Gobi Desert and southwesterly wind in the southern China (Figures 6(b) and 6(d)). Southwesterly wind still prevailed through the Korean peninsula including the study area. Thus, dusts generated from Gobi Desert might pass by the eastern Mongolia-Nei-Mongo-southeastern China and finally reached the Korean eastern coastal city, sequentially. As a result, dusts transported from both Gobi Desert and Nei-Mongo could make a great contribution to the increase of local PM concentration in the city.

In Figure 7(b), as dust particles passed by 3 km height of Gobi Desert and 2000 m height of Nei-Mongo flew toward the Korean east coast and reached 2000~500 m heights in the city at 17:00 LST, October 27, when a maximum PM concentration took place. Thus, huge amounts of dusts generated from both Gobi Desert and Nei-Mongo could be transported to the city and made a great contribution to the increases of PM_{10} , $\text{PM}_{2.5}$, and PM_1 concentration near the ground surface of the city. Similar patterns of backward particle trajectories could continuously exist until 03:00 LST, October 28 (Figure 7(c)). After 03:00 LST until 09:00 LST, October 28, dust transportation from Gobi Desert toward the Korean coastal city was very difficult as shown in Figure 7(d). Even though some amounts of dusts from not Gobi Desert, but Nei-Mongo (outside a box in the figure), passed by the southern China and the Yellow Sea and finally reached the Korean eastern coast, the transported dusts should be not much and local PM concentrations could be under little influence of the dusts.

4.3. Effect of Synoptic-Scale Geopotential Tendency Corresponding to Vorticity on High PM Concentration. Vorticity equation can be derived using horizontal momentum equations. It can be obtained by differentiating the x component equation of momentum with respect to y and the y component equation with respect to x and then subtraction of former differential equation from later differential equation $\zeta = \partial v/\partial x - \partial u/\partial y$ [27].

Vorticity equation has a great advantage in order to investigate upward or downward of motion of air. Downward motion of air occurs in positive vorticity area at 500 hPa level (approximately 5.5 km height) and oppositely upward motion in negative vorticity area. Opposite to the 500 hPa level, downward motion of air near the ground surface (approximately 1,000 hPa level) occurs in negative vorticity area and vice versa. Holton [27], Sanders and Gyakum [29], and Reed and Albright [30] explained that the region of positive relative vorticity (ζ ; $\times 10^{-5} \text{ sec}^{-1}$) at the 500 hPa level causing convergence of air parcel and sequentially its downward motion toward the ground surface matches the region of the negative geopotential tendency ($-\partial\Phi/\partial t$; m day^{-1}) at the 500 hPa level. Atmospheric depth in the negative

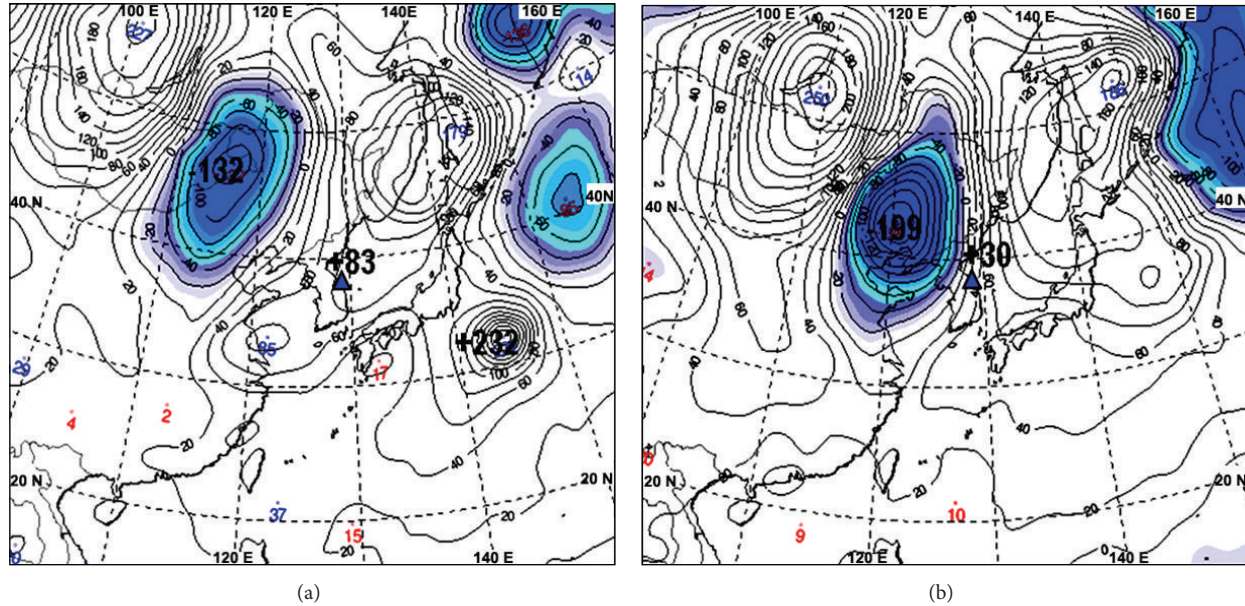


FIGURE 9: Geopotential tendency ($\partial\Phi/\partial t$; m day^{-1}) at 500 hPa level at (a) 09:00 LST October 27, 2003, and (b) 21:00 LST. Triangle indicates Gangneung city. Shadow (white) area indicates negative (positive) geopotential tendency, which implies the shrunken (expansion) rate of geopotential height change at 500 hPa level for a day. As a positive tendency at 09:00 LST (21:00 LST) in Gangneung city was $+83 \text{ m day}^{-1}$ ($+30 \text{ m day}^{-1}$), the net one of -53 m for 12 hours implies a 53 m-shrunken atmospheric depth at 21:00 LST, causing a maximum PM_{10} at 17:00 LST.

geopotential tendency area should be reduced and vertically shrunken (Figure 8). On the other hand, the region of negative relative vorticity ($-\zeta$) inducing divergence of air parcel at the 500 hPa level and its upward motion from the ground surface toward the 500 hPa level matches the region of the positive geopotential tendency, ($+\partial\Phi/\partial t$; m day^{-1}) with vertical expansion of atmospheric depth of 500 hPa level.

For applying geopotential tendency theory, we used every 6-hour weather maps of geopotential height at 500 hPa level supplied by Korea Meteorological Administration (KMA). At 09:00 LST, October 27, when huge amounts of dusts from Gobi Desert and Nei-Mongo began to make a contribution to the increase of PM concentrations at Gangneung city, geopotential tendency at 500 hPa level for a day in the city was $+80 \text{ m day}^{-1}$ (Figure 9(a)). The positive value of $+83 \text{ m day}^{-1}$ implies that atmospheric depth of 500 hPa level to the ground surface should be vertically expanded to more 83 m day^{-1} than one day before. On the other hand, the tendency at 21:00 LST was changed into $+30 \text{ m day}^{-1}$, which implied still the expansion of 500 hPa level to be up to 30 m day^{-1} for 24 hours (Figure 9(b)). Thus, the net variation of geopotential tendency between 09:00 LST and 21:00 LST for 12 hours could be reduced to -53 m , resulting in atmospheric depth to be shrunken. Similarly to the case of 21:00 LST, synoptic-scale shrunken atmospheric layer of 100 m could force nocturnal surface inversion layer in the city to be further more shrunken at night. Thus, resultantly much more shrunken nocturnal surface inversion layer might cause a maximum PM_{10} concentration as well as $\text{PM}_{2.5}$ and PM_1 in the coastal city at 17:00 LST.

Figures 10(a) and 10(b) indicate vorticity ($\times 10^{-5} \text{ sec}^{-1}$) at 500 hPa level at 09:00 LST October 27, 2003, and 21:00 LST, respectively. At 0900 LST October 27, Gangneung city was in negative vorticity area at the 500 hPa level, which caused upward motion of air with a magnitude of $-4 \times 10^{-5} \text{ sec}^{-1}$ from the ground surface toward the 500 hPa height. At 21:00 LST, the city was still in negative vorticity area at the 500 hPa level, but upward motion of air with negative vorticity of $-4 \times 10^{-5} \text{ sec}^{-1}$ became weaker than one by its reduction to negative vorticity of $-2.5 \times 10^{-5} \text{ sec}^{-1}$, resulting in the shrunken of atmospheric depth between the 500 hPa level to the ground surface.

4.4. Effects of Atmospheric Boundary Layer on High PM Concentration. As shown in Figure 2, under the intensive intrusion of dusts from Gobi Desert toward the city during the dust period, high PM_{10} , $\text{PM}_{2.5}$, and PM_1 concentrations were detected at 09:00 LST at the beginning time of office hour and 17:00 LST at the ending time of office hour, due to emission of gases and particulate matters from high density-traffic vehicles on the road, similarly to ones in the nondust period. As daytime went on after sunrise, convective boundary layer (CBL) due to thermal convection in the inland basin of the mountain top in the west of the city was much more developed than one at 09:00 LST, up to about 500 m in Figure 11(a), similarly to ones on October 26 (non-Yellow Dust Event period). Under the similar driving mechanism, thermal internal boundary layer (TIBL) during the day was also developed along the eastern slope of the mountain from the coast of the study area to the top of the mountain with about 300 m thickness.

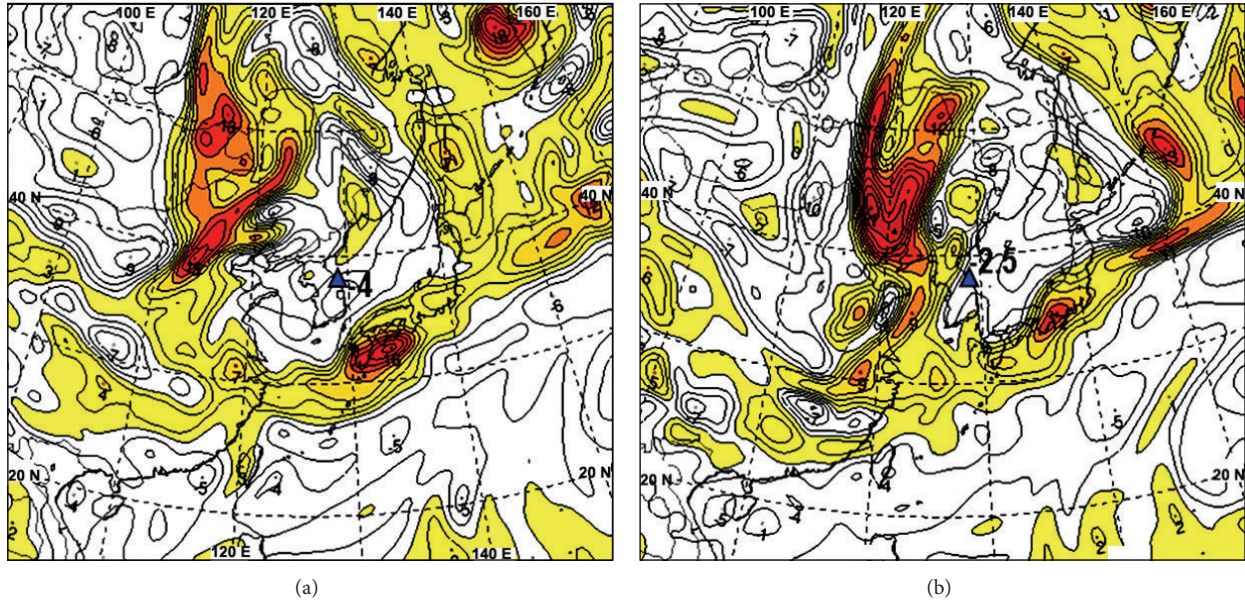


FIGURE 10: Variations of vorticities ($\zeta = \partial v/\partial x - \partial u/\partial y; \times 10^{-5} \text{ sec}^{-1}$) at 500 hPa level at (a) 09:00 LST October 27, 2003, and (b) 21:00 LST. Triangle in the center indicates Gangneung city. Colorful (white) area indicates positive (negative) vorticity, which implies the downward (upward) motion of air at the 500 hPa level and corresponds to negative (positive) geopotential tendency area. Upward motion of air at the 500 hPa level with negative vorticity of $-2.5 \times 10^{-5} \text{ sec}^{-1}$ at 21:00 LST became weaker than one with negative vorticity of $-4 \times 10^{-5} \text{ sec}^{-1}$ at 09:00 LST, resulting in shrunken atmospheric depth.

The maximum developments of CBL and TIBL occur around 12:00~15:00 LST, when maximum thermal convection takes place [31, 32]. Thus, although particulate matters emitted from vehicles on the road of the coastal city could increase for daytime hours, the particulates emitted from the ground surface of the city were uplifted to the top of the vertically developed TIBL and PM concentrations near the ground surface were generally very low on October 26 in the Gangneung coast. However, as the PM concentrations at Gangneung city continuously increased on October 27, due to huge amounts of dusts transported from Gobi Desert and Nei-Mongo toward the city, their concentrations with their still increasing trends were slightly lower at both 12:00 LST and 15:00 LST than 09:00 LST (Figures 2 and 11(a)).

On the other hand, from 16:00 LST, October 27 until 04:00 LST, October 28, as huge amounts of dusts transported from Gobi Desert and Nei-Mongo toward Gangneung city under northerly wind (China), southwesterly wind (Yellow Sea) and southwesterly wind (Korean peninsula) increased rapidly and also combined with the dust and gases emitted from the ground surface of Gangneung city, local PM_{10} concentration continuously increased to a maximum value of $154.57 \mu\text{g m}^{-3}$ at 17:00 LST, October 27, which was $84.7 \mu\text{g m}^{-3}$ larger than a maximum one of $69.87 \mu\text{g m}^{-3}$ at 18:00 LST, October 26 (non-Yellow Sand Event period). Similarly, maximum value of $\text{PM}_{2.5}$ (PM_1) also reached $93.19 \mu\text{g m}^{-3}$ ($76.05 \mu\text{g m}^{-3}$), which was much larger than ones of $27.19 \mu\text{g m}^{-3}$ ($20.21 \mu\text{g m}^{-3}$), respectively.

Particularly, shortly after sunset around 17:00 LST in Korea, nocturnal cooling of the ground surface causes cooling of air masses near ground surface and produces nocturnal

surface inversion layer (NSIL), which is much more shrunken than the daytime thermal internal boundary layer (Figure 11(b)). Both dusts transported from Gobi Desert toward Gangneung city should combine with ones from vehicles on the road and heating boilers from resident area of Gangneung city. The combined dusts were trapped under much shallower and shrunken NSIL of about 50~100 m depth, resulting in the increase of PM concentrations with their maximum values around 17:00 LST.

In the previous research by Choi and Choi [20], nocturnal surface inversion layer in the coastal basin of Gangneung city was developed to 200~250 m height over the ground surface in March. Differently from their researches, in our case, synoptic-scale shrunken atmospheric depth from 500 hPa level to the ground surface due to the reduction of geopotential tendency for 12 hours (-53 m) could directly cause the decrease of nocturnal surface inversion layer depth. Thus, nocturnal surface inversion layer at 17:00 LST, October 27, could be about 150~200 m shallower than usual daytime thermal internal boundary layer. Thus, the shallower NSIL might make more contribution to the occurrence of a maximum PM concentration at 17:00 LST.

Reed and Sanders [33] explained theoretically that potential vorticity can be used as a tracer like air parcel or dust. Haynes and McIntyre [34] showed that potential vorticity can be diluted or concentrated only by flow across isentropes and it cannot be created or destroyed within a layer bounded by isentropic surfaces. Thus, Choi and Zhang [9] described in detail the dust transportation route, using relative vorticity and depicting shade area in Figure 11(b) with the big magnitudes of potential vorticity near the ground surface

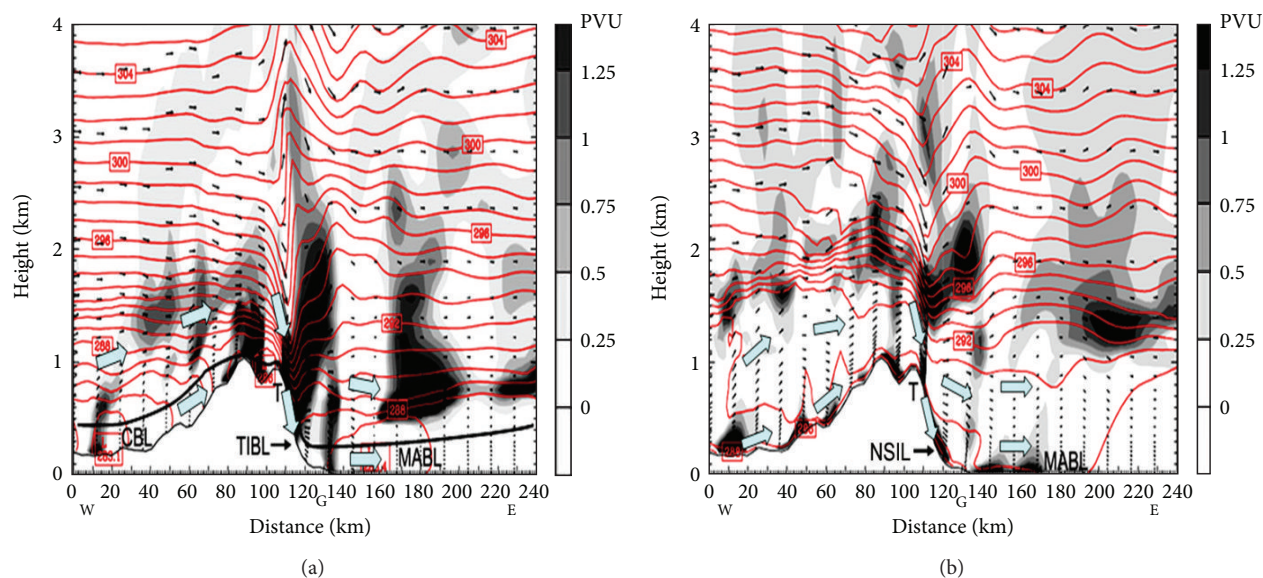


FIGURE 11: (a) Vertical profiles of potential temperature (k), wind speed (m/s), and potential vorticity ($\text{PVU} = 10^{-6} \text{ m}^2 \text{ s}^{-1} \text{ k kg}^{-1}$) on a horizontal cutting line in the third domain of WRF model simulation in Figure 6 at (a) 09:00 LST and (b) 17:00 LST, October 27, 2003. Thick line, CBL, TIBL, G, and MABL on the bottom in (a) and (b) denote the top of convective boundary layer, thermal internal boundary layer, Gangneung city, and marine atmospheric boundary layer, respectively. Shade area near the surface in (b) is nocturnal surface inversion layer (NSIL) much shallower than TIBL in (a), where the dusts transported from the northern China combining with the dust particles floated from Gangneung city were merged into the ground surface, resulting in high PM concentrations at 17:00 LST at the city, similar to [9, 20, 31, 32].

of downwind side area and the shade area implied the accumulation of air masses inside a strong stable atmospheric layer. Thus, in Figures 11(a) and 11(b), the shade area with dense isotherm near the ground surface of the mountain and coast at 17:00 LST, October 27, denotes the merge of dust particles inside the NSIL, showing a maximum PM concentration in Figure 2.

5. Conclusions

Huge transportation of dusts was detected from Gobi Desert and Nei-Mongo in the northern China toward the Korean coastal city from 09:00 LST, October 27, to 05:00 LST, October 28, using the analysis of backward trajectories by HYSPLIT model and simulated surface wind by WRF model, and local concentrations of PM during Yellow Sand period were more than three times higher than ones before or after the event period. Under the combination of dusts transported from China, high PM concentrations occurred at 09:00 LST (beginning time of office) due to particulate and gases locally emitted from vehicles of a high traffic density on the road in the city, and maintaining their increasing trends with time for daytime hours, maximum ones were detected at 17:00 LST (ending time of office), additionally with the operation of heating boilers from the resident area near sunset, showing abrupt higher PM concentrations.

The reduction of geopotential tendency of 500 hPa level for 12 hours corresponding to positive vorticity caused vertically shrunken synoptic-scale atmospheric depth, which could force nocturnal surface inversion layer to be further

shrunken with at least 200 m shortly around sunset. The combined dusts from Gobi Desert with ones emitted from the Gangneung city should be merged into the ground surface and trapped within much shrunken stable surface inversion layer, resulting in a maximum PM_{10} concentration as well as $\text{PM}_{2.5}$ and PM_1 in the city at 17:00 LST.

Conflict of Interests

The authors declare that there is no conflict of interests regarding the publication of this paper.

Acknowledgments

This work was funded by the Korea Meteorological Administration Research and Development Program under Grant CATER 2006-2308 "Generation mechanism and prediction of wind storm in the mountainous coast" in 2011~2012 research year. This paper includes a partial fulfillment of Ph.D. dissertation of Dr. Mi Sook Lee in 2012.

References

- [1] X. Zhang, R. Arimoto, Z. An et al., "Atmospheric trace elements over source regions for Chinese dust: concentrations, sources and atmospheric deposition on the Loess Plateau," *Atmospheric Environment A*, vol. 27, no. 13, pp. 2051-2067, 1993.
- [2] Y. Chung and M. Yoon, "On the occurrence of yellow sand and atmospheric loadings," *Atmospheric Environment*, vol. 30, no. 13, pp. 2387-2397, 1996.

- [3] Y. S. Chung, H. S. Kim, L. Natsagdorj, D. Jugder, and S. J. Chen, "On yellow sand occurred during 1997–2000," *Journal of Korean Meteorological Sciences*, vol. 37, pp. 305–316, 2001.
- [4] H. Choi, "Comparison of PM_{10} , $PM_{2.5}$ and PM_1 concentrations in a mountainous coastal city, Gangneung before and after the Yellow Dust event in spring," *Journal of the Environmental Sciences*, vol. 17, no. 6, pp. 633–645, 2008.
- [5] H. Choi, "Impact of fine particulate matters transported from Gobi Desert to particulate concentrations (PM_{10} , $PM_{2.5}$, PM_1) for Yellow Sand Event period in Fall—Case study of October 27, 2003," *Journal of Climate Research*, vol. 5, no. 3, pp. 219–233, 2010.
- [6] H. Choi, "Characteristics of hourly variation of gaseous pollutant concentration at Gangneung, Korea for Yellow Sand Event period in winter—case study of February 14–16, 2005," *Journal of Climate Research*, vol. 6, no. 1, pp. 59–76, 2011.
- [7] X. Wang, Y. Ma, H. Chen et al., "The relation between sandstorms and strong winds in Xinjiang, China," *Water, Air, and Soil Pollution*, vol. 3, no. 2, pp. 67–79, 2003.
- [8] Y. Zhang and Y. Zhong, "The simulation and diagnosis for a strong wind associated with northeast low," *Acta Meteorologica Sinica*, vol. 43, pp. 97–105, 1985.
- [9] H. Choi and Y. H. Zhang, "Predicting duststorm evolution with the vorticity theory," *Atmospheric Research*, vol. 89, no. 4, pp. 338–350, 2008.
- [10] I. Tegen and I. Fung, "Modeling of mineral dust in the atmosphere: sources, transport, and optical thickness," *Journal of Geophysical Research D*, vol. 99, no. 11, pp. 22987–22914, 1994.
- [11] V. R. Kotamarthi and G. R. Carmichael, "The long range transport of pollutants in the Pacific Rim region," *Atmospheric Environment A*, vol. 24, no. 6, pp. 1521–1534, 1990.
- [12] G. R. Carmichael, M. Hong, H. Ueda et al., "Aerosol composition at Cheju Island, Korea," *Journal of Geophysical Research D*, vol. 102, no. 5, pp. 6047–6061, 1997.
- [13] I. G. McKendry, J. P. Hacker, R. Stull, S. Sakiyama, D. Mignacca, and K. Reid, "Long-range transport of Asian dust to the Lower Fraser Valley, British Columbia, Canada," *Journal of Geophysical Research D*, vol. 106, no. 16, pp. 18361–18370, 2001.
- [14] T. Lin, "Long-range transport of yellow sand to Taiwan in Spring 2000: observed evidence and simulation," *Atmospheric Environment*, vol. 35, no. 34, pp. 5873–5882, 2001.
- [15] M. T. David, J. F. Robert, and L. W. Douglas, "April 1998 Asian dust event: a southern California perspective," *Journal of Geophysical Research D*, vol. 106, no. 16, pp. 18371–18379, 2001.
- [16] K. Kim, G. Choi, C. Kang et al., "The chemical composition of fine and coarse particles in relation with the Asian Dust events," *Atmospheric Environment*, vol. 37, no. 6, pp. 753–765, 2003.
- [17] M. S. Lee and J. D. Chung, "Impact of yellow dust transport from Gobi Desert on fractional ratio and correlations of temporal PM_{10} , $PM_{2.5}$ and PM_1 at Gangneung city in fall," *Journal of the Environmental Sciences*, vol. 21, no. 2, pp. 217–231, 2012.
- [18] I. Tegen and R. Miller, "A general circulation model study on the interannual variability of soil dust aerosol," *Journal of Geophysical Research D*, vol. 103, no. 20, pp. 25975–25995, 1998.
- [19] H. Choi and M. S. Speer, "Effects of atmospheric circulation and boundary layer structure on the dispersion of suspended particulates in the Seoul metropolitan area," *Meteorology and Atmospheric Physics*, vol. 92, no. 3–4, pp. 239–254, 2006.
- [20] H. Choi and D. S. Choi, "Concentrations of PM_{10} , $PM_{2.5}$, and PM_1 influenced by atmospheric circulation and atmospheric boundary layer in the Korean mountainous coast during a duststorm," *Atmospheric Research*, vol. 89, no. 4, pp. 330–337, 2008.
- [21] H. Choi, Y. H. Zhang, and K. H. Kim, "Sudden high concentration of TSP affected by atmospheric boundary layer in Seoul metropolitan area during duststorm period," *Environment International*, vol. 34, no. 5, pp. 635–647, 2008.
- [22] H. Choi, D. S. Choi, and S. M. Choi, "Meteorological condition and atmospheric boundary layer influenced upon temporal concentrations of PM_{10} , $PM_{2.5}$ at a Coastal City, Korea for Yellow Sand Event from Gobi Desert," *Disaster Advances*, vol. 3, no. 4, pp. 309–315, 2010.
- [23] H. Choi, "Trapping effect of a calm zone by lee side-internal gravity waves and cyclonic winds on sudden high concentrations of particulate matters combined with the Yellow Dusts from Gobi Desert in the Korean eastern coast," *Disaster Advances*, vol. 6, no. 11, pp. 101–111, 2013.
- [24] L. Uzan and P. Alpert, "The coastal boundary layer and air pollution—a high temporal resolution analysis in the East Mediterranean coast," *The Open Atmospheric Science Journal*, vol. 6, pp. 9–18, 2012.
- [25] H. Choi and M. S. Lee, "Atmospheric boundary layer influenced upon hourly PM_{10} , $PM_{2.5}$, PM_1 concentrations and their correlations at Gabgbeubg city before and after Yellow Dust transportation from Gobi Desert," *Journal of Climate Research*, vol. 7, no. 1, pp. 30–54, 2012.
- [26] KMA, Korean Meteorological Administration, 2003.
- [27] J. R. Holton, *An Introduction to Dynamic Meteorology*, Academic Press, 4th edition, 2004.
- [28] H. Choi, M. S. Lee, and S. M. Choi, "Cold sea surface temperature near Cheju Island responding to strong cyclonic wind and positive geopotential tendency behind a typhoon center along its track," *Journal of Marine Science and Technology*, vol. 20, no. 6, pp. 684–692, 2012.
- [29] F. Sanders and J. R. Gyakum, "Synoptic-dynamic climatology of the "bomb" (extratropical surface cyclone)," *Monthly Weather Review*, vol. 108, no. 10, pp. 1589–1606, 1980.
- [30] R. J. Reed and M. D. Albright, "A case study of explosive cyclogenesis in the eastern Pacific," *Monthly Weather Review*, vol. 114, no. 12, pp. 2297–2319, 1986.
- [31] H. Choi and S. M. Choi, "Generation of windstorm in the eastern mountainous coast of Korea," *Disaster Advances*, vol. 3, no. 2, pp. 24–34, 2010.
- [32] H. Choi, Y. H. Zhang, and S. Takahashi, "Recycling of suspended particulates by the interaction of sea-land breeze circulation and complex coastal terrain," *Meteorology and Atmospheric Physics*, vol. 87, pp. 109–120, 2004.
- [33] R. J. Reed and F. Sanders, "Investigation of the development of a mid-tropospheric frontal zone and its associated vorticity field," *Journal of Meteorology*, vol. 10, pp. 338–349, 1953.
- [34] P. H. Haynes and M. E. McIntyre, "On the evolution of vorticity and potential vorticity in the presence of diabatic heating and frictional or other forces," *Journal of Atmospheric Sciences*, vol. 44, pp. 828–841, 1987.

Research Article

Changes in Glaciers and Glacial Lakes and the Identification of Dangerous Glacial Lakes in the Pumqu River Basin, Xizang (Tibet)

Tao Che,¹ Lin Xiao,¹ and Yuei-An Liou²

¹ Cold and Arid Regions Environmental and Engineering Research Institute, Chinese Academy of Science, Lanzhou, Gansu 730000, China

² Center for Space and Remote Sensing Research, National Central University, Chung-Li 32001, Taiwan

Correspondence should be addressed to Yuei-An Liou; yueian@csrslr.ncu.edu.tw

Received 27 October 2013; Accepted 18 December 2013; Published 20 January 2014

Academic Editor: Chung-Ru Ho

Copyright © 2014 Tao Che et al. This is an open access article distributed under the Creative Commons Attribution License, which permits unrestricted use, distribution, and reproduction in any medium, provided the original work is properly cited.

Latest satellite images have been utilized to update the inventories of glaciers and glacial lakes in the Pumqu river basin, Xizang (Tibet), in the study. Compared to the inventories in 1970s, the areas of glaciers are reduced by 19.05% while the areas of glacial lakes are increased by 26.76%. The magnitudes of glacier retreat rate and glacial lake increase rate during the period of 2001–2013 are more significant than those for the period of the 1970s–2001. The accelerated changes in areas of the glaciers and glacial lakes, as well as the increasing temperature and rising variability of precipitation, have resulted in an increased risk of glacial lake outburst floods (GLOFs) in the Pumqu river basin. Integrated criteria were established to identify potentially dangerous glacial lakes based on a bibliometric analysis method. It is found, in total, 19 glacial lakes were identified as dangerous. Such finding suggests that there is an immediate need to conduct field surveys not only to validate the findings, but also to acquire information for further use in order to assure the welfare of the humans.

1. Introduction

A vast amount of studies has been conducted to increase our understanding on the changing cryosphere and its climate connection. Globally averaged temperature data show an increase of 0.85°C over the period of 1880–2012, and the total increase between the average of the 1850–1900 period and the 2003–2012 period is 0.78°C [1]. Due to rising temperatures, the areas of China's glaciers have decreased by 5–10% [2]. With the accelerated retreat of glaciers, glacial lakes have been expanding over recent decades [3, 4]; therefore, glacial lakes are also considered to be an indicator of climate change [5].

Some glacial lakes are located in valleys below glaciers and are dammed by unstable moraines formed during the Little Ice Age. Occasionally, a moraine breaks, releasing the lake's stored water and discharging large volumes of water with debris, which causes downstream flooding along the river channel. This phenomenon, generally known as a glacial lake outburst flood (GLOF), is one of the most serious disasters to

occur in the Himalayan regions of China, Nepal, India, Pakistan, and Bhutan [6–10]. To assess GLOFs, remote sensing techniques are cheaper and faster than traditional field investigations and have thus been recommended for investigating glaciers and glacial lakes [11, 12].

Due to the more frequent GLOF events in the Himalayas over the past several decades, the risks to human life and property located downstream of dangerous glacial lakes have increased. Substantial progress has been achieved in different regions of the Himalayas, and several criteria have been used to identify potentially dangerous glacial lakes [13–22]. The International Centre for Integrated Mountain Development (ICIMOD), in collaboration with partners in different countries, has begun to prepare a standardized glacial inventory for the entire Hindu Kush-Himalayan region for use as a basis for GLOF risk assessment [23].

Among the river basins in the Himalayas, the Pumqu and Poiqu river basins are two of the most concentrated areas of glacial lakes. A Chinese/Nepalese joint team carried out

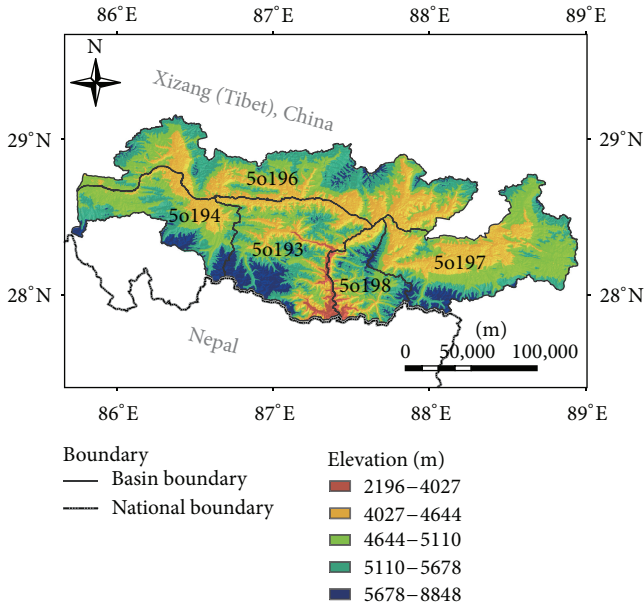


FIGURE 1: Location of the Pumqu river basin and its subbasins.

the first expedition to inventory glaciers and glacial lakes in the Pumqu and Poiqu river basins of Xizang (Tibet) in 1987 [24]. Later, the changes in glacial lakes in post-1986 in the Poiqu river basin were again investigated [5]. However, after another ten years [25, 26], the changes in glaciers and glacial lakes have not been studied in detail.

The aims of this work are (1) to investigate the changes in glaciers and glacial lakes in the Pumqu river basin based on remote sensing data acquired in 2013 and (2) to identify potentially dangerous glacial lakes in the Pumqu river basin by integrating the latest criteria from recent reports.

2. Data and Methodology

2.1. Study Area. The Pumqu river basin is situated in the southwestern region of the Tibet Autonomous Region of China (Figure 1). This basin is bounded in the north by the Mimanjinzhu Range and in the south by the world's highest mountain range, the Himalayan Range. The basin extends into the Biakuco continental lake in the west. The Yap Mountains separate the Pumqu and Poiqu river basins. The eastern part of the basin extends to Mountains Qumo, Xaya, and Joding, which border the Nyangqu river, a tributary of the Yarlungzangbo river. The total drainage area of the Pumqu river basin is 25,307 km². The Pumqu river flows through Nepal and into the Ganges through the Kosi. Based on hydrological maps and the guidelines of the world glacier inventory (WGI), the Pumqu river basin is subdivided into five subbasins (Figure 1), which also represent a glacier code basis.

2.2. Methods. The Operational Land Imager (OLI) and Thermal Infrared Sensor (TIRS) are instruments on board the Landsat 8 satellite, which was launched in February of 2013.

In total, we acquired five series of Landsat 8 OLI/TIRS images with no or low cloud cover in June, 2013. The images used in this study are Level 1 GeoTIFF Data Products, which were preliminarily calibrated. Digital elevation model (DEM) data with a resolution of 90 meters from the Shuttle Radar Topography Mission (SRTM) were used to obtain topographic information [27].

Glacier and glacial lake datasets collected in the 1970s and 2001 were used as historical data [25, 26]. The original data obtained in the 1970s included aerial photos and digital topographic maps based on aerial surveys from 1974 to 1983. The topographic maps from the 1970s were produced from aerial surveys, and two levels of maps 1:100,000 and 1:50,000, respectively, were adopted [25]. The original data for 2001 included sixteen images from the Advanced Spaceborne Thermal Emission and Reflection Radiometer (ASTER) and two images from the China-Brazil Earth Resources Satellite (CBERS), and their spatial resolutions were 15 m and 30 m, respectively. In this study, panchromatic images (band 8) from Landsat 8 OLI were registered with digital topographic maps using the software of Earth Resource Data Analysis System (ERDAS) Imagine. The registration accuracy was within 15 m (one pixel) in most areas. Furthermore, the images of other bands were resized to 15 m and were registered using the reference information from the panchromatic band.

A manual interpretation method was used to outline the glaciers and glacial lakes based on false color composite (FCC) images (6, 5, and 3 bands). DEM data were used to determine the divide line of the conjunct glaciers. The accuracy of manual interpretation has been demonstrated as optimal for identifying glaciers and glacial lakes because it allows for the consideration of both spectral characters and information regarding texture, patterns, shapes, and shadows. Finally, the spatial attributes of glaciers and glacial lakes were calculated using the topological analysis function of ArcInfo software based on the DEM data, while the physical attributes were duplicated from the historical data in the 1970s and 2001. The volumes of glacier and glacial lake were calculated based on the areas [28, 29]

$$V_g = (-11.32 + 53.21A_g^{0.3}) A_g \times 10^{-3}, \quad (1)$$

$$V_l = 0.104A_l^{1.42},$$

where V_g and A_g represent the volume (km³) and area (km²) of glacier, while V_l and A_l represent the volume (km³) and area (km²) of glacial lake, respectively. It should be noted that these two formulas were developed in another research field and were not validated in this study. Therefore, the volumes can only be considered as a reference.

To identify potentially dangerous glacial lakes, a bibliometric analysis was adopted to define criteria. First, reports associated with the identification of dangerous glacial lakes published over the last 10 years were collected. Second, overview and review papers were removed, so that only original and independent research papers were used to derive the index of identification. Third, a two-dimensional table was established based on the indices and their frequencies. Correlated indices were combined, such as the area and

TABLE 1: Summary of glacier inventories in the Pumqu river basin for the 1970s, 2001, and 2013 periods.

Subbasin	Number of glaciers			Areas of glaciers (km ²)			Changing ratio of area (%)		Ice reserve (km ³)		
	1970s	2001	2013	1970s	2001	2013	1970s–2001	1970s–2013	1970s	2001	2013
5o193	358	333	314	689.05	654.47	545.02	-5.02	-20.90	78.52	74.73	55.32
5o194	110	113	112	294.09	281.88	279.66	-4.15	-4.91	32.50	29.01	27.25
5o196	58	37	18	13.37	4.20	1.99	-68.59	-85.12	0.43	0.09	0.04
5o197	226	222	214	280.85	259.48	252.57	-7.61	-10.07	21.23	19.72	18.21
5o198	247	195	181	184.48	130.57	104.16	-29.22	-43.54	10.27	7.32	5.24
Total	999	900	839	1461.84	1330.60	1183.40	-8.98	-19.05	142.95	130.87	106.06

TABLE 2: Summary of glacial lake inventories in the Pumqu river basin for the 1970s, 2001, and 2013 periods.

Subbasin	Number of glacial lakes			Areas of glacial lakes (km ²)			Increasing ratio of area (%)		Lake volume (10 ⁶ m ³)		
	1970s	2001	2013	1970s	2001	2013	1970s–2001	1970s–2013	1970s	2001	2013
5o193	62	61	72	9.15	9.65	10.13	5.41	10.73	200.54	221.15	215.54
5o194	16	15	15	7.08	7.94	7.47	12.09	5.42	313.99	357.05	333.37
5o196	37	36	55	9.35	9.91	10.71	6.00	14.53	285.63	306.68	313.07
5o197	25	24	36	6.63	7.46	11.39	12.46	71.84	171.75	205.86	333.04
5o198	59	60	76	9.40	12.15	13.05	29.22	38.82	218.37	315.44	334.40
Total	199	196	254	41.61	47.09	52.75	13.18	26.76	1190.28	1406.18	1529.42

volume of a glacial lake or the gradient ratio of a downstream channel and the slope of a dam. Fourth, it was assumed that the frequently used indices were more important. These indices were ordered based on their importance, and the most important indices were selected as the final criteria. Weight of each criterion was calculated based on its frequency of usage. Finally, all weights of criteria that are conformed to the properties of glacial lake were accumulated as the dangerous degree. A glacial lake with the larger degree is more dangerous.

3. Results

3.1. Distribution and Change of Glaciers and Glacial Lakes. The number and areas of glaciers throughout the entire basin and in each sub-basin of the study area were calculated for the 1970s, 2001, and 2013 periods (see Table 1). The glaciers were primarily distributed in the southern region, and the average area of the glaciers was small. The number of glaciers in the Pumqu river basin was 999 in the 1970s, 900 in 2001, and 839 in 2013. The glacier areas were 1,462 km² in the 1970s, 1,330 km² in 2001, and 1,183 km² in 2013. Over the past four decades, the number of glaciers decreased by 160, while the glacier area decreased by 278.44 km² (19.05%). It is found that similar findings are obtained as compared with the previous study.

It is found that small glaciers decreased faster than larger glaciers in the past four decades (Figure 2). Such findings are consistent with those found from the previous study [25]. However, the rate of changes in areas of glaciers during the period of 2001–2013 is more significant than those for the period of the 1970s–2001. Meanwhile, the glaciers in the southwest region were relatively stable (5o194 sub-basin).

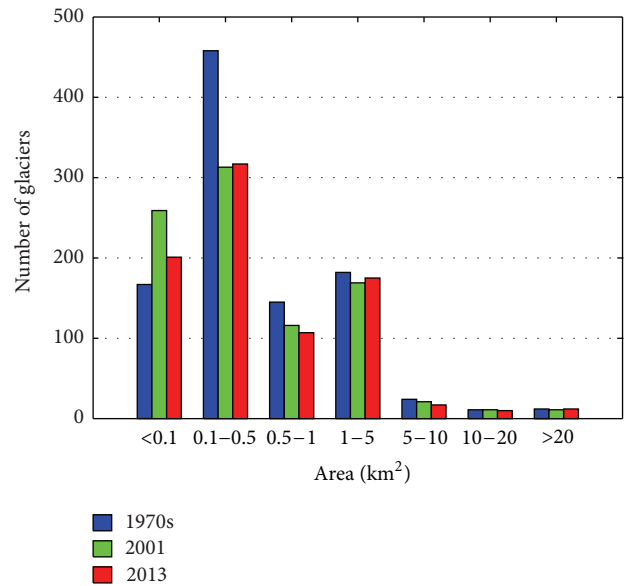


FIGURE 2: Changes in number and areas of glaciers for the 1970s, 2001, and 2013 periods.

Table 2 presents the number and areas of glacial lakes in the Pumqu river basin for the 1970s, 2001, and 2013 periods. The expansion of glacial lake is very clear in the past four decades. The number of glacial lakes was almost not changed during the period of 1970s–2001, while the area of glacial lakes was increased by 13.18%. In the past decade, more than 50 glacial lakes have newly formed, and the area of glacial lakes increased by 26.76% over the past four decades. Similar to the changes in glaciers, the rate of changes in area of glacial

TABLE 3: Integrated criteria for identifying potentially dangerous glacial lakes.

Index	Criteria	Frequencies	Weight
Type of glacial lake	End moraine-dammed lake	10	0.15
Area of lake	Larger than 0.2 km ²	10	0.15
Distance between lake and its mother glacier	Smaller than 500 m	10	0.15
Average slope of glaciers	Larger than 7 degree	7	0.10
Slope of the downstream	Larger than 20 degree	7	0.10
Top width of dam	Less than 60 meters	7	0.10
Area of glacier	Larger than 2 km ²	6	0.09
Slope between lake and its mother glacier	Larger than 8 degree	5	0.07
Change of lake area	Larger than 10% of decade	4	0.06
Elevation of lake	Higher than 5000 meters	2	0.03

lakes during the period of 2001–2013 is more significant than those for the period of the 1970s–2001. Similar results were also obtained in the Poiqu river basin [5].

On the other hand, the number of glacial lakes was stable, while the areas were expanded from the 1970s to 2001 periods. The number of glacial lakes with areas less than 0.1 km² was decreased, while that with areas between 0.5 and 1.0 km² was increased from the 1970s to 2001 periods (Figure 3). However, both the number and areas of glacial lakes have significantly risen since 2001 (Figure 3). There were many new glacial lakes with areas less than 0.1 km², and the number of glacial lakes with larger areas was increased for the period of 2001–2013.

3.2. Identification of Potentially Dangerous Glacial Lakes. Many researchers have reported indices for the identification of potentially dangerous glacial lakes [29–31]. In this work, study areas located in the Tibet Plateau regions were selected and analyzed to obtain suitable criteria for the Pumqu river basin [13–22]. The indices and criteria used in these ten papers are listed in Table 3. The glacial lake type, the distance between the mother glacier and the glacial lake, the glacial lake area, the average slope of the glacier, the slope of the downstream region, the dam width, the mother glacier area, the slope between the lake and its mother glacier, the change in lake area, and the lake elevation were adopted as indices based on the literature analysis. Note that the values within the criteria represented most of the previous reports.

According to the statistics shown in Table 3, all studies agreed that an end moraine-dammed lake with an area larger than 0.2 km² for which the distance between the lake and its mother glacier is less than 500 m is dangerous. However, the lake area was used in seven cases, while the lake volume was used in six cases. It is difficult to obtain the lake volume, which is calculated from the lake area via empirical equations [29]. Thus, these two indices were combined as the lake area.

Most of the studies argued that the average slope of the glacier, the slope of the downstream region, and the dam width are important factors. Half of the studies considered the area of the mother glacier, the slope between the lake and its mother glacier, and changes in the lake area. Only two studies considered the glacial lake elevation, because a higher elevation indicates a greater potential energy once the dam is broken.

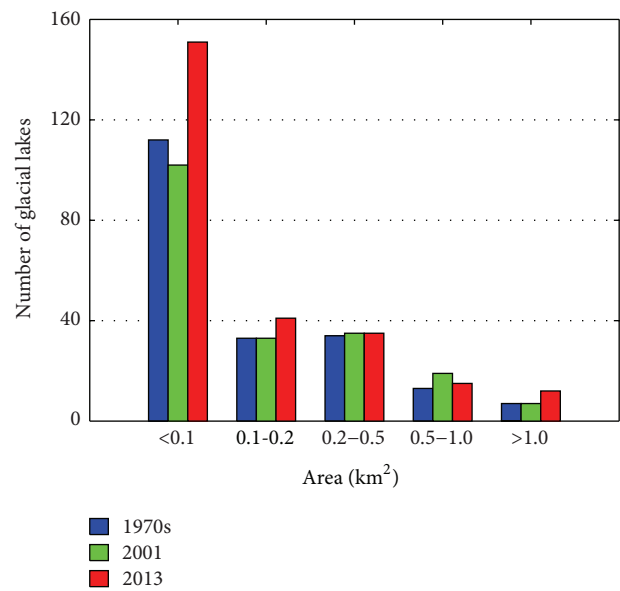


FIGURE 3: Changes in number and areas of glacial lakes for the 1970s, 2001, and 2013 periods.

In addition to the above-mentioned indices, the number of mother glaciers and the height and stability of the dam were each used in two studies. The number of mother glaciers can be reflected by the area of mother glaciers, while it is challenging to determine the height and stability of a dam from remote sensing data. Therefore, these two indices were excluded in the integrated criteria in this work.

To identify potentially dangerous glacial lakes in the Pumqu river basin, the criteria and their weights in Table 3 were adopted. The SRTM DEM data were used to obtain the slope of the glacier, the slope of the downstream region, the slope between the lake and its mother glacier, and the lake elevation. The areas and changes in glaciers and glacial lakes were obtained from the datasets for the 1970s, 2001, and 2013 periods, while the width of the dam and the distance between the lake and its mother glacier were measured from the OLI images.

The total weight of each lake was calculated based on the criteria and weights in Table 3. The dangerous degrees were

TABLE 4: Number of glacial lakes with different hazard levels in each subbasin.

Subbasin	Number of glacial lakes	Hazard level (total weight)				
		1 (0–0.19)	2 (0.2–0.39)	3 (0.4–0.59)	4 (0.6–0.79)	5 (0.8–1.0)
5o193	72	11	37	19	4	1
5o194	15	0	0	8	4	3
5o196	55	15	31	8	1	0
5o197	36	2	3	11	9	11
5o198	76	8	23	21	20	4
Total	254	36	94	67	38	19

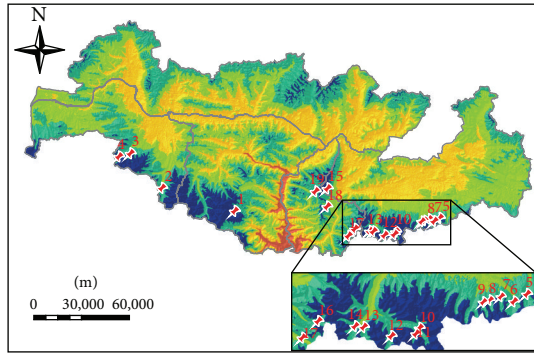


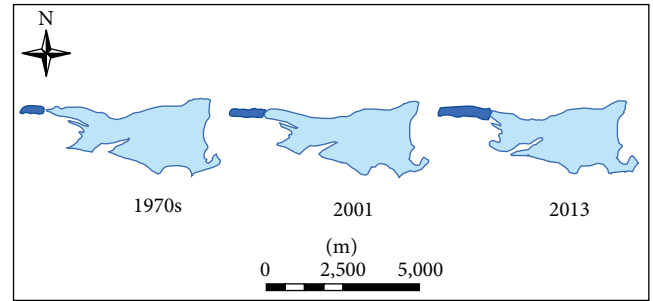
FIGURE 4: Distribution of potentially dangerous glacial lakes in the Pumqu river basin (the ID is according to Table 4).

divided into five levels with equal interval (e.g., 0.2), and those lakes with highest hazard level were considered as potentially dangerous. Totally, there are 19 glacial lakes with the highest hazard level (Table 4), almost all of which are in the southern basins (particularly in sub-basin of 5o197), where glaciers and glacial lakes are densely located (Figure 4). The potentially dangerous glacial lakes are recommended for further detailed investigations and field surveys because a potential breakout could have catastrophic effects on human life and property in China and Nepal. For information to the field work, the basic attributes of these lakes were listed in Table 5.

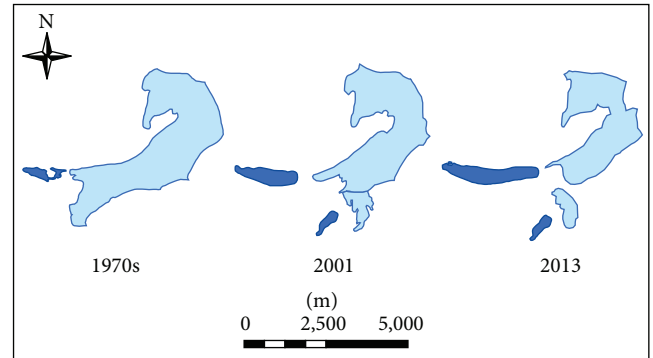
Figure 5 shows two examples of the morphological changes of potentially dangerous glacial lakes (Gelhaipuco Lake and Coqong Lake). Their locations and other characteristics are presented in Table 5 the ID of Gelhaipuco is “19” and Coqong Lake is “16,” respectively. Figure 5 clearly shows the relationship between glacial lake expansion and mother glacier shrinkage in different periods.

4. Discussion

4.1. Accuracy of Glacier and Glacial Lake Data. The glaciers and glacial lakes were mapped by manual interpretation, which has been considered the most accurate method for outlining glaciers and glacial lakes. However, the original



(a)



(b)

FIGURE 5: Morphological changes in two dangerous glacial lakes, (a) Gelhaipuco Lake and (b) Coqong Lake. (Dark blue represents glacial lakes while light blue represents glaciers.)

datasets had different spatial resolutions. The uncertainty of the glacier and glacial lake areas depends on the register accuracy and the spatial resolution of the remote sensing data. The register accuracy is one pixel in most study areas, although the error can reach two pixels in very rugged regions. In the 1970s, the original data were obtained from topographic maps with map scales of 1 : 100,000 and 1 : 50,000, indicating a spatial resolution of 50 m and 25 m, respectively. For the 2001 data, the resolutions of the ASTER and CBERS images are 15 m and 30 m. For the 2013 data, the OLI image resolution has been enhanced to 15 m. Therefore, the uncertainty can be calculated based on the register error ($R \times R$) and the error induced by the spatial resolution ($2 \times R \times R \times \sqrt{I}$), where R is the spatial resolution [32, 33]. For the lowest resolution (50 m), the register error is 0.0025 km^2 and the spatial resolution error is 0.005 km^2 for the glacier and glacial

TABLE 5: Potentially dangerous glacial lakes in the Pumqu river basin.

ID	Subbasin	Longitude	Latitude	Elevation (m)	Area (m ²)
1	5o193	87°02.83'E	28°04.16'N	5597.03	746 023
2	5o194	86°34.91'E	28°11.95'N	5069.80	1 381 460
3	5o194	86°22.81'E	28°23.72'N	5469.70	925 628
4	5o194	86°18.23'E	28°22.64'N	5347.70	3 748 580
5	5o197	88°21.24'E	28°01.42'N	5150.85	538 032
6	5o197	88°19.25'E	28°00.37'N	5104.19	380 862
7	5o197	88°17.26'E	28°01.04'N	5237.12	508 882
8	5o197	88°15.47'E	28°00.67'N	5240.75	581 487
9	5o197	88°14.45'E	28°00.36'N	5244.71	372 990
10	5o197	88°04.42'E	27°56.96'N	5479.38	1 348 830
11	5o197	88°04.03'E	27°56.16'N	5566.11	853 070
12	5o197	88°00.27'E	27°55.83'N	5331.51	1 147 950
13	5o197	87°55.82'E	27°57.16'N	5017.86	1 094 160
14	5o197	87°54.49'E	27°57.07'N	5183.23	952 025
15	5o197	87°38.39'E	28°11.68'N	5352.83	545 510
16	5o198	87°48.64'E	27°57.87'N	5259.75	454 416
17	5o198	87°46.21'E	27°55.61'N	4918.94	1 084 740
18	5o198	87°38.39'E	28°05.62'N	5197.41	693 135
19	5o198	87°33.68'E	28°10.70'N	5024.18	1 013 480

lake areas. These errors are very small and can thus be ignored. However, the presence of very small glacial lakes and water ponds in different periods can lead to a larger uncertainty for the number of glacial lakes. Therefore, glacial lakes with an area larger than 0.02 km² were analyzed in this work to obtain consistent datasets for the past four decades.

One issue that may influence the accurate classification/interpretation of glacial lakes is the fact that glacial lake areas are always larger in the summer due to the high and concentrated precipitation during the summer monsoon. High temperatures in summer also result in more water supplies (primarily melt water from glaciers, snow cover, and permafrost terrains) in glacial lakes. Therefore, when using remote sensing images for long-term monitoring of glacial lakes, one must take temporal consistency into account [34]. In this study, the dates of remote sensing images acquisition were inconsistent with three periods of 1970s, 2001, and 2013, which may lead to the uncertainties in glacial lake area.

4.2. Changes in Glacier and Glacial Lake. Temperature and precipitation are major factors controlling glacier change and glacial lake activities and are also direct causes of GLOFs. Annually averaged air temperature and precipitation data from 1971 to 2012 were acquired at the Dingri meteorological station (Figure 6). The temperature data were measured in the air 2 m above the surface, and the precipitation data include rainfall, snowfall, large-scale precipitation, and convective precipitation. The meteorological data indicate an increasing trend in air temperature but not an obvious trend in precipitation (Figure 6). Besides the trends of temperature, the monthly maximum air temperature data were collected for the evaluation of glacier melting (Figure 7). Because

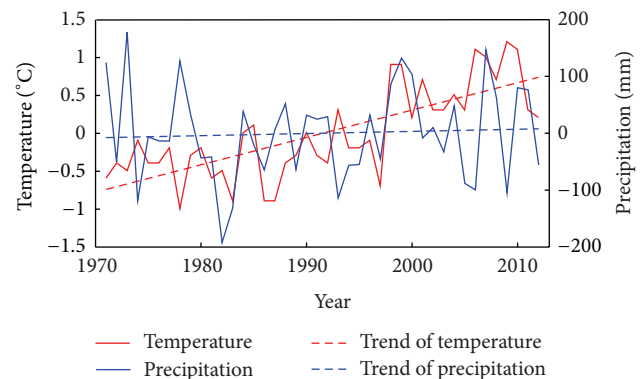


FIGURE 6: Anomalies in air temperature and precipitation from 1971 to 2012 at the Dingri meteorological station.

the elevation of Dingri station is 4300 m and the mean elevation of glacial lake is 5100 m, which can be considered as the elevation of end of glaciers, the air temperatures were corrected based on -0.6°C per 100 m according to the observations at the nearby meteorological station. However, the average air temperature was also higher than 0°C from May to September (the figure was not shown here). Therefore, both the temperature and its trend indicate the glaciers were accelerated in melting in summer. In agreement with the previous reports [25, 26], it can be concluded that climate warming is the main reason for glacier recession in the Pumqu river basin and, hence, glacial lake expansion. Statistics also showed that with the rising temperatures and increased variability of precipitation, the frequency of GLOF events is expected to increase [35].

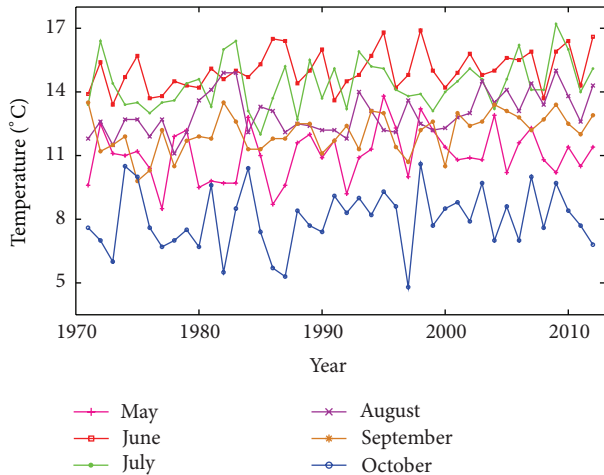


FIGURE 7: Monthly maximum air temperature from 1971 to 2012 at the elevation of 5100 m.

4.3. Potentially Dangerous Glacial Lakes. Potentially dangerous glacial lakes were identified based on our literature analysis, as well as remote sensing and DEM data. A sudden increase in temperature can lead to rapid glacier melting (even glacier calving) based on previous reports of historical GLOF events [16, 36, 37]. High temperatures can also destabilize surrounding sediments (e.g., the moraine dam). With the increased temperatures in the Pumqu river basin, the possibility of GLOF events has risen. Moreover, the interannual fluctuations in precipitation for the period of 2000–2012 were significantly larger than those for the period of 1971–2000. The standard deviation of precipitation for the period of 1971–2000 was 81.23 mm, while it grew up to 85.55 mm for the period of 2000–2012. These extremes in temperature and precipitation have been persistently increasing under the background of global changes. Thus, these potentially dangerous glacial lakes should receive more attention.

Note that the moraine dam properties, such as the presence of bedrock, ice, and pipes, cannot be interpreted by remote sensing data with a resolution of 15 m [38]. Therefore, we recommend that a field survey should be carried out in the next few years to obtain a more reliable evaluation of the dangerous lakes identified in this work. For confirmed dangerous lakes, substantial mitigation measures should be immediately implemented to reduce the risk of outburst. This work has provided basic information regarding potentially dangerous glacial lakes, which is very useful to the organization of field work.

5. Conclusion

This study used remote sensing images supplemented by DEM data to update the inventory of glaciers and glacial lakes in the Pumqu river basin, Tibetan Plateau. The changes in glaciers and glacial lakes over the past four decades were also analyzed. The results indicate that there are currently 839 glaciers and 254 glacial lakes in the study area, with total area of 1183.4 km² and 52.75 km², respectively. Between the 1970s

and 2013 periods, the number of glaciers decreased by 160, while the glacier area decreased by 276.57 km² (19.05%). The glacial lake area rose by 11.14 km² (26.76%), and the number of lakes increased by 55. The retreat of glaciers and expansion of glacial lakes (both in number and area) were particularly significant during the period of 2001–2013.

Based on a literature analysis, integrated criteria were established for the identification of potentially dangerous glacial lakes. Based on these criteria and their weights, 19 potentially dangerous glacial lakes were identified, most of which are located in the southern part of the basin. The outlet of the Pumqu river basin is the boundary between China and Nepal, so that potential GLOFs could have a catastrophic effect on lives and properties in the downstream communities. Therefore, a field survey is recommended to investigate the dangerous glacial lakes identified in this work and to conduct mitigation measures for highly dangerous glacial lakes.

Conflict of Interests

The authors declare that there is no conflict of interests regarding the publication of this paper.

Acknowledgments

The authors appreciate the reviewers for their constructive comments to improve the quality of the paper. Landsat 8 OLI data were provided by USGS, and SRTM DEM data were provided by NASA. This work was supported by the China State Key Basic Research Project (2013CBA01802), the Chinese National Natural Science Foundation (41271356), and National Science Council (NSC 102-2111-M-008-027; 102-2221-E-008-034).

References

- [1] Working group I, "Climate change 2013: the physical science basis, summary for policymakers," IPCC 5th Assessment Report, 2013.
- [2] X. Li, G. Cheng, H. Jin et al., "Cryospheric change in China," *Global and Planetary Change*, vol. 62, no. 3-4, pp. 210–218, 2008.
- [3] T. Che, L. Xin, P. K. Mool, and J. Xu, "Monitoring glaciers and associated glacial lakes on the east slopes of Mount Xixabangma from remote sensing images," *Journal of Glaciology and Geocryology*, vol. 27, no. 6, pp. 801–805, 2005 (Chinese).
- [4] X. Wang, K. Wu, L. Jiang et al., "Wide expansion of glacial lakes in Tianshan Mountains during 1990–2010," *Acta Geographica Sinica*, vol. 68, no. 7, pp. 984–993, 2013 (Chinese).
- [5] X. Chen, P. Cui, Y. Li, Z. Yang, and Y. Qi, "Changes in glacial lakes and glaciers of post-1986 in the Poiqu River basin, Nyalam, Xizang (Tibet)," *Geomorphology*, vol. 88, no. 3-4, pp. 298–311, 2007.
- [6] Y. Ding and J. Liu, "Glacier lake outburst flood disasters in China," *Annals of Glaciology*, vol. 16, pp. 180–184, 1992.
- [7] S. K. Jain, A. K. Lohani, R. D. Singh, A. Chaudhary, and L. N. Thakural, "Glacial lakes and glacial lake outburst flood in a Himalayan basin using remote sensing and GIS," *Natural Hazards*, vol. 62, no. 3, pp. 887–899, 2012.

- [8] P. K. Mool, "Glacier lake outburst floods in Nepal," *Journal of Nepal Geological Society*, vol. 11, pp. 273–280, 1995.
- [9] R. Kattelmann, "Glacial lake outburst floods in the Nepal Himalaya: a manageable hazard?" *Natural Hazards*, vol. 28, no. 1, pp. 145–154, 2003.
- [10] S. R. Bajracharya and P. K. Mool, "Glaciers, glacial lakes and glacial lake outburst floods in the Mount Everest region, Nepal," *Annals of Glaciology*, vol. 50, no. 53, pp. 81–86, 2009.
- [11] S. D. Richardson and J. M. Reynolds, "An overview of glacial hazards in the Himalayas," *Quaternary International*, vol. 65–66, pp. 31–47, 2000.
- [12] A. Kääh, C. Huggel, L. Fischer et al., "Remote sensing of glacier- and permafrost-related hazards in high mountains: an overview," *Natural Hazards and Earth System Science*, vol. 5, no. 4, pp. 527–554, 2005.
- [13] R. Lv, *A Study of Typical Mountain Hazards Along Sichuan-Tibet Highway*, Chengdu University of Science and Technology Press, Chengdu, China, 1999 (Chinese).
- [14] Z. Cheng, P. Zhu, and Y. Gong, "Typical debris flow triggered by ice-lake break," *Journal of Mountain Science*, vol. 21, no. 6, pp. 716–720, 2003 (Chinese).
- [15] J. Huang, C. Wang, G. Wang, and C. Zhang, "Application of fuzzy comprehensive evaluation method in risk degree determination for ice-lake outburst—an example of Luozha county in Tibet," *Earth and Environment*, vol. 33, supplement, 2005.
- [16] X. Chen, P. Cui, Z. Yang, and Y. Qi, "Risk assessment of glacial lake outburst in the Poiqu River Basin of Tibet autonomous region," *Journal of Glaciology and Geocryology*, vol. 29, no. 4, pp. 509–516, 2007 (Chinese).
- [17] T. Bolch, M. F. Buchroithner, J. Peters, M. Baessler, and S. Bajracharya, "Identification of glacier motion and potentially dangerous glacial lakes in the Mt. Everest region/Nepal using spaceborne imagery," *Natural Hazards and Earth System Sciences*, vol. 8, no. 6, pp. 1329–1340, 2008.
- [18] X. Wang, S. Liu, W. Guo, F. Yu, and J. Xu, "Hazard assessment of moraine-dammed lake outburst floods in the Himalayas China," *Acta Geographica Sinica*, vol. 64, no. 7, pp. 782–790, 2009.
- [19] Y. Shu, *Hazard assessment of Moraine-dammed lake outbursts in the Himalayas, Tibet and propagating numerical simulation [M.S. thesis]*, Jilin university, Jilin, China, 2011.
- [20] Z. Li, T. Yao, Q. Ye, C. Li, and W. Wang, "Monitoring glacial lake variations based on remote sensing in the Lhozhag District, Eastern Himalayas, 1980–2007," *Journal of Natural Resources*, vol. 26, no. 5, pp. 836–846, 2011.
- [21] L. Zhang, *Outburst susceptibility estimation of glacier lakes in Nielamu, Tibet, based on presort method [M.S. thesis]*, Jilin university, Jilin, China, 2012 (Chinese).
- [22] J. Liu, Z. Cheng, and X. Chen, "The hazard assessment of glacier-lake outburst in Palongzangbu River," *Journal of Mountain Science*, vol. 30, no. 3, pp. 369–377, 2012 (Chinese).
- [23] J. D. Ives, R. B. Shrestha, and P. K. Mool, *Formation of Glacial Lakes in the Hindu Kush-Himalayas and GLOF Risk Assessment*, ICIMOD, Kathmandu, Nepal, 2010.
- [24] LIGG/WECS/NEA, *Report on First Expedition to Glaciers and Glacier Lakes in the Pumqu (Arun) and Poique (Bhote-Sun Kosi) River Basins, Xizang (Tibet), China, Sino-Nepalese Investigation of Glacier Lake Outburst Floods in the Himalaya*, Science Press, Beijing, China, 1988.
- [25] R. Jin, X. Li, T. Che, L. Wu, and P. Mool, "Glacier area changes in the Pumqu river basin, Tibetan Plateau, between the 1970s and 2001," *Journal of Glaciology*, vol. 51, no. 175, pp. 607–610, 2005.
- [26] T. Che, R. Jin, X. Li, and L. Wu, "Glacial lakes variation and the potentially dangerous glacial lakes in the Pumqu basin of Tibet during the last two decades," *Journal of Glaciology and Geocryology*, vol. 26, no. 4, pp. 397–402, 2004 (Chinese).
- [27] A. Jarvis, H. I. Reuter, A. Nelson, and E. Guevara, "Hole-filled SRTM for the globe Version 4," CGIAR-CSI SRTM 90m Database, 2008, <http://srtm.csi.cgiar.org>.
- [28] C. Liu and L. Ding, "The newly progress of glacier inventory in Tianshan Mountains," *Journal of Glaciology and Geocryology*, vol. 8, no. 2, pp. 167–170, 1986 (Chinese).
- [29] C. Huggel, A. Kääh, W. Haerberli, P. Teyssiere, and F. Paul, "Remote sensing based assessment of hazards from glacier lake outbursts: a case study in the Swiss Alps," *Canadian Geotechnical Journal*, vol. 39, no. 2, pp. 316–330, 2002.
- [30] R. J. McKillop and J. J. Clague, "Statistical, remote sensing-based approach for estimating the probability of catastrophic drainage from moraine-dammed lakes in southwestern British Columbia," *Global and Planetary Change*, vol. 56, no. 1–2, pp. 153–171, 2007.
- [31] T. Bolch, J. Peters, A. Yegorov, B. Pradhan, M. Buchroithner, and V. Blagoveshchensky, "Identification of potentially dangerous glacial lakes in the northern Tien Shan," *Natural Hazards*, vol. 59, no. 3, pp. 1691–1714, 2011.
- [32] D. K. Hall, K. J. Bayr, W. Schöner, R. A. Bindschadler, and J. Y. L. Chien, "Consideration of the errors inherent in mapping historical glacier positions in Austria from the ground and space (1893–2001)," *Remote Sensing of Environment*, vol. 86, no. 4, pp. 566–577, 2003.
- [33] R. S. Williams, D. K. Hall, O. Sigurbsson, and J. Y. L. Chien, "Comparison of satellite-derived with ground-based measurements of the fluctuations of the margins of Vatnajökull, Iceland, 1973–1992," *Annals of Glaciology*, vol. 24, pp. 72–80, 1997.
- [34] C. Liu, "Glacier lakes and their outburst behaviors in the Himalayas, Xizang," in *Proceedings of the 4th National Conference on Glaciology and Geocryology (Glaciology)*, pp. 141–150, Science Press, Beijing, China, 1990 (Chinese).
- [35] S. R. Bajracharya, P. K. Mool, and B. R. Shrestha, "The impact of global warming on the glaciers of the Himalaya," in *Proceedings of the International Symposium on Geodisasters, Infrastructure Management and Protection of World Heritage Sites*, pp. 231–242, 2006.
- [36] Z. Yao, R. Duan, X. Dong, and C. Yu, "The progress and trends of glacial lakes research on Qinghai-Tibet Plateau," *Progress in Geography*, vol. 29, no. 1, pp. 10–14 (Chinese).
- [37] M. Chiarle, S. Iannotti, G. Mortara, and P. Deline, "Recent debris flow occurrences associated with glaciers in the Alps," *Global and Planetary Change*, vol. 56, no. 1–2, pp. 123–136, 2007.
- [38] P. Cui, D. Ma, N. Chen, and Z. Jiang, "The initiation, motion and mitigation of debris flow caused by glacial lake outburst," *Quaternary Sciences*, vol. 23, no. 6, pp. 621–628, 2003 (Chinese).

Research Article

Validation of ASTER Surface Temperature Data with *In Situ* Measurements to Evaluate Heat Islands in Complex Urban Areas

Bonggeun Song and Kyunghun Park

Department of Environmental Engineering, Changwon National University, 20 Changwondaehak-ro Uichang-gu Changwon-si, Gyeongsangnam-do 641-773, Republic of Korea

Correspondence should be addressed to Kyunghun Park; landpkh@changwon.ac.kr

Received 27 August 2013; Accepted 6 December 2013; Published 20 January 2014

Academic Editor: Yuriy Kuleshov

Copyright © 2014 B. Song and K. Park. This is an open access article distributed under the Creative Commons Attribution License, which permits unrestricted use, distribution, and reproduction in any medium, provided the original work is properly cited.

This study compared Advanced Spaceborne Thermal Emission Reflection Radiometer (ASTER) surface temperature data with *in situ* measurements to validate the use of ASTER data for studying heat islands in urban settings with complex spatial characteristics. Eight sites in Changwon, Korea, were selected for analyses. Surface temperature data were extracted from the thermal infrared (TIR) band of ASTER on four dates during the summer and fall of 2012, and corresponding *in situ* measurements of temperature were also collected. Comparisons showed that ASTER derived temperatures were generally 4.27°C lower than temperatures collected by *in situ* measurements during the daytime, except on cloudy days. However, ASTER temperatures were higher by 2.23–2.69°C on two dates during the nighttime. Temperature differences between a city park and a paved area were insignificant. Differences between ASTER derived temperatures and onsite measurements are caused by a variety of factors including the application of emissivity values that do not consider the complex spatial characteristics of urban areas. Therefore, to improve the accuracy of surface temperatures extracted from infrared satellite imagery, we propose a revised model whereby temperature data is obtained from ASTER and emissivity values for various land covers are extracted based on *in situ* measurements.

1. Introduction

Cities all over the world are experiencing more common urban heat islands (UHIs), whereby urban settlements are hotter than rural areas because of the rapid increase in artificial land cover such as asphalt [1–4]. Urban heat islands can generate tropical nighttime conditions and exacerbate heat waves, which negatively affects the health and welfare of urban residents [5–8]. Moreover, temperature increases from UHIs greatly increase energy consumption from the use of coolers [9, 10] and the aggregated effects from UHIs can cause changes in urban ecosystems [11]. The problems associated with UHIs are expected to worsen with global warming and UHIs are rapidly expanding into a global environmental issue of concern [12–14].

To alleviate adverse effects from UHIs, a wide range of studies have been performed using data on land surface temperatures (LSTs) extracted from remotely sensed thermal infrared data [15–18]. Surface temperature data derived from satellite images can be used to assess characteristics of UHIs such as how temperatures vary across the canopy layer of

roofs and other surface features [19–23] or how temperatures are related to the surface energy balance [24–28]. In addition, satellite images of surface temperature data can supplement *in situ* temperature measurements collected by meteorological networks. Thus, satellite data can be used to analyze the general features of atmospheric UHIs in urban areas [29, 30].

To use satellite image-based surface temperature data for heat island studies in urban areas with complex spatial characteristics, important factors that influence surface temperatures must be considered comprehensively [31, 32]; these factors include the coverage texture type, the color of the surface layer, sky view factors, street geometry, traffic loads, and other anthropogenic activities. It is also important to validate the accuracy of satellite image surface temperature data by comparing it to *in situ* surface temperature data. Such analyses are necessary to diagnose UHIs more accurately and prepare appropriate relief plans.

Several recent studies have been conducted to validate or improve the accuracy of satellite temperature measurements by comparing satellite image surface temperature

data to temperatures measured onsite. Mihalcea et al. [33] compared surface temperatures from onsite measurements and Advanced Spaceborne Thermal Emission Reflection Radiometer (ASTER) video images according to supraglacial debris coating and depth. Rigo et al. [34] validated the effectiveness of thermal infrared satellite images by comparing the earth radiation energy extracted from the images to data collected from eight fixed weather stations that were installed in urban, suburban, and rural areas of Basel, Switzerland. Nichol et al. [35] attempted to investigate UHIs and validate the accuracy of ASTER image surface temperature data by measuring surface temperatures at 18 sites located throughout the urban region of Kowloon in Hong Kong and the nonurban area of the New Territories in Hong Kong. In Scottsdale, Arizona, which is located in the Phoenix Metropolitan Area, Hartz et al. [36] classified land cover into asphalt, concrete, roof, and plant life and measured the surface temperature of each material using a thermal infrared camera. Then, the results were compared to surface temperatures derived from ASTER video images. All of these studies found that satellite temperature data were useful as surrogate measures for *in situ* temperature data.

Nonetheless, most relevant studies to date that compare *in situ* temperature data to satellite-based measurements are limited to homogeneous areas or rural areas. In addition, studies that have analyzed UHIs in urban areas with complex spatial characteristics are limited by their use of low resolution satellite images. Therefore, this study aimed to validate the accuracy of satellite image surface temperature data in an urban area through comparisons of relatively high resolution ASTER video data to onsite temperature measurements. Analyses were conducted in the urban area of Changwon, Gyeongsangnam-do, Korea, which is going through rapid urbanization and has various land use and coverage characteristics. Additionally, we evaluated and compared temperature measurements collected during the day and the night because thermal characteristics can vary diurnally.

2. Materials and Methods

2.1. Experiment Site. The urban area of Changwon, Gyeongsangnam-do, Korea ($35^{\circ}14'01.02''\text{N}$, $128^{\circ}41'19.95''\text{E}$), has a population of approximately 500,000 people. The area is 125.91 km^2 wide, and it is located in a basin surrounded by mountains that are approximately 600 m in height. The city, in which residential, commercial, and business areas are concentrated, contains a large floating population (i.e., non-residential population) and dense traffic. Its annual average temperature is 15°C , and the annual precipitation is 1,396 mm [37].

The experiment site was established as the first planned city in Korea [38]. The site contains clear divisions of residential, commercial, and industrial quarters. It is composed of various structural patterns and coverage materials such as asphalt, concrete, greenery, sidewalk bricks, and tiles. In this study, we selected a total of eight sites for analyses, including a university campus, an urban park, a commercial area, low-rise apartments, high-rise apartments, a single residential

area, an open lawn square of homogeneous coverage material, and a sidewalk brick square (Figure 1). These sites were selected because of their diverse land use and coverage characteristics, and *in situ* measurements at these sites were compared to data from satellite images.

2.2. Setup of GIS Data and Satellite Imagery

2.2.1. ASTER Video Data. Satellite image-based surface temperature data were extracted using the Level 2B03 Product (surface kinetic temperature) from the thermal infrared (TIR) band of ASTER. The ASTER instrument, located onboard the Terra satellite, is composed of three sensors: SWIR (short wave infrared), VNIR (visible near infrared), and TIR (thermal infrared). It also has 14 spectrum channels to analyze radiance. Among them, the TIR generates products between channels 10 and 14 ($8.15\text{--}11.65\ \mu\text{m}$) [39]. The spatial resolution of the ASTER 2B03 product is 90 m, and it is used to generate data for the Temperature Emissivity Separation (TES) algorithm used for determining the emissivity of land coverage values [36, 40].

This study collected four ASTER video images on almost cloudless, sunny days between June and September 2012. In particular, the acquisition times were at 02:10 pm UTC on July 28, 2012 (daytime), 01:31 am UTC on September 21, 2012 (nighttime), 02:16 pm UTC on September 23, 2012 (daytime), and 01:37 am UTC on September 28, 2012 (nighttime). Surface temperatures were extracted after geometric corrections and coordinate transformations had been performed using the Geodetic Reference System (GRS) 80 equipped with PG-STEAMER version 4.2 (Pixoneer Corp.) software, an image processing program.

2.2.2. Urban Characteristics Data. Surface fabric classification of the eight subject areas was performed through onsite investigations and the use of 10 cm high spatial resolution aerial photograph orthoimagery and land coverage maps from the Changwon Environment Atlas. The land coverage maps in the Changwon Environment Atlas are composed of very detailed GIS spatial data that contain 31 coverage properties such as structures, asphalt, concrete, trees, and bare lands at a 1:1,000 scale [41]. The reserve surface fabrics were selected after considering the unclassified fabrics based on the land coverage maps. A total of 21 surface fabrics, identifiable on the maps when compared to the aerial photograph, were ultimately selected.

Temperatures may vary in areas with the same surface fabric because trees and buildings will form shadows during the daytime that alter the amount of radiant energy flowing into the surface [42]. Thus, shaded areas during the daytime of July 28th and September 23rd were classified as surface fabrics and reflected in the analyses. Analyses were performed through use of the Hillshade function of the ArcGIS 9.3 program using digital terrain models (DTM) extracted from light interferometry detection and ranging (LiDAR) images with a 1 m spatial resolution. The input variables of sun altitude and azimuth were matched to the times of the video collection. The values used were as follows: $63^{\circ}52'51.60''$ and $188^{\circ}31'40.10''$ for the July 28 and $44^{\circ}17'04.40''$ and

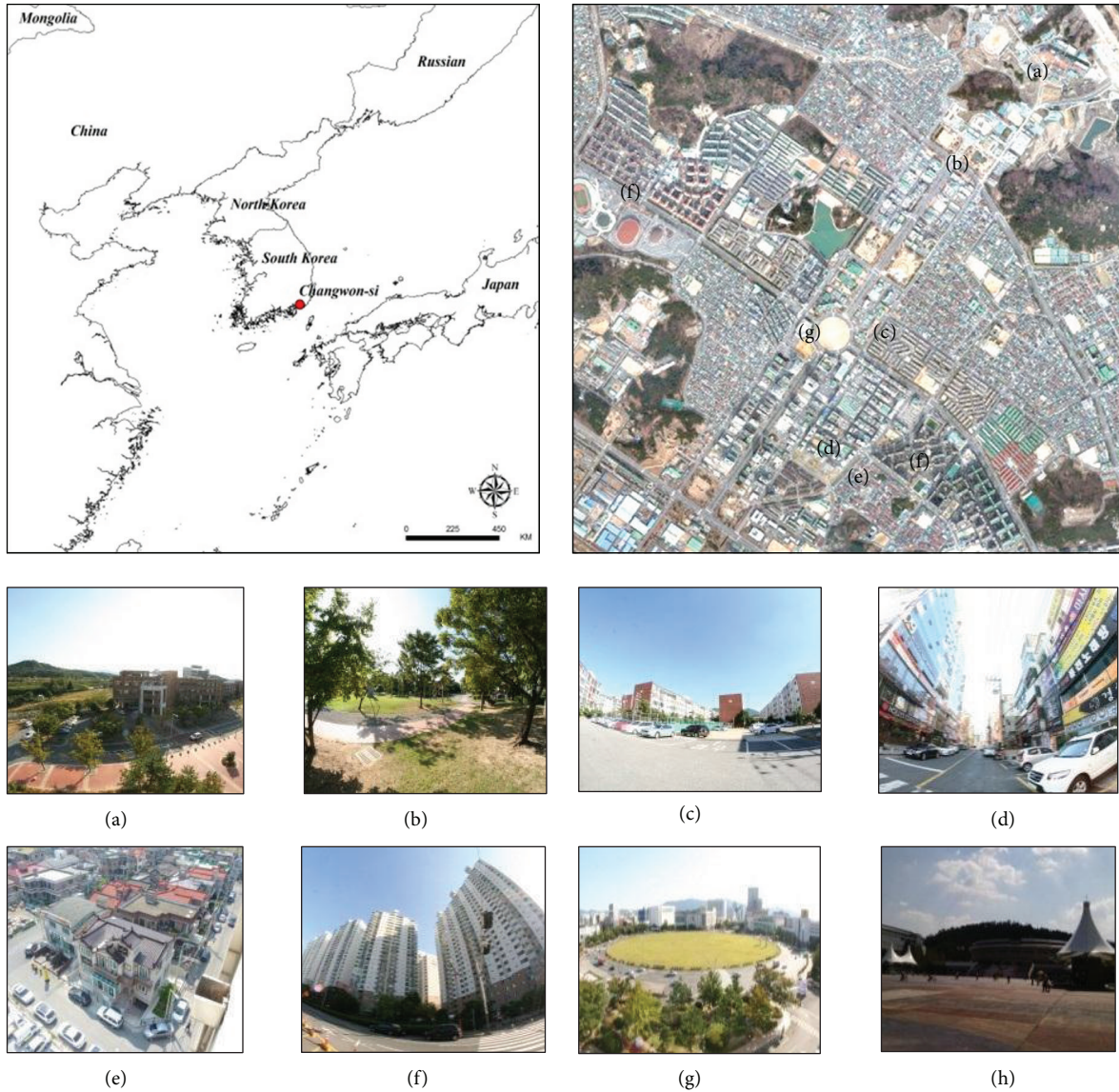


FIGURE 1: The experiment site and the eight measurement sites in the urban area of Changwon, Republic of Korea. (a) University campus, (b) urban park, (c) low-rise apartments, (d) commercial area, (e) single residential, (f) high-rise apartments, (g) lawn square, and (h) sidewalk brick square.

220°47'57.60" for the September 23. Because the inflow of radiant energy was blocked in shaded areas, the surface temperatures in these regions were almost equivalent to air temperatures; hence, site temperatures measurements were substituted as surface temperatures at some locations [43].

2.3. In Situ Measurement Data and Methods

2.3.1. Measurements of Surface Temperature and Weather Variables. By considering the composition ratio of the surface fabric and measurement times at each subject site, a total of 366 points were chosen from the 8 sites for analyses (78 places in the university campus, 64 in the park, 53 in the low-rise apartments, 63 in the commercial area, 41 in the single residential area, 55 in the high-rise apartments, 6 from

the lawn square, and 6 from the sidewalk bricks) (Figure 2). Onsite measurements were carried out for approximately an hour at each site (daytime: 14:00 - 15:00 and nighttime: 01:00 - 02:00). The measurements were collected so that the data would span 30 minutes before and after the time in which the satellite took pictures.

Temperatures were measured using thermal infrared thermometers that were held 10 cm vertically off the surface. A portable Kestrel 4500 Weather Meter was also used to measure weather related variables such as temperature, relative humidity, and wind speed at each measuring point (air temperature accuracy: $\pm 1.0^{\circ}\text{C}$, wind speed accuracy: $\pm 3\%$, and relative humidity (RH) accuracy: $\pm 3\%$).

To account for changes in the surface temperature according to the elapsed site measurement time, we attempted to

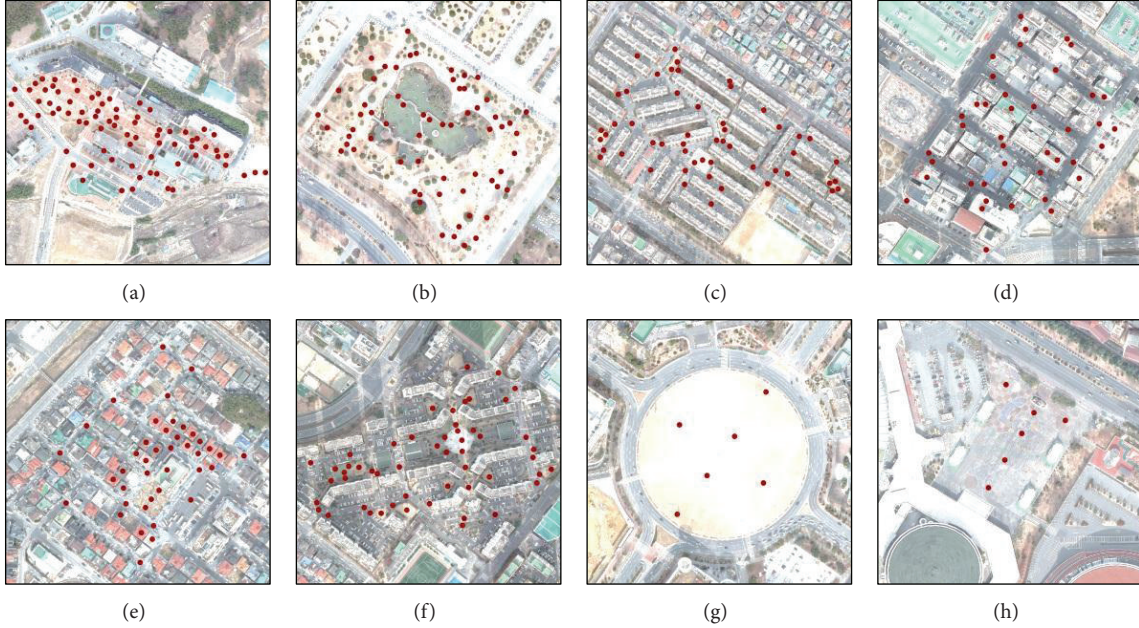


FIGURE 2: Surface temperature measurement points within the eight subject sites. (a) University campus (78 points), (b) urban park (64 points), (c) low-rise apartments (53 points), (d) commercial area (63 points), (e) single residential (41 points), (f) high-rise apartments (55 points), (g) lawn square (6 points), and (h) sidewalk brick square (6 points).

TABLE 1: Area ratio and division of sunny and shaded areas per location per date.

Date	Site							
	UC	P	LR	CA	SR	HR	LS	SS
28 July 2012								
Sunny (%)	98.7	90.2	81.2	76.1	85.3	67.5	96.6	89.6
Shade (%)	10.4	9.8	18.8	24.0	14.7	32.5	3.4	10.4
23 September 2012								
Sunny (%)	82.7	81.9	67.8	63.5	77.1	55.7	92.6	83.3
Shade (%)	17.3	18.1	32.2	36.6	22.9	44.3	7.4	16.7

UC: university campus, P: urban park, LR: low-rise apartments, CA: commercial area, SR: single residential, HR: high-rise apartments, LS: lawn square, and SS: sidewalk brick square.

perform a correction through the use of linear regression techniques. However, the temperature differences over time were below 0.5°C ; hence, the data were not corrected for time differences. Furthermore, we were limited in our ability to perform measurements on top of single residential buildings; hence, roof temperatures in these areas were measured using thermal imaging cameras (temperature accuracy: $\pm 2^{\circ}\text{C}$) from the roofs of nearby high-rise business buildings.

2.3.2. Emissivity Calculation Method. Emissivity refers to the ability of a surface fabric to absorb, transmit, and reflect external radiant energy. Emissivity values are rated against a black body, which theoretically will only absorb energy without reflecting it [44].

Surface temperature data extracted from the satellite image represents radiant temperature, which is the temperature conversion of radiant energy released from the surface, and it is closely related to the emissivity for surface fabrics [33, 45]. Valor and Caselles [46] and Caselles et al. [47] stated, “retrieval of LST from TIR data requires an accurate measurement of emissivity values of the surface.” Therefore, it is necessary to compare it to actual measurements of emissivity from various surface fabrics of the urban area.

Emissivity was calculated using the Stefan-Boltzmann law as follows:

$$\varepsilon_i = \frac{L_i}{\varepsilon_{0.95} \times \sigma \times (273.15 + T_{si})^4}. \quad (1)$$

Here, ε_i is the emissivity of fabric i , L_i is the earth radiant energy of fabric i measured by the CNR4 net-radiometer, $\varepsilon_{0.95}$ is the set emissivity of the thermal infrared thermometer (0.95), T_{si} is the surface temperature of the fabric i using a thermal infrared thermometer, and σ is the Stefan-Boltzmann constant ($5.67 \times 10^{-8} \text{ W m}^{-2} \text{ K}^{-4}$).

Emissivity for each surface fabric was calculated after measuring the surface temperature and radiant energy of the 21 surface fabrics classified in the city characteristic data (Table 2). Radiant energy was measured using a CNR4 net-radiometer (Kipp and Zonen Inc.) by holding it horizontally approximately 10 cm away from the surface for a minute to two. The surface temperature was measured by holding a thermal infrared thermometer (Testo 381 model, accuracy: $\pm 1.5^{\circ}\text{C}$, emissivity: 0.95) 10 cm perpendicular to the surface.

Measurements were performed during 10:00 to 16:00 on three days, May 27, June 5, and June 24, which consisted

TABLE 2: Surface temperature and emissivity of different surface fabrics measured onsite. Surface temperatures that were measured in shaded areas during the day were excluded.

Surface fabric	Emissivity	Surface temperature											
		Daytime						Nighttime					
		28 July 2012			23 September 2012			21 September 2012			28 September 2012		
No.	Mean (°C)	SD	No.	Mean (°C)	SD	No.	Mean (°C)	SD	No.	Mean (°C)	SD		
Metal roof	0.99	1	44.5	—	1	36.8	—	1	19.1	—	1	17.0	—
Roof tile (brown)	0.98	12	55.9	5.2	7	47.7	4.0	12	15.6	0.6	12	13.6	1.7
Roof tile (black)	0.99	6	57.4	7.0	6	46.9	5.1	6	15.6	1.8	6	15.0	1.3
Roof tile (green)	0.99	1	51.7	—	1	41.5	—	1	17.9	—	1	16.9	—
Wooded board	0.95	4	69.0	0.6	6	52.2	1.9	9	12.1	3.3	7	12.2	0.6
Sand and bare	0.96	20	47.8	6.6	17	30.6	6.5	20	15.7	0.9	20	15.1	0.7
Sidewalk brick	0.96	40	50.1	3.9	40	39.3	5.0	47	17.8	2.1	46	17.9	1.2
Water	1.00	6	27.0	0.4	6	21.4	0.8	6	17.3	1.2	6	19.9	0.4
Tree and lawn	0.97	67	37.7	3.3	88	28.4	4.1	92	14.2	2.1	91	15.3	1.2
Asphalt	0.96	75	58.5	4.2	53	45.5	3.7	76	19.6	1.3	75	18.7	1.2
Green roof	0.93	7	40.0	3.9	5	26.2	3.0	7	15.9	1.0	4	16.7	1.0
Urethane	0.96	2	66.2	1.1	2	49.3	0.2	2	15.3	0.1	2	14.4	0.5
Artificial turf	0.96	6	56.1	3.2	6	39.9	1.2	6	17.0	0.9	6	16.8	0.7
Gravel	0.98	14	52.3	3.6	14	37.5	2.4	15	13.9	1.1	15	15.0	1.1
Concrete	0.97	8	54.2	2.6	8	40.5	2.6	9	19.7	0.8	9	18.8	0.7
Concrete roof (green)	0.98	7	57.4	2.4	4	43.0	3.5	5	18.1	1.2	5	18.0	0.6
Concrete roof (gray)	0.98	16	58.7	2.7	13	43.7	4.1	15	19.9	2.2	15	18.4	1.8
Tile	1.00	5	48.7	7.0	6	30.5	4.1	6	19.6	1.0	6	17.7	0.4
Flagstone	0.96	5	57.2	1.6	6	42.1	2.3	6	15.7	1.8	6	17.7	0.5
Granite	0.98	1	48.0	—	1	41.3	—	1	21.4	—	1	19.3	—
Homogeneous lawn	—	6	43.5	6.9	6	33.0	1.8	6	12.8	0.8	6	12.3	0.5
Homogeneous sidewalk brick	—	6	62.0	1.1	6	46.2	0.8	6	15.3	0.5	6	19.3	0.8

of clear weather. Measurement points were selected with the composition ratio of surface fabric per subject area in mind and measurements were collected in spots that were as homogeneous as possible (i.e., not mixed with other fabric types).

2.4. Comparison Method for ASTER and In Situ Measurements of Surface Temperature. Direct comparisons between the surface temperatures of satellite derived pixel images and geographically identical pixel locations were performed for ASTER image data and onsite measurements. To do so, the entire field measurement site was divided into Vector GRIDs of 90 m × 90 m, which was identical to the spatial resolution of the ASTER image (Figure 3).

For the field measured surface temperatures, the mean surface temperature of each GRID was calculated after analyzing the area ratio per surface fabric per GRID according to the following equation:

$$T_s = \sum_{i=1}^n \left[\left\{ \sqrt[4]{\frac{0.95}{\varepsilon_i} (273.15 + T_{si})^4} - 273.15 \right\} \times A_i \right]. \quad (2)$$

Here, T_s is the mean surface temperature per GRID, ε_i is the emissivity of fabric i , T_{si} is the surface temperature of fabric i , and A_i is the area ratio of the fabric i .

The mean surface temperature calculated for each GRID was compared to the surface temperature of the exact location on the ASTER image. The difference in the surface temperature between the satellite image and the field measurement was contemplated in connection with the spatial characteristics of the subject area and the pixels.

3. Results and Discussion

3.1. Spatial Patterns of ASTER Surface Temperature. Figure 4 shows the surface temperature results that were extracted from the ASTER images. Surface temperature was high during the day mostly in places covered with concrete and asphalt. Although the commercial area, low-rise apartments, and high-rise apartments had higher surface temperatures during the night compared to the daytime, the differences were insignificant. According to the image taken on July 28, portions of the commercial area, high-rise apartments, and single residential area had low surface temperatures due to the influence of clouds.

Among the mean surface temperatures at each of the 8 sites, the block square (07/28: 44.3°C, 09/23: 33.2°C) had the highest temperature during the day, and the commercial area (09/21: 19.4°C, 09/28: 19.0°C) and the high-rise apartments (09/21: 18.7°C, 09/28: 19.2°C) had the highest temperatures during the night (Table 3).

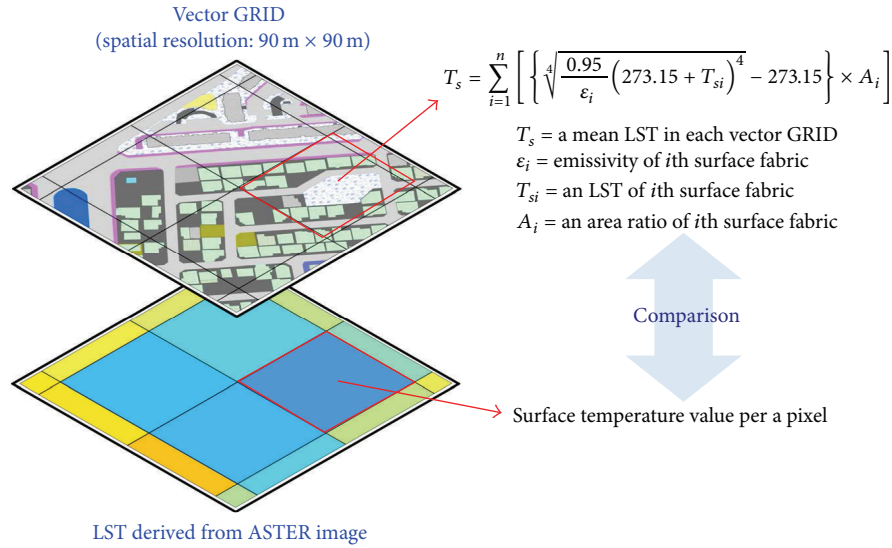


FIGURE 3: Surface temperature comparison of values collected by ASTER images and field measurements.

3.2. Classification of Surface Fabric and Shaded Areas per Location. Figure 5 shows the classification of surface fabric. The university campus was mostly composed of asphalt, sidewalk bricks, trees, and grass. Low-rise apartments and commercial areas were mostly composed of concrete on the building roofs (grey) and asphalt. Single residential areas had a high amount of asphalt and tiled roofs of various colors. High-rise apartments were composed of various fabrics such as asphalt, concrete (grey) sidewalk bricks, trees, grass, and tile. Asphalt was common in the areas around homogeneous lawn squares and sidewalk brick plazas.

Analyses of the shaded areas created by buildings and other structures were limited to the date the satellite photography and field measurements took place. As the altitude of the sun was higher and the azimuth was smaller on July 28 than on September 23, the amount of shaded area was smaller. The commercial area and the high-rise apartment area, which were packed with tall buildings, had a high percentage of shaded areas (Figure 6), while the lawn square area was the least affected by the shade because of its location in an open space (Table 1).

3.3. Emissivity and Surface Temperature by Field Measurements. Of the 21 types of surface fabrics, water and tile had the highest emissivity of 1.00, while the green roof system had the lowest at 0.93, according to measurement results of the emissivity per surface fabric (Table 2). The results of Sobrino et al. [45] demonstrated an emissivity of 0.985 for water surfaces, 0.990 for trees, 0.914 for concrete, 0.965 for asphalt, 0.902 for sidewalk bricks, 0.898 for bright bare soil, 0.970 for dark bare soil, and 0.897 for rooftops. These values were obtained by mapping emissivity per land coverage with ASTER images, and the values were somewhat different from those that were obtained during measurements in this study. Emissivity was especially different for artificial surface textures such as concrete, sidewalk bricks, and rooftops.

Field measurements of surface temperatures showed that temperatures were higher on September 23 than on July 28 by approximately 10°C on average. Wooden boards had the highest surface temperature (07/28: 69.0°C, 09/23: 52.2°C), followed by urethane (07/28: 66.2°C, 09/23: 49.3°C). Water had the lowest surface temperature (07/28: 27.0°C, 09/23: 21.4°C). More open areas such as sidewalk brick squares (07/28: 62.0°C, 09/23: 46.2°C) and lawn squares (07/28: 43.5°C, 09/23: 33.0°C) had higher surface temperatures than areas that were not open spatially (Table 2). This was likely caused by more continuous short wave radiation flowing into open areas.

Nighttime measurements showed little differences in surface temperatures between the different surface fabrics. In general, however, artificial fabrics such as asphalt (09/21: 19.6°C, 09/28: 18.7°C), concrete (09/21: 19.7°C, 09/28: 18.8°C), and granite (09/21: 21.4°C, 09/28: 19.3°C) had relatively higher surface temperatures. Extraordinarily, wooden boards, which had the highest surface temperature during the day, had the lowest temperature during the night (09/21: 12.1°C, 09/28: 12.2°C) and water surfaces, which had the lowest temperature during the day, had the highest temperature during the night (09/21: 17.3°C, 09/28: 19.9°C) (Table 2). This is because water has a large heat capacity. Thus, when water is subjected to external heat energy, the temperature rises and falls slowly and it can be relatively high during the night [48, 49]. Open areas such as lawn squares (09/21: 12.8°C, 09/28: 12.3°C) had lower surface temperatures than lawns that were not as open (09/21: 13.4°C, 09/28: 14.6°C). This is because more compact spaces release less terrestrial radiation energy from the earth to the atmosphere, which leads to a greater aggregation of energy at the surface [18, 50]. Temperatures reached 35.8°C on July 28, 20.2°C on September 21, 27.7°C on September 23, and 20.7°C on September 28.

Surface temperatures calculated for each GRID using field measurement data showed that sidewalk brick squares

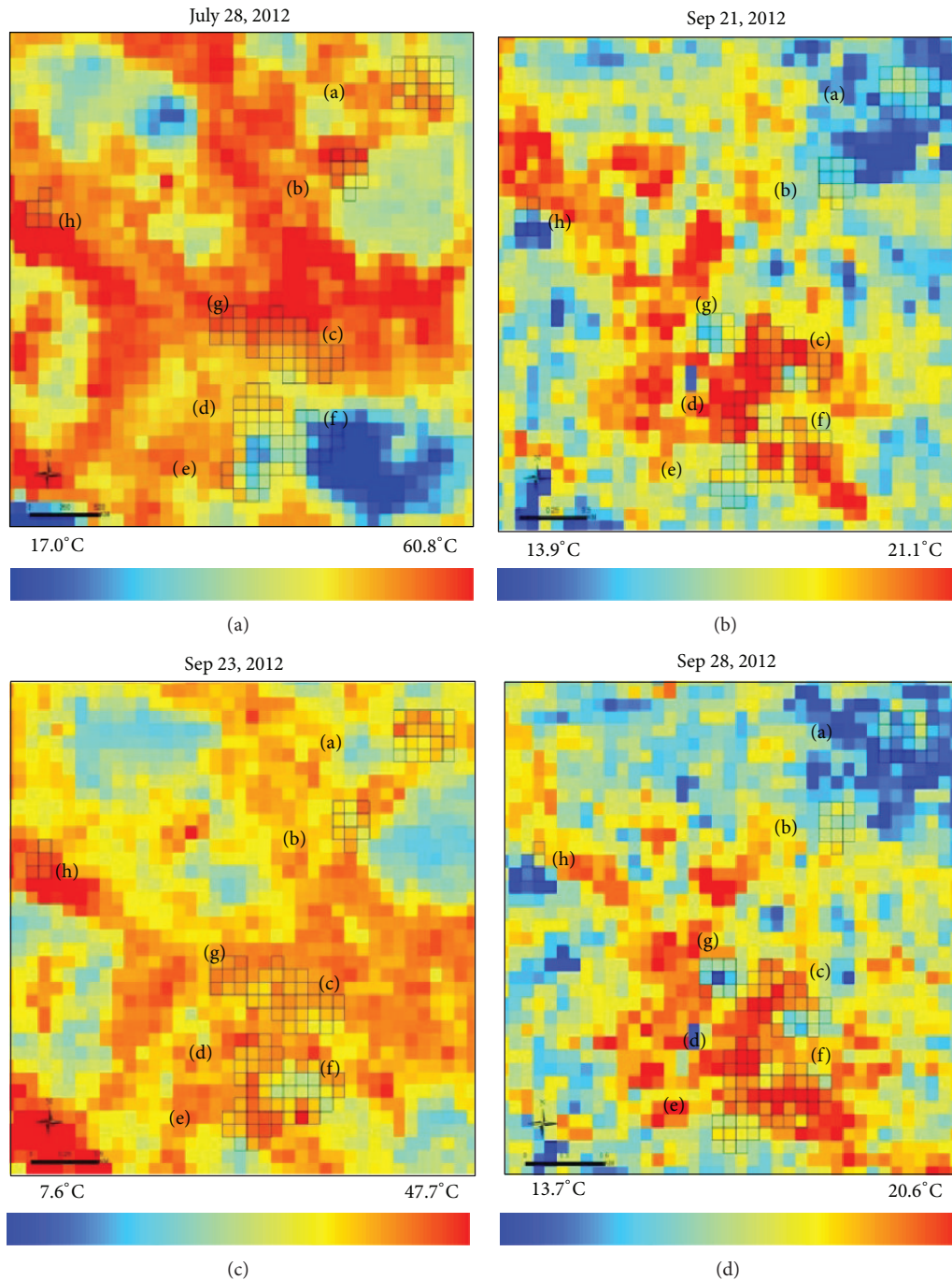


FIGURE 4: Surface temperatures extracted from ASTER images. (a) University campus, (b) urban park, (c) low-rise apartments, (d) commercial area, (e) high-rise apartments, (f) single residential, (g) lawn square, and (h) sidewalk brick square.

had the highest surface temperature during daytime (07/28: 51.0°C, 09/23: 38.2°C), and this was also demonstrated in the ASTER image. Although high-rise apartments had high amounts of asphalt, which typically have a high surface temperature, these areas had relatively low surface temperatures because they were affected by shade (07/28: 32.5%, 09/23: 44.3%) (Table 1). The highest nighttime surface temperatures were measured *in situ* in the commercial area (17.3°C) on September 21 and the sidewalk brick square area (16.9°C)

on September 28. In contrast, lawn squares had the lowest nighttime surface temperatures (09/21: 14.3°C, 09/28: 13.9°C) (Table 3).

3.4. Comparisons of ASTER Image and Field Measured Surface Temperatures. Figure 7 shows a graph of the surface temperature difference between the field-based measurements and the satellite-based measurements for each pixel of the subject sites. Surface temperatures derived from ASTER

TABLE 3: Comparison of mean surface temperatures collected from ASTER images and field measurements at the measurement sites.

	UC	P	LR	CA	SR	HR	HL	HS	
07/28									
Daytime	T_{image} ($^{\circ}\text{C}$)	38.9	41.2	39.9	38.2	37.3	31.9	41.2	44.3
	T_{insitu} ($^{\circ}\text{C}$)	46.5	44.5	47.9	49.8	49.6	46.8	46.7	51.0
	RMSE ($^{\circ}\text{C}$)	8.1	5.4	8.4	11.8	13.4	15.7	6.1	7.9
09/23									
Daytime	T_{image} ($^{\circ}\text{C}$)	30.4	30.4	31.5	32.1	32.2	29.8	32.0	33.2
	T_{insitu} ($^{\circ}\text{C}$)	33.1	34.6	34.7	35.6	36.8	34.3	35.4	38.2
	RMSE ($^{\circ}\text{C}$)	3.2	5.1	3.7	3.8	5.0	4.7	4.4	5.3
09/21									
Nighttime	T_{image} ($^{\circ}\text{C}$)	17.0	17.3	19.0	19.4	17.7	18.7	17.6	17.3
	T_{insitu} ($^{\circ}\text{C}$)	15.3	15.3	16.5	17.3	16.4	16.4	14.3	16.0
	RMSE ($^{\circ}\text{C}$)	1.9	2.3	2.6	3.1	1.6	2.4	3.7	1.9
09/28									
Nighttime	T_{image} ($^{\circ}\text{C}$)	16.5	17.8	18.7	19.0	18.5	19.2	17.3	17.3
	T_{insitu} ($^{\circ}\text{C}$)	15.0	15.5	16.1	16.5	15.8	16.0	13.9	16.9
	RMSE ($^{\circ}\text{C}$)	1.6	2.4	2.7	2.5	2.8	3.3	3.9	1.1

UC: university campus, P: urban park, LR: low-rise apartments, CA: commercial area, SR: single residential, HR: high-rise apartments, and HL: homogenous lawn, HS: homogenous sidewalk brick.

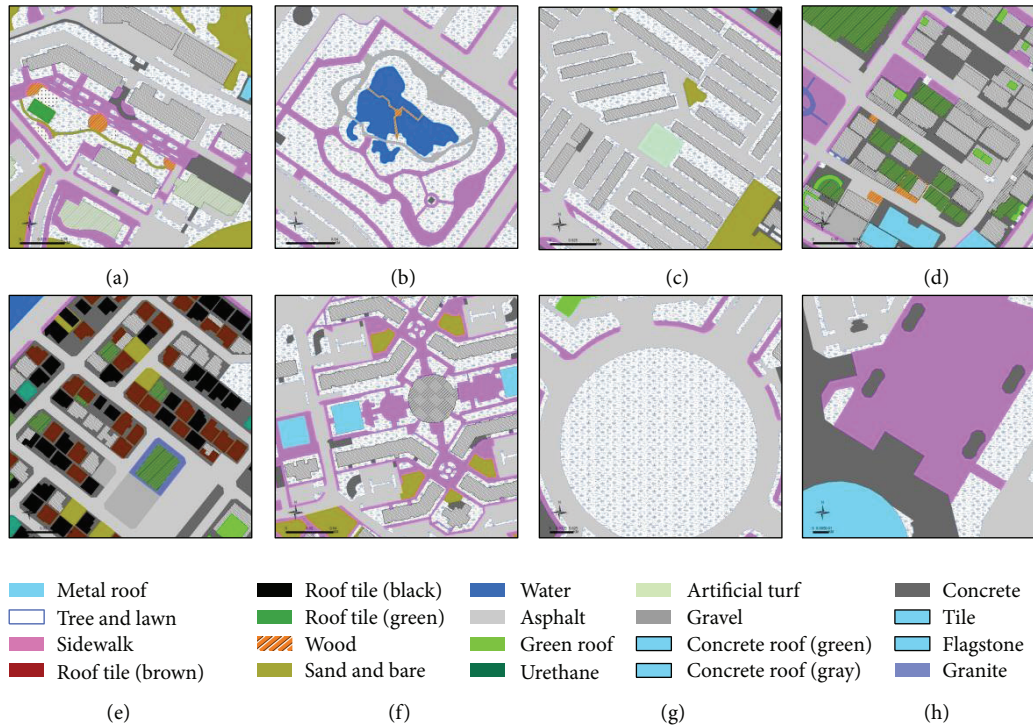


FIGURE 5: Classification of surface fabric for each location. (a) University campus, (b) urban park, (c) low-rise apartments, (d) commercial area, (e) single residential, (f) high-rise apartments, (g) lawn square, and (h) sidewalk brick square.

images differed greatly from those measured onsite (between 20 and 30 $^{\circ}\text{C}$) in the commercial area and parts of the high-rise apartment area on July 28 because of the influence of clouds. Hence, the root mean square error (RMSE) was relatively high in these areas and it amounted to 10.73 $^{\circ}\text{C}$. Satellite

image surface temperatures of the water area in the park were 7.8 $^{\circ}\text{C}$ higher than field measured temperatures. Except for a clouded area, the single residential area showed large differences in temperature; in contrast, adjacent vegetation covered areas showed very little differences in temperature



FIGURE 6: Shaded area analysis results for the high-rise apartments (a) and the commercial area (b).

that only amounted to 0.8°C . In pixels composed of identical fabrics such as grass and sidewalk bricks, the differences were very small and amounted to 0.5°C and 0.4°C , respectively. The park area had some of the lowest differences in temperature according to the RMSE (Table 3).

The RMSE was 2.23°C on September 21. The vegetation area pixel, which had the least difference in the single residential area data from July 28, had the largest difference of 3.9°C on September 21. Pixels composed of identical grass fabric also demonstrated differences more than 5°C , and the differences were the greatest for the data from September 21. Subject areas with small temperature variances included the single residential area (1.6°C), the university campus (1.9°C), and the sidewalk brick square (1.9°C) (Table 3).

Similar patterns were observed on September 23 and July 28. Surface temperatures from the satellite images of water in the park were higher than the field-measured surface temperatures by 1.7°C . In the single residential area, the pixels with vegetation had the least difference (0.1°C). Interestingly, in the homogeneous lawn pixels and the vegetation pixels in the university campus, the surface temperatures from the satellite images were higher than the field measured temperatures. The university campus (3.2°C), low-rise apartment area (3.7°C), and the commercial area (3.8°C) had low RMSEs (Table 3).

On September 28th, similar to the nighttime of September 21st, the homogeneous lawn pixel had the greatest temperature differences range from 5.9°C to 6.4°C . In the single residential area, however, and unlike the data observed on September 21st, other pixels along with the vegetation pixels displayed large temperature differences. Homogeneous sidewalk bricks had the lowest RMSE of 1.1°C , followed by the university campus (1.6°C) (Table 3).

Therefore, as the results of the comparisons described above show, the temperature data derived from satellite images has accuracy problems that vary according to land coverage and land use in the urban area. First, higher building densities are associated with larger differences between satellite-based and field-based temperature measurements. According to an earlier study by Hartz et al. [36], areas with greater population have greater temperature differences between ASTER image measurements and field measurements of surface temperatures. Barring et al. [51] and Eliasson [2] discovered that more densely built up areas had greater

surface temperature differences of about $4\sim 8^{\circ}\text{C}$. Voogt and Oke [16] speculated that the limited horizontal surface view from ASTER was the cause of the discrepancy. Therefore, in a spatial structure with high density characteristics, the amount of radiation energy from the earth sensed by the satellite may be misjudged because of the limited horizontal surface view. For example, during the night denser areas (e.g., commercial areas, low-rise apartments, and high-rise apartments) had greater differences in temperature between satellite and field measurement data. This is believed to be because in areas packed with buildings, the radiation energy released from the earth into the atmosphere is blocked and aggregated in the earth [18, 50]; and because satellites cannot sense this, it causes differences. Moreover, denser areas had greater differences in surface temperatures for the satellite imagery between the walls of the buildings, and not the temperature of the surface, and field measurements due to the off-nadir angle (ASTER = 22.5°) of the satellite image. Furthermore, there may be effects on the emissivity values used to extract the surface temperatures from the satellite images. According to Han et al. [52], "a 1% change in emissivity can change the surface temperature up to 2 K." Therefore, because satellite images have low spatial resolutions, they are limited in their ability to analyze exact and detailed emissivity values in urban areas composed of various surface fabrics, and the resulting data will show different surface temperatures from field measurements.

4. Conclusions

In this paper, we compared surface temperatures measured onsite and via ASTER images during both the day and the night to validate the accuracy of surface temperature satellite imagery used frequently in UHI studies. The results indicated that surface temperatures from field measurements were higher than those derived from satellite images during the day, while the opposite pattern was observed during the night, except for in a few locations. Despite the influence of clouds on the images from July 28, the temperature difference between ASTER images and field measurements was smaller during the night than during the day. While surface temperature differences were small for pixels containing trees and grass during the day, at night the artificial fabrics showed a lesser difference.

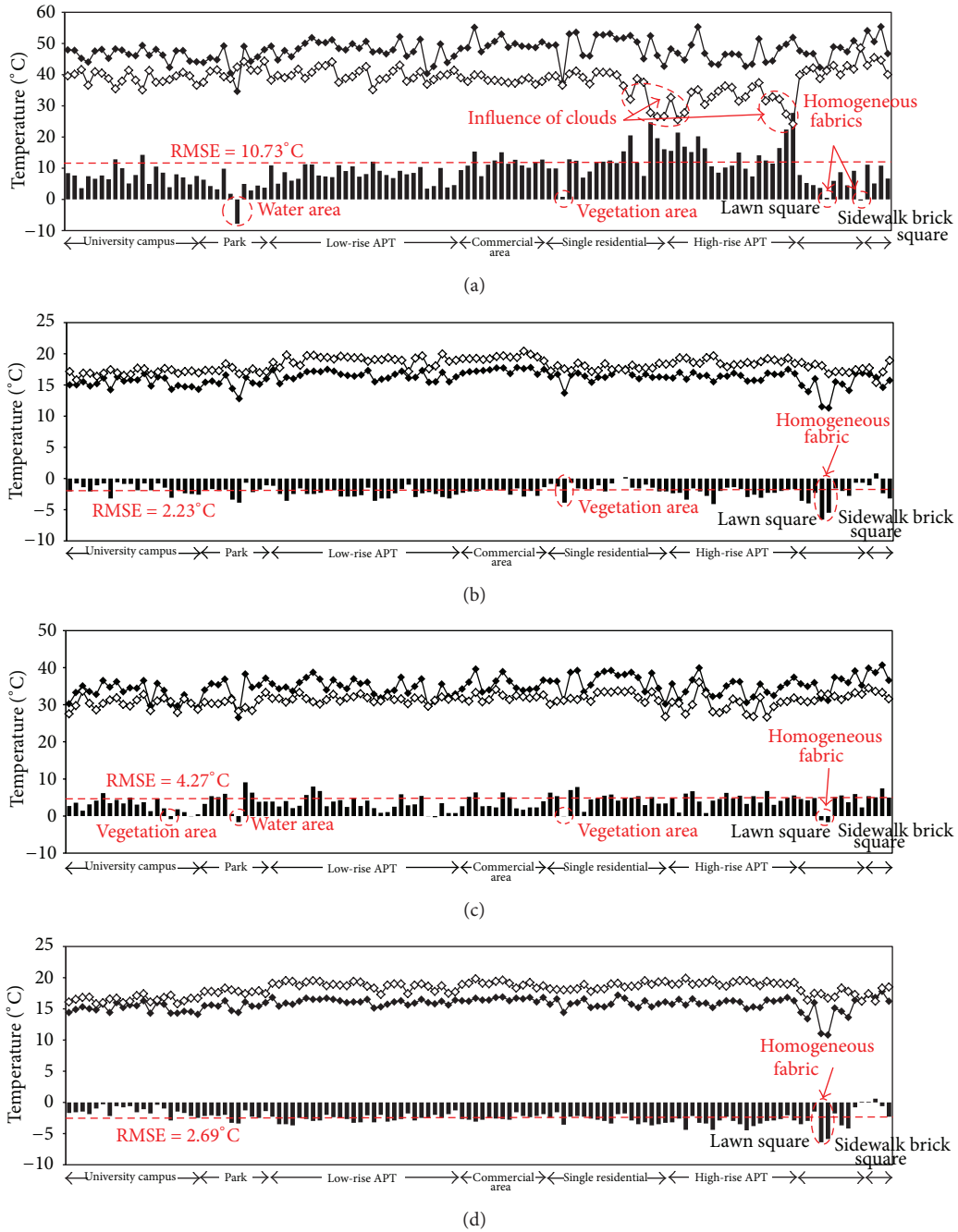


FIGURE 7: Analysis results for pixel-based surface temperatures collected by ASTER images and field measurements. (a) 07/28, (b) 09/21, (c) 09/23, and (d) 09/28 (◇: ASTER images, ◆: field measurements, ■: field measurements, ASTER images, and dashed lines: RMSE).

This study confirmed problems with the accuracy of surface temperature data derived from satellite images, and these problems vary according to the time of day and the presence of different urban area characteristics. In particular, areas of high density displayed greater discrepancies in temperature compared to open areas. The difference in temperature between field-based and satellite-based measurements was also affected by whether the surface fabric was artificial or not. Overall, differences between infrared satellite image surface temperature data and onsite measurements may be

caused by the off-nadir angle of the satellite image, the limited horizontal surface view of earth's surface, the low spatial resolution of the satellite image, and the application of emissivity values that do not consider the complex spatial characteristics of urban areas. To improve the accuracy of surface temperatures extracted from infrared satellite imagery, we propose a revised model whereby temperature data is obtained from ASTER and emissivity values for various land covers that are extracted based on *in situ* measurements.

In the future, we will aim to use the data collected in this study to develop a way to improve the accuracy of satellite derived surface temperature data in urban areas. Also, we plan on further assessing the relationship between radiant energy and surface temperatures according to variations in the spatial characteristics of urban areas. Such studies may help to improve the usability of satellite image data in urban areas and likely will also aid urban planners, developers, and researchers in mitigating the adverse effects of heat islands.

Conflict of Interests

The authors declare that there is no conflict of interests regarding the publication of this paper.

Acknowledgments

This research was supported by Korea Aerospace Research Institute (KARI) (no. 2012-0091-0000) and Basic Science Research Program through the National Research Foundation of Korea (NRF) funded by the Ministry of Education, Science and Technology (no. 2013-0095-0000).

References

- [1] T. R. Oke, *Boundary Layer Climates*, Methuen, London, UK, 2nd edition, 1987.
- [2] I. Eliasson, "Urban nocturnal temperatures, street geometry and land use," *Atmospheric Environment*, vol. 30, no. 3, pp. 379–392, 1996.
- [3] K. G. Lee and W. H. Hong, "A study on the urban heat environment pattern analysis and alleviation plan," *The Architectural Institute of Korea*, vol. 24, no. 9, 2008.
- [4] H. Takebayashi and M. Moriyama, "Study on the urban heat island mitigation effect achieved by converting to grass-covered parking," *Solar Energy*, vol. 83, no. 8, pp. 1211–1223, 2009.
- [5] S. L. Harlan, A. J. Brazel, L. Prasad, W. L. Stefanov, and L. Larsen, "Neighborhood microclimates and vulnerability to heat stress," *Social Science and Medicine*, vol. 63, no. 11, pp. 2847–2863, 2006.
- [6] R. S. Kovats and S. Hajat, "Heat stress and public health: a critical review," *Annual Review of Public Health*, vol. 29, pp. 41–55, 2008.
- [7] R. Laforteza, G. Carrus, G. Sanesi, and C. Davies, "Benefits and well-being perceived by people visiting green spaces in periods of heat stress," *Urban Forestry and Urban Greening*, vol. 8, no. 2, pp. 97–108, 2009.
- [8] E. Ng, L. Chen, Y. Wang, and C. Yuan, "A study on the cooling effects of greening in a high-density city: an experience from Hong Kong," *Building and Environment*, vol. 47, no. 1, pp. 256–271, 2012.
- [9] S. H. Baek, A. Shimizu, H. Y. Kim, and E. H. Jung, "Evaluation of thermal environment improvement effect from public design improvement project on the urban street space," *Journal of the Environmental Sciences*, vol. 20, no. 9, pp. 1105–1114, 2011.
- [10] E. L. Krüger, F. O. Minella, and F. Rasia, "Impact of urban geometry on outdoor thermal comfort and air quality from field measurements in Curitiba, Brazil," *Building and Environment*, vol. 46, no. 3, pp. 621–634, 2011.
- [11] S. Knapp, I. Kühn, O. Schweiger, and S. Klotz, "Challenging urban species diversity: contrasting phylogenetic patterns across plant functional groups in Germany," *Ecology Letters*, vol. 11, no. 10, pp. 1054–1064, 2008.
- [12] G. Luber and M. McGeehin, "Climate change and extreme heat events," *American Journal of Preventive Medicine*, vol. 35, no. 5, pp. 429–435, 2008.
- [13] D. E. Bowler, L. Buyung-Ali, T. M. Knight, and A. S. Pullin, "Urban greening to cool towns and cities: a systematic review of the empirical evidence," *Landscape and Urban Planning*, vol. 97, no. 3, pp. 147–155, 2010.
- [14] B. G. Song and K. H. Park, "The classification of spatial patterns considering formation parameters of urban climate: the case of Changwon city, South Korea," *Journal of Environmental Impact Assessment*, vol. 20, no. 3, pp. 299–311, 2011.
- [15] D. A. Quattrochi and J. C. Luvall, "Thermal infrared remote sensing for analysis of landscape ecological processes: methods and applications," *Landscape Ecology*, vol. 14, no. 6, pp. 577–598, 1999.
- [16] J. A. Voogt and T. R. Oke, "Thermal remote sensing of urban climates," *Remote Sensing of Environment*, vol. 86, no. 3, pp. 370–384, 2003.
- [17] Q. Weng, D. Lu, and J. Schubring, "Estimation of land surface temperature-vegetation abundance relationship for urban heat island studies," *Remote Sensing of Environment*, vol. 89, no. 4, pp. 467–483, 2004.
- [18] L. Klok, S. Zwart, H. Verhagen, and E. Mauri, "The surface heat island of Rotterdam and its relationship with urban surface characteristics," *Resources, Conservation and Recycling*, vol. 64, pp. 23–29, 2012.
- [19] J. E. Nichol, "A GIS-based approach to microclimate monitoring in Singapore's high-rise housing estates," *Photogrammetric Engineering & Remote Sensing*, vol. 60, no. 10, pp. 1225–1232, 1994.
- [20] J. A. Voogt and T. R. Oke, "Effects of urban surface geometry on remotely-sensed surface temperature," *International Journal of Remote Sensing*, vol. 19, no. 5, pp. 895–920, 1998.
- [21] Q. Weng, H. Liu, and D. Lu, "Assessing the effects of land use and land cover patterns on thermal conditions using landscape metrics in city of Indianapolis, United States," *Urban Ecosystems*, vol. 10, no. 2, pp. 203–219, 2007.
- [22] H. Liu and Q. Weng, "Seasonal variations in the relationship between landscape pattern and land surface temperature in Indianapolis, USA," *Environmental Monitoring and Assessment*, vol. 144, no. 1–3, pp. 199–219, 2008.
- [23] Q. Weng and D. Lu, "A sub-pixel analysis of urbanization effect on land surface temperature and its interplay with impervious surface and vegetation coverage in Indianapolis, United States," *International Journal of Applied Earth Observation and Geoinformation*, vol. 10, no. 1, pp. 68–83, 2008.
- [24] T. N. Carlson, J. K. Dodd, S. G. Benjamin, and J. N. Cooper, "Satellite estimation of the surface energy balance, moisture availability and thermal inertia," *Journal of Applied Meteorology*, vol. 20, no. 1, pp. 67–87, 1981.
- [25] X. Zhang, Y. Aono, and N. Monji, "Spatial variability of urban surface heat fluxes estimated from Landsat TM data under summer and winter conditions," *Journal of Agricultural Meteorology*, vol. 54, no. 1, pp. 1–11, 1998.
- [26] S. Kato and Y. Yamaguchi, "Analysis of urban heat-island effect using ASTER and ETM+ Data: separation of anthropogenic heat discharge and natural heat radiation from sensible heat flux," *Remote Sensing of Environment*, vol. 99, no. 1–2, pp. 44–54, 2005.

- [27] A. Buyantuyev and J. Wu, "Urban heat islands and landscape heterogeneity: linking spatiotemporal variations in surface temperatures to land-cover and socioeconomic patterns," *Landscape Ecology*, vol. 25, no. 1, pp. 17–33, 2010.
- [28] J. Li, C. Song, L. Cao, F. Zhu, X. Meng, and J. Wu, "Impacts of landscape structure on surface urban heat islands: a case study of Shanghai, China," *Remote Sensing of Environment*, vol. 115, no. 12, pp. 3249–3263, 2011.
- [29] G. Fu, Z. Shen, P. Shi, Y. Zhang, and J. Wu, "Estimating air temperature of an alpine meadow on the Northern Tibetan Plateau using MODIS land surface temperature," *Acta Ecologica Sinica*, vol. 31, pp. 8–13, 2011.
- [30] A. Benali, A. C. Carvalho, J. P. Nunes, N. Carvalhais, and A. Santos, "Estimating air temperature in Portugal using MODIS LST data," *Remote Sensing of Environment*, vol. 124, pp. 108–121, 2012.
- [31] A. Chudnovsky, E. Ben-Dor, and H. Saaroni, "Diurnal thermal behavior of selected urban objects using remote sensing measurements," *Energy and Buildings*, vol. 36, no. 11, pp. 1063–1074, 2004.
- [32] Q. Weng, "Thermal infrared remote sensing for urban climate and environmental studies: methods, applications, and trends," *ISPRS Journal of Photogrammetry and Remote Sensing*, vol. 64, no. 4, pp. 335–344, 2009.
- [33] C. Mihalcea, B. W. Brock, G. Diolaiuti et al., "Using ASTER satellite and ground-based surface temperature measurements to derive supraglacial debris cover and thickness patterns on Miage Glacier (Mont Blanc Massif, Italy)," *Cold Regions Science and Technology*, vol. 52, no. 3, pp. 341–354, 2008.
- [34] G. Rigo, E. Parlow, and D. Oesch, "Validation of satellite observed thermal emission with in-situ measurements over an urban surface," *Remote Sensing of Environment*, vol. 104, no. 2, pp. 201–210, 2006.
- [35] J. E. Nichol, W. Y. Fung, K.-S. Lam, and M. S. Wong, "Urban heat island diagnosis using ASTER satellite images and 'in situ' air temperature," *Atmospheric Research*, vol. 94, no. 2, pp. 276–284, 2009.
- [36] D. A. Hartz, L. Prashad, B. C. Hedquist, J. Golden, and A. J. Brazel, "Linking satellite images and hand-held infrared thermography to observed neighborhood climate conditions," *Remote Sensing of Environment*, vol. 104, no. 2, pp. 190–200, 2006.
- [37] Changwon city hall homepage, <http://www.changwon.or.kr>.
- [38] B. G. Song and K. H. Park, "An analysis of cold air generation area considering climate-ecological function-focus on Chagnwon-si, Gyeongsangnam-do," *Journal of the Korean Association of Geographic Information Studies*, vol. 13, no. 1, pp. 114–127, 2010.
- [39] S. Kato and Y. Yamaguchi, "Estimation of storage heat flux in an urban area using ASTER data," *Remote Sensing of Environment*, vol. 110, no. 1, pp. 1–17, 2007.
- [40] A. R. Gillespie, S. Rokugawa, S. J. Hook, T. Mansunaga, and A. B. Kahle, "Temperature/Emissivity Separation Algorithm Theoretical Basis Document, Version 2.4," NASA contract NAS5-31372, Washington, DC, USA, 1999.
- [41] Changwon-si, "The construction of Changwon-si environmental atlas and GIS DB (1st)," Changwon-si Research Report, Changwon, Republic of Korea, 2009.
- [42] S. Kato, T. Matsunaga, and Y. Yamaguchi, "Influence of shade on surface temperature in an urban estimated by ASTER data," *International Archives of the Photogrammetry, Remote Sensing and Spatial Information Science*, vol. 38, pp. 925–929, 2010.
- [43] K.-S. Cheng, Y.-F. Su, F.-T. Kuo, W.-C. Hung, and J.-L. Chiang, "Assessing the effect of landcover changes on air temperature using remote sensing images-A pilot study in northern Taiwan," *Landscape and Urban Planning*, vol. 85, no. 2, pp. 85–96, 2008.
- [44] D. E. Sabol Jr., A. R. Gillespie, E. Abbott, and G. Yamada, "Field validation of the ASTER Temperature-Emissivity Separation algorithm," *Remote Sensing of Environment*, vol. 113, no. 11, pp. 2328–2344, 2009.
- [45] J. A. Sobrino, R. Oltra-Carrió, J. C. Jiménez-Muñoz et al., "Emissivity mapping over urban areas using a classification-based approach: application to the Dual-use European Security IR Experiment (DESIREX)," *International Journal of Applied Earth Observation and Geoinformation*, vol. 18, pp. 141–147, 2012.
- [46] E. Valor and V. Caselles, "Mapping land surface emissivity from NDVI: application to European, African, and South American areas," *Remote Sensing of Environment*, vol. 57, no. 3, pp. 167–184, 1996.
- [47] V. Caselles, C. Coll, E. Valor, and E. Rubio, "Mapping land surface emissivity using AVHRR data application to La Mancha, Spain," *Remote Sensing Reviews*, vol. 12, no. 3-4, pp. 311–333, 1995.
- [48] S. P. Arya, *Introduction to Micrometeorology*, Academic Press, 2nd edition, 2003.
- [49] B. G. Song, *Development of integrated spatial environmental assessment and planning methods for improving the urban climate and air quality [M.S. thesis]*, Changwon National University, Changwon, Republic of Korea, 2011.
- [50] E. Erell, D. Pearlmutter, and T. Williamson, *Urban Microclimate: Designing the Spaces Between Buildings*, Earthscan, Washington, DC, USA, 2012.
- [51] L. Barring, J. O. Mattsson, and S. Lindqvist, "Canyon geometry, street temperatures and urban heat island in Malmo, Sweden," *Journal of Climatology*, vol. 5, no. 4, pp. 433–444, 1985.
- [52] K.-S. Han, A. A. Viau, and F. Anctil, "An analysis of GOES and NOAA derived land surface temperatures estimated over a boreal forest," *International Journal of Remote Sensing*, vol. 25, no. 21, pp. 4761–4780, 2004.

Review Article

Impacts of Two Types of El Niño and La Niña Events on Typhoon Activity

Po-Chun Hsu, Chung-Ru Ho, Shin-Jye Liang, and Nan-Jung Kuo

Department of Marine Environmental Informatics, National Taiwan Ocean University, Keelung 20224, Taiwan

Correspondence should be addressed to Chung-Ru Ho; b0211@mail.ntou.edu.tw

Received 6 September 2013; Revised 8 December 2013; Accepted 8 December 2013

Academic Editor: Yuriy Kuleshov

Copyright © 2013 Po-Chun Hsu et al. This is an open access article distributed under the Creative Commons Attribution License, which permits unrestricted use, distribution, and reproduction in any medium, provided the original work is properly cited.

The HadISST (Hadley Centre Sea Ice and Sea Surface Temperature) dataset is used to define the years of El Niño, El Niño Modoki, and La Niña events and to find out the impacts of these events on typhoon activity. The results show that the formation positions of typhoon are farther eastward moving in El Niño years than in La Niña years and much further eastward in El Niño Modoki years. The lifetime and the distance of movement are longer, and the intensity of typhoons is stronger in El Niño and in El Niño Modoki years than in La Niña years. The Accumulated Cyclone Energy of typhoon is highly correlated with the Oceanic Niño Index with a correlation coefficient of 0.79. We also find that the typhoons anomalously decrease during El Niño years but increase during El Niño Modoki years. Besides, there are two types of El Niño Modoki, I and II. The intensity of typhoon in El Niño Modoki I years is stronger than in El Niño Modoki II years. Furthermore, the centroid position of the Western Pacific Warm Pool is strongly related to the area of typhoon formation with a correlation coefficient of 0.95.

1. Introduction

Recent studies have found that there are two types of El Niño in the tropical Pacific, namely: Eastern-Pacific El Niño (EP-El Niño) and Central-Pacific El Niño (CP-El Niño) [1, 2]. The EP-El Niño is the canonical El Niño; a band of anomalous warm ocean water occurs in the eastern tropical Pacific. The CP-El Niño is also called El Niño Modoki, which is the band of anomalous warm ocean water occurring in the central equatorial Pacific. In this study, to avoid the confusion of the nomenclature used, hereafter the Eastern-Pacific El Niño is named as El Niño and the Central-Pacific El Niño is named as El Niño Modoki. The occurrences of anomalous warm water at different regions may cause different changes in air pressure, sea surface height, precipitation, and wind field [3–7]. Yu and Kao [8] and Kao and Yu [9] pointed out that the generation mechanism of the El Niño tied to thermocline variations but the El Niño Modoki may be affected significantly by atmospheric forcing than by basin-wide thermocline variations. Changes of oceanic environment in El Niño and La Niña events may alter the formation and intensity of a typhoon because warmer oceanic environment is more

suitable for its formation and intensity increase [10–16]. Besides the influence of El Niño and La Niña events, Wang et al. [17] showed that different impacts of El Niño and El Niño Modoki events may also change the formation locations, durations, and intensities of tropical cyclones. They indicated that tropical cyclone tends to be more intense in El Niño years than in El Niño Modoki years. Furthermore, according to the rainfall anomaly patterns in southern China, C. Wang and X. Wang [18] indicated that there are two groups of El Niño Modoki, I and II. Different groups are associated with different atmospheric circulation patterns in the western North Pacific and therefore affect the typhoon tracks in the western North Pacific. However, the typhoon tracks, the effects of other characteristics of typhoons, such as the formation position, lifetime, and range of movement, and moving speed are still not clear. To statistically investigate the characteristics of typhoons in these abnormal events and their relationships with changes of the western Pacific warm pool (WPWP), we conduct this study using the Hadley Centre Sea Ice and Sea Surface Temperature (HadISST) dataset and the typhoon datasets from the Japan Meteorological Agency (JMA) and the Joint Typhoon Warning Center (JTWC).

2. Data and Methods

The Oceanic Niño Index (ONI) provided by the Climate Prediction Center in the National Oceanic and Atmospheric Administration (NOAA) is used to define El Niño and La Niña events. The anomalous ONI value of five consecutive months at or above +0.5 is defined as an El Niño event and at or below -0.5 is defined as a La Niña event. The El Niño Modoki Index (EMI) and the second mode of the empirical orthogonal functions (EOF) resulting from tropical Pacific sea surface temperature anomaly (SSTA) data are used to identify the El Niño Modoki pattern. The SSTA data is derived from HadISST, which is a monthly dataset with a spatial resolution of $1^\circ \times 1^\circ$. The El Niño Modoki Index (EMI) is defined as

$$\text{EMI} = [\text{SSTA}]_A - 0.5 \times [\text{SSTA}]_B - 0.5 \times [\text{SSTA}]_C, \quad (1)$$

where the brackets with a subscript represent the area-averaged SSTA over the central Pacific region A (10°S – 10°N , 165°E – 140°W), the eastern Pacific region B (15°S – 5°N , 70°W – 110°W), and the western Pacific region C (10°S – 20°N , 125°E – 145°E), respectively.

The area and sea surface temperature (SST) of WPWP might be affected by El Niño, El Niño Modoki, and La Niña events. To find out the changes of WPWP with typhoon characteristics during these events, the study area is limited to 40.5°N – 30.5°S and 120.5°E – 119.5°W . The area within the 28°C isotherm of SST is defined as the area of WPWP. It can be calculated by [19]

$$A = \sum_{i=1}^n \cos \phi_i \times (111.319 \text{ km})^2, \quad (2)$$

where A is the area of WPWP, ϕ_i is the latitude of the pixel within the WPWP, $(111.319 \text{ km})^2$ is the area of each 1° grid, and n is the total number of pixels in the WPWP. The centroid of the WPWP is then defined as [20]

$$\bar{x} = \sum_{i=1}^n \frac{x_i}{n}, \quad \bar{y} = \sum_{i=1}^n \frac{y_i}{n}, \quad (3)$$

where x_i is the zonal position of a pixel and y_i is the meridional position of a pixel within the WPWP.

Typhoon data is obtained from JMA and JTWC. The contents of both datasets include longitude, latitude, lifetime, minimum pressure and maximum wind, length of movement, average moving speed, and range of movement of a typhoon. Typhoon grading intensity standards with reference to the JMA are according to the definition of National Hurricane Center. The Accumulated Cyclone Energy (ACE) formula is used to identify the intensity of a typhoon and is defined as [21]:

$$\text{ACE} = 10^{-4} \sum_{i=1}^N \sum_{j=1}^T V_{ij}^2, \quad (4)$$

where N is the number of typhoon in a year of each event, T is the total number of 6-hourly estimate in a typhoon, and V is the 6-hourly maximum sustained wind speed in knot

(kt). The ACE index is widely used by NOAA and recent studies [22–26]. It is a wind energy index, a combination of the number of typhoon, the existence time of a typhoon, and the intensing of a typhoon at each observing time.

3. Results

3.1. El Niño, El Niño Modoki, and La Niña. The years of El Niño and La Niña in the period of 1950–2012 are defined by ONI. We have identified 19 El Niño events and 21 La Niña events during the data span. In the El Niño years, warm water moves from west to east with Kelvin waves in the tropical Pacific and replaces the cold surface water of the Humboldt Current. Extensive Pacific warming and the reduction in easterly trade winds limit upwelling of cold water in the equatorial eastern Pacific. The La Niña year is the opposite of the El Niño year; SST across the eastern and central equatorial Pacific is lower than normal. The El Niño Modoki has its warm SST anomaly in the 10°S – 10°N , 165°E – 140°W . We applied the empirical orthogonal function (EOF) analysis to the tropical Pacific SST to identify modes of variability relevant to the El Niño Modoki pattern and identified El Niño Modoki events by EMI and the EOF results. Four patterns of SSTA in the equatorial Pacific are shown in Figure 1. From 1977 to 2012, the El Niño Modoki events occurred in eight years. The EOF1 pattern counts about 50% of the tropical Pacific SST variability. Comparing the time series of its principal component with the normalized ONI, the correlation coefficient is up to 0.94. The EOF2 explains 12% of the tropical Pacific SST variability and shows the El Niño Modoki pattern in the equatorial Pacific. The warmest SST occurs in the central Pacific, flanked by colder water to the west and east. The correlation coefficient between EMI and the second principle component is 0.84.

Previous study [18] shows that there are two groups of El Niño Modoki. Here we use the definitions of ONI and EMI and find the two types of El Niño Modoki, I and II. For El Niño Modoki I, it is the year of El Niño Modoki defined by EMI and is also the year of an El Niño year defined by ONI. For El Niño Modoki II, it is the year of El Niño Modoki defined by EMI but is a normal year defined by ONI. Using this definition, the years of El Niño, El Niño Modoki I, El Niño Modoki II, and La Niña events are listed in Table 1.

3.2. Activity of Western Pacific Typhoon. The best track data of typhoon provided by JMA are used in this study. There are 1594 typhoons found from 1951 to 2011, 492 in El Niño years, 512 in La Niña years, and 590 in normal years. The average of formation position of typhoons is at 15.2°N , 140.6°E in El Niño years, at 17.2°N , 135°E in La Niña years, and at 16.2°N , 136.5°E in normal years. Comparing El Niño and El Niño Modoki years in the period of 1977 to 2011, typhoon began its extended lifecycle at 14.8°N , 140.2°E in El Niño years, at 15.6°N , 141.4°E in El Niño Modoki I years, and at 15.4°N , 141.7°E in El Niño Modoki II years (Figure 2).

Statistical results of formation position, ACE, number, maximum wind speed, lifetime, distance of movement, minimum pressure, moving speed, and moving range of

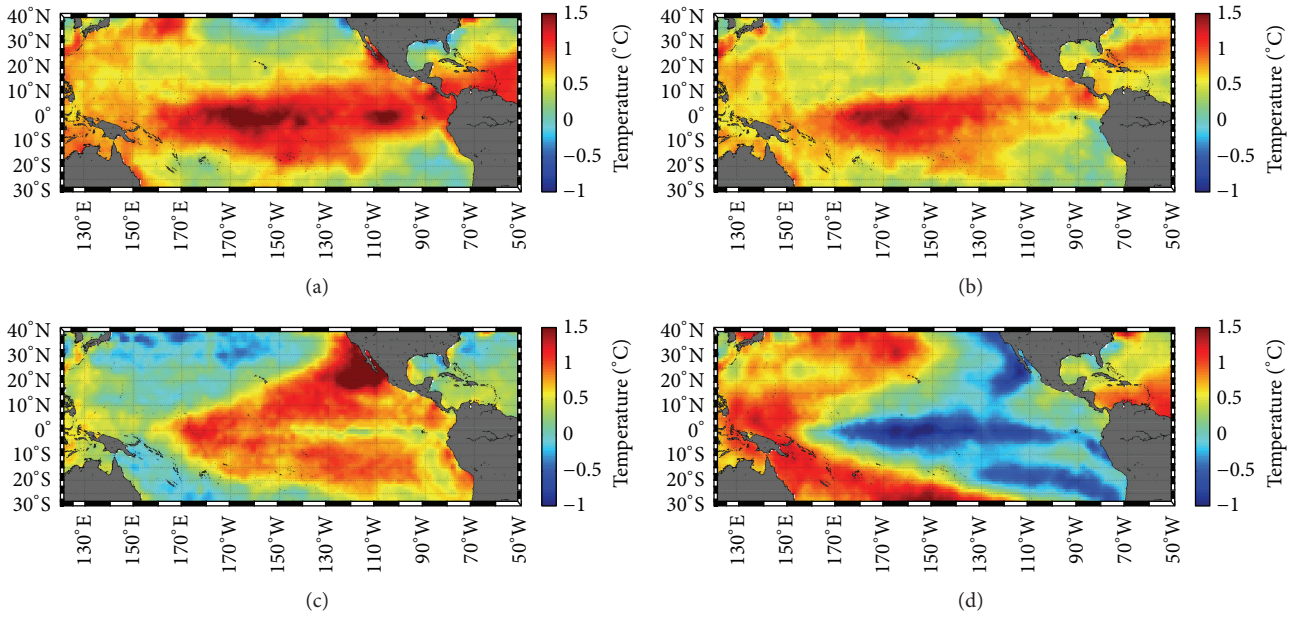


FIGURE 1: SST anomaly of (a) 2009-2010, (b) 2002-2003, (c) 1992-1993, and (d) 2010-2011 as examples for El Niño, El Niño Modoki I, El Niño Modoki II, and La Niña events, respectively.

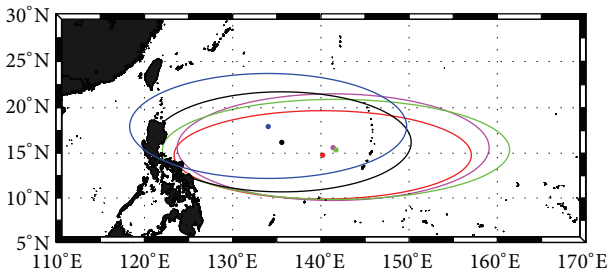


FIGURE 2: The average formation area of typhoon in El Niño years (Red), El Niño Modoki I years (Magenta), El Niño Modoki II years (Green), La Niña years (Blue), and normal years (Black). The semimajor and semiminor axes of an ellipse are the standard deviation of formation positions of typhoons in longitude and latitude, respectively.

typhoon are summarized in Table 2. The lifetime, distance of movement, and movement range of typhoon are larger in El Niño/El Niño Modoki years than those in La Niña years. However, the moving speed is less different between the two events. In the period of 1977 to 2011, the lifetime, distance of movement, and movement range of typhoon are larger in El Niño Modoki I than in El Niño Modoki II years, but the moving speed is almost the same. The average formation position of typhoons is moved further eastward in El Niño years than in La Niña years and much further eastward in El Niño Modoki years. We also make a statistical analysis of typhoon in the northwest Pacific during the period of 1951 to 2011 and find that the typhoon strength and movement in El Niño and La Niña years are similar to the time period 1977–2011. Comparing to earlier relevant works [27, 28], although the definition of El Niño and El Niño Modoki years in these

TABLE 1: The years of El Niño, El Niño Modoki I, El Niño Modoki II, and La Niña events from 1950 to 2012.

Event	Year (from July to June of next year)
El Niño	1951-52, 1957-58, 1963-64, 1965-66, 1968-69, 1969-70, 1972-73, 1976-77, 1982-83, 1987-88, 1997-98, 2006-07, 2009-10
El Niño Modoki I	1977-78, 1986-87, 1991-92, 1994-95, 2002-03, 2004-05
El Niño Modoki II	1990-91, 1992-93
La Niña	1950-51, 1954-57, 1962-63, 1964-65, 1967-68, 1970-72, 1973-76, 1984-85, 1988-89, 1995-96, 1998-01, 2007-08, 2010-12

works is slightly different, the results all indicate that the typhoons anomalously decrease during El Niño years but increase during El Niño Modoki years.

We use ACE to measure overall activity of typhoon during a year. The calculation of average ACE (Unit: 10^4 kt^2) shows 292.1 in El Niño years, 316.1 in El Niño Modoki I years, 306.6 in El Niño Modoki II years, 217.5 in normal years, and 160.9 in La Niña years. This result indicates that the longer distances of typhoon movement and the higher maximum wind speed of typhoon result in larger ACE value. This observation is consistent with the aforementioned statistical results. Figure 3 shows the mean ACE of a year in the five events. Figure 4 is a scatter plot of ACE and ONI with a coefficient of determination (R^2) of 0.6. This clarifies that the formation position and the intensity of typhoon are obviously affected by El Niño, El Niño Modoki, and La Niña events.

The definition of maximum wind speed of typhoons provided by JMA (10 min mean) is different from that of

TABLE 2: The statistic results of typhoon in Niño years, El Niño Modoki I years, El Niño Modoki II years, normal years, and La Niña years from 1977 to 2011.

1977~2011	Formation position of latitude (°N)	Formation position of longitude (°E)	ACE (10^4 kt ²)	Number	Maximum wind speed (kt)	Lifetime (hour)	Distance of movement (km)	Minimum pressure (hPa)	Moving speed (km/hour)	Moving range of longitude (°)	Moving range of latitude (°)
El Niño	14.8 ± 4.9°N	140.2 ± 16.9°E	292.1 ± 57.0	24.2 ± 2.4	75 ± 24	151 ± 80	3008 ± 1639	955 ± 30	20.6 ± 6.3	17.4 ± 11.3	14.1 ± 9.6
El Niño Modoki I	15.6 ± 5.9°N	141.4 ± 17.7°E	316.1 ± 89.7	28.3 ± 4.9	71 ± 23	143 ± 85	2986 ± 1701	960 ± 28	22.0 ± 7.7	16.7 ± 10.5	13.8 ± 9.6
El Niño Modoki II	15.4 ± 5.5°N	141.7 ± 19.7°E	306.6 ± 58.5	30 ± 2	69 ± 22	142 ± 79	2856 ± 1530	961 ± 29	21.0 ± 7.4	15.7 ± 10.4	13.5 ± 9.1
Normal	16.2 ± 5.5°N	135.6 ± 14.7°E	217.5 ± 33.0	26.3 ± 3.4	68 ± 22	125 ± 71	2557 ± 1470	963 ± 27	21.4 ± 8.3	14.9 ± 9.4	12.2 ± 8.7
La Niña	17.9 ± 5.8°N	134.0 ± 15.7°E	160.9 ± 48.2	22.3 ± 5.1	63 ± 22	106 ± 67	2181 ± 1383	969 ± 26	21.4 ± 8.8	12.3 ± 9.5	10.6 ± 7.8

TABLE 3: Percentage of different typhoon categories of each event for JMA and JTWC from 1977 to 2011.

Event/data	JMA			JTWC		
	Tropical storm	Category 1 + 2	Category 3 + 4 + 5	Tropical storm	Category 1 + 2	Category 3 + 4 + 5
El Niño	33.9%	38.0%	28.1%	25.8%	28.3%	45.8%
El Niño Modoki I	41.8%	44.1%	14.1%	32.7%	29.6%	37.7%
El Niño Modoki II	41.7%	45.0%	13.3%	25.9%	39.7%	34.5%
Normal	44.5%	44.5%	11.0%	35.4%	33.3%	31.2%
La Niña	54.7%	36.8%	8.5%	41.5%	27.7%	30.8%

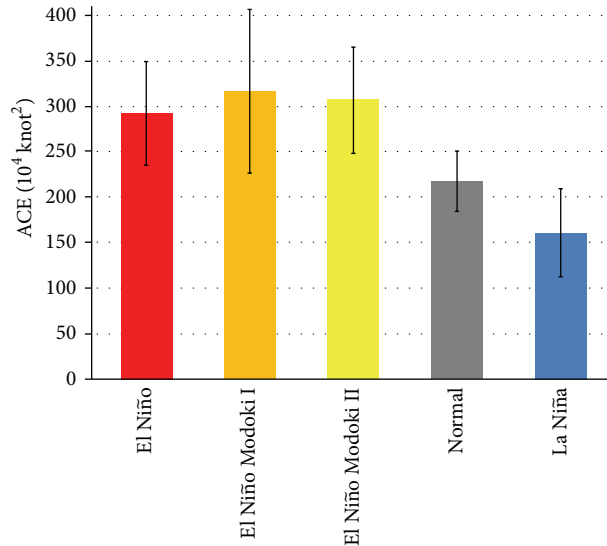


FIGURE 3: The mean of ACE of a year in the five events. The bar represents one standard deviation.

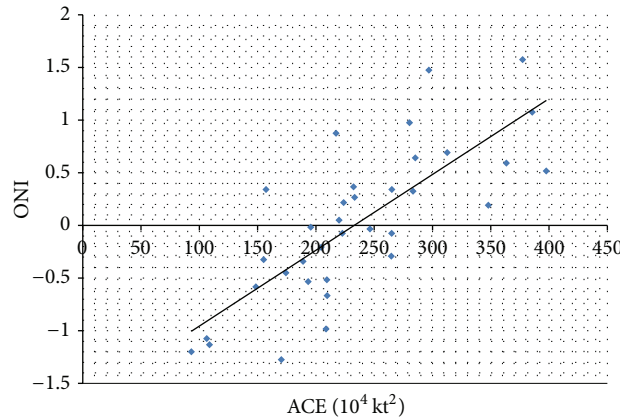


FIGURE 4: Relationship between ACE and ONI ($R^2 = 0.6$).

JTWC (1 min mean). Therefore, the occurrence percentage of typhoon strength from both datasets may be different. A comparison of both datasets from 1977 to 2011 is shown in Table 3. Categories 1 to 5 are classified by the Saffir-Simpson hurricane wind scale. The rating is based on a hurricane’s sustained wind speed. Tropical storm is defined as the maximum sustained winds between 34 and 64 knots, Category 1 is reserved for maximum sustained winds between 64 and 83 knots, Category 2 is 83–96 knots, Category 3 is 96–113 knots, Category 4 is 113–136 knots,

and Category 5 is exceeding 137 knots. Hurricanes reaching Category 3 and higher are considered major hurricanes because of their potential for significant loss of life and damage. Category 1 and 2 storms require preventive measures (<http://www.nhc.noaa.gov/aboutsshws.php>). Therefore, we divided the Category of Saffir-Simpson scale into two parts for analysis, Category 1 + 2 and Category 3 + 4 + 5. The results show that the occurrence frequency of Category 1 + 2 and Category 3 + 4 + 5 is reduced in La Niña years. For strong typhoon cases, that is, Category 3 + 4 + 5, both datasets show

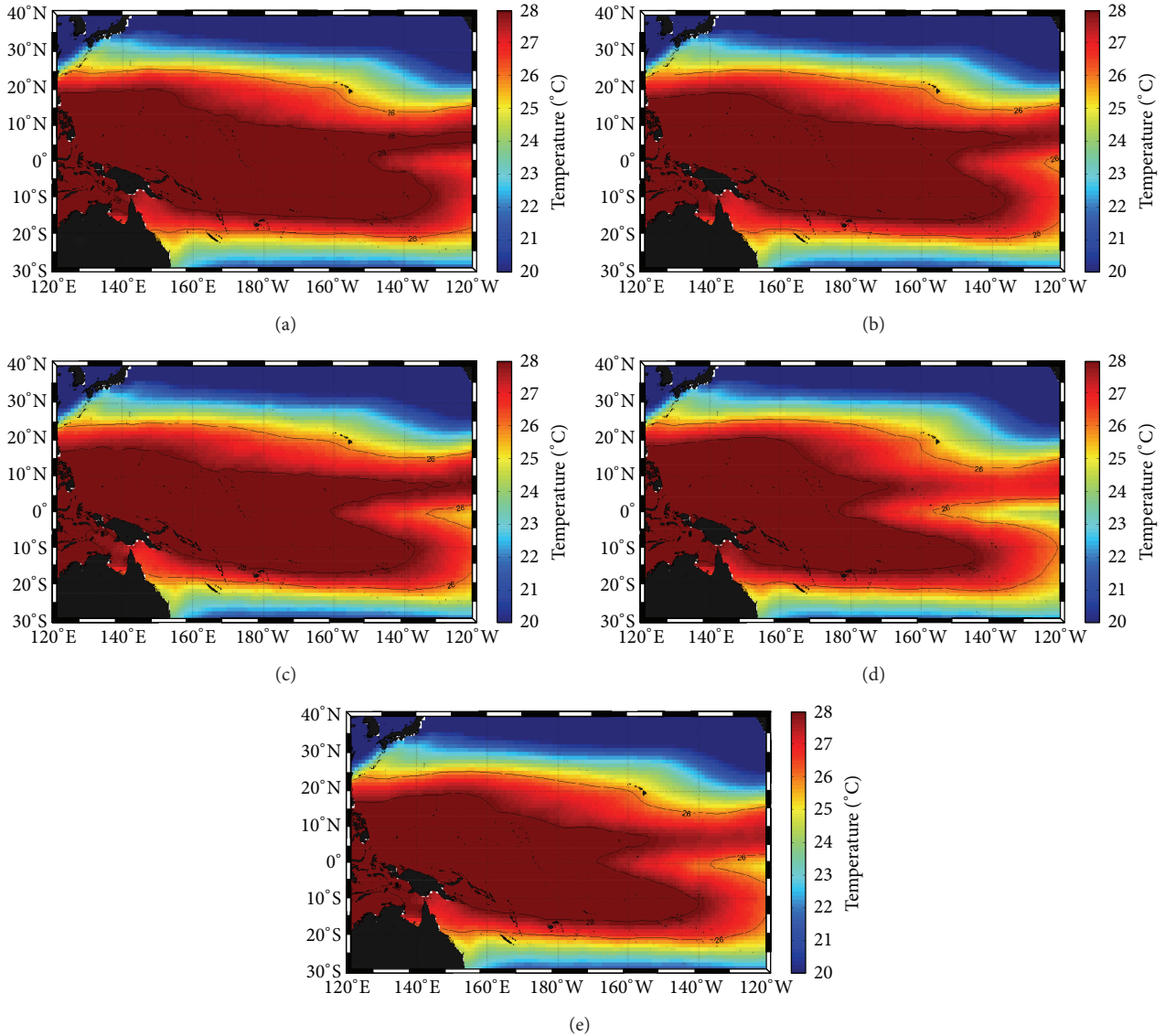


FIGURE 5: The distribution of average SST in (a) El Niño, (b) El Niño Modoki I, (c) El Niño Modoki II, (d) La Niña, and (e) normal years.

that the most occurrence is in El Niño years and then followed by El Niño Modoki I years, El Niño Modoki II years, normal years, and La Niña years, respectively.

3.3. Area and Centroid of Western Pacific Warm Pool. Figure 5 shows the distribution of average SST in El Niño, El Niño Modoki I, El Niño Modoki II, La Niña, and normal years. Compared to normal years, warm water moves from west to the eastern tropical Pacific in El Niño years, moves to the central tropical Pacific in El Niño Modoki years, and shrinks to the western tropical Pacific in La Niña years. Due to the effect of El Niño, El Niño Modoki, and La Niña events on the SST distribution, the WPWP area is also changed in different events. The average area of WPWP is $3.53 \times 10^7 \text{ km}^2$ in El Niño years, $3.43 \times 10^7 \text{ km}^2$ in El Niño Modoki I years, $3.35 \times 10^7 \text{ km}^2$ in El Niño Modoki II years, $3.14 \times 10^7 \text{ km}^2$ in normal years, and $3.16 \times 10^7 \text{ km}^2$ in La Niña years as shown in

Figure 6. Figure 7 reveals the average location of the centroid of WPWP in different events. It is at 0.6°N , 170.1°E in El Niño years, at 0.6°N , 168.3°E in El Niño Modoki I years, at 0.5°N , 169.4°E in El Niño Modoki II years, at 0.9°N , 164.1°E in normal years, and at 0.9°N , 162.3°E in La Niña years. A comparison between the location of the centroid of WPWP and the formation of typhoon in different events is displayed in Figure 8. The correlation coefficient between locations of WPWP centroid and typhoon formation is up to 0.95. This implies that El Niño, El Niño Modoki, and La Niña events indeed affect the formation position of a typhoon.

4. Conclusions

This is a preliminary study on the impacts of El Niño, El Niño Modoki, and La Niña events on the typhoon activity. We identify 19 El Niño events and 21 La Niña events during the period

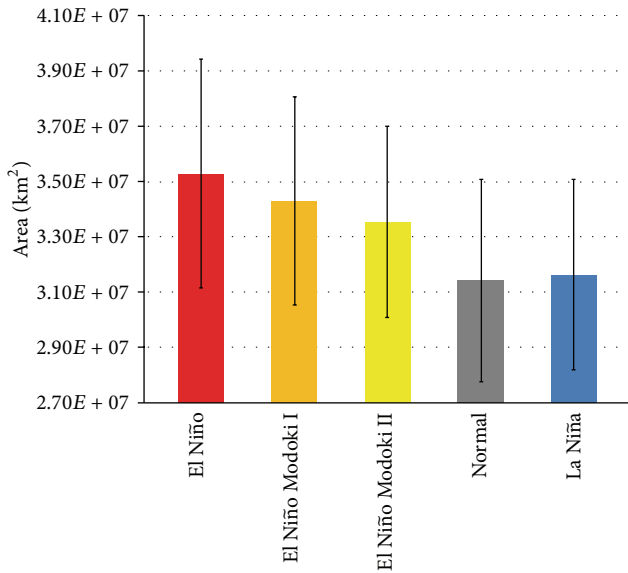


FIGURE 6: The average WPWP area in the five events. The bar represents one standard deviation.

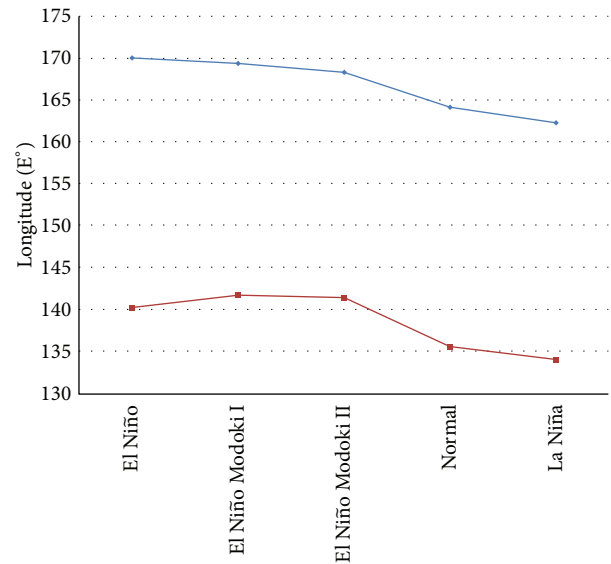


FIGURE 8: The centroid of WPWP (Blue) and the formation position of typhoon (Red) in five events.

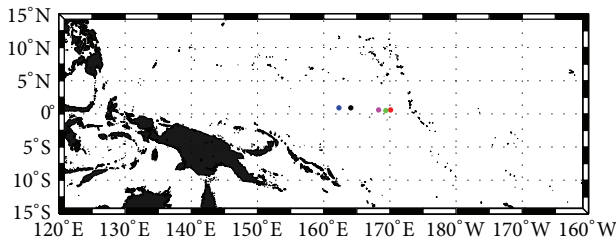


FIGURE 7: The average location of the centroid of WPWP in different events. El Niño (Red), El Niño Modoki I (Magenta), El Niño Modoki II (Green), La Niña (Blue), and the normal (Black), respectively.

of 1950–2012. We also find that there are two types of El Niño Modoki, I and II. The statistical results show that the lifetime, length of movement, and range of movement of typhoons are larger in El Niño years than those in La Niña years. The intensity in El Niño years is relatively strong, but the moving speed is almost the same as that in La Niña years. The average intensity of typhoon in El Niño Modoki I years is stronger than that in El Niño Modoki II years. The formation positions of typhoon are moved further eastward in El Niño years than that in La Niña years and much further eastward in El Niño Modoki years. ACE and ONI is corrected with a correlation coefficient of 0.79. The WPWP area is larger in El Niño and El Niño Modoki years than that in La Niña years. The centroid of the WPWP and the position of the typhoon formation are highly correlated with a correlation coefficient of 0.95.

Acknowledgments

The authors appreciate the Met Office Hadley Centre for Climate Change for providing the HadISST data, as well as the Japan Meteorological Agency and the Joint Typhoon Warning Center for providing typhoon data. Two anonymous

reviewers providing useful comments and suggestions are also grateful. This work was supported by the National Science Council of Taiwan through Grants NSC 98-2611-M-019-017-MY3 and NSC 102-2611-M-019-011.

References

- [1] K. Ashok, S. K. Behera, S. A. Rao, H. Y. Weng, and T. Yamagata, “El Niño Modoki and its possible teleconnection,” *Journal of Geophysical Research C*, vol. 112, no. 11, Article ID C11007, 2007.
- [2] K. Ashok and T. Yamagata, “Climate change: the El Niño with a difference,” *Nature*, vol. 461, no. 7263, pp. 481–484, 2009.
- [3] J. S. Kug, F. F. Jin, and S. I. An, “Two types of El Niño events: cold tongue El Niño and warm pool El Niño,” *Journal of Climate*, vol. 22, no. 6, pp. 1499–1514, 2009.
- [4] J. V. Ratnam, S. K. Behera, Y. Masumoto, K. Takahashi, and T. Yamagata, “Anomalous climatic conditions associated with the El Niño Modoki during boreal winter of 2009,” *Climate Dynamics*, vol. 39, no. 1-2, pp. 227–238, 2012.
- [5] I. Zubiaurre and N. Calvo, “The El Niño-Southern Oscillation (ENSO) Modoki signal in the stratosphere,” *Journal of Geophysical Research D*, vol. 117, no. 4, pp. 4722–4727, 2012.
- [6] S. W. Yeh, J. S. Kug, B. Dewitte, M. H. Kwon, B. P. Kirtman, and F. F. Jin, “El Niño in a changing climate,” *Nature*, vol. 461, pp. 515–515, 2009.
- [7] H. Lopez and B. P. Kirtman, “Westerly wind bursts and the diversity of ENSO in CCSM3 and CSM4,” *Geophysical Research Letters*, vol. 40, no. 17, pp. 4722–4727, 2013.
- [8] J.-Y. Yu and H.-Y. Kao, “Decadal changes of ENSO persistence barrier in SST and ocean heat content indices: 1958-2001,” *Journal of Geophysical Research D*, vol. 112, no. 13, Article ID D13106, 2007.
- [9] H.-Y. Kao and J.-Y. Yu, “Contrasting eastern-Pacific and central-Pacific types of ENSO,” *Journal of Climate*, vol. 22, no. 3, pp. 615–632, 2009.

- [10] H.-M. Kim, P. J. Webster, and J. A. Curry, "Impact of shifting patterns of Pacific Ocean warming on North Atlantic tropical cyclones," *Science*, vol. 325, no. 5936, pp. 77–80, 2009.
- [11] G. H. Chen and R. H. Huang, "Influence of monsoon over the warm pool on interannual variation on tropical cyclone activity over the western North Pacific," *Advances in Atmospheric Sciences*, vol. 25, no. 2, pp. 319–328, 2008.
- [12] X.-H. Yan, C.-R. Ho, Q. Zheng, and V. Klemas, "Temperature and size variabilities of the western Pacific warm pool," *Science*, vol. 258, no. 5088, pp. 1643–1645, 1992.
- [13] X.-H. Yan, Y. He, W. T. Liu, Q. Zheng, and C.-R. Ho, "Centroid motion of the Western Pacific warm pool during three recent El Niño-Southern Oscillation events," *Journal of Physical Oceanography*, vol. 27, no. 5, pp. 837–845, 1997.
- [14] S. Cravatte, T. Delcroix, D. X. Zhang, M. Mcphaden, and J. Leloup, "Observed freshening and warming of the western Pacific Warm Pool," *Climate Dynamics*, vol. 33, no. 4, pp. 565–589, 2009.
- [15] C.-Y. Lin, C.-R. Ho, Q. Zheng, S.-J. Huang, and N.-J. Kuo, "Variability of sea surface temperature and warm pool area in the South China Sea and its relationship to the western Pacific warm pool," *Journal of Oceanography*, vol. 67, no. 6, pp. 719–724, 2011.
- [16] H.-M. Kim, P. J. Webster, and J. A. Curry, "Modulation of North Pacific tropical cyclone activity by three phases of ENSO," *Journal of Climate*, vol. 24, no. 6, pp. 1839–1849, 2011.
- [17] C. Z. Wang, C. X. Li, M. Mu, and W. S. Duan, "Seasonal modulations of different impacts of two types of ENSO events on tropical cyclone activity in the western North Pacific," *Climate Dynamics*, vol. 40, no. 11-12, pp. 2887–2902, 2013.
- [18] C. Wang and X. Wang, "Classifying El Niño Modoki I and II by different impacts on rainfall in Southern China and typhoon tracks," *Journal of Climate*, vol. 26, no. 4, pp. 1322–1338, 2013.
- [19] D. P. Chambers, B. D. Tapley, and R. H. Stewart, "Long-period ocean heat storage rates and basin-scale heat fluxes from TOPEX," *Journal of Geophysical Research*, vol. 102, no. 5, pp. 10525–10533, 1997.
- [20] C.-R. Ho, X.-H. Yan, and Q. Zheng, "Satellite-observations of upper-layer variabilities in the western Pacific warm pool," *Bulletin of the American Meteorological Society*, vol. 76, no. 5, pp. 669–679, 1995.
- [21] G. D. Bell, M. S. Halpert, R. C. Schnell et al., "Climate assessment for 1999," *Bulletin of the American Meteorological Society*, vol. 81, no. 6, pp. S1–S50, 2000.
- [22] H. M. Kim, M. I. Lee, P. J. Webster, D. Kim, and J. H. Yoo, "A physical basis for the probabilistic prediction of the accumulated tropical cyclone kinetic energy in the western North Pacific," *Journal of Climate*, vol. 26, no. 20, pp. 7981–7991, 2013.
- [23] G. Skok, J. Bacmeister, and J. Tribbia, "Analysis of tropical cyclone precipitation using an object-based algorithm," *Journal of Climate*, vol. 26, no. 8, pp. 2563–2579, 2013.
- [24] T. E. Larow, L. Stefanova, D. W. Shin, and S. Cocke, "Seasonal Atlantic tropical cyclone hindcasting/forecasting using two sea surface temperature datasets," *Geophysical Research Letters*, vol. 37, no. 2, Article ID L02804, 2010.
- [25] R. N. Maue, "Recent historically low global tropical cyclone activity," *Geophysical Research Letters*, vol. 38, no. 14, Article ID L14803, 2011.
- [26] S. S. Chand and K. J. E. Walsh, "Modeling seasonal tropical cyclone activity in the Fiji region as a binary classification problem," *Journal of Climate*, vol. 25, no. 14, pp. 5057–5071, 2012.
- [27] P. K. Pradhan, B. Preethi, K. Ashok, R. Krishnan, and A. K. Sahai, "Modoki, Indian Ocean dipole, and western North Pacific typhoons: possible implications for extreme events," *Journal of Geophysical Research D*, vol. 116, no. 18, Article ID D18108, 2011.
- [28] G. Chen and C. Y. Tam, "Different impacts of two kinds of Pacific Ocean warming on tropical cyclone frequency over the western North Pacific," *Geophysical Research Letters*, vol. 37, no. 1, Article ID L01803, 2010.

Research Article

A WebGIS-Based Information System for Monitoring and Warning of Geological Disasters for Lanzhou City, China

Fang Miao and Qi Yuan

Cold and Arid Regions Environmental and Engineering Research Institute, Chinese Academy of Sciences (CAS), Lanzhou 730000, China

Correspondence should be addressed to Qi Yuan; qiyuan@lzb.ac.cn

Received 5 September 2013; Revised 6 November 2013; Accepted 27 November 2013

Academic Editor: Chung-Ru Ho

Copyright © 2013 F. Miao and Q. Yuan. This is an open access article distributed under the Creative Commons Attribution License, which permits unrestricted use, distribution, and reproduction in any medium, provided the original work is properly cited.

Monitoring and warning of geological disasters accurately and in a timely fashion would dramatically mitigate casualties and economic losses. This paper takes Lanzhou city as an example and designs a Web-based system, namely the information system for geological disaster monitoring and warning (ISGDMW). Presented are its framework, key developing technologies, database, and working flow. The information system adopts a Browser/Server (B/S) structure and has three-tier architecture, combining in-situ monitoring instruments, the wireless sensor network, WebGIS techniques and the grey system theory. The framework of the ISGDMW can be divided into three categories: (1) in-situ monitoring system, it aims to monitor geological disaster sites and get state information of geological disaster sites; (2) database, manage in-situ monitoring data, antecedent field investigating data and basic data; (3) analyzing and warning system, analyze in-situ monitoring data, understand the deformation trend of the potential geological disaster, and release disaster warning information to the public. The ISGDMW allow the processes of geological disaster monitoring, in-situ monitoring data analysis, geological disaster warning to be implemented in an efficient and quick way, and can provide scientific suggestions to commanders for quick response to the possibility of geological disaster.

1. Introduction

To mitigate geological disaster, we should depend on both real-time in situ data and quick response to the possibility of geological disaster. WebGIS is the integrated product of geographic information system (GIS) and internet technologies; in WebGIS, the internet technologies are connected with GIS in order to take advantage of their special characteristics, such as easy usability, use of the GIS data such as input, adjustment, manipulation, analysis, and output of geographical information and to bring out related service on the internet. Whereas previous standalone GIS had restricted application capability on the network, the WebGIS makes it possible to retrieve and analyze spatial data through the web. The internet also provides a medium for processing georelated information with no location restrictions [1]. In addition, WebGIS promotes the sharing and synthesis of multisource data and enables widespread sharing of spatial data and geosciences models [2]. Therefore, WebGIS offers a powerful and advanced approach to prevent and mitigate

geological disaster, and it has played a significant role in terms of transmitting catastrophe data, analyzing the disaster condition, and releasing disaster information [3–7]. In situ monitoring data can be used to grasp the deformation trend of the geological disaster; therefore, in situ monitoring instruments (e.g., inclinometers, rain gauges, piezometers, and extensometers) must be playing an important role in the process of geological disaster mitigation [7–10].

In this paper, we comprehensively utilize the advantages of in situ monitoring instruments, the wireless sensor network, and WebGIS techniques in terms of in situ monitoring, transmitting data, disaster analysis, and data management to design a Web-based system, namely, the information system for geological disaster monitoring and warning (ISGDMW). Deformation trends of the landslide and debris flow are analyzed automatically with the grey system method and threshold rainfall, respectively, based on ISGDMW. ISGDMW is a novel platform and is designed to improve practical efficiency of geological disaster mitigation in Lanzhou city.

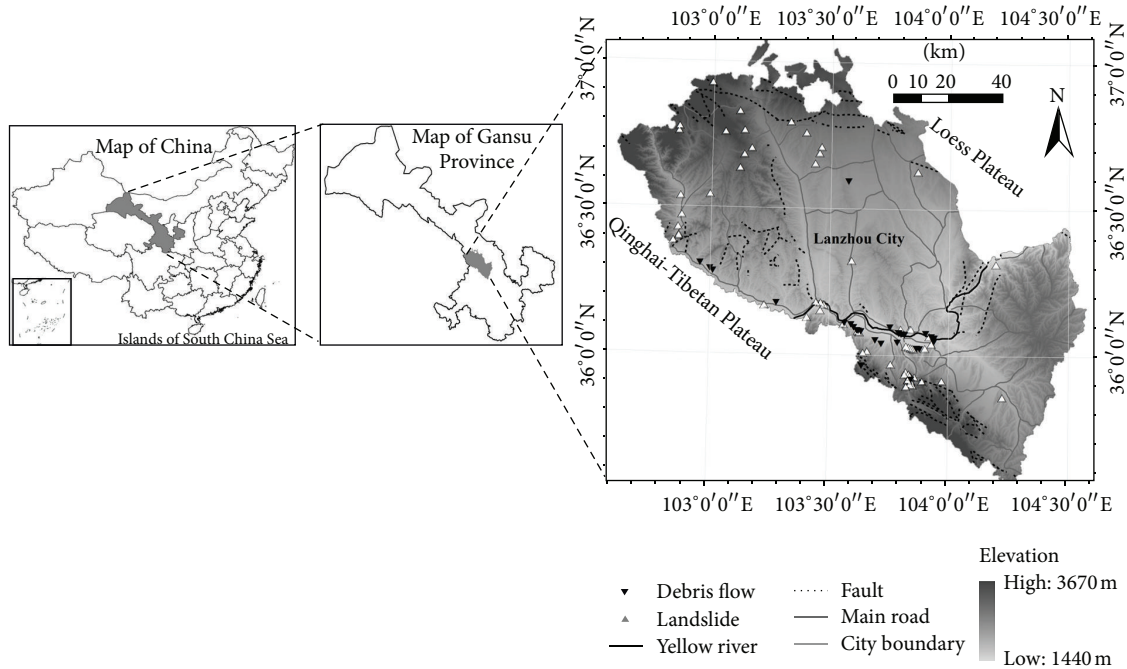


FIGURE 1: The study area, landslide sites, and debris flow sites with high risk were investigated and supplied by the Lanzhou Bureau of Land and Resources.

2. Study Area

Lanzhou city is located in the transitional zone between the Qinghai-Tibet Plateau and the Loess Plateau (Figure 1). In this area, geological conditions are very complex, and some deep and large gullies exist in most parts of the territory. These geological and geographic backgrounds lead to Lanzhou being prone to landslides and debris flow disasters. The latest statistics [11] show that the existing landslide sites (including unstable slopes) number 417 in Lanzhou. In addition, in Lanzhou, the rainfall from April to September accounts for about 86.8% of the annual precipitation [11] and always occurs in the form of heavy rain and storms. This pattern of rainfall is consistent with the fact that landslide disasters and debris flow always occur during the months of April to September in Lanzhou. In the last 5 years (from 2008 to 2012), 16 serious landslide disasters broke out in this city; each landslide disaster caused economic losses of more than 0.1 million CNY; 14 among the 16 serious landslide disasters were triggered by heavy rainfall and the other 2 landslide disasters were triggered by snow and ice melt; detailed presentation is shown in Table 1. At 18:00 Beijing standard time, May 16, 2009, the most serious landslide disaster occurred at Jiuzhou district in Lanzhou. This landslide disaster caused the death of 7 people and the 1 person injury of, and the direct economic loss of 20.6 million CNY was recorded. The Jiuzhou landslide belongs to loess landslide category. The length and width of Jiuzhou landslide were 160 and 40 meters, respectively, and covered an area of about 7500 m^2 with an average depth of about 4.0 meters. The total volume was about $6.2 \times 10^4 \text{ m}^3$. Figure 2 demonstrates the front view of the Jiuzhou landslide.

3. Landslide and Debris Flow Forecasting Method

3.1. Grey System Forecasting of Landslide Deformation. The grey system theory was initiated by Deng [12]. The concept of the grey system, in its theory and successful application, is now well known in China. It is able to (1) analyze the indeterminate and incomplete data to establish the systematic relations [13] and (2) forecast time series accurately and this has been quite a popular subject for researchers both in the past and at present [14]. It assumes that the internal structure, parameters, and characteristics of the observed system are unknown. The system state can be predicted by a differential equation from the recent historical measurements [13]. Although the historical measurements are too complex or chaotic, they always contain some governing laws [14]. The grey prediction has been widely used in applications of geography [15], agriculture [16], runoff prediction [17], displacement prediction of landslide [18], prediction of slope stability [19], power demand [20], stock market [21], and so forth. This theory is also coupled with the WebGIS to forecast timely deformation in the field of engineering geology, such as the deformation of landslides and host rock in the cavity [7].

The model GM (1, 1), one of the grey models, is the most widely used in the literature, pronounced as “grey model first order one variable”. This model is a time series forecasting model. The differential equations of the GM (1, 1) model have time varying coefficients. In other words, the model is renewed as the new data become available to the prediction model. The GM (1, 1) model can only be used in positive data sequences [22]. In this paper, since all

TABLE 1: Serious landslide disaster records in Lanzhou from 2008 to 2012. It was recorded and supplied by the Lanzhou Bureau of Land and Resources.

Occurrence date	Site	Trigger factor	Casualties	Economic losses (0.1 million CNY)
March 28, 2008	Chengguan district	Snow and ice melt	1	20.0
July 18, 2008	Gaolan county	Rainfall	1	10.0
September 19, 2008	Gaolan county	Rainfall		50
May 16, 2009	Chengguan district	Rainfall	8	2060.0
September 14, 2009	Chengguan district	Rainfall	3	80.0
September 15, 2009	Qilihe district	Rainfall		30.0
October 22, 2009	Qilihe district	Rainfall		130.0
August 16, 2010	Honggu district	Rainfall		10
October 19, 2010	Chengguan district	Rainfall		10
April 26, 2011	Xigu district	Rainfall		100
August 29, 2011	Yuzhong county	Rainfall		16
October 8, 2011	Xigu district	Rainfall		86
March 17, 2012	Chengguan district	Snow and ice melt		600
April 20, 2012	Yuzhong county	Rainfall		30
May 21, 2012	Chengguan district	Rainfall		50
May 21, 2012	Chengguan district	Rainfall		100

* Source from Lanzhou Bureau of Land and Resources.



FIGURE 2: Jiuzhou landslide outburst at 18:00 Beijing standard time, May 16, 2009. The left image is the remote viewing of Jiuzhou landslide; the right image is the close viewing of Jiuzhou landslide.

the primitive data points are positive, grey models can be used to forecast the trend of deformation of landslide in this paper.

The basic procedure for grey prediction is listed as follows [23].

Step 1. Construct a data series that contains the recently measured displacement of a landslide:

$$\begin{aligned} z^{(0)} &= \{z^{(0)}(1), z^{(0)}(2), \dots, z^{(0)}(n)\} \\ &= \{z^{(0)}(k); k = 1, 2, \dots, n\}, \end{aligned} \quad (1)$$

where $z^{(0)}(k)$ is the measurement from sensory information at time k and n is the length of the data series.

Step 2. Form a new data series $z^{(1)}$ by an accumulated generating operation (AGO):

$$\begin{aligned} z^{(1)} &= \{z^{(1)}(1), z^{(1)}(2), \dots, z^{(1)}(n)\} \\ &= \{z^{(1)}(k); k = 1, 2, \dots, n\}, \end{aligned} \quad (2)$$

where

$$z^{(1)}(k) = \left\{ \sum_{i=1}^k z^{(0)}(i), k = 1, 2, \dots, n \right\}. \quad (3)$$

Step 3. Form the grey differential equation

$$\frac{dz^{(1)}}{dt} + az^{(1)} = b \quad (4)$$

with initial condition $z^{(1)}(1) = z^{(0)}(1)$. The coefficients, a and b , can be obtained by using the least square method, as shown in

$$\hat{a} = \begin{bmatrix} a \\ b \end{bmatrix} = (B^T B)^{-1} B^T Y, \quad (5)$$

where

$$B = \begin{bmatrix} -Z^{(1)}(2) & 1 \\ -Z^{(1)}(3) & 1 \\ \dots & \dots \\ -Z^{(1)}(n) & 1 \end{bmatrix}, \quad Y = \begin{bmatrix} z^{(0)}(2) \\ z^{(0)}(3) \\ \dots \\ z^{(0)}(n) \end{bmatrix}. \quad (6)$$

$Z^{(1)}(k) = \alpha z^{(1)}(k) + (1 - \alpha)z^{(1)}(k - 1)$, $k = 2, 3, \dots, n$, and α is the weighting factor, according to relevant literature [13]; in this paper, we specify α is a constant with 0.5.

Step 4 (obtain the prediction value). Once a and b in (4) are obtained, the grey differential equation can be used to predict the value of state z at time instant $k + 1$.

The AGO grey prediction model can be obtained:

$$\hat{z}^{(1)}(k + 1) = \left[z^{(0)}(1) - \frac{b}{a} \right] e^{-ak} + \frac{b}{a}, \quad k = 0, 1, \dots \quad (7)$$

Then the prediction value of the state can be calculated by an inverse accumulated generating operation (IAGO):

$$\begin{aligned} \hat{z}^{(0)}(k + 1) &= \hat{z}^{(1)}(k + 1) - \hat{z}^{(1)}(k) \\ &= (1 - e^{-a}) \left[z^{(0)}(1) - \frac{b}{a} \right] e^{-ak}. \end{aligned} \quad (8)$$

For instance, the following figure (Figure 3) that includes 13 ensembles, the former 11 ensembles which represent the measured displacement of a landslide and the latter 2 ensembles that represent the forecasted displacement of the landslide based on both the basic procedure of grey prediction theory and the measured displacement of the landslide.

3.2. Critical Rainfall of Debris Flow Forecasting. Real-time assessment of debris flow disaster is fundamental for building warning systems that can mitigate its risk. A convenient method to assess the possible occurrence of a debris flow is the comparison of measured and forecasted rainfall with rainfall threshold curves (RTC) [24]. Therefore, how to define the RTC is a key issue in order to prepare efficient forecasting in a mountainous region (e.g., Lanzhou) that is prone to rain-triggered debris flow.

Rainfall, especially heavy rainfall, is the most critical natural triggering factor in Lanzhou. Rainfall intensity and duration of storms have been shown to influence the triggering of debris flows. The relationship between intense rainfall and debris flow initiation has been widely analyzed and documented in the literature in a number of different settings and environments throughout the world [25].

To define triggering thresholds, Bacchini and Zannoni [25] compared rainfall data to the occurrence of debris flows to examine the relations between debris flow initiation and

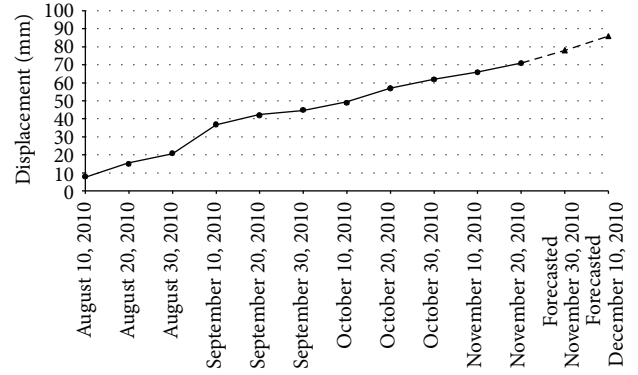


FIGURE 3: Data series of measured and forecasted displacements of a landslide, assuming that the current date is November 20, 2010, from August 10, 2010 to November 20, 2010; the landslide displacement meter measured a data series that contains 11 measured displacements of a landslide, based on the formulas (1)–(8) and 11 measured displacements. It can calculate and forecast landslide displacement value in the next 10 days (November 20, 2010–November 30, 2010 and November 30, 2010–December 10, 2010). Black solid circles denote the measured displacement of a landslide; black solid triangle points denote the forecasted displacement of the landslide.

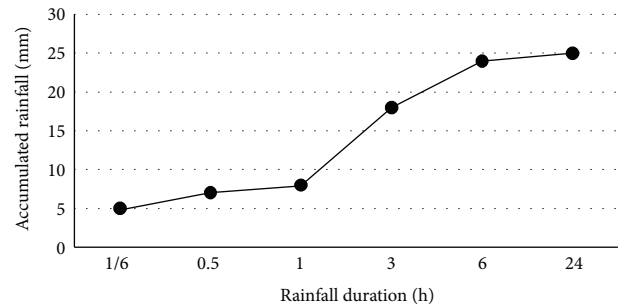


FIGURE 4: Rainfall threshold curve.

rainfall in the area of Cancia (Dolomites, Northeastern Italy). Tan and Duan [26] had studied the relation between debris flow initiation and minimum rainfall in China and preliminarily defined the RTC, but the result was not as accurate as possible due to the fact that it is a large-scale result. Wu et al. [27] considered that local condition, especially natural condition (e.g., precipitation, topography, and geology), is a key factor to assess this issue; simultaneously, other relevant studies [26] should not be neglected in the research. Under this methodology, Wu et al. [27] had identified the critical rainfall of debris flow initiation in Lanzhou. The new advance published by Wu et al. [27] is a local-scale result and as accurate as possible; thus, it is suitable to forecast debris flow in Lanzhou and be coupled with ISGDMW; detailed information about the new progress is presented in Table 2 and Figure 4.

According to Table 2, in Lanzhou city, the critical rainfall in 10 minutes, 30 minutes, 1 hour, 3 hours, 6 hours, and 24 hours is 5 mm, 7 mm, 8 mm, 18 mm, 24 mm, and 25 mm, respectively. RTC represents the relationship between rainfall

TABLE 2: Critical rainfall to trigger debris flow in Lanzhou.

Rainfall duration (h)	Accumulated rainfall (mm)
1/6	5
0.5	7
1	8
3	18
6	24
24	25

duration and critical rainfall. From Table 2, we plotted the RTC which is especially suitable for Lanzhou (Figure 4). When it rains, the algorithm of comparing the latest accumulated rainfall value measured by rain gauge and the rainfall threshold curve is implemented automatically in the analyzing module of ISGDMW. If the latest accumulated rainfall value is located above the curves, this debris flow site is considered to be dangerous. It is important to emphasize that Wu et al. [27] had only studied the relationship between rainfall duration and critical rainfall within 24 hours due to the shortage of data. So, in case the rainfall duration is over 24 hours, as long as the accumulated rainfall is greater than 25 mm, the corresponding debris flow site is still considered to be dangerous; the same conclusion is also applicable to situation of rainfall duration being less than 10 minutes but the accumulated rainfall being more than 5 mm.

4. System Design

4.1. *Framework of ISGDMW.* The framework of ISGDMW is shown in Figure 5 and can be divided into three parts.

- (1) Part 1. In situ monitoring system: it mainly includes landslide monitoring instruments, debris flow monitoring instruments, and wireless sensor network. These monitoring instruments were installed into the geological disaster sites and get up-to-date information of geological disaster sites. In situ monitoring data should be transmitted to the data center and uploaded to the system database through the wireless sensor network.
- (2) Part 2. Database: it is used for managing and integrating the spatial and nonspatial data related to geological disasters. Those data include in situ monitoring information, antecedent field investigating data, and basic data. In the database, the SQL Server2008 database software is often employed as a database platform, and the ArcSDE middleware, which is developed by ESRI Company, is chosen as the space database engine.
- (3) Part 3. Analyzing and warning system: it consists of 4 modules: basic module, analyzing module, releasing module, and monitoring module; each module has a different function (please see detailed information in Figure 5). The core of analyzing and warning system is the analyzing module, the theoretical bases-the grey system; and rainfall threshold were coupled into the analyzing module, so it is the connection between

the theoretical bases and ISGDMW. Analyzing and warning system mainly aims to analyze in situ monitoring data and the deformation of the potential geological disaster sites. Based on the grey system theory and measured displacement of landslide, deformation trend of landslide is analyzed automatically by ISGDMW, while the current state of debris flow is analyzed through comparing accumulated rainfall with the rainfall threshold. Finally, analyzed results (namely, output data from ISGDMW) and warning information will be released to the public through the internet, E-mail, and message based on the releasing module of ISGDMW.

4.2. *Database of ISGDMW.* Database of the ISGDMW is the fundamental component. On the one hand, it assists in management of the data related to geological disaster effectively, and on the other hand it provides data support for analyzing geological disaster conditions. The system database is divided into two categories, namely, spatial data and nonspatial data and can be demonstrated in Figure 6 particularly.

(i) Spatial Data

- (1) Vector layers mainly include administrative maps, land-use/land-cover change maps (LUCC), road maps, soil maps, vegetation type maps, geology maps, fault and seismic belt maps, and river maps.
- (2) Raster layers mainly include digital elevation model (DEM), slope gradient maps, and vegetation cover maps.
- (3) Theme layers mainly include the field surveying map of potential geological disaster sites which are generated by antecedent field surveying tasks implemented by the Lanzhou Bureau of Land and Resources. In some of those potential geological disaster sites monitoring instruments will be installed in situ.

(ii) Nonspatial Data

- (1) Monitoring data: it mainly includes rainfall data which is gathered from rain gauge and displacement data of landslide which is measured by a special instrument-displacement meter for landslide surface monitor. Those data are imported into the database through a wireless sensor network.
- (2) Auxiliary data: it involves gross domestic product (GDP) and the population of every village or community. This data is the official reference to geological disaster preventing and control.

4.3. *Working Flow of ISGDMW.* According to the sequence of data acquirement, data analysis, and the releasing of warning information, the process of geological disaster mitigation and prevention based on the platform of ISGDMW can be designed in three stages and explained as follows (as shown in Figure 7).

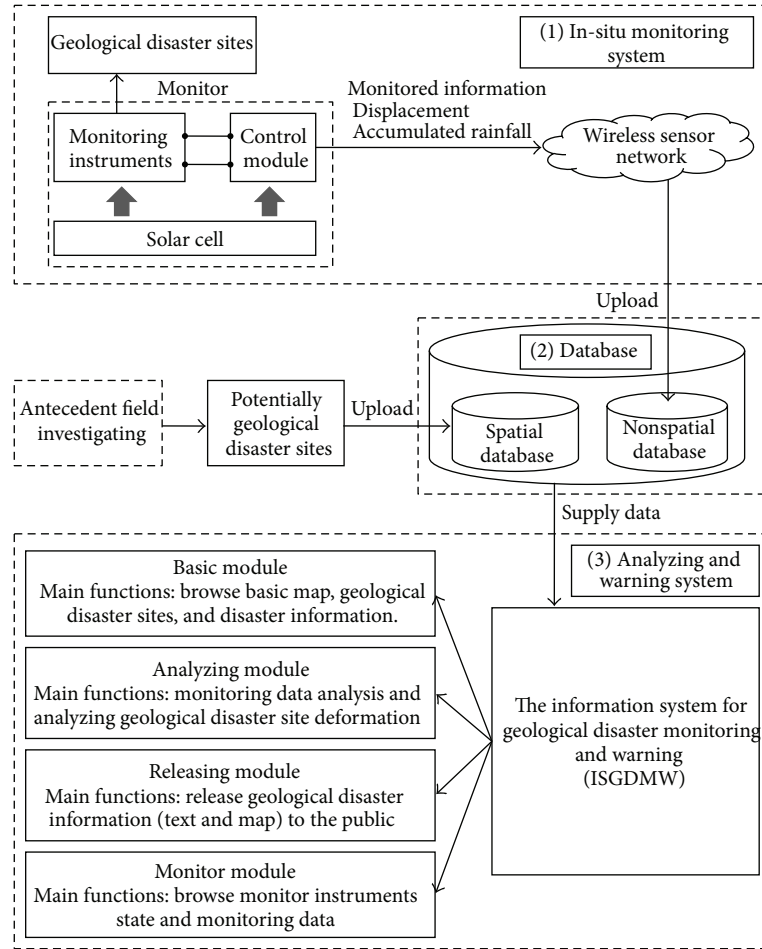


FIGURE 5: Framework of ISGDMW.

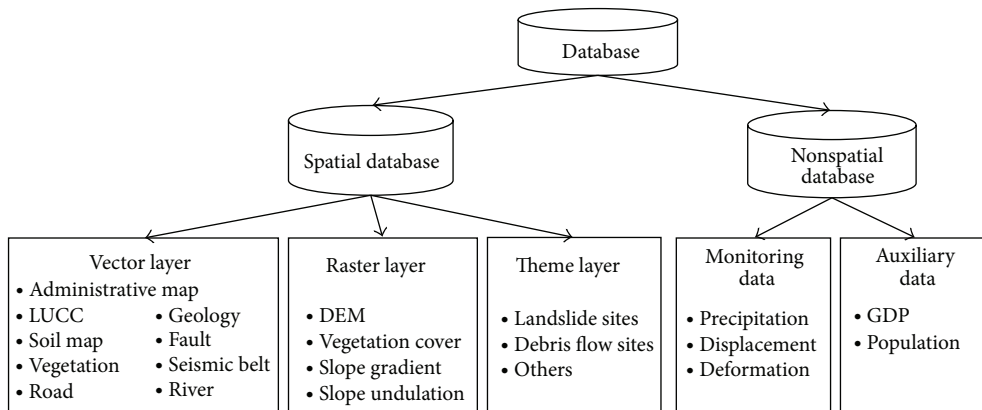


FIGURE 6: Architecture of database of ISGDMW.

(i) *Stage One: In Situ Monitor and Upload Data.* Landslide monitoring instruments automatically measure the displacement of landslides and wirelessly send the displacement value to the nonspatial database every 10 days; debris flow monitoring instruments automatically collect accumulated rainfall when it rains and then wirelessly send the accumulated rainfall value to the nonspatial database every 5 minutes.

(ii) *Stage Two: Analyze In Situ Data.* The professional managers immediately start the analyzing module of SGDMW when the latest data from in situ monitoring instruments is inputted into the nonspatial database. Deformation trends of landslide are calculated by the grey system method which had been coupled with SGDMW, and calculated result is the displacement of landslide in the next 10 days.

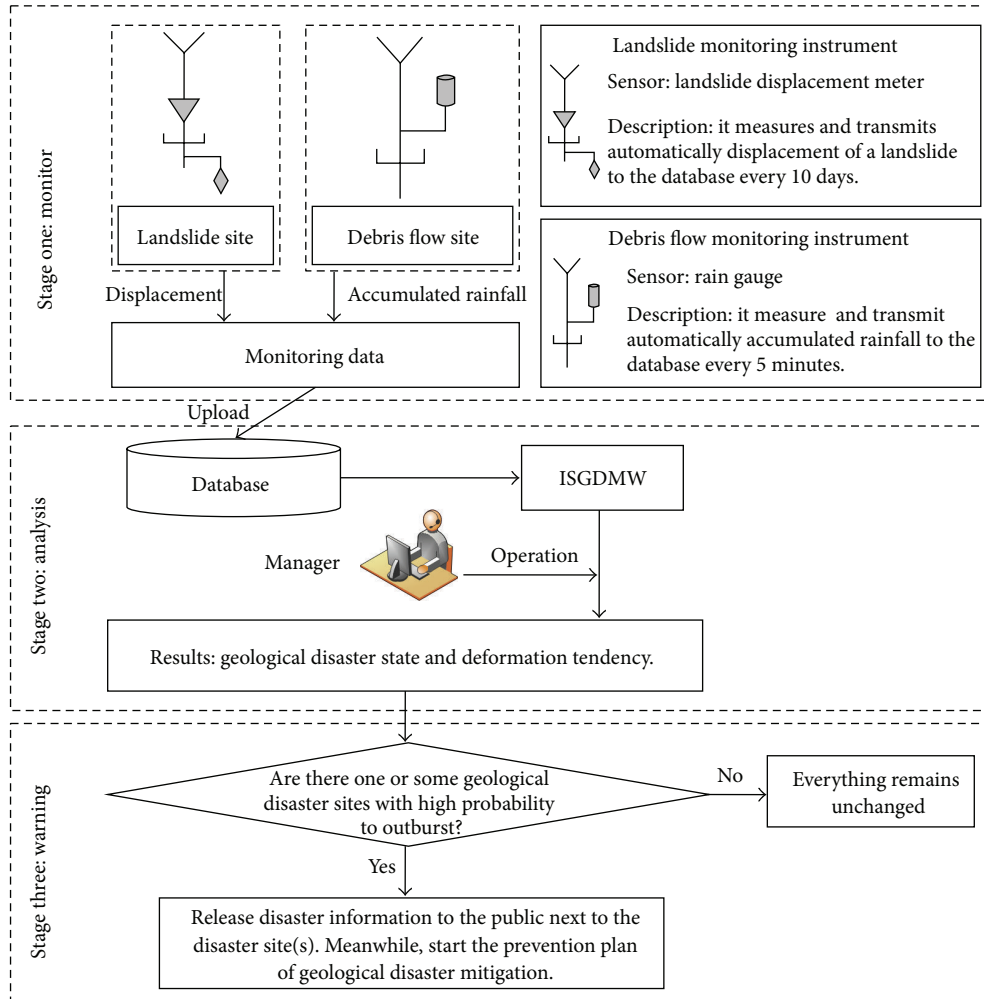


FIGURE 7: Working flow of geological disaster monitoring and warning based on ISGDMW.

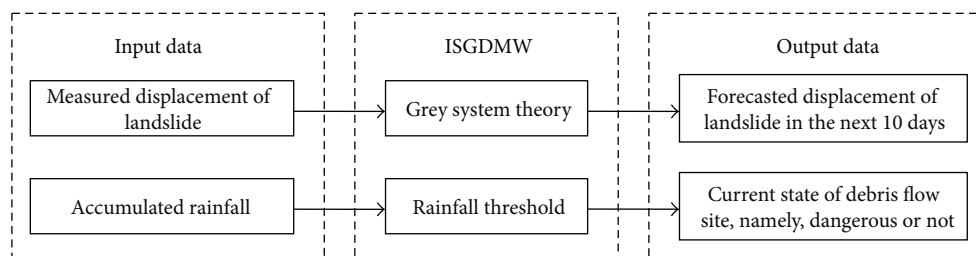


FIGURE 8: Data flow of stage two in the working flow of geological disaster monitoring and warning based on ISGDMW.

The current state of debris flow is analyzed by comparing the accumulated rainfall with the threshold rainfall of debris flow occurrence in Lanzhou; if the accumulated rainfall is more than the threshold rainfall of debris flow occurrence, then this debris flow site is considered as dangerous. That is to say, in this stage, the in situ monitoring instrument inputs measured displacement of landslide into the database and then the analyzing module of SGDMW automatically reads the measured displacement and forecasts the displacement of landslide in the next 10 days. The same process also occurs in

analyzing the current state of debris flow. The data flow of this stage is shown in Figure 8.

(iii) *Stage Three: Releasing Warning Information.* For landslides and debris flows with sharp deformation or dangerous state, the professional manager must send warning messages to the governor who governs the region which is impacted by the geological disaster site(s) and release warning information on the internet through the analyzing module of SGDMW.

When the governor receives a warning message, he or she must immediately alarm the public about the disaster warning message by means of oral announcement, broadcast, mobile phone, loudspeaker, sound the drum (or bell), sending out messengers, and so forth. Meanwhile, the governor must start prevention plans for the geological disaster and evacuate people from dangerous sites to safety shelters.

4.4. Developed Technology. The ISGDMW adopts a browser/server structure based on a web service and can be divided into three tiers, namely, Data tier, Service tier, and Application tier. The users in Application tier are acting as terminals via the internet. Ordinary users such as the public could simply use internet browsers (IE or Firefox) to access the released information which the server provides. Other professional users such as professional managers could use more powerful desktop tools to access the server and perform sophisticated tasks [10]. In the Service tier, ArcGIS Server9.3 software which is one of the server GIS products from ESRI (Environmental Systems Research Institute, Inc.) was chosen as the basic platform for the server application, which can be used to introduce advanced GIS function to the internet environment and to publish information based on GIS. In the Data tier, SQL Server2008 software and ArcSDE9.3 software are used for managing and integrating the spatial and nonspatial data. The Dell server and Windows Server2008 operating system were used as the application environment of the system, and the ASP.net technology, MicrosoftVS2008.net developing environment, C# programming language, and Dreamweaver software were chosen as the implementing means of the ISGDMW.

5. Conclusions

In general, geological disasters in the mountainous area are frequent and complex in China and in situ monitoring and a quick response are the key methods for mitigating geological disasters in those areas. In this paper, a WebGIS-based platform, that is, ISGDMW, has been designed to enable effective integration of in situ monitoring data management, geological disaster analysis, sending warning messages, and enabling a prompt response. The ISGDMW had been implemented and tentatively run during the past few months, but it still has a little bug in the codes and is kept in checking. We need to stress that our design scheme of the system is valuable for others because the system has three significant features, including simplicity, automation, and user friendliness. However, since the geological disaster is paroxysmal and complicated, ISGDMW must be further enhanced in two aspects, namely, in situ monitoring instruments and accurate analyzing methods, so as to more timely and accurately grasp the inner activity and state of every potential geological disaster site. Moreover, this highly advanced, easy-to-operate system can be considered as a prototype for developing geological monitoring and warning systems in other regions that are prone to geological disasters.

Acknowledgments

The authors thank all editors for supplying this chance and thank all viewers for their valuable suggestions and

comments. This research was supported by the “Western light” Talent Project of the Chinese Academy of Sciences (no. Y028A11001).

References

- [1] S. Verma, R. K. Verma, A. Singh et al., *Advances in Computer Science, Engineering & Applications*, Springer, Berlin, Germany, 2012.
- [2] C. Qu, H. Ye, and Z. Liu, “Application of WebGIS in seismological study,” *Acta Seismologica Sinica*, vol. 24, no. 1, pp. 97–106, 2002.
- [3] K. H. Kim, Y. Kawata, H. Kawakata, and R. Goto, “A study on the development and distribution of WebGIS-based flood hazard map,” *Journal of Japan Society for Natural Disaster Science*, vol. 23, no. 4, pp. 539–551, 2005.
- [4] F. Martinelli and C. Meletti, “A WebGIS application for rendering seismic hazard data in Italy,” *Seismological Research Letters*, vol. 79, no. 1, pp. 68–78, 2008.
- [5] V. Pessina and F. Meroni, “A WebGis tool for seismic hazard scenarios and risk analysis,” *Soil Dynamics and Earthquake Engineering*, vol. 29, no. 9, pp. 1274–1281, 2009.
- [6] F. C. Yu, C. Y. Chen, S. C. Lin, Y. C. Lin, S. Y. Wu, and K. W. Cheung, “A web-based decision support system for slopeland hazard warning,” *Environmental Monitoring and Assessment*, vol. 127, no. 1–3, pp. 419–428, 2007.
- [7] X. G. Li, A. M. Wang, and Z. M. Wang, “Stability analysis and monitoring study of Jijia River landslide based on WebGIS,” *Journal of Coal Science and Engineering*, vol. 16, no. 1, pp. 41–46, 2010.
- [8] S. Gabriele, G. D. Aquila, and F. Chiaravalloti, *GeoSpatial Visual Analytics*, Springer, Dordrecht, The Netherlands, 2009.
- [9] L. Martino, C. Ulivieri, M. Jahjah, and E. Loreti, “Remote sensing and GIS techniques for natural disaster monitoring,” in *Space Technologies for the Benefit of Human Society and Earth*, pp. 331–382, Springer, Dordrecht, The Netherlands, 2009.
- [10] H. X. Lan, C. D. Martin, C. R. Froese et al., “A web-based GIS for managing and assessing landslide data for the town of Peace River, Canada,” *Natural Hazards and Earth System Science*, vol. 9, no. 4, pp. 1433–1443, 2009.
- [11] Z. Q. Ding and Z. H. Li, *Geological Disaster and Prevention in Lanzhou City*, Gansu Science and Technology Press, Lanzhou, China, 2009 (Chinese).
- [12] J. L. Deng, “Control problems of grey systems,” *Systems and Control Letters*, vol. 1, no. 5, pp. 288–294, 1982.
- [13] J. F. Chen, Z. G. Shi, S. H. Hong, and K. S. Chen, “Grey prediction based particle filter for maneuvering target tracking,” *Progress in Electromagnetics Research*, vol. 93, pp. 237–254, 2009.
- [14] E. Kayacan, B. Ulutas, and O. Kaynak, “Grey system theory-based models in time series prediction,” *Expert Systems with Applications*, vol. 37, no. 2, pp. 1784–1789, 2010.
- [15] Y. Y. Cao, “Modeling for grey forecasting of calamities in geography,” *Youthgeogrphers*, vol. 2, pp. 6–11, 1987.
- [16] S. An, J. Yan, and X. Yu, “Grey-system studies on agricultural ecoengineering in the Taihu lake area, Jiangsu, China,” *Ecological Engineering*, vol. 7, no. 3, pp. 235–245, 1996.
- [17] H. V. Trivedi and J. K. Singh, “Application of grey system theory in the development of a runoff prediction model,” *Biosystems Engineering*, vol. 92, no. 4, pp. 521–526, 2005.
- [18] W. Gao, *Computational Methods in Engineering & Science*, Springer, Berlin, Germany, 2007.

- [19] P. Lu and M. S. Rosenbaum, "Artificial neural networks and grey systems for the prediction of slope stability," *Natural Hazards*, vol. 30, no. 3, pp. 383–398, 2003.
- [20] C. C. Hsu and C. Y. Chen, "Applications of improved grey prediction model for power demand forecasting," *Energy Conversion and Management*, vol. 44, no. 14, pp. 2241–2249, 2003.
- [21] Y. F. Wang, "Predicting stock price using fuzzy grey prediction system," *Expert Systems with Applications*, vol. 22, no. 1, pp. 33–38, 2002.
- [22] J. L. Deng, "Introduction to grey system theory," *The Journal of Grey System*, vol. 1, no. 1, pp. 1–24, 1989.
- [23] C. C. Wong, B. C. Lin, and C. T. Cheng, "Fuzzy tracking method with a switching grey prediction for mobile robot," in *Proceedings of the 10th IEEE International Conference on Fuzzy Systems*, pp. 103–106, Melbourne, Australia, December 2001.
- [24] M. N. Papa, V. Medina, F. Ciervo, and A. Bateman, "Estimation of debris flow critical rainfall thresholds by a physically-based model," *Hydrology and Earth System Sciences Discussions*, vol. 9, no. 11, pp. 12797–12824, 2012.
- [25] M. Bacchini and A. Zannoni, "Relations between rainfall and triggering of debris-flow: case study of Cancia (Dolomites, Northeastern Italy)," *Natural Hazards and Earth System Science*, vol. 3, no. 1-2, pp. 71–79, 2003.
- [26] B. Y. Tan and A. Y. Duan, "Study on prediction for rainstorm debris flow along mountain district railway," *Journal of Natural Disasters*, vol. 4, no. 2, pp. 43–52, 1995 (Chinese).
- [27] H. Wu, L. Shao, and D. D. Lu, "The geological calamity and the rainstorm intensity in Lanzhou City," *Arid Meteorology*, vol. 23, no. 1, pp. 63–67, 2005 (Chinese).

Research Article

Impacts of Pond Change on the Regional Sustainability of Water Resources in Taoyuan, Taiwan

Yuei-An Liou, Tai-Sheng Wang, and Hai-Po Chan

Center for Space and Remote Sensing Research (CSRSR), National Central University, Chung-Li 32001, Taiwan

Correspondence should be addressed to Yuei-An Liou; yueian@csrsr.ncu.edu.tw

Received 27 October 2013; Accepted 27 November 2013

Academic Editor: Chung-Ru Ho

Copyright © 2013 Yuei-An Liou et al. This is an open access article distributed under the Creative Commons Attribution License, which permits unrestricted use, distribution, and reproduction in any medium, provided the original work is properly cited.

Taoyuan tableland faces the increasing water demand associated with the expansion of industrialization and urbanization. The county currently relies on the Shihmen Reservoir as the single water supply system. It will be of great concern in the shortage of water resources. This study aims to explore the impact of changes in farm ponds on the regional agricultural environment in Taoyuan County with multiyear (1993, 2003, and 2010) SPOT satellite imagery. Results show that farm ponds have decreased by 10.55 million m^2 from 1993 to 2010, and the existing farm ponds were 18.80 million m^2 in 2010, equivalent to the irrigation water of 21.10~31.65 million m^3 (tons) and 37.61~56.41 million m^3 (tons), respectively. The existing farm ponds are able to provide the water supply for 1.88~2.82 thousand hectares of agricultural land, accounting for 6.70%~10.50% of total agricultural area of Taoyuan County. Corresponding to the government's promotion policy (2012) on activating fallow land, if we redeploy the existing farm ponds for activating fallow fields, it will lessen the water supply burden of Shimen Reservoir. Thus, farm ponds remain the significant water facilities. For the sustainable agriculture, farm ponds shall be classified and cherished as a public asset for the future development.

1. Introduction

In the past agricultural society, people were plagued with insufficient water supply for field irrigation in Taoyuan tableland. Farmers usually dig farm ponds for the irrigation purpose by taking the advantages of the impermeable characteristics of red and yellow soil. At the peak period, there were nearly eight thousand ponds in Taoyuan County, brought the reputation such as “one-thousand-pond town” and “one-thousand-lake County” [1]. However, since the 1920s, after the constructing of Shimen Reservoir, Taoyuan Canal and Shimen Canal, and other irrigation facilities, the ponds have gradually vanished. Coupled with the rapid expansion of industrialization and urbanization progress, the landscape development has been changed, which also brought the indirect impacts to the ponds. According to the statistics in 2008, the number of ponds was about 3,345, but only around 2,800 left by the year of 2009 [2].

Since the year of 1983, Taiwan government implemented the six-year plan on rice production and paddy field transfer to address the financial issue of poor rice sales. However, it is not until 1995 the rice supply and demand has reached

balance [3]. The land fallowing policy caused the agricultural land fallow area rapid increase, thus resulted in the rice field area decline of 40.78% from 1983 to 2006 [4]. According to the statistics 2011, the fallow land area in Taoyuan County summed up to 26.86 thousand hectares [5], demonstrating the main reason of ponds disappearance.

Taiwan initiated the land fallow policy for nearly 28 years since the accession to the World Trade Organization. As much as 200 thousand hectares agricultural land has fallow in the whole island, and these fallow lands not only breed weeds, pests, and rodents but also spend the government annual budget for maintenance. In recent years, global climate change has caused the volatile food supply internationally. The government plans to promote the activation of fallow land in the hope to boost the food self-sufficiency rate [6].

The existing farm ponds in Taoyuan County can be redeployed as the irrigation facilities and improve irrigation water recycling rate for the regional agriculture development. Therefore, this study combined multiyear (1993, 2003, and 2010) SPOT satellite imagery and statistical analysis to investigate the land-use and land-cover (LULC) changes impact on the regional agriculture environment. Analysis

assessments on the usage possibility of existing ponds for regional irrigation and farmland water conservancy facilities are also provided.

2. Remote Sensing and Water Reuse

2.1. Remote Sensing and Land Change. Remote sensing technology has been developed since the 1960s. With the advance of modern physics, spatial technology, electrical technology, computer technology, information technology, environment technology, and so on, it becomes an up-to-date and feasible integral detection method [7–9]. Satellite remote sensing is a reliable full-length, real-time, and periodical data acquisition technology. The application of these techniques on the large-scale LULC change provides not only the basic spatial information, but also the assistance for the better decision making on the environmental resources control aspect [10]. Remote sensing has been widely used in agriculture, forestry, geology, geography, geomorphology, oceanography, hydrology, meteorology, LULC change, landscape change monitoring, earth resource exploration, military reconnaissance, and other various areas [7].

Remote sensing technology provides key tools for the earth and environment observations. Satellite remote sensed data for land cover, land use, and its changes play a key role for many diverse applications. Natural resource management, planning, and monitoring programs rely on accurate data of the land cover in the target region. In addition, compared to other monitoring methods, the extensive analysis of remotely sensed data has proven to be more cost effective for large regions.

LULC change can be regarded as a social process to meet human's needs, and thus its development is strongly dependent on environmental and social factors. Therefore, understanding and effectively controlling the process of LULC change are the hot issue for the regional sustainable development such as environmental protection and natural resources exploitation. LULC data in different periods can be used to investigate the LULC change in urban areas by the statistical analysis and thus display the LULC change in each period [11].

2.2. Water Reuse. For the agricultural irrigation needs in early days, farm ponds were excavated as the main water facilities because of terrain and environment features in Taoyuan tableland. However, since the construction of Shimen Reservoir, Taoyuan Canal, and Shimen Canal, the original functions of farm ponds have been replaced. The proposed fallow grants policy in the past decades also likely caused farm ponds to vanish gradually (decreased from 8,000 at the peak period to 2,800 in the year of 2010).

Water reuse offers a climate independent water source that is dependable, locally controlled, and generally beneficial to the environment. Water reuse also allows communities to become less dependent on groundwater and surface water sources and can decrease the diversion of water from sensitive ecosystems.

Dyer [12] had raised awareness on water crisis issues, pointing out that although the earth's arable land area increased by only 10% in the past, irrigation water has increased threefold, indicating the increasing water demand in the world. More water and energy are required to meet the food production, as well as industrial, services, and other livelihood and development needs. According to the report from United Nations in 2013, due to the global population growth and climate change, water use around the globe becomes increasingly competitive. One-third of the population in the world is under the middle and high levels of water scarcity. By 2030, nearly half the world's population will face the issue of water shortages. Water demand is expected to increase by 40%, coupled with the rise of emerging market economies, and water demand will grow geometrically. The future evolution trend of water use is more people worldwide with less water. It is estimated that, by 2050, 45% of the world population and the country will be affected by the chronic shortage of water resources, indicating that the issue becomes increasingly serious.

Water conservation and recycling issues have raised a worldwide attention. The event such as the World Water Day on March 22, 2013, proposed a "Recycle a Bucket of Water a Day" slogan to advocate for the sustainable management of freshwater resources in the planet. Therefore, in addition to the wastewater recycling plan in Taoyuan County, the existing pond facilities can be redeployed as the small-size artificial reservoir to uplift the usage of water resources.

3. Study Areas and Methods

3.1. Study Area. Taoyuan County locates in the tableland, northwest of Taiwan, a total of 13 townships, including Xinwu Township, Guanyin Township, Dayuan Township, Luzhu Township, Gueishan Township, Taoyuan Township, Bade Township, Chungli Township, Yangmei Township, Pingzhen Township, Longtan Township, Daxi Township, and Fusing Township, as shown in Figure 1. Most lands in Taoyuan are barren soil because of its terrain features. This study focuses on LULC changes of the pond (water body) and farmland (vegetation) areas. In order to exclude the influence of water bodies such as rivers and reservoirs in this area, image processing technology was applied to trim the area along the boundaries of hills and rivers of Taoyuan County. The preprocessed study area image is shown in Figure 2.

3.2. Image Processing. The goal of image processing is to create an enhanced image that is more useful or to perform some of the interpretation and recognition tasks. We took various periods of SPOT satellite imagery, including the 1993 (SPOT-2), 2003 (SPOT-5), and 2010 (SPOT-5), with the spatial resolution of 12.5 m, 10 m, and 10 m, respectively. However, as the radiation image, satellite images were distorted or deformed with geometric errors because of atmospheric scattering, sun angle difference, vehicles form, surface curvature of the flight trajectory parameters, other factors and etcetera. To correct the above errors and acquire the true data, we applied the following three steps: (i) image preprocessing; (ii) image classification, and (iii) image accuracy assessment.

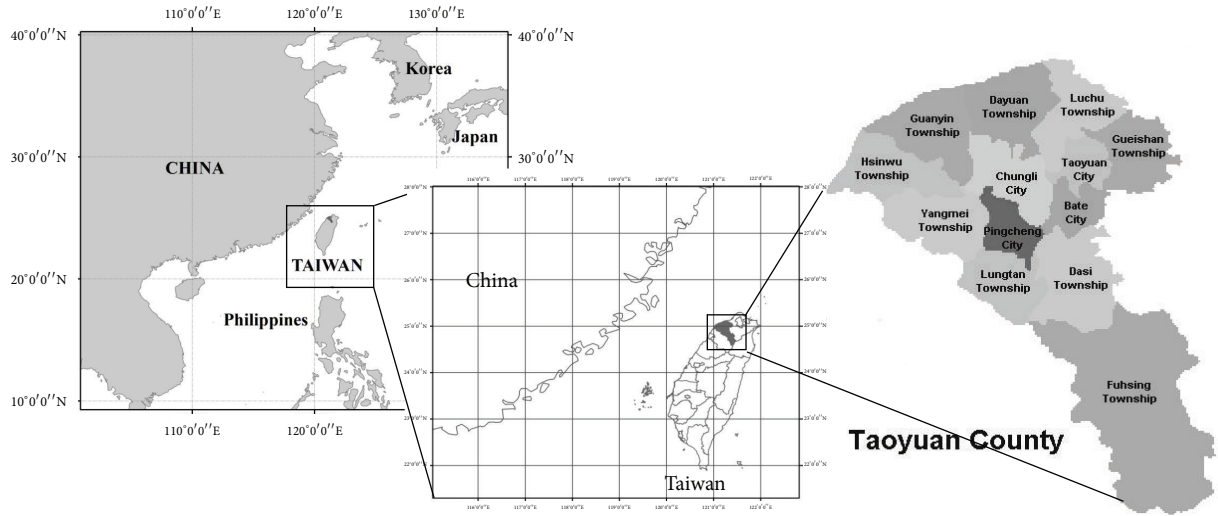


FIGURE 1: Geographic location of Taoyuan County, Taiwan.

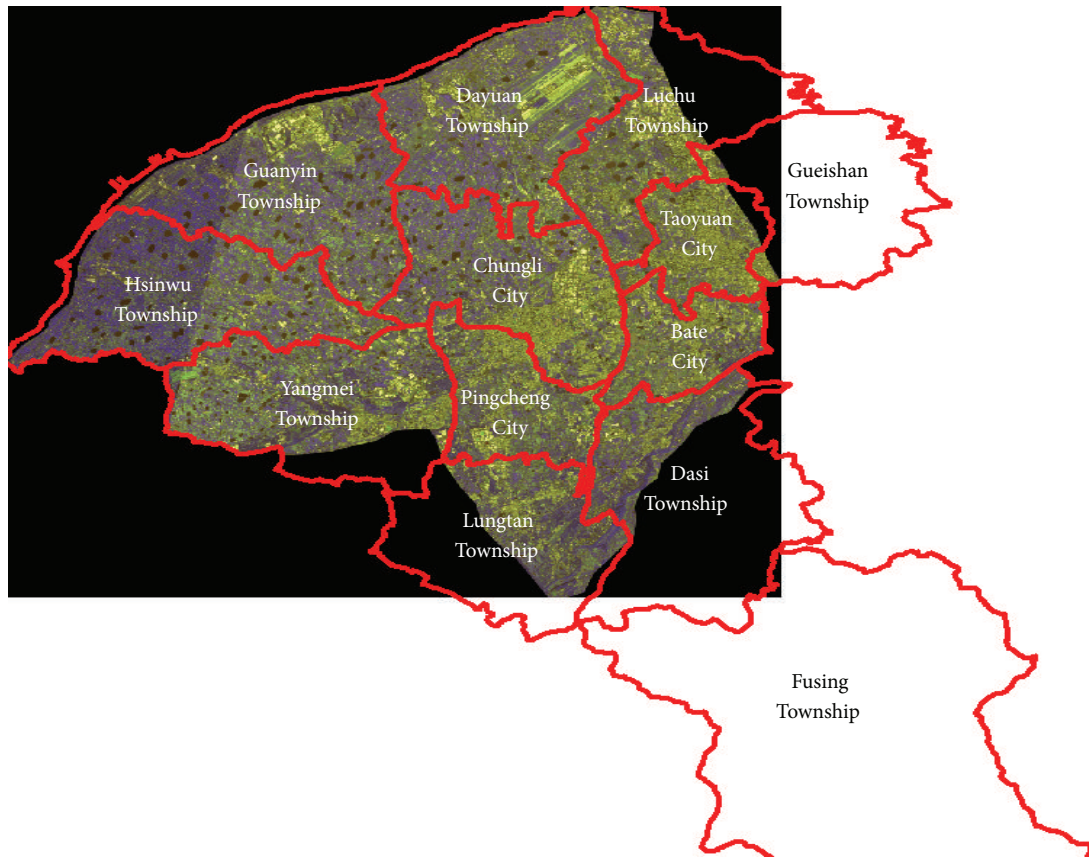


FIGURE 2: Preprocessed study area (excluding highlands (forest) and reservoir (water body)).

3.3. *Image Classification.* The basic principle of image classification lies in the fact that similar objects have similar spectral properties. The electromagnetic radiation reflected by objects of the same nature is similar overall and these objects will thus have similar spectral signatures. Since the spectral signatures of the objects observed by satellites are converted into different colors in digital images, objects of

the same kind will appear in closely related colors. Besides, the colors in a digital image are merely a conventional transposition of numerical values; it is also possible to classify the pixels by their numerical values.

Satellite image classification methods are broadly divided into supervised and unsupervised classifications. Both use the similarity measure, but the former classifies images according

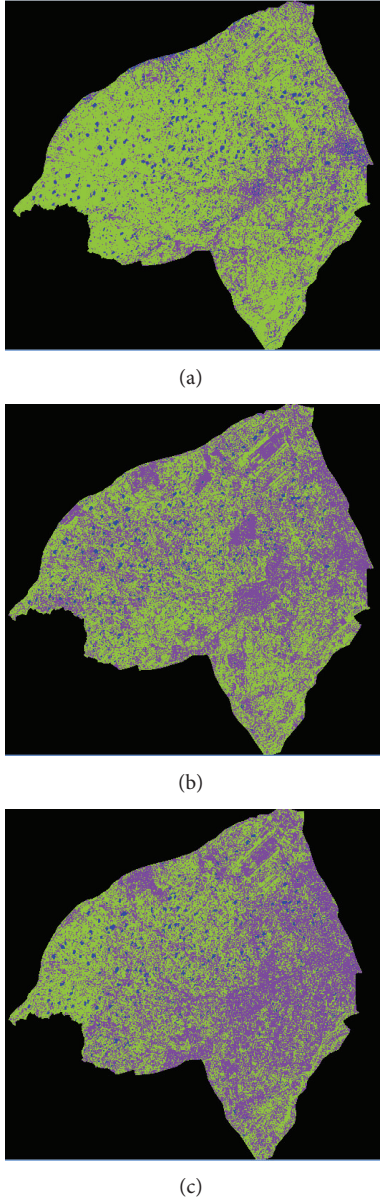


FIGURE 3: Color indexed LULC classification map from the SPOT series of satellites (blue: water body; green: vegetation; purple: non-vegetation). (a) 1993 SPOT-2; (b) 2003 SPOT-5; (c) 2010 SPOT-5.

TABLE 1: The accuracy assessment of images classification.

Accuracy assessment	Year		
	1993	2003	2010
Overall accuracy	93.26%	92.88%	94.38%
Kappa index	0.84	0.88	0.90

to the similarity with a set of pre-given images (“references” or “templates”), and the latter classifies the images according to the innate grouping or clustering within the images.

In detail, each pixel on the image is classified according to the recorded surface spectral reflectivity (DN value). Using the specific statistical and analysis process, each pixel in the

TABLE 2: The statistics of LULC changes in 1993, 2003, and 2010.

Feature type	1993 (m ²)	2003 (m ²)	2010 (m ²)
Water body	29, 352, 656	18, 945, 800	18, 804, 200
Vegetation	444, 161, 250	310, 832, 500	281, 818, 300
Nonvegetation	156, 671, 563	300, 244, 100	329, 399, 900
Total	630, 185, 469	630, 022, 400	630, 022, 400

image was thus given a specific value, which represents the particular category of land cover [13].

3.4. Accuracy Assessment. The accuracy of a classification is assessed by comparing the classification with reference data that is believed to accurately reflect the true land cover. Sources of reference data include among others ground truth data, higher resolution satellite images, and maps derived from aerial photo interpretation. Hence, the accuracy assessment reflects the difference between the classification and the reference data.

In this study, the accuracy of the image classification is estimated by the error matrix. Error matrix is used to compare the classified image and ground truth data for the accuracy assessment (the producer’s accuracy and user’s accuracy).

4. Results and Discussion

4.1. Image Analysis. By taking advantage of multiyear SPOT satellite imagery (1993, 2003, and 2010), we have classified the data into three categories (Figure 3): (i) water body area (ponds), (ii) vegetation area (farmland), and (iii) non-vegetation area (buildings and bare land) in accordance with the unsupervised classification (Iterative Self-Organizing Data Analysis Techniques; ISODATA Classification).

To assess the accuracy of classification, we also randomly selected 267 points in the study area and artificially assigned the land cover category as ground truth data. The derived error matrix and Kappa index (Table 1) are greater than 90% and 0.8 and thus display that the image classification result is of high reliability.

4.2. Statistical Analysis. Land cover changes among 1993, 2003, and 2010 as shown in Table 2. Results show that non-vegetation area has increased 110% (172.73 million m²), the water body has reduced 35.94% (10.55 million m²), and the vegetation area has lost 36.55% (162.34 million m²) in Taoyuan County between the year of 1993 and 2010, individually. Furthermore, we find that 6.2% of nonvegetation (buildings and bare land) area came from the water body (ponds) area and 93.8% from the vegetation (farmland) area during the past 18 years.

4.3. Ponds Change. The water storage in farm ponds provides the water resources for farmland irrigation; the disappearance of farm ponds thus impacts the regional agriculture environment in Taoyuan County. If we ignore the influence of hydrological factors such as infiltration and runoff, the

vanishing ponds water storage is 21.10–31.65 million tons for the average depth of 2~3 meters of farm ponds [5]. Again, if we make assessment based on the requirement of 0.02 million tons of irrigation water for one hectare of farmland each time [14], the vanishing ponds water could supply for approximately 1.06~1.58 thousand hectare farmland. However, the total area of existing farm ponds was approximately 18.80 million m² in 2010, equivalent to the irrigation water of 37.61~56.41 million tons. This means that if we take advantage of the existing farm ponds for activating fallow fields, it will subsequently reduce the water supply burden of Shimen Reservoir. Therefore, the ponds remain the significant water facilities in this region.

4.4. Fallow Land Activation. In recent years, Taiwan government promotes policy of food self-sufficiency and at same time reduces fallow subsidies to activate the fallow land. Nevertheless, the prerequisite is to tackle the issue of increasing demand of water use. If the county government continues to rely on the Shihmen Reservoir as the unitary water supply system for civilians, industries, and farm irrigations, it will be a great concern for regional agricultural development in the water shortage. According to statistics in 2011, the existing fallow land is around 26.86 thousand hectares in Taoyuan County [5]. Once collaborating with the government activation policy on fallow land, the existing farm ponds are able to provide 6.7%~10.5% water use for irrigation. Moreover, if the ponds can be deepened around one meter above the average depth, the maximum water storage of ponds will increase to approximately 75.22 million tons, which accounts for nearly half (48.94%) of the irrigation water demand. This deployment obviously improves the regional water reuse rate. Hence, if the county government takes advantage of existing ponds to water fallow farmland, it will not only relieve the burden of the reservoir but also save the ponds from disappearance and thus help stabilize the Taoyuan regional agriculture development and uplift food self-sufficiency rate.

5. Conclusions

Satellite remote sensing is a reliable full-length, real-time, and periodical data acquisition technology. The application of these techniques on the large-scale LULC change not only provides the basic spatial information, but also the assistance for the better decision making on the environmental resources control aspect. Research results on the changes of LULC over the past 18 years (from 1993 to 2010) in Taoyuan show that the increasing rate of nonvegetation (buildings and bare land) area is 110%, the decreasing rate of water body (ponds) area is 35.94%, and the decreasing rate of vegetation area is 36.55%, respectively. Also, image change detection analysis implies that the nonvegetation (buildings and bare land) areas are primarily converted from the vegetation (farmland) areas. Therefore, we are able to catch the whole picture of LULC changes in the study area and comprehend its potential impacts on the regional sustainable development and also to provide the proactive fact-grounded

policy recommendations for the government agencies. The future work will be the focus of higher resolution satellite images applying to distinguish LULC change and the corresponding impact on the social, economic, and natural environment, such as the urban desertification issue. Such work is especially required because many issues concerning the expected environmental changes and societal impacts associated with the recently approved Taoyuan Aerotropolis Project in 2013 remain unknown. It is planned that the initial investment and the developed area of the Taoyuan Aerotropolis Project are 495 billion NTD (~16.5 billion USD) and 6770 acres, respectively.

Acknowledgments

The authors are extremely grateful to the CSRSR (Center for Space and Remote Sensing Research, National Central University) satellite receiving station for providing the image from SPOT-2 and SPOT-5. This work was supported by the National Science Council (NSC) under the Grants NSC 101-2221-E-008-019 and NSC 101-2111-M-008-018.

References

- [1] H. T. Chen, "From ponds to irrigations: the evolution of the water resources in Taoyuan Plateau," *Dong Hwa Journal of Humanities*, no. 5, pp. 183–208, 2003.
- [2] S. J. Chyi and H. J. Wu, "Taoyuan tableland Encyclopedia of Taiwan, 2009," <http://taiwanpedia.culture.tw/web/index>.
- [3] Y. C. Teng, "Review and prospect of Taiwan's rice," in *Research Report, Introduction to Kaohsiung District Agricultural Research and Extension Station*, vol. 14, no. 3, pp. 1–23, 2003.
- [4] R. G. Jiang, "Management and use of fallow paddy," in *Introduction to Taitung District Agricultural Research and Extension Station*, 2008.
- [5] Spatial Planning of Agricultural Land, "The correction results of spatial planning of agricultural land resources in Taoyuan County in 2011".
- [6] The Official Website of Council of Agriculture, <http://eng.coa.gov.tw/>.
- [7] Y. A. Liou, S. K. Kar, and L. Y. Chang, "Use of high-resolution formosat-2 satellite images for post-earthquake disaster assessment: a study following the 12 may 2008 Wenchuan earthquake," *International Journal of Remote Sensing*, vol. 31, no. 13, pp. 3355–3368, 2010.
- [8] Y. A. Liou, H. C. Sha, T. M. Chen et al., "Assessment of disaster losses in rice field and yield after tsunami induced by the 2011 Great East Japan earthquake," *Journal of Marine Science and Technology*, vol. 20, no. 6, pp. 618–623, 2012.
- [9] T. Y. Chang, Y. A. Liou, C. Y. Lin, S. C. Liu, and Y. C. Wang, "Evaluation of surface heat fluxes in Chiayi Plain of Taiwan by remotely sensed data," *International Journal of Remote Sensing*, vol. 31, no. 14, pp. 3885–3898, 2010.
- [10] T. S. Wang, *Application of various-scale satellite images to inland water quality monitoring in Taiwan [Ph.D. thesis]*, Department of Civil Engineering and Engineering Informatics, 2010.
- [11] T.-Y. Chou, F.-J. Chien, and T.-C. Lei, "Quantitative analysis study for land use changes detection of urban area," *Journal of Taiwan Land Research*, vol. 6, no. 1, pp. 105–130, 2003.
- [12] G. Dyer, *Climate Wars*, Random House of Canada, 2010.

- [13] Z. H. Tan, "Investigation of the paddy heat sink effect and economic evaluation in Taiwan," *Operation of Irrigation Associations*, pp. 25–49, 2009.
- [14] The Official Website of Taoyuan County Government, "the correction results of spatial planning of agricultural land resources in Taoyuan County in 2008," <http://www.tycg.gov.tw/files/IMC/aB0006996.pdf>.

Research Article

Spatial Downscaling of TRMM Precipitation Using Geostatistics and Fine Scale Environmental Variables

No-Wook Park

Department of Geoinformatic Engineering, Inha University, Incheon 402-751, Republic of Korea

Correspondence should be addressed to No-Wook Park; nwpark@inha.ac.kr

Received 6 September 2013; Revised 19 November 2013; Accepted 27 November 2013

Academic Editor: Chung-Ru Ho

Copyright © 2013 No-Wook Park. This is an open access article distributed under the Creative Commons Attribution License, which permits unrestricted use, distribution, and reproduction in any medium, provided the original work is properly cited.

A geostatistical downscaling scheme is presented and can generate fine scale precipitation information from coarse scale Tropical Rainfall Measuring Mission (TRMM) data by incorporating auxiliary fine scale environmental variables. Within the geostatistical framework, the TRMM precipitation data are first decomposed into trend and residual components. Quantitative relationships between coarse scale TRMM data and environmental variables are then estimated via regression analysis and used to derive trend components at a fine scale. Next, the residual components, which are the differences between the trend components and the original TRMM data, are then downscaled at a target fine scale via area-to-point kriging. The trend and residual components are finally added to generate fine scale precipitation estimates. Stochastic simulation is also applied to the residual components in order to generate multiple alternative realizations and to compute uncertainty measures. From an experiment using a digital elevation model (DEM) and normalized difference vegetation index (NDVI), the geostatistical downscaling scheme generated the downscaling results that reflected detailed characteristics with better predictive performance, when compared with downscaling without the environmental variables. Multiple realizations and uncertainty measures from simulation also provided useful information for interpretations and further environmental modeling.

1. Introduction

Precipitation information has been regarded as one of the important information sources for understanding hydrological, ecological, and environmental systems [1–3]. This information can be obtained from either rain gauge station data or remote sensing data. Although precise precipitation information can be obtained from rain gauge data, few rain gauge data are usually available, which may hinder the generation of reliable maps. Remote sensing data that can provide periodic and exhaustive information can be effectively used to map precipitation information. For example, the Global Precipitation Climatology Project (GPCP) [4] and the Tropical Rainfall Measuring Mission (TRMM) [5] provide precipitation data at regional and global scales [3]. As an international satellite mission, the Global Precipitation Measurement (GPM) mission, scheduled to launch in 2014, will also provide next-generation observations of rain and snow worldwide [6]. Although these missions or projects can provide time-series precipitation information, their spatial resolutions are too coarse to be applied to local analysis (e.g., the finest resolution from TRMM data is 0.25 degree).

In hydrological, ecological, and environmental modeling, various data sets acquired at the different scales are generally used as inputs in addition to precipitation data. Thus, scale conversion or change of support is usually required for the consistent analysis. When coarse scale precipitation data and other fine scale data sets are available; for example, downscaling of the coarse scale precipitation data is required before subsequent modeling is conducted. Downscaling can be regarded as the spatial prediction of unknown values at a finer scale from coarse scale data. In relation to this kind of change of support, several statistical downscaling schemes have been proposed and applied to various research fields [7–11]. The spatial downscaling of coarse scale data can be categorized into two cases according to data availability. In the first case, in which ground measurements are simultaneously available, calibration of the coarse scale data and integration for downscaling are enabled by using the ground measurement data. In the second case, in which no ground measurements are available, direct downscaling of the coarse scale data is only feasible by using spatial correlation information from the available data. If auxiliary environment

variables that are related to the primary attribute of interest are acquired at a relatively finer scale, these data can improve the quality of the downscaling result.

Regarding downscaling of coarse scale precipitation data, auxiliary environmental variables such as topography and vegetation have been used for downscaling with regression analysis [12–17]. Regression analysis can account for the statistical relationships between precipitation and environmental variables, but residuals that cannot be explained by the auxiliary variables usually remain after regression analysis. If the auxiliary variables fail to convey sufficient information on precipitation patterns, the residuals cannot be discarded, resulting in unreliability in the downscaling results. Conventional regression analysis follows the assumption that residuals are spatially independent or uncorrelated. If reasonable spatial correlation structures are observed in the residuals, this correlation information can improve the quality of the downscaling. Recently, Jia et al. [3] proposed a statistical scheme for the downscaling of TRMM data with fine scale elevation and normalized difference vegetation index (NDVI). They first conducted multiple regression analysis at various spatial scales then interpolated the residuals to the fine scale grid, and finally generated downscaling results by adding the trend component by regression analysis at an optimal spatial scale to the residuals at a fine scale. During the interpolation of the residuals, however, they neither considered the spatial patterns nor examined the reproduction of original TRMM values.

Geostatistics has been known as an effective tool for scale conversion and data integration [18, 19]. Spatial downscaling or disaggregation based on geostatistics has been applied to various fields such as land-cover mapping [20], population density estimation [21], and image sharpening [22]. Despite its great potential for spatial downscaling, geostatistics has not, to the author's knowledge, been applied to the downscaling of coarse scale TRMM data with fine scale environmental variables.

In this paper, a geostatistical downscaling scheme is presented that incorporates multiple fine scale environmental variables into downscaling of coarse scale TRMM data in the absence of any ground measurement data. Geostatistical downscaling and data integration are implemented by using area-to-point residual kriging with regression. Elevation and NDVI at a fine scale, which are related to precipitation patterns, are used as auxiliary environmental variables for downscaling of TRMM data. Regression analysis is first conducted to derive statistical relationships between TRMM data and auxiliary environmental variables at an original coarse scale. Then residuals at the coarse scale are downscaled to a finer scale via area-to-point residual kriging by accounting for the spatial correlation information of the input residuals [23]. The final downscaling results are obtained by adding the downscaled residuals to the trend components estimated by regression analysis. This approach can reproduce the original TRMM precipitation values when the downscaling results at a fine scale are upscaled or aggregated to the coarse scale. To quantify the uncertainty of downscaling, stochastic simulation based on block sequential simulation is also implemented. A downscaling experiment using the data sets from

South Korea is carried out to examine the potential and demonstrate the applicability of the presented geostatistical scheme for downscaling.

2. Study Area and Data Sets

For the downscaling experiment, the TRMM 3B43 data acquired in October 2005 over South Korea were experimentally used. The original TRMM data that provide precipitation rates (mm/h) at a 0.25° scale were geocoded to Transverse Mercator (TM) coordinates with a spatial resolution of 25 km, and converted to monthly cumulative precipitation at a cm scale (Figure 1(a)). Both digital elevation model (DEM) and NDVI data at 1 km resolution were used as fine scale auxiliary variables, for topography and a proxy for vegetation, respectively. The DEM was generated from digital topographic maps and MODIS monthly NDVI data were used (Figures 1(b) and 1(c)). DEM and NDVI values at land areas were only considered and sea areas were masked out. Independent precipitation data observed at 69 meteorological observation stations in October 2005 were used to quantitatively evaluate the predictive performance of the presented downscaling scheme. In this experiment, the target scale was set to 1 km, which is the same as that of DEM and NDVI.

3. Geostatistical Downscaling

The geostatistical downscaling scheme presented in this paper is summarized in Figure 2. The main key idea of this approach is that TRMM precipitation values are decomposed into deterministic trends and stochastic residuals. The trend components are estimated using auxiliary environmental variables such as DEM and NDVI. More specifically, statistical relationships between original precipitation values and multiple environmental variables at a coarse scale are first derived via multiple regression analysis. Under the assumption that attribute values at a coarse scale are linear averages of their constituent fine scale point values, these relationships are applied to environmental variables at a fine scale and finally trend components are estimated at a fine scale.

Suppose that a study area of interest consists of K TRMM precipitation blocks acquired at a coarse scale $\{z(v_k), k = 1, \dots, K\}$, where $v_k = v(\mathbf{u}_k)$ is the k th data with its centroid \mathbf{u}_k . In this study, the TRMM data at a coarse scale are regarded as block data. Other data sources are M auxiliary fine scale environmental variables $\{y_i^k(\mathbf{u}_n), i = 1, \dots, M, n = 1, \dots, N\}$ within each k th block data. N denotes the number of discretizing points within each block and its determination depends on the predefined finer scale value.

If the environmental variables show linear relationships with the TRMM precipitation values, the TRMM precipitation data at both coarse and fine scales can be expressed in terms of the environmental variables via multiple linear regression analysis as

$$z(v_k) = a + \sum_{i=1}^M b_i \cdot y_i(v_k) + R(v_k),$$

$$z^k(\mathbf{u}_n) = a + \sum_{i=1}^M b_i \cdot y_i^k(\mathbf{u}_n) + R^k(\mathbf{u}_n),$$
(1)

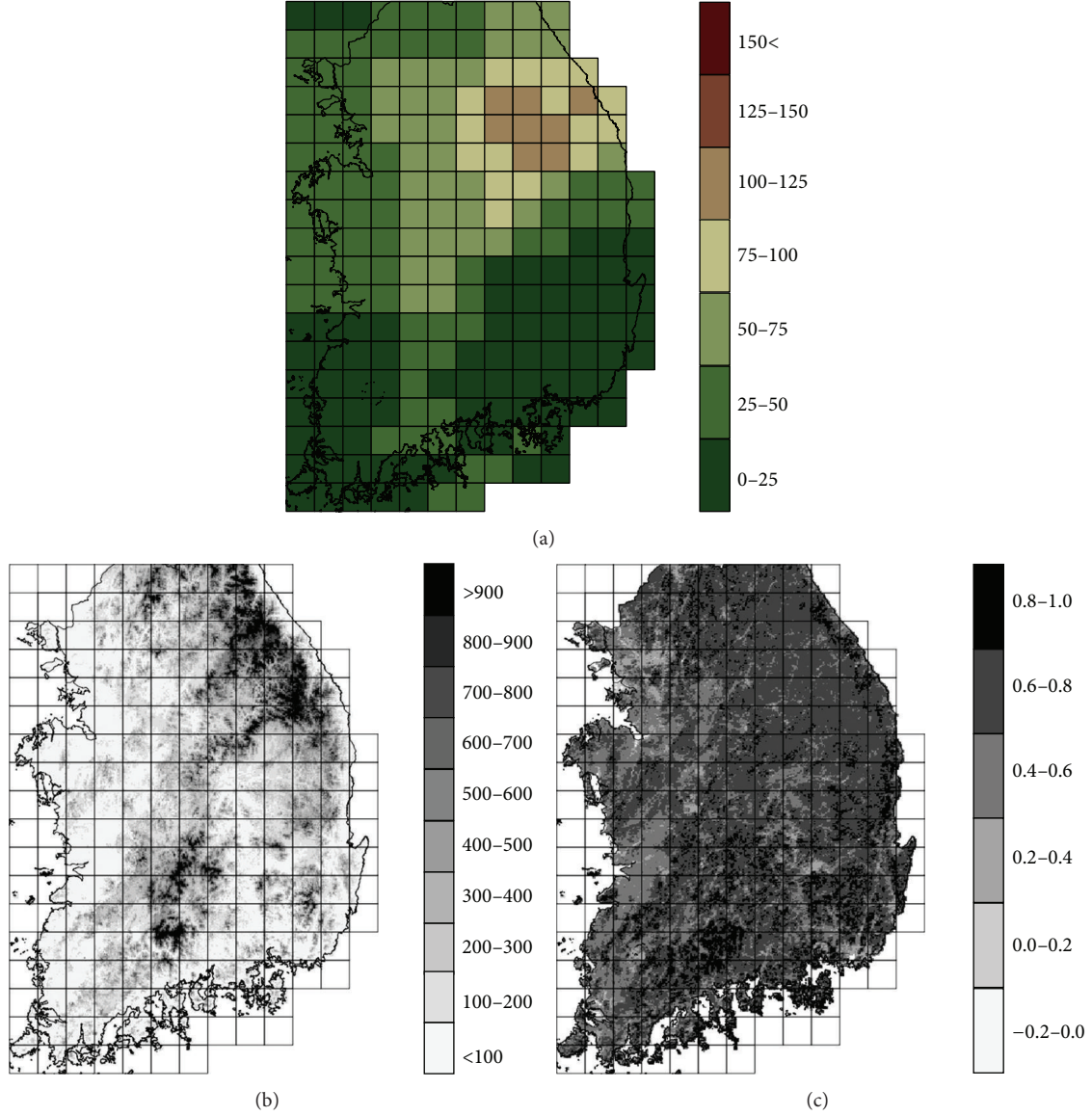


FIGURE 1: Data sets used for the downscaling experiment: (a) TRMM precipitation data (unit: mm), (b) DEM (unit: m), and (c) NDVI. The rectangles denote TRMM blocks and the size of each block is 25 km by 25 km.

where a and b_i are regression coefficients for the intercept and slope of the i th variable, respectively. $z^k(\mathbf{u}_n)$ is the downscaled precipitation value at a target finer scale within the k th block data. $R(v_k)$ and $R^k(\mathbf{u}_n)$ denote the residual components at coarse and fine scales, respectively, which cannot be accounted for by environmental variables.

If the original TRMM data, auxiliary environmental variables, and the residual components at a coarse scale can be expressed by the average values of N fine scale data within each block, respectively, (1) can be reformulated as (2)

$$z(v_k) = a + \sum_{i=1}^M b_i \left[\frac{1}{N} \sum_{n=1}^N y_i^k(\mathbf{u}_n) \right] + \frac{1}{N} \sum_{n=1}^N R^k(\mathbf{u}_n)$$

$$= \frac{1}{N} \sum_{n=1}^N \left[a + \sum_{i=1}^M b_i y_i^k(\mathbf{u}_n) + R^k(\mathbf{u}_n) \right]$$

$$= \frac{1}{N} \sum_{n=1}^N z^k(\mathbf{u}_n). \quad (2)$$

To obtain the downscaled precipitation value ($z^k(\mathbf{u}_n)$), the residual component value ($R^k(\mathbf{u}_n)$) at a fine scale needs to be determined from (2), because the regression coefficients have already been determined from (1). To predict residual components at a fine scale, area-to-point simple kriging proposed in Kyriakidis [23] is applied to the residual components available at a coarse scale. Area-to-point simple kriging predicts the residual component values at a fine scale by a linear combination of neighboring attribute values at a coarse scale [23, 24], as shown in (3):

$$R^k(\mathbf{u}_n) = \sum_{k=1}^K \lambda_k(\mathbf{u}_n) R(v_k), \quad (3)$$

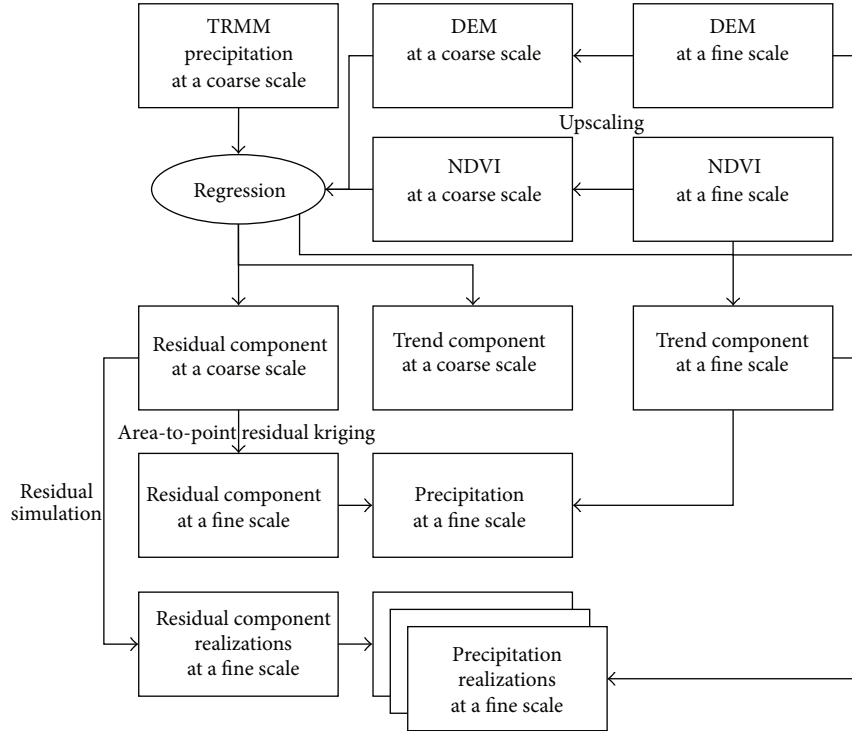


FIGURE 2: Work flows for geostatistical downscaling of coarse scale TRMM precipitation data.

where $\lambda_k(\mathbf{u}_n)$ is a simple kriging weight assigned to the neighboring block residual component $R(v_k)$ at a prediction location. Since the mean value of the residual component is zero, a constant mean value required for simple kriging is set to zero and does not appear in (3).

The simple kriging weight is computed by solving the following simple block kriging system:

$$\sum_{k=1}^K \lambda_k(\mathbf{u}_n) \bar{C}(v_k, v_l) = \bar{C}(v_k, \mathbf{u}_n) \quad k = 1, \dots, K, \quad (4)$$

where $\bar{C}(v_k, v_l)$ and $\bar{C}(v_k, \mathbf{u}_n)$ refer to block-to-block covariance and block-to-point covariance, respectively.

Unlike conventional punctual kriging algorithms, both block-to-block and block-to-point covariances are required to compute the simple kriging weights. These two covariance values can be computed by averaging point covariance values such as the conventional block kriging system [24, 25]. The block-to-block covariance can be computed by averaging the covariance values between any two points discretizing two blocks. The covariance values between the point location and a set of points discretizing the block are averaged to obtain the block-to-point covariance. Thus, a point-support covariance (equivalently, variogram) is required to obtain the above two covariance values. However, only residuals at a coarse scale are available, so it is not feasible to directly obtain the point-support variogram. In relation to this issue, Goovaerts [24] proposed an iterative deconvolution procedure to estimate the point-support variogram from block or areal data irrespective of their shapes. Variogram deconvolution iteratively

finds an optimal point-support variogram model that minimizes the difference between the regularized variogram and the variogram of the coarse scale data [24]. More specifically, after defining an initial point-support variogram model, the theoretically regularized model is computed and compared with the variogram of the coarse scale data. By computing the difference statistic from those two models, the parameters of the point-support variogram model are adjusted to minimize that difference statistic. This procedure is iteratively repeated until the stop criteria are satisfied [24, pp.113–115].

After computing the point-support variogram, the simple kriging weight is computed using (4) and then residual component values at a fine scale are predicted using (3). The final downscaling results are obtained by adding the predicted residual component at a fine scale to the trend component that can be directly computed by applying regression relationships to the auxiliary environmental variable at a fine scale in (1).

An interesting property of area-to-point kriging is its ability for coherent predictions, which means that the average of the predicted values at the fine scale points discretizing a given block reproduces the original block data value [23]. Since the residual component at a fine scale is generated by preserving this coherence property, the final downscaling results could reproduce the original TRMM precipitation values when upscaled.

The downscaling results by area-to-point residual kriging with regression are optimal in the least-squares sense. As discussed in Boucher and Kyriakidis [20]; however, downscaling should be regarded as a kind of under-determined inversion process, since there are many possible attribute values at

a fine scale that lead to the same original values at a coarse scale when upscaled. Thus, stochastic simulation, which can generate multiple alternative realizations of unknown truth at a fine scale, is also applied for downscaling of residual components at a coarse scale. Block sequential simulation proposed by Liu and Journel [26] is applied in this study. By adopting the concept of direct sequential simulation, simulation does not require any data transformation unlike sequential Gaussian simulation. Originally, this simulation algorithm was developed to combine kriging using both block and point data with direct sequential simulation [19, 26]. As only block data (i.e., TRMM precipitation data) are available in this downscaling study, block sequential simulation with block data is implemented to generate multiple downscaling realizations. The same point-support variogram model estimated from variogram deconvolution is also used for simulation. Like the prediction by area-to-point kriging, residuals at a coarse scale are first simulated at a fine scale and final simulation results are obtained by adding the simulated residual components to the trend components.

Simulation aims at generating a set of alternative realizations with the reproduction of spatial patterns, not a single downscaling result like kriging. By comparing the differences between multiple realizations, the uncertainty attached to the prediction can be quantified. In this study, conditional variance values are computed and used as an uncertainty measure.

4. Results and Discussion

4.1. Regression Analysis Results. First, regression analysis was applied to derive statistical relationships between precipitation and the two environmental variables at the original 25 km resolution. For this analysis, DEM and NDVI were upscaled to 25 km resolution data via linear averaging. The linear correlation coefficients between precipitation and environmental variables were 0.56 and 0.26 for DEM and NDVI, respectively. In addition to the two variables, the interaction of DEM with NDVI was included in the multiple regression analysis, since forest areas showing high NDVI values tend to be located in high altitude zones (the linear correlation coefficient between DEM and NDVI was 0.65). From backward stepwise elimination, DEM and the interaction of DEM with NDVI were finally chosen as statistically significant variables and the regression relation between precipitation and those two variables was modeled as

$$z^*(v_k) = 17.508 + 0.513 \text{ DEM}(v_k) - 0.592 \text{ DEM}(v_k) \cdot \text{NDVI}(v_k), \quad (5)$$

where $z^*(v_k)$, $\text{DEM}(v_k)$, and $\text{NDVI}(v_k)$ are the estimated mean (trend component) from regression analysis, DEM, and NDVI values at a block location, respectively. This regression relationship was also applied to the same variables to generate the trend components at 1 km resolution.

The coefficient of determination (R^2) was 0.37, which means that about 37% of the variation of precipitation could be accounted for by these two terms. This value of R^2 implies that a simple application of multiple regression for

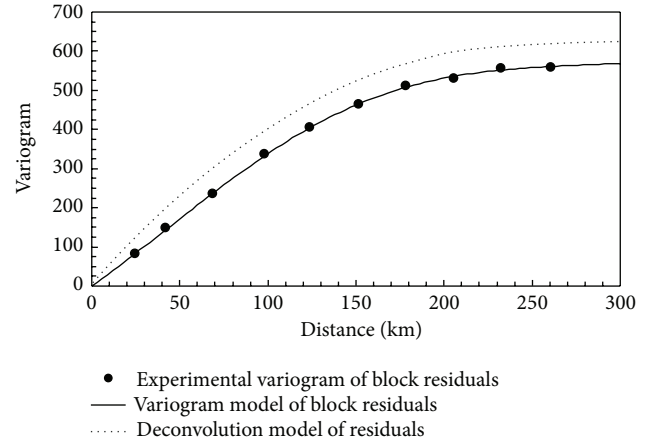


FIGURE 3: Variogram deconvolution results for residual components.

downscaling could not generate reliable downscaling results and that the residuals should be considered for downscaling.

4.2. Variogram Deconvolution Results. After generating residual components from regression analysis at original 25 km resolution, variogram deconvolution was applied to estimate the unknown point-support variogram of the residuals and implemented using SpaceStat software (BioMedware). By considering the target resolution (i.e., 1 km), each block of TRMM data at 25 km resolution was discretized by 25 by 25 points at 1 km resolution.

The variogram deconvolution result is shown in Figure 3. The variogram of residual components at 25 km resolution had a bounded correlation structure with a range of about 266 km. The deconvoluted point-support variogram, which, once regularized, was the most similar to the variogram model of residuals at 25 km resolution, had a greater sill value than that of the residual components at 25 km resolution. It also showed a reasonable correlation structure with two spherical models showing short- and long-range correlation structures, respectively. This bounded variogram model implies that the residual components were spatially correlated unlike the assumption of spatial independence of residuals in regression. Such spatial correlation of the residual components was accounted for in the estimation and simulation of residuals.

4.3. Area-to-Point Residual Kriging Results. The residual components at 1 km resolution were estimated by area-to-point kriging using SpaceStat software and then added to the trend components. To investigate the effects of using auxiliary environmental variables on downscaling results, the original TRMM data were directly downscaled without DEM and NDVI by applying area-to-point kriging to the original block values, not to the residuals. The point-support variogram model of the original TRMM data was also estimated by variogram deconvolution.

The two downscaling results generated by area-to-point kriging are shown in Figure 4. Overall patterns of both downscaling results were very similar to those of the coarse scale

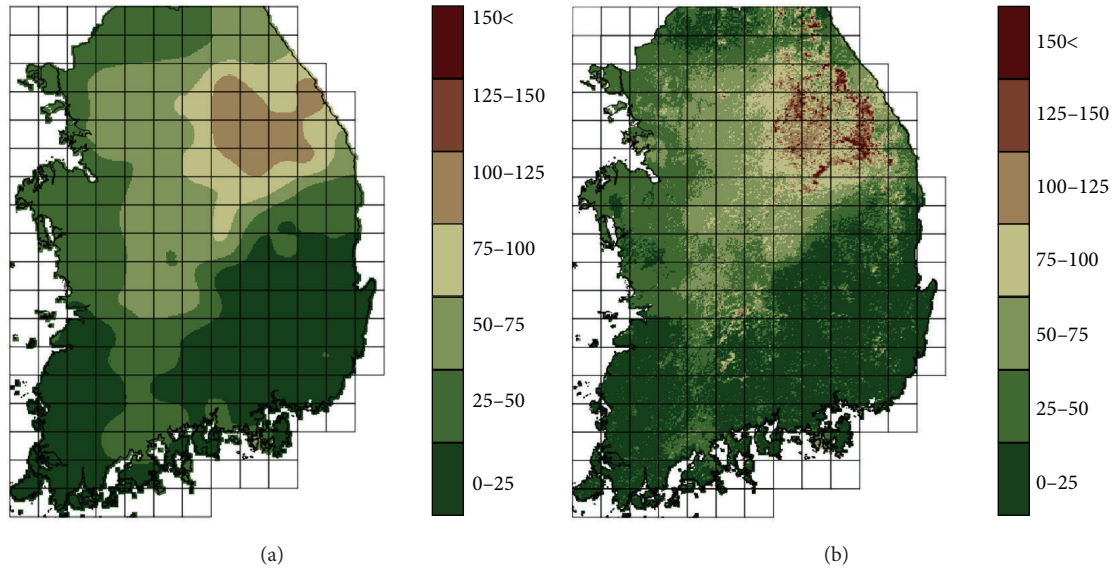


FIGURE 4: Downscaling results by area-to-point residual kriging: (a) downscaling without DEM and NDVI and (b) downscaling with DEM and NDVI.

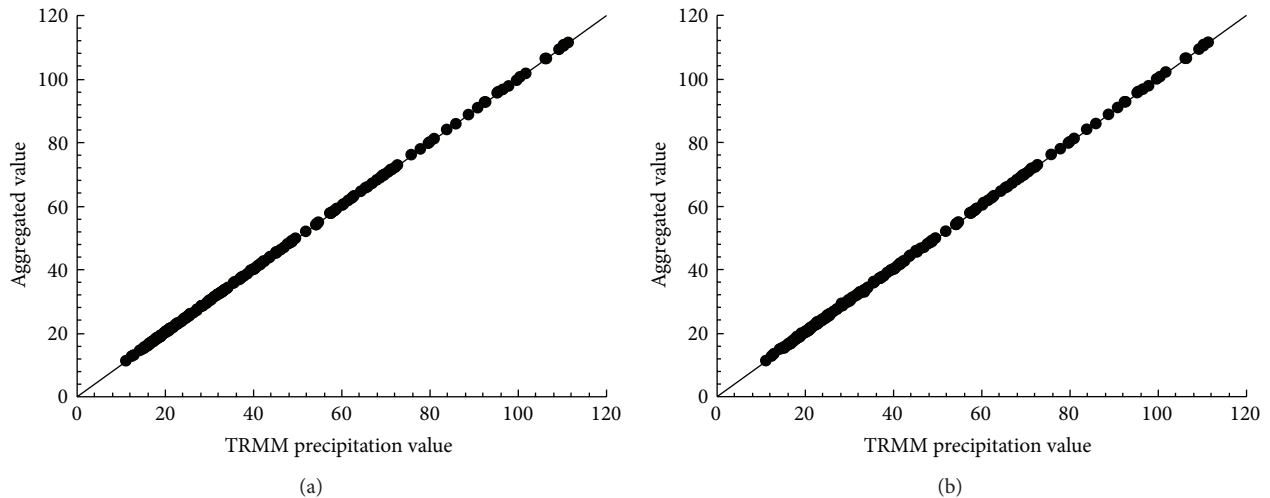


FIGURE 5: Scatterplots of the original TRMM precipitation values versus averages of area-to-point kriging estimates within each block: (a) downscaling without DEM and NDVI and (b) downscaling with DEM and NDVI.

TRMM data in Figure 1(a) (e.g., high precipitation values in Kangwon province areas). As expected, however, the direct downscaling results of the original TRMM data without DEM and NDVI showed very smoothly varying patterns, compared with that of using DEM and NDVI. In addition, local details that reflect both topographic and vegetation patterns were observed in the downscaling result with DEM and NDVI. When both downscaling results were averaged within the original 25 km resolution block, the coherence property was well preserved (Figure 5). The downscaling result without DEM and NDVI perfectly satisfied the coherence property. In the downscaling result with DEM and NDVI, the averaged values at some blocks were slightly different from the original block value. This small discrepancy was observed at some

blocks where only small portions were occupied by lands or islands, and elevation and NDVI values at a finer scale were only available at those land areas. Average values were computed from the land areas within such blocks and sea areas were not considered, which resulted in the slight discrepancy. However, this difference was negligible and the coherency property was well satisfied.

To quantitatively evaluate the effects of using environmental data for downscaling, precipitation values at 69 meteorological observation stations were compared with those of two downscaling results. The predictive performance was quantified using the mean absolute error (MAE) and the root mean square error (RMSE), and validation results are presented in Table 1. As expected, the incorporation

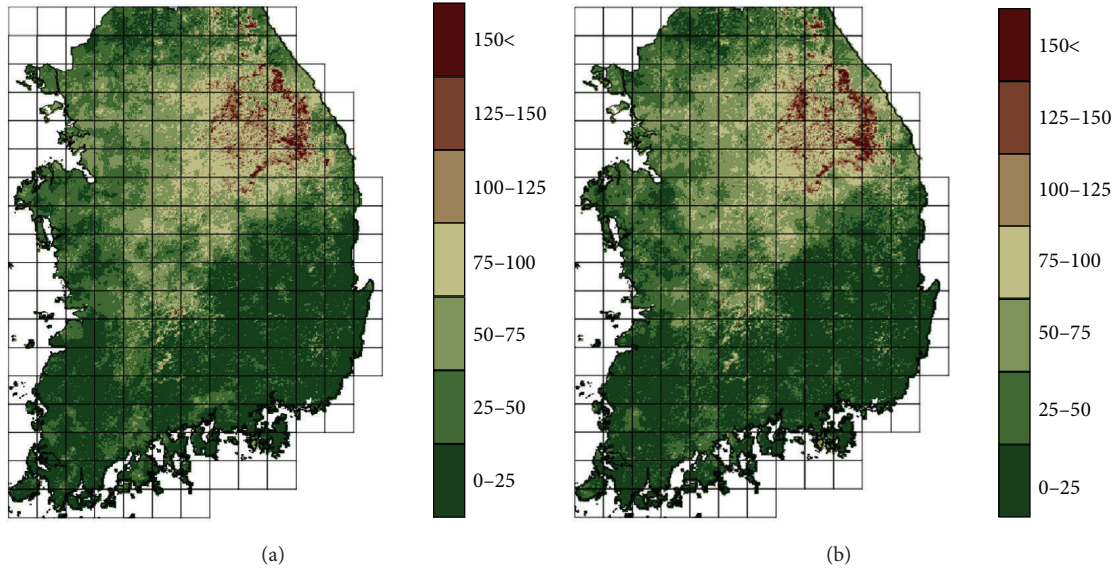


FIGURE 6: Simulation results: (a) 1st realization and (b) 10th realization.

TABLE 1: Predictive performance evaluation results.

	Downscaling without DEM and NDVI using area-to-point kriging	Downscaling with DEM and NDVI using area-to-point residual kriging	Downscaling with DEM and NDVI using ordinary kriging of residuals
MAE	19.98	13.03	17.73
Relative improvement of MAE	—	34.78%	11.30%
RMSE	27.49	20.03	24.81
Relative improvement of RMSE	—	27.14%	9.75%

of DEM and NDVI showed smaller prediction errors and improved MAE and RMSE by 34.78% and 27.14%, respectively, compared to the downscaling without the auxiliary variables. In addition, point ordinary kriging of residuals at the centroid points of original TRMM blocks was also applied to highlight the advantage of area-to-point residual kriging. The variogram model of residuals at 25 km resolution was used for implementation of point ordinary kriging. The predictive performance of point ordinary kriging of residuals showed improved MAE and RMSE (11.30% and 9.75%, resp.), compared to the downscaling without DEM and NDVI via area-to-point kriging (Table 1). However, this result comes mainly from using the auxiliary variables such as DEM and NDVI, regardless of the kriging algorithms applied to the downscaling of residuals. Point ordinary kriging of residuals showed poorer predictive performance than area-to-point residual kriging. In addition, the downscaling result by point ordinary kriging of residuals could not reproduce the original TRMM precipitation values when upscaled.

These quantitative evaluation results confirmed that using both fine scale auxiliary environmental variables and spatial correlation information of residuals within the presented geostatistical scheme can generate reliable downscaling results with better predictive performance, compared to the case without fine scale environmental variables. Regarding downscaling of residuals, the presented geostatistical scheme based on area-to-point residual kriging could account for the support difference between the target scale and the input data scale, and outperformed the simple application of conventional interpolation methods by treating coarse scale block data as point data.

4.4. Simulation Results. Block sequential simulation was implemented using SGeMS software [19] and 50 alternative realizations of precipitation at 1 km resolution were generated. Two of the 50 realizations are given in Figure 6. The overall patterns in the simulation results were similar to those in the kriging result, but local variations were much stronger in the simulation results, which was the typical property of the simulation. When averaged within original 25 km resolution blocks, all realizations well satisfied the coherence property (results are not shown here).

Two summary statistics can be computed from the 50 realizations, the E-type (average) estimate and conditional variance for the overall pattern and the uncertainty measure, respectively, and are given in Figure 7. The E-type estimate and the kriging result in Figure 4(b) showed very similar spatial patterns. Unlike kriging variance that cannot include the effects of surrounding data values [18], conditional variance computed from the 50 realizations, which reflect the differences among the 50 alternative realizations, can be used as a quantitative measure of uncertainty. The lower variance values, which imply few differences among the 50 realizations and, therefore, lower uncertainty, were mainly observed in the southern parts where negative residuals were computed and smaller precipitation values were predicted.

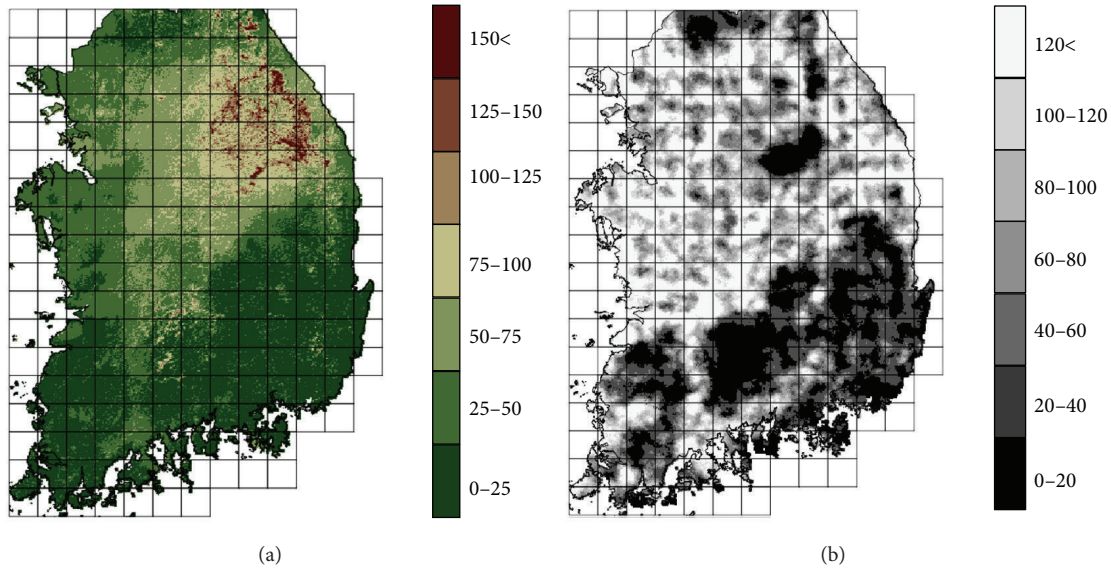


FIGURE 7: Summary statistics values computed from 50 simulations: (a) E-type estimate and (b) conditional variance.

It should be noted that the ultimate goal of stochastic simulation is to generate alternative realizations that can be used for quantification of uncertainty attached to the spatial prediction or downscaling [18, 19], rather than either to generate the E-type estimate as shown in Figure 7(a). More importantly, all realizations are equi-probable or equally important [27], and a single best realization showing the best predictive performance should not be looked for, as discussed in Boucher and Kyriakidis [20]. A set of alternative realizations can be used for modeling the uncertainty about the unknown true precipitation at a fine scale. For example, each downscaled precipitation realization can be fed into hydrological models to generate numerous model outputs. By analyzing these model outputs, the impacts of uncertainty about precipitation information on model outputs (i.e., error or uncertainty propagation) can be investigated. Although multiple alternative realizations and summary statistics were generated via simulation in this experiment, this kind of error or uncertainty propagation problem should be regarded as an important application using simulation.

5. Conclusions

This paper has demonstrated the application of geostatistical kriging and simulation to integrate auxiliary fine scale environmental variables for downscaling of precipitation values derived from coarse scale TRMM data. The environmental variables contribute to the determination of trend components via regression analysis. The residual components that have a reasonable spatial correlation structure are accounted for during downscaling.

An experiment on downscaling of TRMM precipitation data with DEM and NDVI produced reliable downscaling results that not only preserved overall patterns in the original TRMM data, but also presented local details from DEM and NDVI. Improved predictive performance was also obtained, compared to the downscaling without the auxiliary environmental variables. Stochastic simulation provided much richer

information for uncertainty modeling by generating multiple alternative realizations, unlike the single downscaling result by kriging.

The geostatistical downscaling scheme presented in this paper can be applied to areas in which ground measurement data are very sparse or even unavailable, especially in developing countries. Fine scale DEM and NDVI can be obtained from the Shuttle Radar Topography Mission (SRTM) DEM and MODIS data, respectively, and hence used effectively for downscaling of precipitation data in such areas. In addition to downscaling of TRMM precipitation data, the presented scheme can also be extended and generalized to downscaling of other coarse scale remote sensing data, such as coarse scale soil moisture data from the Soil Moisture and Ocean Salinity (SMOS) mission.

The applicability of the presented geostatistical downscaling scheme has been tested on only one TRMM data in this study. The time-series data sets are usually considered in any precipitation patterns analyses. Therefore, more extensive experiments using time-series TRMM precipitation data sets will be required to confirm the major findings of this study. The impacts of variations in correlation strengths between precipitation data and auxiliary variables on downscaling performance should also be included in future work.

Acknowledgments

This research was supported by the Basic Science Research Program through the National Research Foundation of Korea (NRF) funded by the Ministry of Science, ICT, and Future Planning (NRF-2012R1A1A1005024).

References

- [1] P. Goovaerts, "Geostatistical approaches for incorporating elevation into the spatial interpolation of rainfall," *Journal of Hydrology*, vol. 228, no. 1-2, pp. 113-129, 2000.

- [2] P. C. Kyriakidis, J. Kim, and N. L. Miller, "Geostatistical mapping of precipitation from rain gauge data using atmospheric and terrain characteristics," *Journal of Applied Meteorology*, vol. 40, no. 11, pp. 1855–1877, 2001.
- [3] S. Jia, W. Zhu, A. Lü, and T. Yan, "A statistical spatial downscaling algorithm of TRMM precipitation based on NDVI and DEM in the Qaidam Basin of China," *Remote Sensing of Environment*, vol. 115, no. 12, pp. 3069–3079, 2011.
- [4] G. J. Huffman, R. F. Adler, D. T. Bolvin, and G. Gu, "Improving the global precipitation record: GPCP version 2.1," *Geophysical Research Letters*, vol. 36, no. 17, Article ID L17808, 2009.
- [5] C. Kummerow, W. Barnes, T. Kozu, J. Shiue, and J. Simpson, "The Tropical Rainfall Measuring Mission (TRMM) sensor package," *Journal of Atmospheric and Oceanic Technology*, vol. 15, no. 3, pp. 809–817, 1998.
- [6] A. Y. Hou and G. Skofronick-Jackson, "GPM mission overview and US science status," in *Proceedings of the IEEE International Geoscience and Remote Sensing Symposium (IGARSS '13)*, Melbourne, Australia, 2013.
- [7] D. Harris and E. Foufoula-Georgiou, "Subgrid variability and stochastic downscaling of modeled clouds: effects on radiative transfer computations for rainfall retrieval," *Journal of Geophysical Research D*, vol. 106, no. 10, pp. 10349–10362, 2001.
- [8] A. J. Tatem, H. G. Lewis, P. M. Atkinson, and M. S. Nixon, "Super-resolution land cover pattern prediction using a Hopfield neural network," *Remote Sensing of Environment*, vol. 79, no. 1, pp. 1–14, 2002.
- [9] G. Kim and A. P. Barros, "Downscaling of remotely sensed soil moisture with a modified fractal interpolation method using contraction mapping and ancillary data," *Remote Sensing of Environment*, vol. 83, no. 3, pp. 400–413, 2002.
- [10] Y. H. Kaheil, M. K. Gill, M. McKee, L. A. Bastidas, and E. Rosero, "Downscaling and assimilation of surface soil moisture using ground truth measurements," *IEEE Transactions on Geoscience and Remote Sensing*, vol. 46, no. 5, pp. 1375–1384, 2008.
- [11] D. Liu and R. Pu, "Downscaling thermal infrared radiance for subpixel land surface temperature retrieval," *Sensors*, vol. 8, no. 4, pp. 2695–2706, 2008.
- [12] G. Wotling, C. Bouvier, J. Danloux, and J.-M. Fritsch, "Regionalization of extreme precipitation distribution using the principal components of the topographical environment," *Journal of Hydrology*, vol. 233, no. 1–4, pp. 86–101, 2000.
- [13] D. K. Nykanen and D. Harris, "Orographic influences on the multiscale statistical properties of precipitation," *Journal of Geophysical Research D*, vol. 108, no. 8, 2003.
- [14] R. B. Smith and I. Barstad, "A linear theory of orographic precipitation," *Journal of the Atmospheric Sciences*, vol. 61, no. 12, pp. 1377–1391, 2004.
- [15] M. G. Badas, R. Deidda, and E. Piga, "Orographic influences in rainfall downscaling," *Advances in Geosciences*, vol. 2, pp. 285–292, 2005.
- [16] H. Guan, J. L. Wilson, and H. Xie, "A cluster-optimizing regression-based approach for precipitation spatial downscaling in mountainous terrain," *Journal of Hydrology*, vol. 375, no. 3–4, pp. 578–588, 2009.
- [17] W. W. Immerzeel, M. M. Rutten, and P. Droogers, "Spatial downscaling of TRMM precipitation using vegetative response on the Iberian Peninsula," *Remote Sensing of Environment*, vol. 113, no. 2, pp. 362–370, 2009.
- [18] P. Goovaerts, *Geostatistics for Natural Resources Evaluation*, Applied Geostatistics, Oxford University Press, New York, NY, USA, 1997.
- [19] N. Remy, A. Boucher, and J. Wu, *Applied Geostatistics with SGeMS: A User's Guide*, Cambridge University Press, Cambridge, UK, 2009.
- [20] A. Boucher and P. C. Kyriakidis, "Super-resolution land cover mapping with indicator geostatistics," *Remote Sensing of Environment*, vol. 104, no. 3, pp. 264–282, 2006.
- [21] X. H. Liu, P. C. Kyriakidis, and M. F. Goodchild, "Population-density estimation using regression and area-to-point residual kriging," *International Journal of Geographical Information Science*, vol. 22, no. 4, pp. 431–447, 2008.
- [22] E. Pardo-Iguzquiza, P. M. Atkinson, and M. Chica-Olmo, "DSCOKRI: a library of computer programs for downscaling cokriging in support of remote sensing applications," *Computers & Geosciences*, vol. 36, no. 7, pp. 881–894, 2010.
- [23] P. C. Kyriakidis, "A geostatistical framework for area-to-point spatial interpolation," *Geographical Analysis*, vol. 36, no. 3, pp. 259–289, 2004.
- [24] P. Goovaerts, "Kriging and semivariogram deconvolution in the presence of irregular geographical units," *Mathematical Geosciences*, vol. 40, no. 1, pp. 101–128, 2008.
- [25] A. G. Journel and C. J. Huijbregts, *Mining Geostatistics*, Academic Press, New York, NY, USA, 1978.
- [26] Y. Liu and A. G. Journel, "A package for geostatistical integration of coarse and fine scale data," *Computers & Geosciences*, vol. 35, no. 3, pp. 527–547, 2009.
- [27] A. G. Journel, "Modelling uncertainty and spatial dependence: stochastic imaging," *International Journal of Geographical Information Systems*, vol. 10, no. 5, pp. 517–522, 1996.